A study of diapycnal mixing in the Southern Ocean using a tracer release experiment and numerical models

A thesis submitted to the School of Environmental Sciences of the
University of East Anglia in partial fulfilment of the requirements for the
degree of Doctor of Philosophy

By Neill Mackay
November 2014

Abstract

The Diapycnal and Isopycnal Mixing Experiment in the Southern Ocean (DIMES) includes a tracer release experiment and microstructure programme with the aims of diagnosing the strength and variability of mixing in the Southern Ocean. Here numerical models are used to advect and diffuse a tracer in the Antarctic Circumpolar Current, beginning in the Southeast Pacific and progressing through Drake Passage, and model outputs are then compared with observations from the DIMES tracer. The prescribed diapycnal diffusivity fields within the models are varied between different model runs, and the model parameters are optimised using a cost function to give the best fit to the observations. A simple 2D model with dimensions of along-stream distance and depth yields estimates for diapycnal diffusivity of $1.69 \pm 0.05 \times 10^{-5}\ \mathrm{m}^2\ \mathrm{s}^{-1}$ in the Southeast Pacific west of 67°W, and $3.3 \pm 0.4 \times 10^{-4}\ \mathrm{m}^2\ \mathrm{s}^{-1}$ in Drake Passage between 67°W and 58°W at the $27.9\,\mathrm{kgm}^{-3}$ neutral density surface onto which the tracer was released. A more complex 3D model using an offline version of the MITgcm with time-evolving observation-based velocities from the SatGEM product yields similar estimates of $2.5 \pm 0.1 \times 10^{-5}\ \mathrm{m}^2\ \mathrm{s}^{-1}$ and $3.5 \pm 0.5 \times 10^{-4}\ \mathrm{m}^2\ \mathrm{s}^{-1}$ for the Pacific and Drake Passage, respectively.

Point microstructure dissipation measurements collected as part of DIMES are used to construct three-dimensional diffusivity fields which are then used in conjunction with the 3D model to test whether the mixing rates inferred from microstructure and the tracer measurements are consistent with one another. Good agreement is found in the Southeast Pacific, but in Drake Passage, where both topography and current field becomes more heterogeneous, the microstructure estimates are 5 times too low to account for the time and spatially averaged mixing implied by the tracer. By contrast, model diffusivities constructed using predicted rates of lee wave generation from modified linear theory predict the along-stream variation in tracer vertical profile widths reasonably well throughout the model domain, but do not capture the across-stream variation.

Acknowledgements

I would like to thank my supervisors, Marie-Jose Messias, Andy Watson and Alberto Naveira-Garabato for guiding me through this PhD and for all their advice and positive encouragement, and Xiaoming Zhai who joined the project in its final stages and gave up considerable time to helping me with my work over the last few months. I would also like to thank my colleagues on the DIMES project, in particular Jim Ledwell who has been like another member of my supervisory team, always available to offer prompt, detailed and helpful advice on whatever issues arose with my research. Thanks also to my examiners Karen Heywood and Jean-Baptiste Sallee for making my viva an enjoyable experience. Finally my thanks to friends and colleagues Rob Hall for advice on internal wavey-type matters, Ben Webber for being generally clever and helpful, Barnaby Andrews for being a good friend when life provided unwelcome distractions, and Ben Mills for his advice, his unfailingly positive outlook and assurances that the project was “in the bag”.

Contents

List of tables

List of figures

Chapter 1

Introduction

1.1 Motivation

The meridional overturning circulation (MOC) of the global ocean plays an important role in the Earth's climate, and the understanding of the processes that drive it is therefore crucial to our ability to predict how the climate will respond under changing conditions. The MOC is responsible for the transport of up to 5 petawatts of heat meridionally, and mediates the exchange of climatically important gases such as carbon dioxide between the ocean and the atmosphere (Trenberth and Caron, 2001; Rahmstorf, 2002). Diapycnal mixing is a process central to the overturning, as it allows dense, deep waters created at high latitudes to be returned to mid-depths in the ocean (Munk and Wunsch, 1998; Marshall and Speer, 2012). However, the mixing is not well represented in general circulation models, and this shortcoming contributes significantly to explaining the divergence in behaviour between these models (Ferrari and Wunsch, 2009). Over the past two decades, field campaigns aimed at measuring diapycnal diffusivities in the ocean have found its distribution to be very inhomogeneous, with enhanced mixing observed in specific locations near rough topography (e.g. Polzin *et al.*, 1997; Ledwell *et al.*, 2000; St. Laurent *et al.*, 2001), and in particular that significant mixing takes place in certain regions of the Southern Ocean (e.g. Naveira Garabato *et al.*, 2004; Waterman *et al.*, 2013). Such studies have made use of finestructure and microstructure measurements, which rely on certain assumptions to arrive at estimates of mixing (see section 1.3). This thesis makes use of a direct measurement of mixing obtained through a tracer release experiment which was conducted as part of the Diapycnal and Isopycnal Mixing Experiment in the Southern

Ocean (DIMES, see section 2.1), combined with numerical models to study the strength and distribution of diapycnal mixing in and around the Drake Passage region of the Southern Ocean in order to advance our understanding of this important physical process.

1.2 Diapycnal mixing and the overturning circulation

1.2.1 Closing the circulation

The MOC transports heat, carbon and nutrients around the globe and regulates their storage in the deep ocean by providing a link with the atmosphere (Rahmstorf, 2002). Cold, dense water created near the poles due to cooling at the surface by the winds and brine rejection from sea ice formation sinks to great depths in these regions, and must eventually return to the surface in order to 'close' the global circulation (e.g. Munk, 1966; Marshall and Schott, 1999; Hughes and Griffiths, 2006). In the absence of a compensating upwelling of water, the ocean would fill up from the bottom with such waters, becoming unstratified with a thin boundary layer at the surface (Sandstrom, 1908). One way this return flow can be achieved is through diapycnal mixing (across density surfaces) of the dense bottom water with less dense water from above. Such mixing occurs due to the action of 3D small-scale turbulence, and is quantified in terms of an 'eddy' diffusivity K_z (Gregg, 1987). Stommel and Arons (1960) proposed a model of the circulation in which dense water produced in concentrated sources near Antarctica (Antarctic Bottom Water or AABW) and in the North Atlantic (North Atlantic Deep Water or NADW) is brought back to the surface uniformly across the ocean by diapycnal mixing which balances the bottom water formation and thereby closes the overturning circulation.

1.2.2 Munk balance

Based on the theory of uniform upwelling across the whole ocean, Munk (1966) developed a model to estimate the diapycnal diffusivity required to balance the generation of an estimated 25 Sverdrups (1 Sv = 10^6 m^{3}s^{-1}) of bottom water and maintain the abyssal stratification. The one-dimensional equation for a tracer i in steady state is:

$$K_z \frac{\partial^2 C_i}{\partial z^2} = w \frac{\partial C_i}{\partial z} + J = 0 \tag{1.1}$$

where $C_i(z)$ is the distribution of tracer with depth, w is the upwelling velocity and J is a rate of production or loss. Munk fitted profiles of potential temperature and salinity to analytical solutions of equation 1.1 with $J = 0$ to find an estimate for K_z/w, and profiles of Carbon-14 to the full equation to find K_z/w^2. Then solving for both, he found $K_z = 1.3 \times 10^{-4}\ \mathrm{m}^2\,\mathrm{s}^{-1}$. This is several orders of magnitude larger than the values of thermal diffusivity that are found in water due to molecular processes, typically $\sim 10^{-7}\mathrm{m}^2\mathrm{s}^{-1}$ (Gill, 1982). The implication is that the mixing in the ocean must be dominated by turbulent, rather than molecular diffusion.

1.2.3 Localised mixing

In the years following Munk's calculation, a number of efforts were made to measure K_z in the ocean, and it was found in the interior to be around $10^{-5}\mathrm{m}^2\,\mathrm{s}^{-1}$, an order of magnitude smaller than predicted (e.g Ledwell and Watson, 1991; Ledwell *et al.*, 1998; Polzin *et al.*, 1997, see section 1.4 for details). Early evidence from studies in lakes, fjords and in the ocean had suggested a dependence of K_z on the buoyancy frequency N (Gargett, 1984), but more recent work had found enhanced diffusivities near the bottom above certain topography, settling back down to the 'pelagic' background rate a few hundred metres above or a few kilometres away from it (e.g. Polzin *et al.*, 1997; Rudnick *et al.*, 2003, see section 1.4.4). Munk and Wunsch (1998)'s revised picture was then presented as $K_z = 10^{-5}\mathrm{m}^2\,\mathrm{s}^{-1}$ over most of the ocean, with the effects of enhanced mixing at the boundaries being translated into the interior by along-isopycnal processes. It was noted by Muller and Briscoe (2000) that, based on evidence at that time, boundary mixing probably could not account for the required $10^{-4}\mathrm{m}^2\,\mathrm{s}^{-1}$ of mixing in the pycnocline, unless mixing 'hotspots' had been missed by observations. Much work in the intervening period leading up to the present day has gone into locating and sampling these hotspots, but it is now generally accepted that while diapycnal mixing still must play a role in maintaining the abyssal stratification and closing the overturning circulation, the picture is more complex than was first thought.

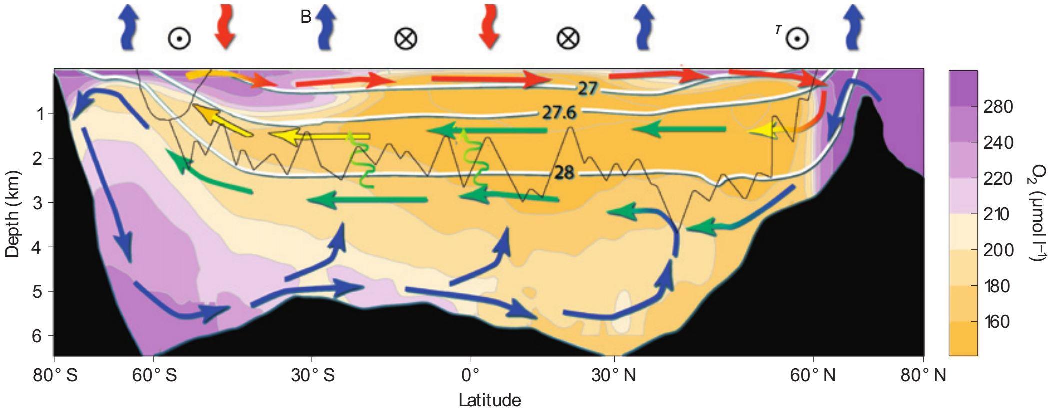

Figure 1.1: A schematic of the meridional overturning circulation (from Marshall and Speer, 2012). Background colours are zonally averaged oxygen concentrations. The jagged thin black line is the approximate depth of the Mid-Atlantic Ridge and the Scotia Ridge. Buoyancy fluxes are indicated by red (surface waters being made less dense) and blue (surface waters being made denser) arrows above the box. The broad pattern of zonal surface wind stress (τ) is indicated by $\odot$ (eastward) and $\otimes$ (westward). Isopycnal surfaces are plotted as white lines at $27\,\mathrm{kgm}^{-3}$, $27.6\,\mathrm{kgm}^{-3}$ and $28\,\mathrm{kgm}^{-3}$ (neutral density). The circulating arrows represent the zonally averaged circulation.

1.2.4 A modern view of the MOC

Figure 1.1 shows a representation of the modern view of the MOC. The zonally averaged circulation consists broadly of two counter-rotating cells, separated approximately by the $27.6\,\mathrm{kgm}^{-3}$ neutral density surface (Marshall and Speer, 2012). The upper cell is associated with NADW, which flows south and upwells along the sloping isopycnals of the Southern Ocean, then is driven north by an Ekman transport induced by westerly winds, gains buoyancy due to heat and precipitation from the atmosphere, and finally is subducted and exported back northwards at intermediate depth. The lower cell is associated with denser southward flowing deep water which upwells near Antarctica, loses buoyancy due to cooling by the winds and brine rejection from ice formation, and becomes AABW before returning north at depth (Rintoul, 2006). The adiabatic upwelling in the Southern ocean is an important aspect of the circulation, since it constitutes an alternative route for dense waters to return to the surface without the need for diabatic (diapycnal) mixing (see section 1.2.5).

1.2.5 Southern Ocean Dynamics

The Southern Ocean's role in the global circulation is important for a number of reasons. The Antarctic Circumpolar Current (ACC), which flows uninterrupted in an approximately eastward direction around Antarctica, links the other ocean basins, turning the circulation into a global phenomenon (Rintoul, 2006). Carrying around 137Sv of water through Drake Passage, where the flow is funnelled through a narrow gap between the southern tip of South America and the Antarctic Peninsular, the transport of the ACC is the largest in the ocean (Cunningham *et al.*, 2003). The ACC flow is made up of a number of fast meandering 'jets' associated with sharp cross-stream gradients ('fronts') in temperature and salinity, which are able to penetrate all the way to the ocean floor because the Southern Ocean is weakly stratified. The three main fronts are the Subantarctic Front, the Polar Front, and the Southern ACC front (see figure 1.2). The weak stratification also means that bottom topography has a stronger than average influence on the mean flow (Ferrari and Wunsch, 2009).

A key element to the MOC picture is that while isopycnals are nearly flat across most of the ocean, in the Southern Ocean they slope steeply and outcrop near Antarctica, providing an adiabatic route for dense water to return to the surface where it may gain buoyancy through interactions with the atmosphere (e.g. Olbers *et al.*, 2004; Olbers and Visbeck, 2005; Marshall and Speer, 2012). The tilt of the surfaces can be explained as the result of a competition between processes. Strong westerly winds blowing over the ACC set up an Ekman layer at the surface, the average direction of which is northwards due to the action of the coriolis force in the southern hemisphere. This causes an upwelling of water to the south of the ACC and a downwelling to the north of it, which in turn causes the isopycnals to tilt. The resulting zonally averaged circulation is known as a 'Deacon cell' (e.g. Toggweiler and Samuels, 1995; Speer *et al.*, 2000). Buoyancy forcing at the surface (increase to the north due to heating from the sun and decrease to the south due to ice formation) also contributes to the tilt. The horizontal density gradient due to the tilt of the isopycnals supports the current shear of the ACC known as the thermal wind (Marshall and Speer, 2012).

The lack of a land boundary (i.e. the fact that Drake Passage is open) means that no zonal pressure gradients can exist above the height of topography, and hence there is no

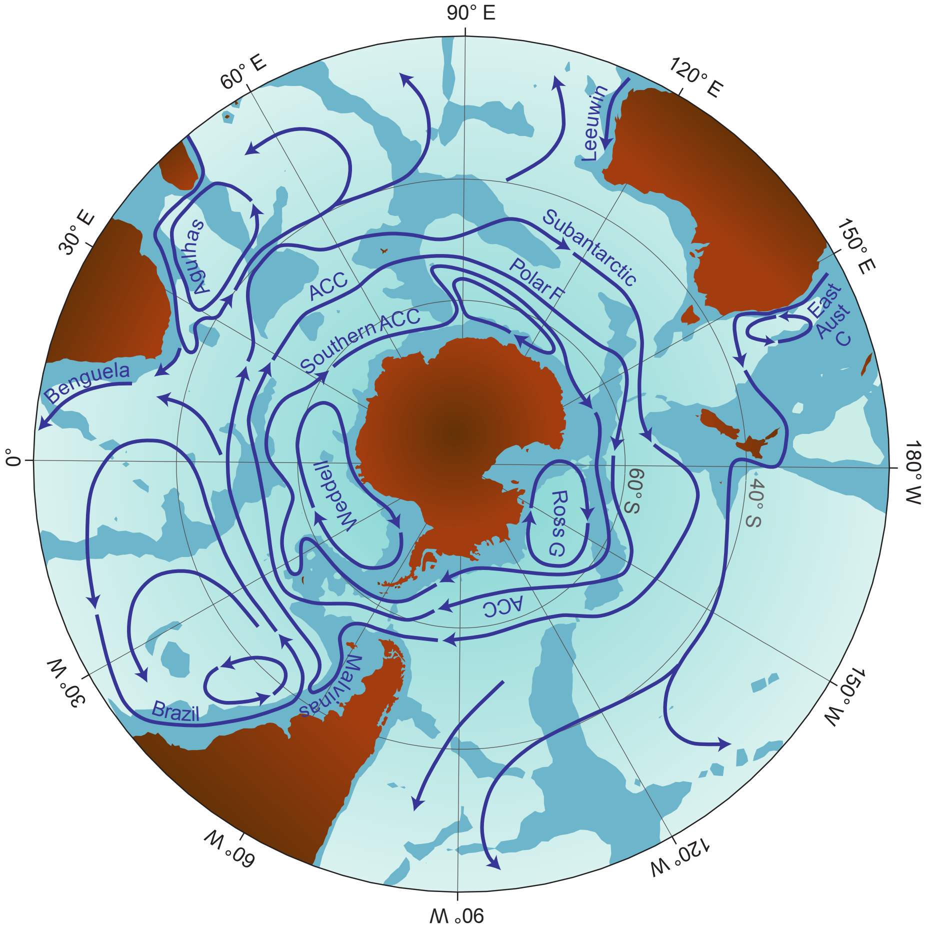

Figure 1.2: A schematic showing the main currents in the Southern Ocean (from Rintoul, 2009)

north-south mean flow above topography and below the Ekman layer (Toggweiler and Samuels, 1995). The southward transport along the sloping isopycnals of the Southern Ocean is achieved through isopycnal stirring by eddies, which work against the wind-driven equatorward transport, having a competing effect which tends to flatten isopycnals (Speer *et al.*, 2000). Isopycnal diffusivities, K_h, are orders of magnitude larger than K_z because movement along isopycnals does not have to work against the density stratification, and because the horizontal scale of the ocean is much larger than its vertical scale. This aspect of the circulation means that diapycnal mixing only needs to bring the bottom water to mid depths, and the Southern Ocean thus provides a link between the upper and lower cells of the MOC (Rintoul, 2006). Geostrophic eddies have been shown to be very important to the circulation in the Southern Ocean (e.g. Karsten *et al.*, 2002). Naveira Garabato *et al.* (2007) suggest that there exists a coupling between diapycnal mixing and isopycnal mixing due to these eddies impinging on the sea floor topography.

1.2.6 Energy and the overturning circulation

The sinking of high density fluid at the poles lowers the potential energy of the ocean system, so the upwelling return flow therefore requires a source of energy. This energy comes almost entirely in the form of kinetic energy from two main sources: the wind and the tides, with a much smaller contribution from buoyancy forcing due to interactions with the atmosphere (e.g. Munk and Wunsch, 1998; Wunsch and Ferrari, 2004). The energy input by the wind may be transferred to the circulation indirectly through large-scale geostrophic motions over bottom topography (Munk and Wunsch, 1998) such as the ACC in the Southern Ocean; or directly as the wind blows over the ocean surface. The latter sets up the Ekman layer, which drives the circulation from above (Brown *et al.*, 2007). The wind provides around 1 TW of power to the circulation directly and at least 0.5 TW indirectly; this being only a small fraction of the total energy available, most of it having been dissipated in the surface mixed layer (Wunsch and Ferrari, 2004). Tidal power inputs around 3.5 TW, most of which is dissipated near continents, but a significant fraction, up to around 1 TW, is available for abyssal mixing (Munk and Wunsch, 1998; Egbert and Ray, 2000).

Gill *et al.* (1974) showed that the potential energy in the ocean's mean circulation can be converted into eddies by baroclinic instability, a phenomenon that releases available potential energy in a rotating fluid where a horizontal density gradient exists (Marshall and Plumb, 2008). Of the approximately 2-3 TW of potential energy released by the circulation, around half is by the large scale overturning, and half is from the creation of eddies by baroclinic instability (Wunsch and Ferrari, 2004). The latter seems capable of releasing between $30 - 100\%$ of the wind power input to the circulation (Ferrari and Wunsch, 2009). It is also the mechanism responsible for removing the potential energy stored in the sloping isopycnals of the Southern Ocean (Rintoul, 2009). The eddy energy due to baroclinic instability may be dissipated by the interaction of the resulting baroclinic eddies with bottom topography, generating lee waves and subsequent diapycnal mixing (see section 1.3); this process may be particularly important in the Southern Ocean (Marshall and Naveira Garabato, 2008).

1.3 Mixing Processes

1.3.1 Internal gravity waves

Gravity waves are generated at an interface between two layers of different densities within a fluid. If a lighter fluid overlays a denser one, and the interface is perturbed (e.g. by the wind in the case of air overlying the sea surface) such that a parcel of denser fluid is raised up to the level of the overlying lighter fluid, the parcel will experience a restoring force downwards due to gravity. Equally as it returns to its equilibrium position and overshoots due to momentum, a buoyancy restoring force will act upwards, setting up an oscillation. For internal waves, the restoring force becomes the ‘reduced gravity’, due to the density difference between layers of water in the ocean with different density (Gill, 1982), and they may propagate vertically as well as horizontally (Gregg *et al.*, 2003). Such waves do not require a sharp density interface to exist; a stably stratified fluid (such as exists over most of the ocean) is enough. Garrett and Munk (1972b) devised a theory for the power spectrum of internal waves in the ocean, a phenomenon they describe as ‘ubiquitous’, and to which the pelagic diffusivity of $10^{-5}\mathrm{m}^2\,\mathrm{s}^{-1}$ has been attributed (e.g. Munk and Wunsch, 1998; Wunsch and Ferrari, 2004).

1.3.2 The Garret-Munk spectrum

In their original prescription, which has been revised a number of times (e.g. Garrett and Munk, 1975; Cairns and Williams, 1976; Müller *et al.*, 1978), Garrett and Munk (1972b) described an internal wave power spectrum that is horizontally isotropic, and dependent on the local buoyancy frequency N, where N is defined by:

$$N(z) = \sqrt{-\frac{g}{\rho}\frac{\partial \rho}{\partial z}}, \tag{1.2}$$

g is the acceleration due to gravity, z is depth and ρ is density. They therefore expected the power due to internal waves to be smallest at the bottom of the ocean, since N decreases with depth (it is now known that this is not the case, as there are strong sources of internal wave energy at the bottom topography - see section 1.3.3.2). In the ocean, internal waves are possible with frequencies between f, the inertial frequency (also known as the Coriolis frequency, equal to $2\Omega sin$(latitude), where Ω is the Earth’s angular velocity),

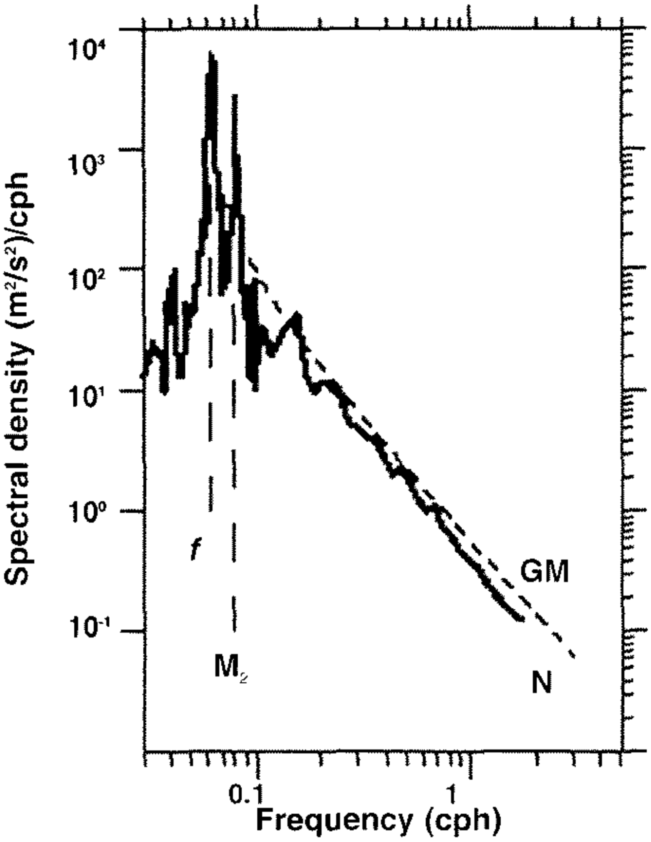

Figure 1.3: Energy level due to internal waves with frequency (from Muller and Briscoe, 2000). Solid line is from measured values, dotted line labelled 'GM' is ω^{-2} dependence. Inertial (f) tidal (M_2) and bouyancy (N) frequencies are marked.

and N, the buoyancy frequency. Garrett and Munk (1979) describe a dispersion relation between waves of frequency ω and their horizontal and vertical wavenumbers k and m, respectively:

$$\omega^2 = (N^2k^2 + f^2m^2)/(k^2 + m^2). \tag{1.3}$$

For ω slightly larger than f, the motion of water particles is almost horizontal and circular, with a velocity vector that rotates anticyclonically (anticlockwise in the southern hemisphere if viewed from above). As ω increases, the motion becomes increasingly elliptical and towards the vertical, until at ω close to N it is nearly an up-and-down oscillation. The power spectrum described by the Garret-Munk theory (hereafter 'GM') has a peak at the inertial frequency, a 'continuum' with a dependence on ω^{-2}, and a cut off at N (see figure 1.3). Observations confirm the validity of the GM model in most places in the ocean, but it does have some limitations (Muller and Briscoe, 2000). The assumption of horizontal isotropy is not consistent with what we now know about the localised nature of the sources of internal waves, for example due to the interactions of tidal and geostrophic eddy flows with bottom topography (see section 1.3.3.2). An additional peak not predicted by the theory at the M_2 tidal frequency is observed (see figure 1.3). Finally, there are temporal variations and a depth dependence of the inertial peak which are not reproduced by GM.

1.3.3 Internal waves and mixing

1.3.3.1 Breaking internal waves and dissipation

Garrett and Munk (1972a) explain how mixing can result from the 'breaking' of internal waves. High shear can result in shear instability and subsequent mixing if the Richardson number is below a critical value of 1/4. The Richardon number is given by:

$$Ri = \frac{N^2}{(du/dz)^2} \tag{1.4}$$

where N is the local buoyancy frequency and du/dz is the shear. In the presence of an internal wave field, fine scale shear may be much larger than the local average shear, and hence the probability of shear instability is much higher.

Osborn and Cox (1972) pointed out that the energy which goes into turbulent mixing must ultimately be dissipated on the molecular scale. Some of the available kinetic energy goes into mixing, increasing the potential energy of the system, and some is dissipated. Osborn (1980) devised an equation (now known as the Osborn relation) to predict the amount of mixing as a proportion of the dissipation, ϵ:

$$K_z < 0.2\frac{\epsilon}{N^2} \tag{1.5}$$

Where N is the buoyancy frequency. The '$<$' indicates that the 'mixing efficiency' of 0.2 for the ratio of mixing to dissipation is an upper limit according to the theory, derived from the critical flux Richardson number $R_f \leq 0.15$, above which turbulence cannot be maintained in steady state. This value has been used extensively for diagnosing mixing from measurements of dissipation (see section 1.4.4), but there are suggestions that it may be lower (e.g. Arneborg, 2002).

1.3.3.2 Sources of internal waves

There are two main sources of internal waves in the ocean: bottom currents can generate internal waves through interaction with topography (Bell, 1975), and inertial waves are generated by variable wind stress on the surface (Thorpe, 1975). A third mechanism is interior generation from wave-wave interactions (Garrett and Munk, 1979).

Inertial waves can result in shear (Kelvin Helmholtz) instabilities when the shear is large, and this process seems capable of causing the background observed mixing of the order $10^{-5}\mathrm{m}^2\,\mathrm{s}^{-1}$ but not the higher values seen near topography (Ferrari and Wunsch, 2009).

Bottom generated internal waves fall into two categories: internal tides and lee waves. Internal tides are internal waves of tidal period, generated by the time dependent flow of tides over, for example, an ocean ridge (e.g. Rudnick *et al.*, 2003, see section 1.4.4). The vertical shear associated with internal tides, or with other internal waves to which they transfer their energy, can lead to instability and subsequent mixing (Garrett and Kunze, 2007). Egbert and Ray (2000) showed using analysis of satellite altimetry that internal waves due to tides produce significant mixing in the open ocean.

Lee waves can be generated by tidal or geostrophic bottom flows interacting with topography. Similarly to internal tides, they propagate upwards from their source on the ocean floor and can lead to instabilities and internal wave breaking providing the energy for mixing. In the classical lee wave problem, a sinusoidal bottom topography with height $h(x) = h_0 cos(kx)$ is defined, where x is a horizontal coordinate, k is the wave number of the generated waves, and h_0 is a characteristic topographic height scale; and a steady current U_0 flows over it in a stratified fluid with buoyancy frequency N. Lee waves are only then able to radiate upwards for the range $f < U_0 k < N$, where f is the inertial frequency (Gill, 1982).

1.3.3.3 The energy cascade and finescale parameterisation

There must be a mechanism to transmit the energy from the generation scales of inertial, tidal and lee waves down to the small scales of dissipation. This downscale cascade can happen though wave-wave interactions as internal waves can transfer energy among themselves due to nonlinear terms in the equations of motion (Garrett and Munk, 1979), through interactions between internal waves and the mean flow (Waterman *et al.*, 2013), or through scattering at mesoscale eddies, fronts and topography (Muller and Briscoe, 2000). The cascade forms the basis for finescale parameterisations, which allow dissipation (and hence diffusivity) associated with internal wave breaking to be estimated from observations of current shear and density finestructure on vertical scales of 10-100m, such as may be obtained from CTD (Conductivity-Temperature-Depth) and ADCP (Acoustic Doppler Current Profiler) measurements (e.g. Waterman *et al.*, 2013). In these parameterisations, characteristics of the internal wave field such as bouyancy frequency are combined with predictions from the GM spectrum to extrapolate from observed to dissipation scales (Polzin *et al.*, 1995). In a study of internal waves in the ACC, Waterman *et al.* (2013) found that finescale parameterisations tended to overpredict the dissipation near topography and underpredict it at mid-depths. In the regions where the overprediction was found, the internal wave field was dominated by upward propagating higher frequency waves (lee waves), whereas underprediction was seen where near-inertial, downward propagating waves dominated.

1.3.4 Other diapycnal mixing processes

There are some processes which can cause diapycnal movement of water masses (either upwards or downwards) which do not involve turbulent mixing, and consequently are not detected by measurements of dissipation or of the internal wave field.

Thermobaricity and cabbeling are effects due to nonlinearities in the equation of state of seawater, dependent on the differing effects of pressure on the expansion or contraction of a water parcel given its heat and salt content. They arise when water masses of the same density but differing temperature and salinities mix isopycnally. The movement of water masses due to thermobaricity may be upward or downward through isopycnals; cabbeling only causes movement downward (McDougall, 1987). These effects may be significant in the Southern Ocean due to large isopycnal gradients of temperature and pressure on outcropping isopycnals (Klocker and McDougall, 2010a).

A third effect of nonlinearities that causes diapycnal movement of water masses is neutral helicity. This arises from the fact that it is not possible to uniquely define continuous surfaces in the ocean which are truely isopycnal, i.e. such that a water parcel moving along the surface experiences no buoyant restoring forces (Klocker and McDougall, 2010a).

Neutral helicity therefore becomes a factor when oceanographers make use of defined continuous density surfaces such as potential density or neutral density.

Double diffusive processes, the best known of which is salt fingering, are due to the fact that the molecular diffusion of heat is faster than that of salt. When warm, salty water overlies cooler, fresher water, a ‘finger’ of the upper layer may extend down into the lower layer, and as the heat diffuses sideways into the surrounding water it becomes denser than its surroundings and the finger continues to extend. Similarly a finger from the lower layer extending upwards will have heat diffusing into it, making it less dense so it continues to grow (Brown *et al.*, 2007).

In regions where both salt fingering and turbulent mixing due to breaking internal waves take place, the two processes are in competition, the former promoting a flux of density upgradient and the latter a downgradient flux (St. Laurent and Schmitt, 1999). Salt fingering can therefore have noticeable effects in some relatively quiet areas of the ocean, for example in the Arctic and the Caribbean (Schmitt, 1994); however in highly energetic regions such as Drake Passage we expect that the effects of salt fingering will be obliterated by turbulent mixing.

1.3.5 Southern Ocean Mixing

Wunsch (1998) estimated that of the 1TW of work done by the wind on the circulation, around 80% happens in the Southern Ocean. Much of this energy goes into generating a strong mesoscale eddy field. The resulting combination of strong mean flows and energetic eddies interact with the rough bottom topography found over much of the region to generate lee waves, which then break, causing enhanced diapycnal mixing (Nikurashin and Ferrari, 2010a). Nikurashin and Ferrari (2013) have estimated that around a third of global water mass transformation is driven by lee waves, most of which takes place in the Southern Ocean. They also note that most lee wave driven mixing takes place deeper than the $27.6\,\mathrm{kgm}^{-3}$ neutral density surface, i.e. in the AABW.

Lee wave driven mixing has been shown to be more important than that associated with tides in the Southern Ocean, as geostrophic eddies dominate the bottom flow (e.g. Naveira Garabato *et al.*, 2003; Nikurashin and Ferrari, 2013). In fact, Nikurashin and Ferrari (2010b) calculate that in Drake Passage, radiation by geostrophic motions exceeds the energy radiated by tides by a factor of 10. The importance of lee wave generation in the Southern Ocean is further highlighted by Scott *et al.* (2011), who calculated a global value of 0.44TW of energy due to lee waves, of which 92% is generated in the southern hemisphere, and 72% south of 30S. The global rate is comparable to that produced by tide-topography interaction. They also find that the energy carried by the lee waves propagates at a shallow angle of 16 degrees to the vertical, i.e. nearly directly upwards. Marshall and Naveira Garabato (2008) predict that bottom enhanced diapycnal mixing of up to $5 \times 10^{-3}\ \mathrm{m}^2\,\mathrm{s}^{-1}$ can be supported by the breaking of internal lee waves in the Southern Ocean. Naveira Garabato *et al.* (2007) propose a cycle where baroclinic instability causes the growth of eddies, which are dampened by the generation of internal waves as the eddy flows meet topography. Although some ocean models include parameterizations for tidal driven diapycnal mixing, none has yet been implemented for lee waves, so the water mass transformation is likely to be underestimated in these models (Nikurashin and Ferrari, 2013).

Sloyan (2005) found that K_z decays slowly with height above the bottom across the ACC. According to Polzin (1999, 2004), the scale height for the decay of lee waves and tides away from their source is dependent on, respectively, the near bottom geostrophic velocity and the near bottom tidal velocity. Lumpkin and Speer (2007) find that buoyancy gain in the Southern Hemisphere can help to account for the discrepancy between the Munk value of $10^{-4}\mathrm{m}^2\,\mathrm{s}^{-1}$ and the smaller measured values of diapycnal mixing. Zika *et al.* (2009) use known distributions of temperature and salinity in the Southern Ocean to relate the strength of the overturning to a ratio of isopycnal to diapycnal mixing, deriving an estimate for K_z of $10^{-4}\mathrm{m}^2\,\mathrm{s}^{-1}$. After estimating high rates of diapycnal mixing in the Scotia Sea, Naveira Garabato *et al.* (2004) suggest that the much of the upwelling required to close the deep cell of the circuliation could occur in the Southern Ocean, at the expense of the ocean basins to the north. Diapycnal mixing in the Southern Ocean is therefore a good candidate for closing the overturning circulation, providing the link between the deepest water and the upper cell of the MOC.

1.4 Measurements of diapycnal mixing

1.4.1 Methods of measuring mixing

Attempts to measure diapycnal mixing in the ocean fall into four categories: budget methods, tracer release experiments, finestructure measurements, and microstructure measurements. Budget studies use measurements of the flow into and out of an ocean basin combined with measurements of properties such as temperature and salinity. Under the assumption of steady state, inflows must be balanced either by outflows at the depth of the inflows or by mixing up to a depth above the basin boundaries, and heat and mass balances may therefore be used to diagnose diffusivity.

In a tracer release experiment, the distribution of a conserved scalar deliberately injected into the ocean is monitored as it spreads in three dimensions over time. The tracer compound, or ‘dye’, is dissolved in the water so that its distribution becomes a proxy for the movement of water masses. Diffusion models in one, two or three dimensions can be applied to diagnose the diffusivity, e.g. for the 1D case (from Gargett, 1984):

$$\frac{\partial C}{\partial t} = K_z \frac{\partial^2 C}{\partial z^2} \tag{1.6}$$

where C is the concentration of the injected scalar, z is depth, t is time and K_z is the vertical diffusivity. Equation 1.6 assumes a constant value for K_z. For a depth dependent diffusivity, the following equation applies (Gargett, 1984):

$$\frac{\partial C}{\partial t} = K_z \frac{\partial^2 C}{\partial z^2} + \frac{\partial K_z}{\partial z}\frac{\partial C}{\partial z} \tag{1.7}$$

Alternatively, the spread in the horizontal or vertical second moments of the tracer patch with time may be used to estimate, respectively, the horizontal or vertical diffusivity.

Microstructure profilers measure variations of vertical velocity shear on centimetre scales to derive estimates of turbulent dissipation using the following formula (from Oakey, 1982):

$$\epsilon = \frac{15}{2}\nu \overline{\left(\frac{\partial u}{\partial z}\right)^2} \tag{1.8}$$

where ν is the molecular viscosity and u is the current velocity. This may then be converted to diffusivity using the Osborn relation (Eq. 1.5).

Vertical profiles of velocity and density on scales of 10-100m, gathered respectively by LADCPs (Lowered-ADCPs) and CTD sensors, are known as ‘finestructure’. Finestructure data may be combined with finescale parameterisations to arrive at diffusivity (see section 1.3.3.3). These measurements are effectively direct measurements of the internal wave field.

1.4.2 Budget studies

Hogg *et al.* (1982) used the budget method to estimate the diffusivity for the Brasil Basin in the South Atlantic. Current meter and CTD data were collected in the Vema channel, which connects the Argentine and Brasil basins, and used to estimate how much Antarctic water flows northward through the channel. They found K_z to be between 3-4$\times 10^{-4}$ $\mathrm{m}^2\,\mathrm{s}^{-1}$ for the basin, and also found the horizontal diffusivity $K_h = 400\mathrm{m}^2\mathrm{s}^{-1}$ by relating downstream advection and cross stream diffusion to the horizontal temperature distribution.

Heywood *et al.* (2002) estimated the diffusivity in the Scotia Sea, an area of the Southern Ocean with rough bottom topography. There are relatively few places where dense water can enter the basin from the south, and nowhere that water at the depth of the inflows can escape to the north without mixing upwards. Using temperature, salinity and current velocity measurements, they found a basin averaged diffusivity of 39×10^{-4} $\mathrm{m}^2\,\mathrm{s}^{-1}$.

1.4.3 Tracer studies

Early tracer experiments in the ocean used fluorescent dyes (e.g. Schuert, 1970; Ewart and Bendiner, 1981). However, these tracers have lifetimes of only a few days, so have limited usefulness in assessing ocean mixing on a large scale. Ledwell and Watson (1991) pioneered a new type of tracer, sulphur hexaflouride (SF_6), which due to its being detectable in concentrations of 10^{-17}mol l^{-1} with electron capture gas chromatography has a lifetime in the ocean of more than 1 year. In a prototype experiment, SF_6 was released into the Santa Monica Basin off the coast of California and surveyed at intervals as it diffused. In each tracer survey, samples of water around the depth of the isopycnal surface onto which the tracer had been released were gathered and analysed for their tracer concentration. A background of SF_6 in the water was measured before the release, and subtracted from sampled concentrations. Profiles of tracer concentration with depth were averaged, the profile statistics being the basis for the key results. To diagnose the vertical diffusivity from the mean tracer profile, diffusion was viewed as Fickian, varying slowly with depth, and a 1D model fitted to the data, varying the input K_z to minimise a cost function. Diffusivity for the basin was found to be $2.9 \pm 0.6 \times 10^{-5}\ \mathrm{m^2\,s^{-1}}$ averaged over 6 months from the tracer release, and $2.5 \pm 0.8 \times 10^{-5}\ \mathrm{m^2\,s^{-1}}$ for the interior. The first few weeks of the experiment before the tracer had spread to the basin walls allowed for the separate measurement of interior mixing to be achieved, and it was suggested that there was evidence of boundary mixing, although inconclusive. The mean tracer profile with depth was skewed with a deep tail, indicating an enhancement of K_z towards the bottom of the basin. In addition, the isopycnal diffusivity was estimated from the growth of the lateral second moment of the tracer patch. They found that ‘streakiness’ - the tendency of the tracer to form long thin regions of high tracer concentration with little or no tracer in between - largely disappeared within 2-5 months, the time taken for the tracer to mix to the basin boundaries.

A second experiment with SF_6 was carried out by Ledwell and Bratkovich (1995) in the Santa Cruz basin, adjacent to the Santa Monica Basin. Using similar methods, they found $K_z = 1.0 \times 10^{-4}\ \mathrm{m^2\,s^{-1}}$ while the tracer was still mixing to the basin walls, increasing to $10 \times 10^{-4}\ \mathrm{m^2\,s^{-1}}$ later, providing more conclusive evidence that the overall diapycnal mixing was contributed to disproportionately by the boundary region. The larger value of interior mixing compared with the Santa Monica Basin experiment was attributed to the fact that the buoyancy frequency in the Santa Monica Basin was 5 times greater (i.e. the Santa Cruz basin was more weakly stratified).

A larger scale experiment, termed the ‘North Atlantic Tracer Release Experiment’ (NATRE), was carried out by Ledwell *et al.* (1998) in the south-eastern part of the subtropical gyre between 1992-1994. They used a neutrally bouyant sled for the tracer injection with a feedback system to ensure it stayed on the ‘target’ isopycnal surface, an advancement on the earlier system which was manually controlled. Diapycnal diffusivities of $0.12 \times 10^{-4}\ \mathrm{m^2\,s^{-1}}$ for the first 6 months and $0.17 \times 10^{-4}\ \mathrm{m^2\,s^{-1}}$ after 2 years were found, the latter being an average over a 100m thick layer around the $26.75\ \mathrm{kgm^{-3}}$ surface (potential density referenced to the surface) between 20°N and 26°N and between 30°W and $45°$W. The asymmetry of the mean tracer profile indicated a positive gradient in K_z with depth (K_z increasing upward), which they suggested was due to salt fingering. The main tracer peak had also sunk in the water column from its intended injection density, and it was suggested this was because tracer was absorbed onto sinking particles and then de-absorbed. Cabbeling was also offered as a contributing explanation, since it tends to make water denser (McDougall, 1987). Lateral diffusion of the NATRE tracer was also examined, and found to be scale dependent; values ranging from $0.07\mathrm{m}^2\mathrm{s}^{-1}$ at 0.1-1km scales up to $1000\mathrm{m}^2\mathrm{s}^{-1}$ at 100-1000km scales. They suggested that submesoscale processes and the initial condition set the smallest scale isopycnal mixing, that mesoscale eddies dominate the middle scale, and that gyre-scale strain is responsible for mixing on the largest scales.

Further ocean tracer release experiments using SF_6 followed. Watson *et al.* (1999) carried out a study in the Greenland Sea gyre at a similar depth to that of NATRE, and found diffusivities around 10 times higher, again attributable to the weaker stratification in the Greenland Sea. The Brazil Basin, which has on its eastern side the rough topography of the Mid Atlantic Ridge, was studied by Ledwell *et al.* (2000). By fitting a 1D model with a gradient in K_z with depth to the mean tracer profile, they estimated the diapycnal diffusivity at the tracer target depth (around 4000m) as $3 \times 10^{-4}\ \mathrm{m}^2\,\mathrm{s}^{-1}$, in agreement with Hogg *et al.* (1982) (see section 1.4.2), and at 500m below the target to be $8 \times 10^{-4}\ \mathrm{m}^2\,\mathrm{s}^{-1}$. They also found that individual tracer vertical profiles were wider towards the east of the basin where the tracer isopycnal was closer to the bottom. As with Ledwell *et al.* (1998), the tracer peak was found to have sunk, tracer presumably having been transported on sinking particles.

By the mid-2000s, the concentration of SF_6 in the atmosphere had increased to the point where it was becoming useful for transient tracer experiments, which use tracers to study the oceanic uptake of atmospheric compounds. CFCs had previously been used for such experiments, but their atmospheric concentrations were declining. In order that the use of SF_6 might be continued for transient tracer experiments it was necessary to find an alternative for deliberate ocean tracer releases to avoid the issue of contamination. Ho *et al.* (2008) carried out another tracer experiment in the Santa Monica Basin, this time to test the usefulness of trifluoromethyl sulphur pentaflouride (CF_3SF_5), a compound with similar properties to SF_6. Both tracers were released concurrently, and the final vertical profiles were found to be very similar. An agreement was made to stop using SF_6 in tracer release experiments in order to preserve its usefulness as a transient tracer. No significant background of $\mathrm{CF_3SF_5}$ was found before the release, meaning that it was not necessary to remove a background to carry out the analysis.

In February 2009, a large scale tracer release experiment to study mixing in the Southern Ocean using $\mathrm{CF_3SF_5}$ was begun as a part of the Diapycnal Mixing Experiment in the Southern Ocean (DIMES). 76kg of tracer was released onto the $27.906\,\mathrm{kgm}^{-3}$ neutral density surface near $58°$S, $107°$W between the Polar and Subantarctic Fronts at a depth of around 1500m (Ledwell *et al.*, 2011). After 1 year the tracer was surveyed (see figure 2.2 for the locations of the tracer stations), and averaged concentration profiles as a function of neutral density were transformed to depth coordinates using the mean depth-density relation for the region, obtaining a nearly gaussian profile. The tracer evolution was modelled from its initial distribution to 1 year in the same way as was done by Ledwell *et al.* (1998), yielding a diffusivity estimate of $1.3 \pm 0.2 \times 10^{-5}\ \mathrm{m}^2\,\mathrm{s}^{-1}$ for the region. The uncertainty estimate was based on a combination of the variation of the cost function fitting the 1D model to the measured tracer, uncertainty in the appropriate depth-density profile, and a comparison with the result obtained by an alternative method of taking the difference between the initial and final vertical mean profile second moments. Their conclusion was, having measured a small diffusivity in the SouthEast Pacific sector of the Southern Ocean, that although there may be enhancement of diapycnal mixing in Drake Passage and other areas of rough topography, it is unlikely to account for a global averaged diffusivity of $10^{-4}\mathrm{m}^2\,\mathrm{s}^{-1}$ as predicted by Munk.

1.4.4 Microstructure and finestructure studies

In the late 1960s and early 70s, Cox and collaborators were the first to develop freefalling temperature, and later velocity profiling devices using high-speed thermistors and thin films to allow measurements of these quantities on subcentimeter scales (e.g. Cox *et al.*, 1970; Osborn and Cox, 1972). By the 1990s, technology had developed to the point where high accuracy measurements of turbulent dissipation, ϵ were possible, from which K_z may be found from the Osborn relation (equation 1.5).

In parallel with the NATRE experiment, microstructure and finestructure were taken with a tethered profiler which measured vertical gradients of microscale temperature and velocity, as well as collecting CTD data (Ruddick *et al.*, 1997). They found diffusivities of $1 \times 10^{-5}\ \mathrm{m}^2\,\mathrm{s}^{-1}$ in an autumn survey and $2.2 \times 10^{-5}\ \mathrm{m}^2\,\mathrm{s}^{-1}$ in the spring.

There were also finestructure and microstructure measurements taken alongside the Brazil Basin tracer release experiment. Polzin *et al.* (1997) report that a High Resolution Microstructure Profiler (HRP) recorded profiles of temperature, salinity and horizontal velocity with depth, along with dissipation and temperature variance. They found $K_z = 10^{-5}\mathrm{m}^2\,\mathrm{s}^{-1}$ in the centre of the basin, enhanced 1-2 orders of magnitude over the rough topography of the Mid Atlantic Ridge, particularly within 300m of the bottom. They point out that turbulence due directly to bottom stress can only reach a few tens of metres above the bottom, and therefore suggest that internal waves are responsible for transporting energy upwards, resulting in instability and internal wave breaking and subsequent mixing. Evidence consistent with this theory was also observed in enhanced finescale shear and strain measurements. By contrast to the enhanced mixing over the ridge, they found weak mixing from microstructure measurements all the way to the bottom over smooth topography in the basin, indicating the importance of the particular structure of topography, rather than just proximity to it. They also note that the depth-averaged microstructure data showed a fortnightly modulation in mixing which lagged behind the barotropic tide intensity by a few days, and propose that tidal flows over rough topography provide the energy for mixing.

In the Scotia Sea, Naveira Garabato *et al.* (2004) calculated dissipation and diffusivity using finestructure from CTD and Lowered-ADCP (LADCP) observations in conjunction with the Heywood *et al.* (2002) budget study, finding K_z of up to $10^{-2}\mathrm{m}^2\,\mathrm{s}^{-1}$ over rough topography.

An investigation into tidal mixing along the Hawaiian Ridge as a part of the Hawaii Ocean Mixing Experiment (HOME) was reported by Rudnick *et al.* (2003). Measurements from altimetry, moorings, and microstructure profilers were combined with numerical models, resulting in a picture of a cascade of energy in three stages. The first stage is a fortnightly modulation in tidal energy fluxes over the ridge, indicating a tidal source for the flux. The next stage of the cascade is indicated by enhanced internal wave energy observed in the region surrounding the ridge. Finally, enhanced dissipation giving diffusivities of up to $3 \times 10^{-4}\ \mathrm{m}^2\,\mathrm{s}^{-1}$ was observed over the ridge, decaying away from the ridge to background levels of $10^{-5}\mathrm{m}^2\,\mathrm{s}^{-1}$. Vertical profiles of dissipation were found to be largest at the surface, with a minimum near 2000m, and growing again near the bottom. The resulting diffusivity therefore increases strongly towards the bottom, caused by increasing dissipation and decreasing buoyancy frequency. They concluded that tides interacting with ridges are an important energy source for ocean mixing.

Sloyan (2005) used CTD data from the World Ocean Circulation Experiment (WOCE) to derive estimates for mixing over the whole of the southern hemisphere, estimating dissipation from finescale strain. She found that mixing is dominated by hotspots over complex topography, with mixing enhanced 1-2 orders of magnitude above background levels within 500m-1000m above such topography. Enhancement was also seen throughout the water column in the ACC fronts.

A similar study was carried out by Wu *et al.* (2011) using Argo float data from the Southern Ocean. They used finescale strain combined with finescale parameterisations to calculate diapycnal mixing over a depth range of 300-1800m. They found that enhanced mixing was correlated with rough bottom topography, and that mixing rates decreased with depth over smooth topography, but over rough topography the decrease was observed over the top 1200m, with rates increasing again towards the bottom. They concluded that the observed enhanced mixing was due to the breaking of internal waves resulting from abyssal flows interacting with rough bottom topography, and that, by contrast to observations in other parts of the ocean, these waves extend far above the bottom, dominating mixing below 1200m depth and making a non-negligible contribution in the upper 300-1200m. They also suggested that, since the magnitude of bottom geostrophic flows is much larger than that of baratropic tides in large parts of the Southern Ocean, the observed enhanced mixing is probably due to geostrophic motions impinging on rough topography, rather than internal tides. They estimated the integrated dissipation rate throughout the water column to be comparable to the rate of work done by the wind on the ACC. Finally, they found significant seasonal variation in the upper 300-600m over smooth topography, which decreased in magnitude with depth. The mixing rates were greatest in the winter, coinciding with stronger winds, and they suggested that the seasonality over smooth topography is controlled by the seasonal cycle of near-intertial energy flux input by the wind, extendind to at least 1500m depth. Over rough topography they found the seasonal variability to be less marked because the dominant influence on the mixing here is the ACC, which has no significant seasonal cycle.

Simultaneous CTD and LACDP measurements and Vertical Microstructure Profiler (VMP) measurements were taken during the The Southern Ocean Fine Structure (SOFINE) project. Waterman *et al.* (2013) report diffusivities typically around $10^{-5}\mathrm{m}^2\,\mathrm{s}^{-1}$, but enhanced in the upper 1000-1500m of the water column and in some places near the bottom over rough topography where strong bottom flows exist due to ACC jets, with values as high as $3 \times 10^{-3}\ \mathrm{m}^2\,\mathrm{s}^{-1}$ in a few places. They found that areas where finestructure revealed high internal wave energy were also areas of high dissipation from microstructure.

The first direct measurements of turbulent dissipation in Drake Passage were taken as a part of DIMES at the same time as the Ledwell *et al.* (2011) tracer survey. St. Laurent *et al.* (2012) report on microstructure measurements with an HRP and a VMP, giving an average diffusivity of $0.75 \times 10^{-5}\ \mathrm{m}^2\,\mathrm{s}^{-1}$. Finestructure also from the HRP give the same value. However, EM-APEX floats recording finestructure over a longer period find diffusivity of $1.15 \times 10^{-5}\ \mathrm{m}^2\,\mathrm{s}^{-1}$, in closer agreement with the tracer value (see section 1.4.3). Over the Phoenix Ridge, which runs approximately north to south at a longitude of 66°W across the path of the ACC (see figure 2.2), enhanced dissipation was found up to 1000m above the bottom within frontal zones, where ACC jets reach all the way to the bottom, but no enhancement was seen outside of the fronts. Observations on the 'Albatross' section at approximately 68°W (also on figure 2.2) showed background levels of dissipation typical of the Southeast Pacific at the depth of the tracer target isopycnal. The lack of enhancement on this section may be explained by the fact that, although bottom currents in frontal zones do impinge on topography, the amplitude of topographic variation is smaller than that of the Phoenix Ridge. Since the long timescale of variation of the ACC in this region favours the production of lee waves rather than tidal induced internal waves, the observed enhanced dissipation was attributed to lee waves. LADCP data also showed a predominance of velocities rotating clockwise with depth in the bottom 1000m in regions of enhanced dissipation, indicating that internal waves are upward propagating.

1.4.5 Comparison of methods

1.4.5.1 Advantages and disadvantages

Each of the methods for inferring diapycnal diffusivities that have been presented have their strengths and weaknesses. In the case of many of the studies (e.g. Ledwell *et al.*, 1998, 2000, 2011; Naveira Garabato *et al.*, 2004) multiple methods were used in parallel to allow measurements to be verified against one another, and to combine the strengths of each.

Budget studies have the advantage of very few assumptions, and they give a time averaged measure of mixing, meaning results are accurate where mixing is sporadic (Gargett, 1984). The disadvantage is that they are indirect methods. They also do not distinguish, for example, interior from boundary mixing in a basin (Wunsch and Ferrari, 2004).

The main advantage of tracer studies is that they give a direct measurement of time- and spatially averaged mixing. The disadvantages are that they do not give accurate information about the variation of K_z with depth, or details about the horizontal distribution of vertical mixing (Gargett, 1984). Tracer studies also do not tell us about mechanisms, for example turbulent mixing is not distinguishable from salt fingering as both affect the vertical spread of the tracer.

Microstructure and finestructure measurements tell us about mechanisms: respectively, turbulent dissipation and the internal wave field. They give detailed information about the spatial variability of mixing. However, in the case of microstructure, only a snapshot of the mixing at a particular place and time is possible, and these measurements tend to be biased as profilers can only be deployed in relatively calm weather. Both methods also have inherent assumptions: in the case of microstructure the mixing efficiency to convert ϵ into K_z, and in the case of finestructure the more complex finescale parameterisations used to model the downscale cascade from internal waves to mixing.

1.4.5.2 Comparing tracer with fine- and microstructure

The NATRE project involved both tracer and microstructure measurements of mixing in tandem. St. Laurent and Schmitt (1999) concluded that the mixing implied by the two methods was consistent if salt fingering was taken into account. Ledwell *et al.* (2000) reported that tracer and microstructure measurements on the Brazil Basin experiment were consistent after adjusting for spatial and temporal biases of the microstructure sampling. On the first stage of the DIMES project, mixing inferred from the tracer was about twice that from microstructure, but consistent with finestructure from EM-APEX floats, the latter, like the tracer, being time averages. Ledwell *et al.* (2011) suggested that elevated shear variance in the winter months compared with the summer when microstructure measurements were made is the likely explanation for the tracer-microstructure discrepancy. Salt fingering was not thought to be a significant contributor, as salinity increases with depth almost everywhere in the region.

1.5 Summary

Diapycnal mixing is a crucial process to the overturning circulation of the ocean, and therefore to the Earth's climate. The Southern Ocean plays a disproportionate role in the circulation, connecting the ocean basins via the ACC, and allowing the adiabatic upwelling of dense bottom waters over sloping isopycnals. Despite this alternative route for the return flow, diapycnal mixing is still required to bring dense water to mid depths, and is believed to have a role in linking the upper and lower branches of the overturning circulation. Measurements of diapycnal mixing in the ocean have found it to be around $10^{-5}\mathrm{m}^2\,\mathrm{s}^{-1}$ at mid depths in most places, which is an order of magnitude smaller than the amount required to close the circulation. However, enhanced rates of diapycnal mixing have been observed in regions where currents interact with rough bottom topography, which it is believed are due to the generation and subsequent breaking of internal waves. In particular, tidal and geostrophic flows over topography are believed to be significant sources of internal wave energy. The Southern Ocean contains areas of rough topography and deep reaching strong currents associated with the ACC, and is consequently likely to be a region where significant enhanced diapycnal mixing takes place. The generation of lee waves as geostrophic flows interact with rough bottom topography have been shown to be an important process in providing the energy for this mixing. Drake Passage and the Scotia Sea are two such regions, and therefore may prove to be significant to the closure of the global overturning circulation.

1.6 Objectives

The research presented in the following thesis contributes to the DIMES project, the continuation of which from the studies referred to in section 1.4 includes further surveys of the injected tracer and the sampling of microstructure data in the SouthEast Pacific, Drake Passage and the Scotia Sea. The key objective of the thesis is to assess the current paradigm of enhanced diapycnal mixing at mid-depth over rough topography in the Southern Ocean, with particular focus on the processes driving diapycnal mixing in Drake Passage. The present understanding of this topic stems from indirect measurements of mixing such as finestructure and microstructure, and here new data from the DIMES experiment will be used in conjunction with numerical models in order to accomplish this objective.

Chapter 2

The DIMES tracer experiment

2.1 Introduction

The Diapycnal and Isopycnal Mixing Experiment in the Southern Ocean (DIMES) is a US-UK collaborative project with the key aims of measuring rates of diapycnal and isopycnal mixing in two contrasting regions of the Southern Ocean - the Southeast Pacific and Southwest Atlantic - and characterising the physical processes responsible for the mixing. The ultimate objectives are to test and, if necessary, modify the current theories of mixing in the Southern Ocean and its role in the Southern Ocean overturning.

DIMES comprises a number of elements. The tracer release experiment provides a direct time- and spatially-averaged measurement of mixing, obtained through surveys which map the evolution of its three-dimensional distribution with time, conducted at approximately yearly intervals after release. The tracer was injected in the Southeast Pacific sector of the ACC in February 2009, and subsequent oceanographic cruises relevant to this thesis were carried out in January - February 2010 ('US2'), December 2010 - January 2011 ('UK2'), April 2011 ('UK2.5') and January - March 2012 ('UK3'). Microstructure measurements with Vertical Microstructure Profilers (VMPs) and a High Resolution Profiler (HRP) are used to obtain full depth profiles of turbulent dissipation, giving instantaneous measurements of mixing concurrent with the tracer surveys. EM-APEX floats obtaining continuous finestructure data and RAFOS floats gathering information about horizontal mixing by eddies are deployed alongside the tracer. Finally, a cluster of moorings in the north-east of Drake Passage provides time-series data on finestructure from moored ADCPs and on eddies from current meters.

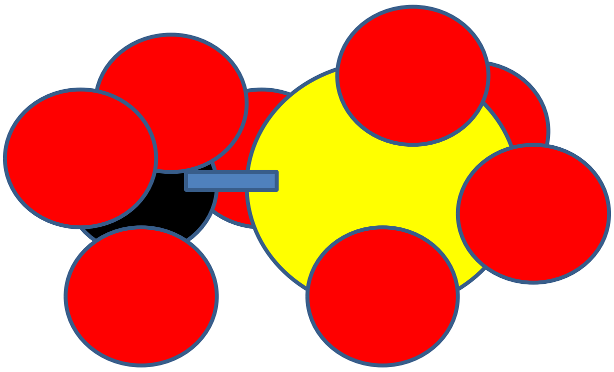

Figure 2.1: A molecule of tracer, trifluoromethyl sulphur pentaflouride ($\mathrm{CF_3SF_5}$). The yellow atom is sulphur, the black atom is carbon, and the red atoms are flourine.

This chapter will detail the methods and some of the results associated with the tracer experiment. In section 2 the tracer will be introduced, and the methods used to collect and analyse samples of tracer explained. In the third section, some methods used to analyse the data will be detailed, followed by key results concerning the evolution of the vertical and horizontal distribution of the tracer, and their implications for diapycnal and isopycnal mixing.

2.2 Methods

2.2.1 The tracer

The tracer used in the DIMES experiment is trifluoromethyl sulphur pentaflouride (chemical symbol $\mathrm{CF_3SF_5}$; see figure 2.1). This man-made molecule is chosen as a purposefully released tracer (Ho *et al.*, 2008) because of our ability to detect it in very low concentrations - equivalent to roughly $1\mathrm{mg}$ of tracer in a cubic kilometre of water - using the methods outlined in section 2.2.3. It is a gas, having a boiling point of $-20°\mathrm{C}$, at atmospheric pressure.

During the injection cruise in February 2009, 76kg of the tracer compound was released in two streaks forming an 'X' pattern near $107°\mathrm{W}$, $58°\mathrm{S}$ (Ledwell *et al.*, 2011). The tracer was released at around 1500m depth, and kept at the density of the 'target' isopycnal surface, $27.906\,\mathrm{kgm^{-3}}$ (neutral density) using a neutrally bouyant sled and a feedback system with a CTD as was used in the NATRE experiment (Ledwell *et al.*, 1998). For the injection, the tracer was stored under pressure as a liquid and forced through tiny holes,

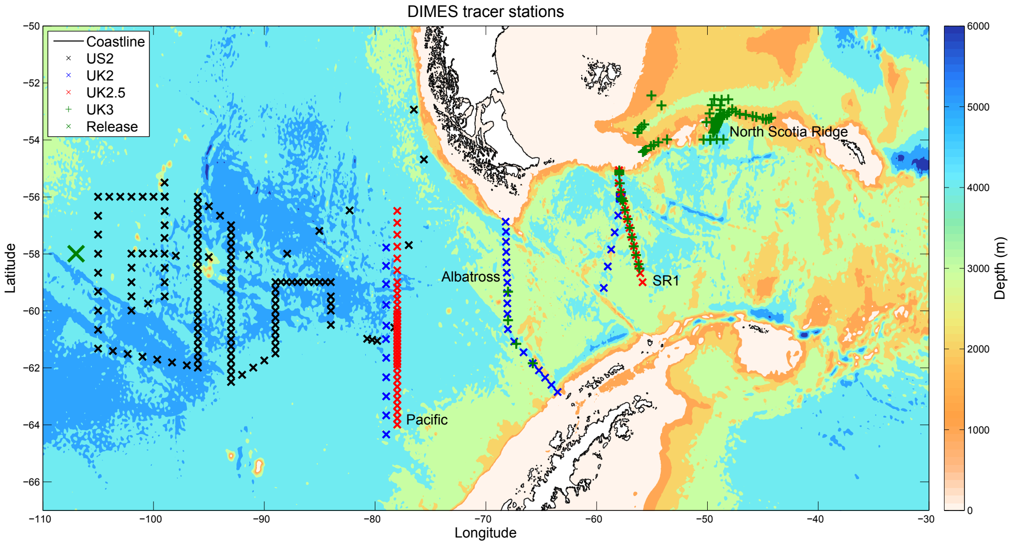

Figure 2.2: A map of the DIMES region. Bathymetry from Smith and Sandwell (1997), with coastline outline in black. Stations where profiles of tracer concentration with depth were gathered on US2 (black crosses), UK2 (blue crosses), UK2.5 (red crosses), and UK3 (green pluses) cruises are marked. Tracer release location is marked with a large green cross.

causing it to form droplets which then dissolve into the seawater (this system was also previously used in NATRE). The initial tracer distribution was then surveyed using both rosette casts and integrating samplers in a similar manner as described by Ledwell *et al.* (1998).

2.2.2 Collecting tracer samples

Figure 2.2 shows the station locations where vertical profiles of tracer concentration with depth were obtained on the US2, UK2, UK2.5, and UK3 cruises. At each station, a ‘rosette’ consisting of 24 10-litre ‘Niskin’ bottles with an attached Conductivity-Temperature-Depth sensor (CTD) is lowered down through the water column on a winch from the ship. As the CTD is brought slowly back up to the ship, Niskins are closed individually at each depth where a water sample is to be obtained. The depths sampled are determined such that a tracer profile centered around the target density is gathered, the density having been calculated from the CTD measurements. Duplicate Niskins are often closed at the most important locations around the target depth to allow for the checking of sample reproducibility, and in addition to provide a backup in the event of a mechanical failure such as a leaked Niskin. Samples are also usually taken near the ocean floor and near the surface, in order that comparisons with water relatively free of tracers, and well ventilated water (water that has recently been in contact with the atmosphere), repectively, may be made.

Once the rosette is on board the ship, water samples are collected from each Niskin. In collecting these samples, care must be taken to minimise the contact the water has with the atmosphere, since the tracer compound will escape into neighbouring air in preference to remaining in solution. Samples are taken from an outlet tap at the bottom of each Niskin via a tygon tube, and introduced slowly into the bottom of 2-litre glass sample bottles. The bottles are filled from the bottom and overflowed once to expel any water that has been in contact with the atmosphere, and then airtight glass stoppers placed on them, while ensuring no air bubbles are trapped inside. The tubes used had been ‘baked’ beforehand to remove any impurities, and are stored in seawater in between stations. The sample bottles were also cleaned with decontaminant and Milli-Q water before use, and are rinsed with seawater from the Niskin to be sampled before being filled. Duplicate samples are typically taken around the target surface to allow for checking of the reproducibility of the tracer sample analysis system. When taking duplicate samples, care must again be taken with the time for which the bottles are overflowed to ensure enough water remains for the duplicate (and any other samples such as salinity that may need to be taken from the Niskin), and additionally to avoid sampling the very last of the water in the Niskin as once a Niskin is opened, the sample water at the top is exposed to the air. Once collected, sample bottles are stored in cold water with ice blocks, as above a certain temperature the tracer compound will begin to ‘degass’ (to escape solution), forming bubbles in the sample.

2.2.3 Analysing tracer samples

The samples are analysed in three stages by an automated design developed at the University of East Anglia following earlier designs from Law *et al.* (1994) and Smethie *et al.* (2000). First a purge and trap system is used to extract the various tracer gases from the water and concentrate it. Then a gas chromatograph separates the different gases, and finally an electron capture detector is used to measure the concentration of each. The gases measured for their concentration were transient tracers sulphur hexaflouride

(SF_6), trifluoro-chloromethane (CFC-13) and dichlorodifluoromethane (CFC-12); and the injected tracer CF_3SF_5.

2.2.3.1 Purge and trap system

The sample bottle is first connected to the purge and trap system, then transferred to a calibrated volume without having any contact with air. Small bubbles of nitrogen gas - the 'carrier' - are then sparged through the sample water to strip out the tracer gases. The carrier gas containing the tracers is then fed into a Unibeads^{TM} 3S 'trap', a u-shaped metal tube containing porous spherical silica beads which absorb the tracer gases while letting the nitrogen pass through. The trap compound is only absorptive at very low temperatures, so is cooled using liquid nitrogen in advance of the sparging process. Once 95% of the tracer has been removed from the water and concentrated in the trap, sparging stops and the trap is heated so that it loses its absorptive properties. The concentrated tracers are then injected into the gas chromatograph (GC) for the next stage of the analysis.

The calibrated volume in which the sample is sparged is relatively large at 1135ml, which maximises the sensitivity of the system since the lower limit for detection is determined by the quantity of tracer that goes to the GC, and a larger volume of water containing a given concentration of tracer will result in a larger tracer quantity. Occasional 'resparges' are carried out, where after a sparged water sample has been analysed for its tracer concentrations, it is kept in the calibrated volume and the sparging process rerun for a second and a third time. The concentrations of tracers measured following the resparges compared with that measured following the first sparge then gives the sparging efficiency, which was 96.1% for CF_3SF_5.

2.2.3.2 Gas chromatograph

The extracted tracers are carried to the GC by the carrier gas. The GC consists of 3 columns: a 1m Porasil B packed pre-column and a 1.5m carbograph AC main column which separate the tracers from each other, and a six inch molecular seive post column which removes N_2O. The materials in the two separation columns cause each tracer to elute at a different time - known as the retention time - so they arrive into the third stage of the analysis, the electron capture detector (ECD), separately. The column material and the carrier gas are known respectively as the stationary phase and the mobile phase of the chromatography process.

2.2.3.3 Electron capture detector

The electron capture detector works by sending pluses of electrons from a beta radiation source across between an anode and a cathode. The beta electrons ionise the nitrogen gas, releasing electrons which flow to the anode. It is the fluorine atoms which make up a significant proportion of all of the tracer compounds (SF_6 - 6 flourine atoms, CFC-12 - 2 flourine atoms, CFC-13 - 3 flourine atoms, CF_3SF_5 - 8 flourine atoms) that explain the high sensitivity of this system, as they are highly electrophilic. This means that they capture many of the free electrons, and hence reduce the current flowing between the electrodes. The ECD then regulates the frequency of the pulses to try to maintain a steady current flow, and outputs the pulse frequency as a voltage, the voltage then being proportional to the quantity of tracer detected.

2.2.3.4 Calibration

The ECD output produces a peak for each tracer, and these are integrated to find an area (see figure 2.3). In the event that it is difficult to identify whether a peak of CF_3SF_5 is present or not, (e.g. for the green surface chromatograph in figure 2.3), a comparison may be made with a sample from deep water, which contains no tracer, in order to establish the shape of the baseline (red chromatograph in figure 2.3). The area of a peak is proportional to the concentration of that tracer, but the system must be calibrated to find the concentration of each tracer that is represented by a unit area of the chromatograph. The calibration is carried out using a gas ‘standard’ containing known concentrations of each tracer. A range of volumes of standard are injected into the system from metal tubular ‘loops’ with known volumes, and a curve is constructed to relate the chromatograph area to the injected concentration for each tracer (see e.g. figure 2.4 for CF_3SF_5). For each tracer it is necessary to inject enough standard to cover the full range of concentrations expected, which in the case of CFC-12 means multiple injections of the largest loop of standard, as this tracer is found in high concentrations at the surface. Calibrations are carried out once a day when possible, and in between calibrations multiple injections of a

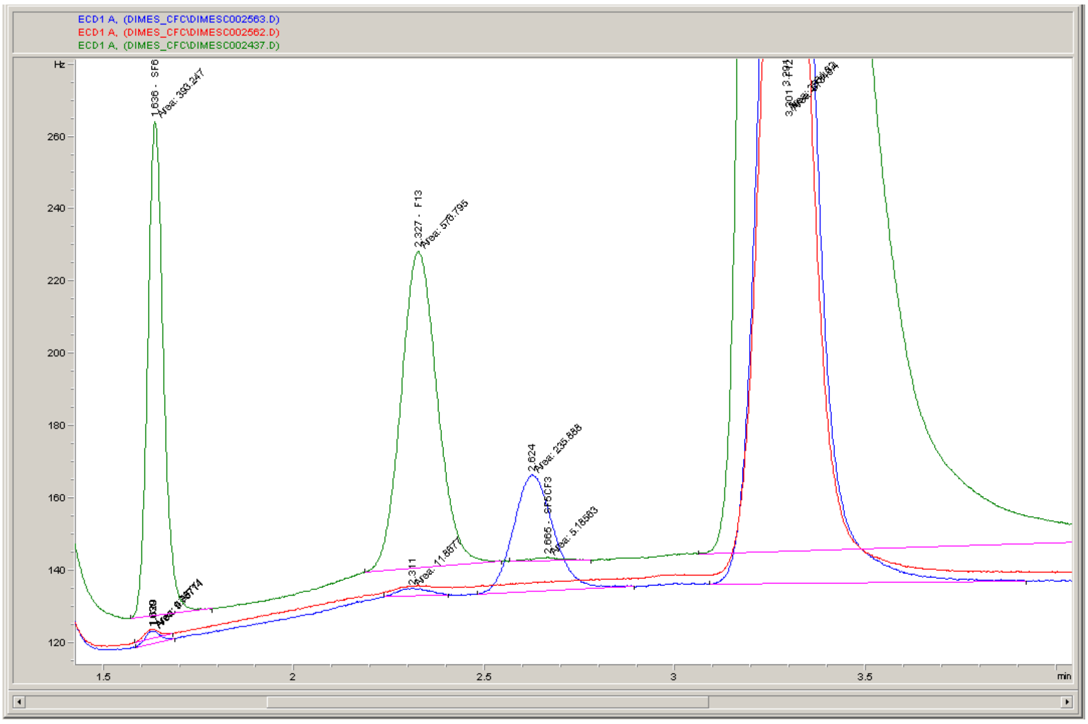

Figure 2.3: Integrated chromatograph outputs from the GC-ECD system. From left to right the peaks are SF_6, CFC-13, CF_3SF_5, and CFC-12. In green is sample from the surface, showing high concentrations of transient tracers and small background of CF_3SF_5; in blue is a sample at the tracer target density; and in red is a tracer free sample from the deep ocean. Taken from RRS James Cook JC054 Cruise Report (Messias *et al.*, 2011).

1ml standard loop are carried out to check for changes in the sensitivity of the system, and from which the calibration curves are adjusted accordingly. The precision of calibration was generally better than 1% for CF_3SF_5 (Messias *et al.*, 2011).

2.3 Results

2.3.1 Data processing methods

2.3.1.1 Depth-density relation

Both the depth, and other quantities needed to determine the density, for each sample are recorded by the CTD. Each profile of tracer concentration therefore can be plotted against depth, or, more relevantly for diapycnal mixing, against density. Since we understand diapycnal mixing in terms of a diffusivity in m^2s^{-1}, but the relationship between depth and density varies for different profiles (i.e. equivalently there is spatial and temporal variation in the stratification), we need a way to standardise the relationship between

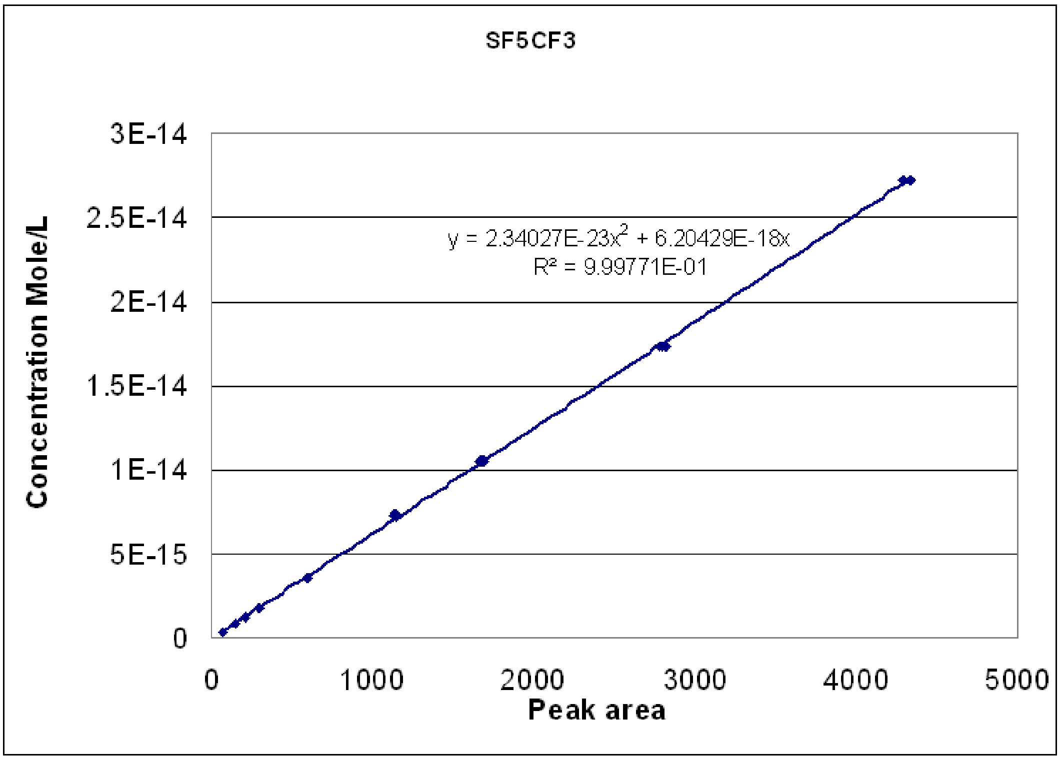

Figure 2.4: Calibration curve for CF_3SF_5. Taken from RRS James Cook JC054 Tracer Report (Messias *et al.*, 2011).

different tracer measurements in order that they may be compared. The first stage is to interpolate the measured depths for each profile onto a standardised density grid, either in potential or neutral density. A mean depth-density relation for a set of profiles may then be calculated by taking the mean across those profiles of the interpolated depths at each point on the density grid. Figure 2.5 shows the depth-density curves in (a) potential density referenced to 1500m ($\sigma_{1.5}$) and (b) neutral density (γ_n) for the UK2, UK2.5 and UK3 cruises, over a density range which covers the diapycnal spread of the tracer around the target density. For analysis where it is neccessary to compare tracer data collected on different cruises, the UK2.5 curve has been used. There are some issues with the neutral density calculation in the Drake Passage region which were highlighted during the analysis carried out for the DIMES paper (Watson *et al.*, 2013), evident here in the slight difference in position of the target surface within the density structure between the two plots. Hence the analysis carried out in this chapter involving a mean depth-density relation uses the data interpolated with potential density. There was also a small (4ppm) error in the salinity calibration on UK2 which was later corrected. However, for

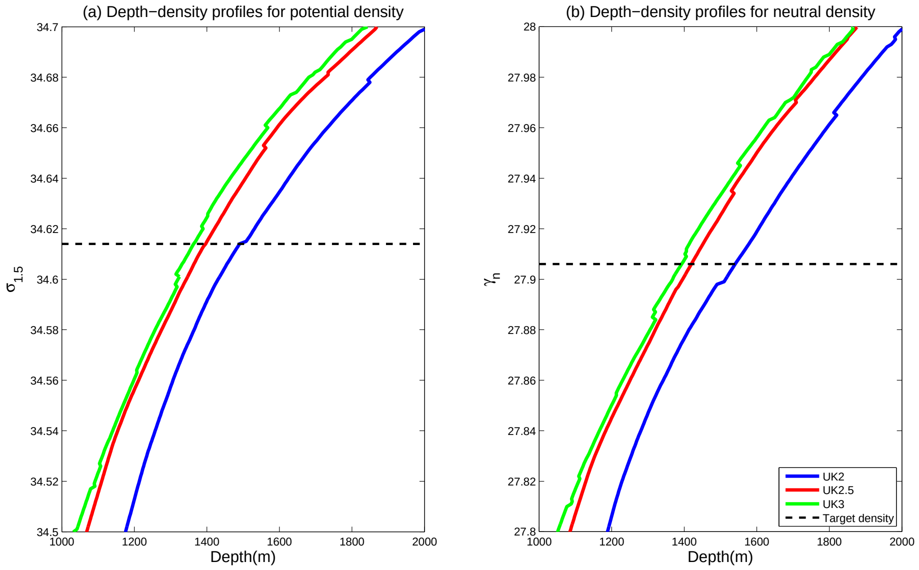

Figure 2.5: Mean depth density relations for tracer stations on the UK2 (blue), UK2.5 (red) and UK3 (green) cruises. The target density is marked with a black dashed line.

the analysis presented here that is referenced by $\sigma_{1.5}$, the correction to this calibration was included, so it cannot explain the apparent difference between the UK2 depth-density profile and the others on figure 2.5.

2.3.1.2 Calculating profile widths

The vertical widths of tracer profiles are the quantity by which the diapycnal spread of the tracer over time is defined, and hence from which diapycnal diffusivities may be deduced. The tracer diffusion results in vertical profiles of concentration which are generally approximately Gaussian in shape, so a Gaussian function is fit to the profiles in order to quantify their vertical width:

$$C(z) = Aexp\left[\frac{-(z-z_{max})^2}{2\sigma^2}\right] \tag{2.1}$$

where A is a scale factor, close to the maximum (or 'peak') tracer concentration, C is the tracer concentration, z is depth, z_{max} is the depth of the peak concentration, and σ is the vertical width. The fitting is done by finding the parameters A, z_{max}, and σ which minimise r^2, the sum of the squares of the differences between the measured and fitted concentrations: $r^2 = \sum_z (C_{fit}(z) - C_{measured}(z))^2$. An example vertical profile of tracer

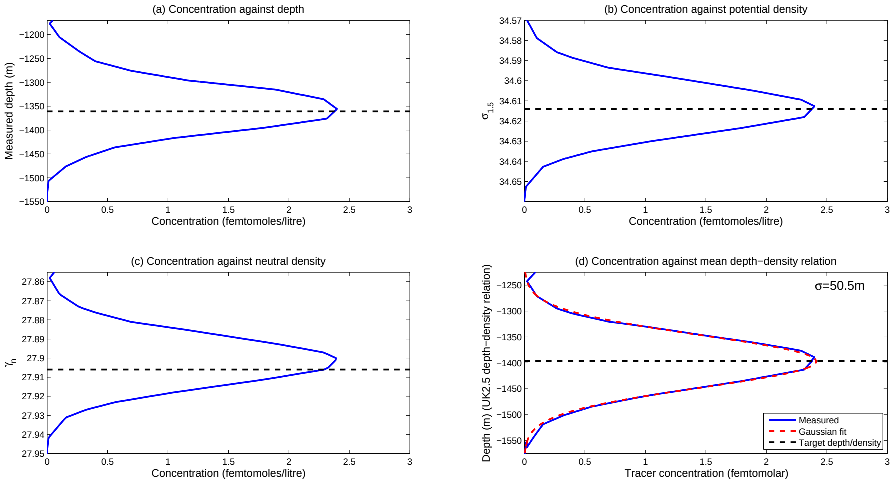

Figure 2.6: An individual tracer vertical concentration profile against (a) depth, (b) potential density referenced to 1500m, (c) neutral density and (d) the mean depth-density relation for UK2.5. Measured tracer concentrations in blue, Gaussian fit in red. Target depth/density is marked with a black dashed line. The vertical width of the profile, σ, obtained from the Gaussian fit using the UK2.5 depth-density relation, is also displayed.

concentration from UK2.5 with Gaussian fits is shown on figure 2.6 plotted against (a) depth, (b) potential density referenced to 1500m, (c) neutral density and (d) the mean depth-density relation for UK2.5. This is a typical profile, taken in the centre of the tracer patch where the target surface is at intermediate depth, and is very close to Gaussian.

2.3.2 Mean profiles

Having standardised the depth-density relationship across all of the measured tracer profiles, taking a mean across a group of profiles may then be used to derive estimates of the time and spatially averaged diapycnal diffusivity experienced by the tracer up to a certain point. The grouping is typically by transect, for example the vertical width of a mean profile constructed from the stations on the ‘Pacific’ transect as marked on figure 2.2 can be used to estimate the diffusivity experienced by the tracer from release to that point. Vertical widths for mean profiles are obtained by fitting Gaussians in the same way as described for individual profiles in section 2.3.1.2. The following formula is then used to find the diapycnal diffusivity K_z:

$$K_z = \frac{{\sigma_f}^2 - {\sigma_i}^2}{2\Delta t} \tag{2.2}$$

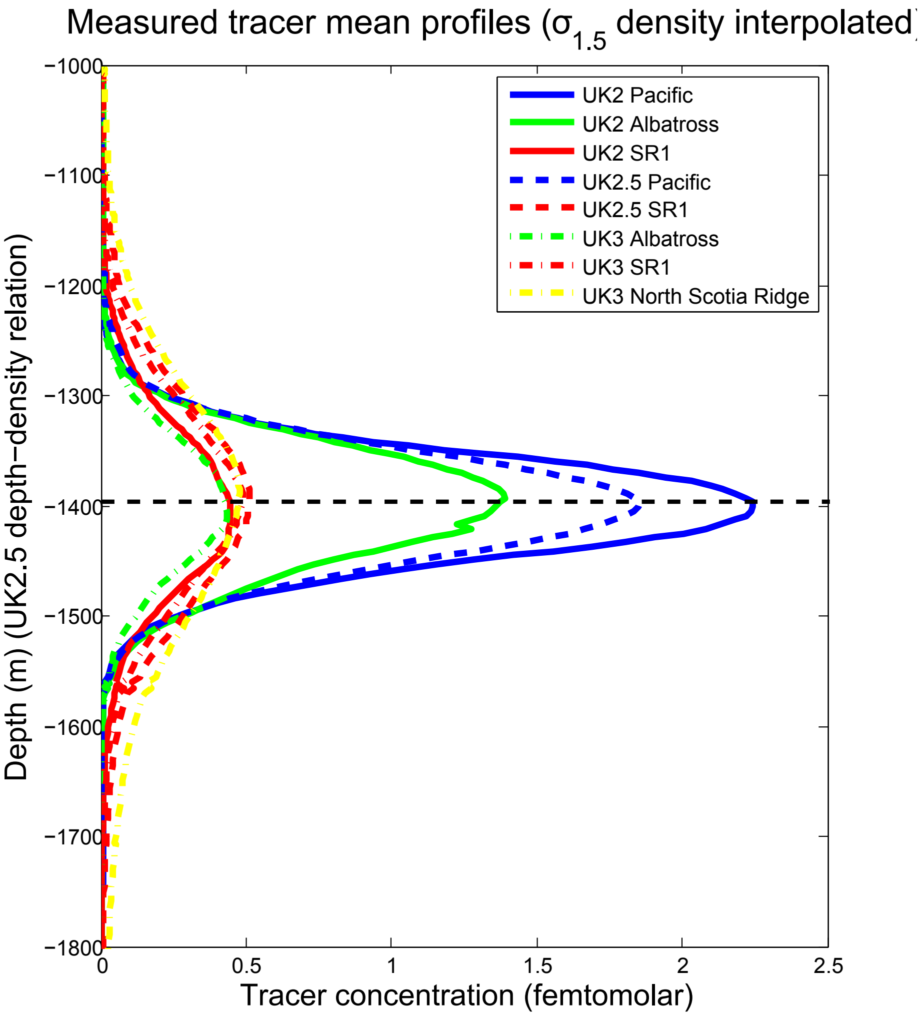

Figure 2.7: Mean profiles of tracer concentration with depth for each of the transects sampled on the UK2 (solid lines), UK2.5 (dashed lines) and UK3 (dashed-dotted lines) cruises. Pacific transect in blue, Albatross transect in green, SR1 transect in red, North Scotia Ridge transect in Yellow (see figure 2.2 for the transects). The concentrations are plotted against the mean depth-density relation for UK2.5, individual profiles having been interpolated onto a $\sigma_{1.5}$ grid before being averaged by transect. The depth of the target density is marked with a black dashed line.

Where σ_i and σ_f are the initial and final mean profile vertical widths in metres and Δt is the time between the measurement of these profiles in seconds. Figure 2.7 shows the mean profiles of each of the transects surveyed on the UK2, UK2.5 and UK3 cruises. As the tracer travels eastwards in the ACC, the peaks become wider and decrease in magnitude due to diapycnal and isopycnal mixing, the former tending to spread the tracer in the vertical and the latter tending to spread it in the horizontal. In this and all other analyses, the concentrations in the first 21 stations of UK2, which were gathered in the same small grid at the location of the DIMES mooring array to the north of SR1, are counted as one station in the SR1 mean profile. The mean concentration across the density interpolated data for these 21 stations is taken to build the concentration profile at the grid.

Cruise	Transect	Vertical width (m)	Diffusivity ($\times 10^{-5}\ \mathrm{m^2\,s^{-1}}$)	Range ($\times 10^{-5}\ \mathrm{m^2\,s^{-1}}$)
UK2	Pacific	46.1	1.75	1.55-1.95
	Albatross	53.0	2.32	1.78-2.92
	SR1	75.2	4.69	2.95-6.83
UK2.5	Pacific	49.5	1.74	1.64-1.84
	SR1	96.2	6.64	5.20-8.25
UK3	Albatross	61.5	1.98	1.62-2.38
	SR1	87.1	3.99	3.30-4.76
	North Scotia Ridge	117.0	7.21	6.11-8.39

Table 2.1: Mean vertical widths of transects on UK2, UK2.5 and UK3 cruises and their implied diapycnal diffusivities, assuming an initial vertical profile width of 5.5m (Ledwell *et al.*, 2011).

Table 2.1 shows the widths of the mean profiles displayed on figure 2.7 with their implied diapycnal diffusivities calculated according to equation 2.2. The initial profile width σ_i is the value reported by Ledwell *et al.* (2011) as the vertical spread of the tracer patch immediately after release. The time between the initial and final profiles Δt is taken to be 1.9 years for UK2, 2.2 years for UK2.5 and 3 years for UK3. The uncertainty ranges are calculated using the standard error on the transect mean profile widths to obtain upper and lower limits on the profile widths, then feeding these estimates into equation 2.2. The diffusivities show a clear pattern that significantly more diapycnal mixing has taken place in Drake Passage (up to SR1) and the Scotia Sea (up to the North Scotia Ridge) when compared with the Southeast Pacific (up to the Albatross transect). However, the fact that the values represent a time and spatial average of the mixing of the tracer from its release up to any given transect means that the diffusivity values for the Drake Passage and Scotia Sea are actually lower than the local value, since the tracer went through the Southeast Pacific before entering Drake Passage and then the Scotia Sea. In order to get more localised values of diapycnal diffusivity, a numerical model is required (see Chapter 3). The higher value of diffusivity implied by the mean profile at SR1 on the UK2.5 cruise compared with UK2 is due to the fact that on UK2.5 the stations sampled on SR1 extended further north and hence closer to the South American continental slope. Consequentially some wide profiles implying intense mixing due to proximity to the slope were measured on the UK2.5 survey (see section 2.3.4 for more details). The slight decrease in the diffusivity estimates at SR1 and the Albatross line when comparing UK2 with UK3 one year later may indicate a leading edge effect. The tracer measured at these locations on UK2 was at the front of the tracer patch, having travelled faster, most likely in frontal jets, than the rest of the tracer, and consequently experienced stronger mixing. By UK3 the tracer sampled at these locations was in the main body of the tracer patch, having moved at a slower pace and therefore experienced comparitively weaker mixing. This phenomenon will be discussed further in Chapter 3.

2.3.3 Column integrals

In order to assess some aspects of the horizontal distribution of the tracer, column integrals are calculated at each station. The column integral is the total amount of tracer per horizontal square metre that is implied by the concentrations measured throughout the water column at a particular station, and is calculated according to:

$$I = 1 \times 10^{-15} \sum_{i} \frac{1}{2}(C(z_i) + C(z_{i+1}))(z_{i+1} - z_i) \tag{2.3}$$

where I is the column integral in picomoles per square metre, z_i, are depths at which tracer concentrations were measured, and $C(z_i)$ are the concentrations at those depths in moles per litre. The fact that there are 10^6 litres in a cubic metre is accounted for in the 10^{-15} factor. The calculation uses the trapezium rule to work out the integral, which implies a linear interpolation of concentrations between points. This is an approximation since we have no information about tracer concentrations between sample depths.

Figures 2.8 to 2.11 show the column integrals for tracer stations on the UK2, UK2.5 and UK3 cruises. On UK2, there are clear reductions in the amount of tracer found at the northern and southern ends of the Albatross transect, indicating that on this transect the north-south extent of the bulk of the tracer was surveyed. On the Pacific transect the edge of the patch appears to have been delineated to the south but not the north on both UK2 and UK2.5. By the time the tracer has entered the Scotia Sea on UK3, it has not been possible to survey its full extent. A pattern emerges that a sharp reduction of tracer

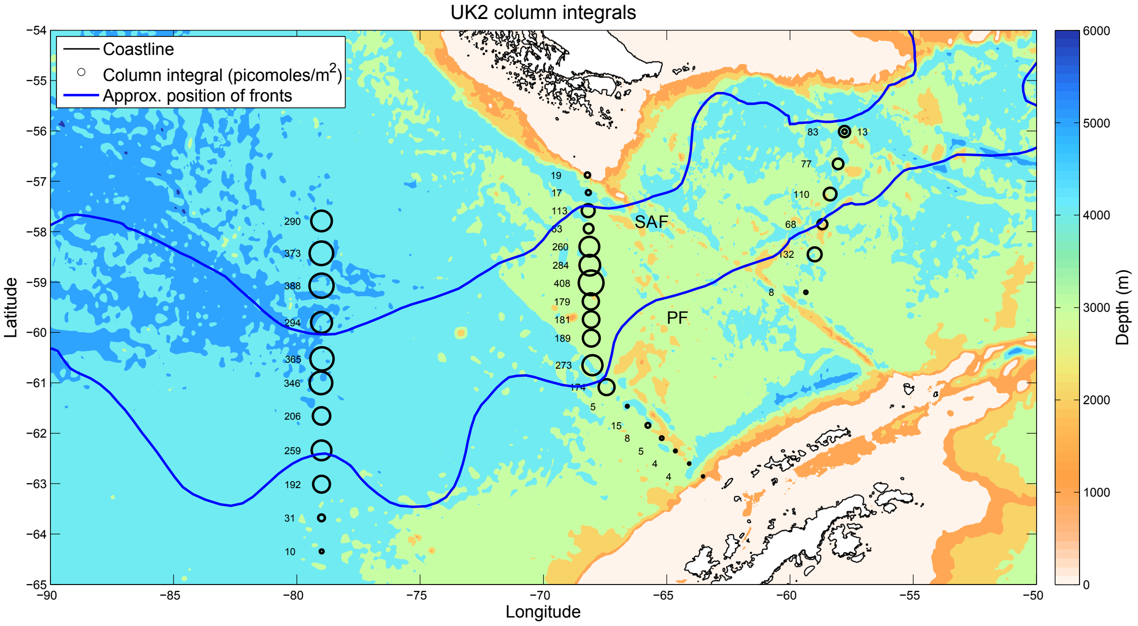

Figure 2.8: Column integrals for UK2. Station locations are marked as circles, their size proportional to the column integral, which is labelled in picomoles/m^2. Transects from left to right are Pacific, Albatross, and SR1. Bathymetry is given by the background colours, and the coastline is marked in black. The blue lines are the positions of the Sub Antarctic Front (SAF) and the Polar Front (PF) (plotted using MATLAB `plot_ACC_fronts` package, Copyright (c) 2013, Chad Greene).

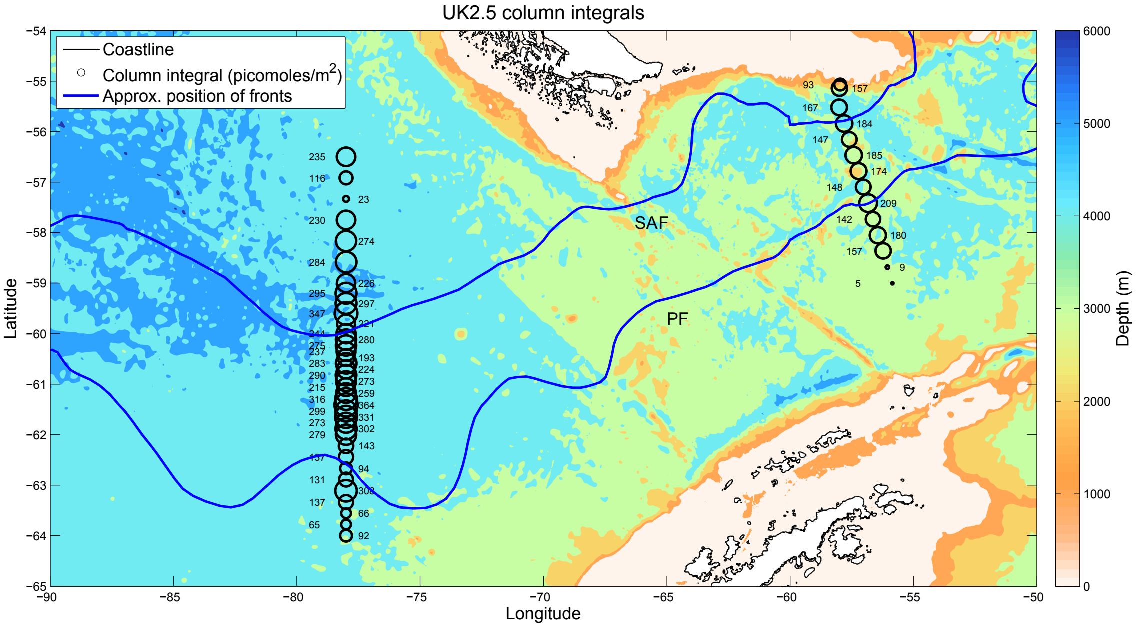

Figure 2.9: As figure 2.8 but for UK2.5. Transects from left to right are Pacific and SR1.

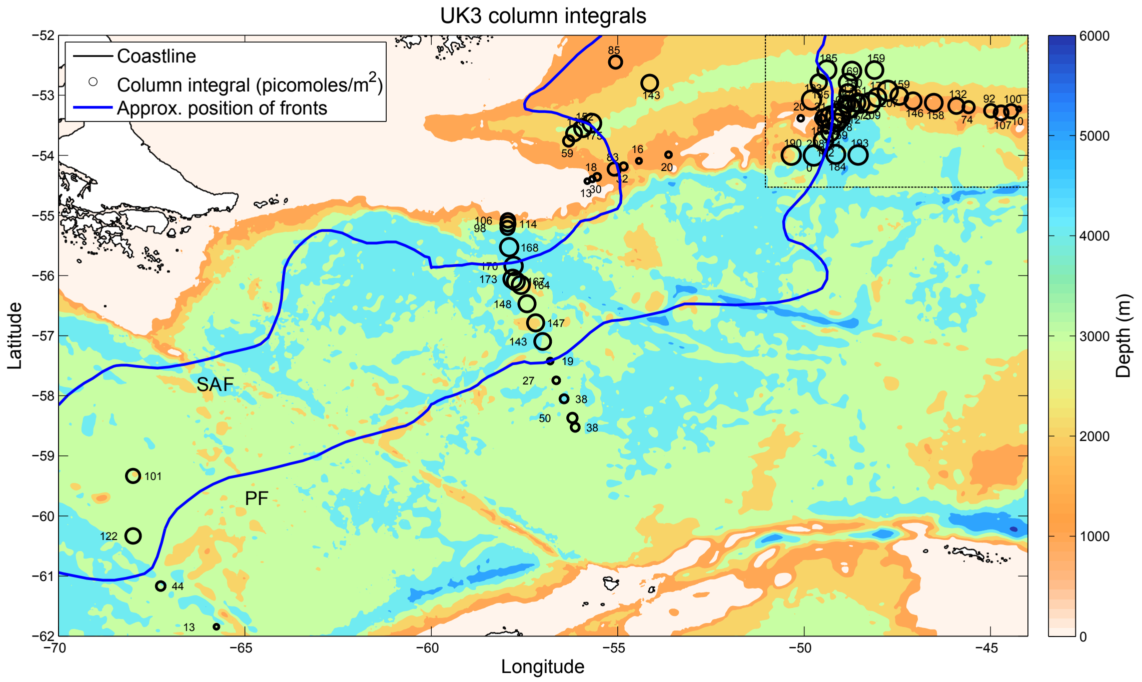

Figure 2.10: As figure 2.8 but for UK3. Transects from left to right are Albatross, SR1 and the North Scotia Ridge. The inset indicated by the black dashed box is shown in figure 2.11

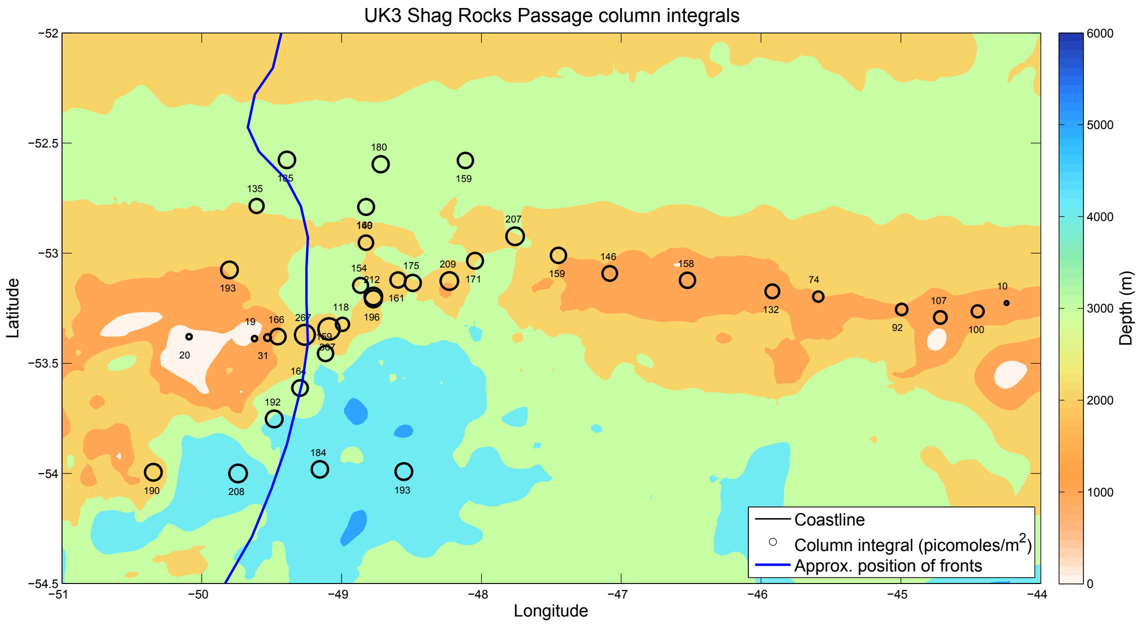

Figure 2.11: Inset from figure 2.10.

is observed which approximately coincides with the plotted Polar Front on the UK2 Pacific, UK2 Albatross, UK2 SR1, UK2.5 Pacific, UK3 Albatross and UK3 SR1 transects. There are theories, such as that described by Ferrari and Nikurashin (2010), suggesting that isopycnal mixing of tracers is suppressed in fronts, where the mean flow advects the tracers through eddies before they have had the chance to mix. The low tracer concentrations found south of the Polar Front on these surveys seems consistent with this.

From previous experiments (e.g. Ledwell *et al.*, 1998), the horizontal distribution of the tracer was expected to be ‘streaky’, with regions of high concentration interspersed with regions where no or very little tracer is found. This is due to the stretching of the tracer patch into streaks by the mesoscale eddy field. From figure 2.8 it can be seen that there is no evidence of streaks from UK2, as everywhere within the main part of the tracer patch that tracer was sampled, similar concentrations are found. In order to establish whether streaks were present but they had not been resolved, a high resolution section on the Pacific transect, with stations spaced only 7.5km apart, was carried out on UK2.5 (figure 2.9). Again similar concentrations have been found all the way along this section (as evidenced by the range of the column integral values), leading to the conclusion that isopycnal mixing on smaller scales had filled in the tracer patch by this stage.

It was also noted on the UK2 cruise that concentrations in general were lower than expected based on a numerical model simulation and considering that a year earlier on US2, column integral values of 1000 picomoles/m^2 were observed in the centre of the tracer patch (Ledwell *et al.*, 2011). Possible explanations for this might be that the tracer had moved more slowly than expected, so the bulk of it had not reached the Pacific transect by the time of UK2, or that it had spread out more in the horizontal than expected, also moving more quickly through Drake Passage as a consequence. The latter explanation seems to fit the data better, since similar amounts of tracer were seen on the Pacific transect on UK2 and 3 months later on UK2.5, and by UK3 the column integrals are small on the Albatross transect, the bulk of the tracer apparently having moved into the Scotia Sea and beyond.

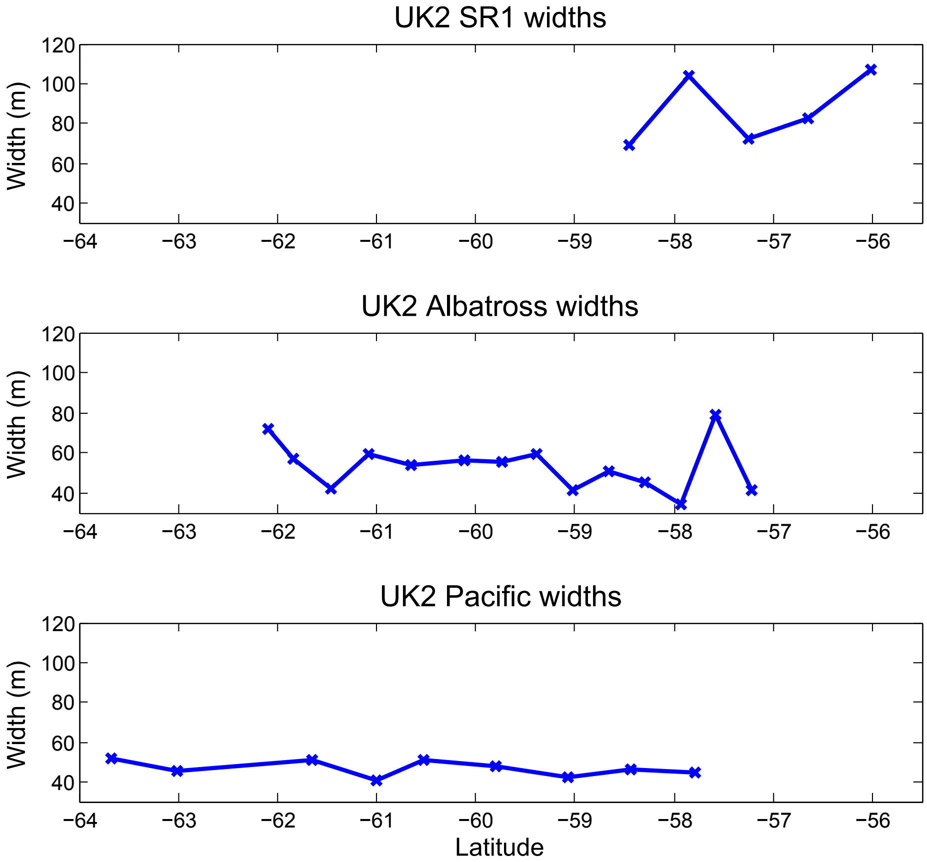

Figure 2.12: Vertical widths of individual tracer profiles from UK2 by transect. Obtained by fitting Gaussians to each profile plotted against the UK2.5 depth-density relation. From top to bottom: SR1, Albatross and Pacific transects (see figure 2.2).

2.3.4 Individual profiles

Figures 2.12 to 2.14 show the vertical widths of individual profiles on the UK2, UK2.5 and UK3 cruises by transect. The North Scotia Ridge transect has been excluded from the UK3 plot because the focus of this thesis is on the diapycnal mixing in the Southeast Pacific and Drake Passage, and the North Scotia Ridge measurements sampled the tracer after it had gone through the Scotia Sea. In general, the meridional variability in the vertical widths is much greater at SR1 and, to a lesser extent, the Albatross transect, than it is in the Pacific transect. This reflects the fact that diapycnal mixing in the Southeast Pacific is relatively homogeneous, whereas it is very inhomogeneous in Drake Passage. There is little pattern obvious, however, in the meridional variation, with the exception

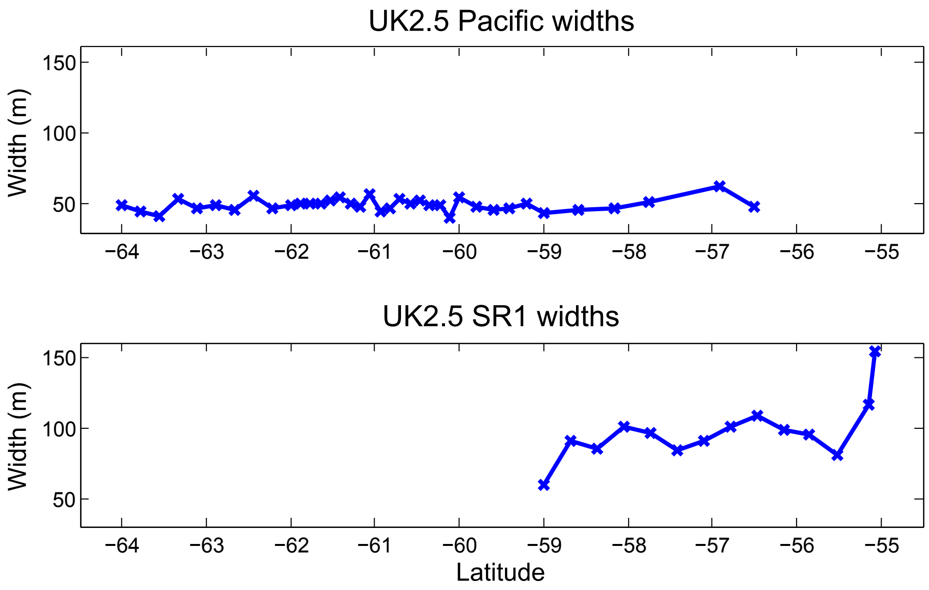

Figure 2.13: As figure 2.12 but for UK2.5. Pacific (top) and SR1 (bottom) transects.

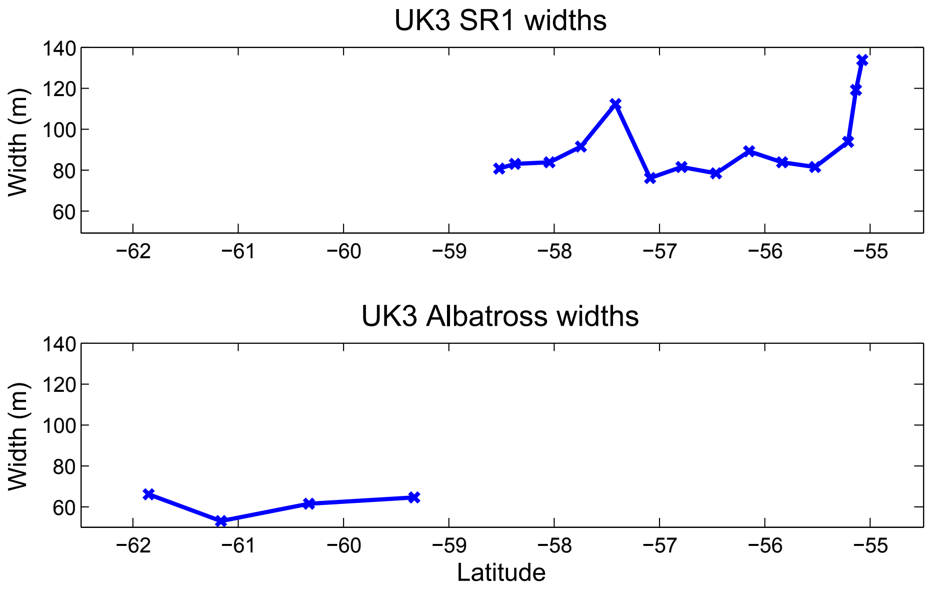

Figure 2.14: As figure 2.12 but for UK3. SR1 (top) and Albatross (bottom) transects.

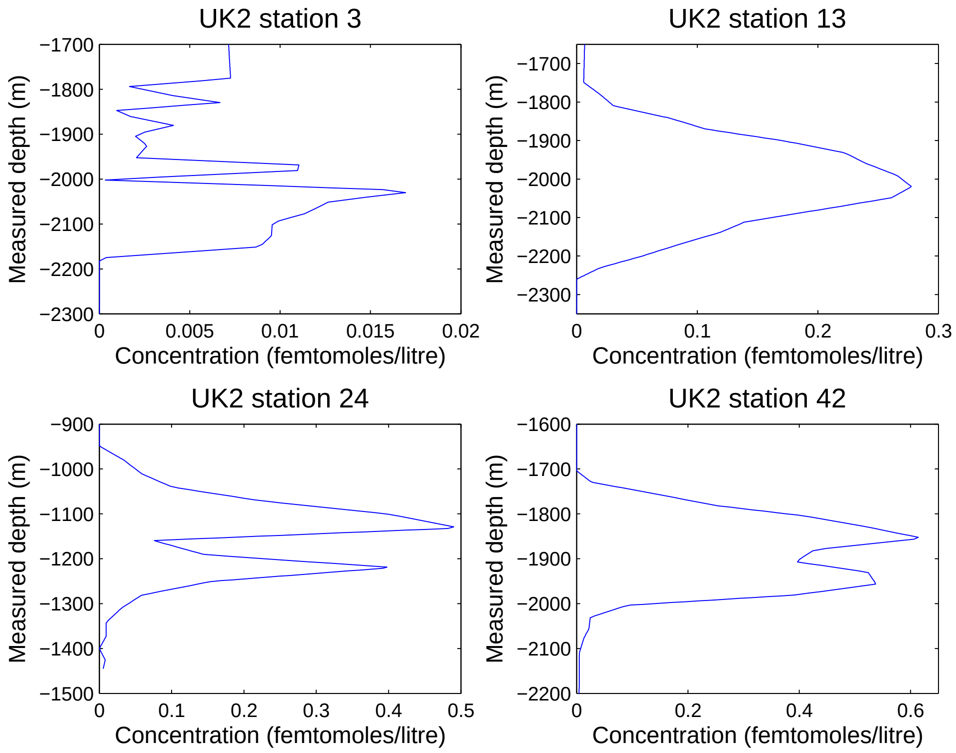

Figure 2.15: Four individual profiles of tracer concentration from UK2, plotted against their measured depths. Stations 3 and 13 (top left and top right) were taken at the grid to the north of SR1 before and after the vessel returning to port. Stations 24 and 42 (bottom left and bottom right) show intrusions, taken on SR1 and the Albatross transect, repectively.

that profiles get siginificantly wider at the extreme northern end of SR1. This is likely to be due to the fact that the tracer isopycnal slopes downwards to the north and so the tracer comes close to the continental slope in this region. Tracer that has followed a path around the continental slope through Drake Passage will have been subjected to strongly enhanced boundary mixing. The profiles at around 58°S on SR1 and 57.5°S on the Albatross transect on UK2 which are significantly wider than their surrounding profiles are the result of ‘intrusions’, where was masses from elsewhere have mixed in isopycnally at the tracer density (see figure 2.15).

Figure 2.15 shows some examples of tracer profiles taken on UK2. Stations 3 and 13 are from the grid to the north of SR1, taken before and after the RRS James Cook was forced to return to port for repairs. Station 3 shows very low concentrations of tracer, and the distribution is filamented, with patches of lower concentration interspersed with high concentrations. This indicates that we were at the leading edge of the tracer patch at this point. About 2 weeks later in the same location, station 13 shows the vertical distribution

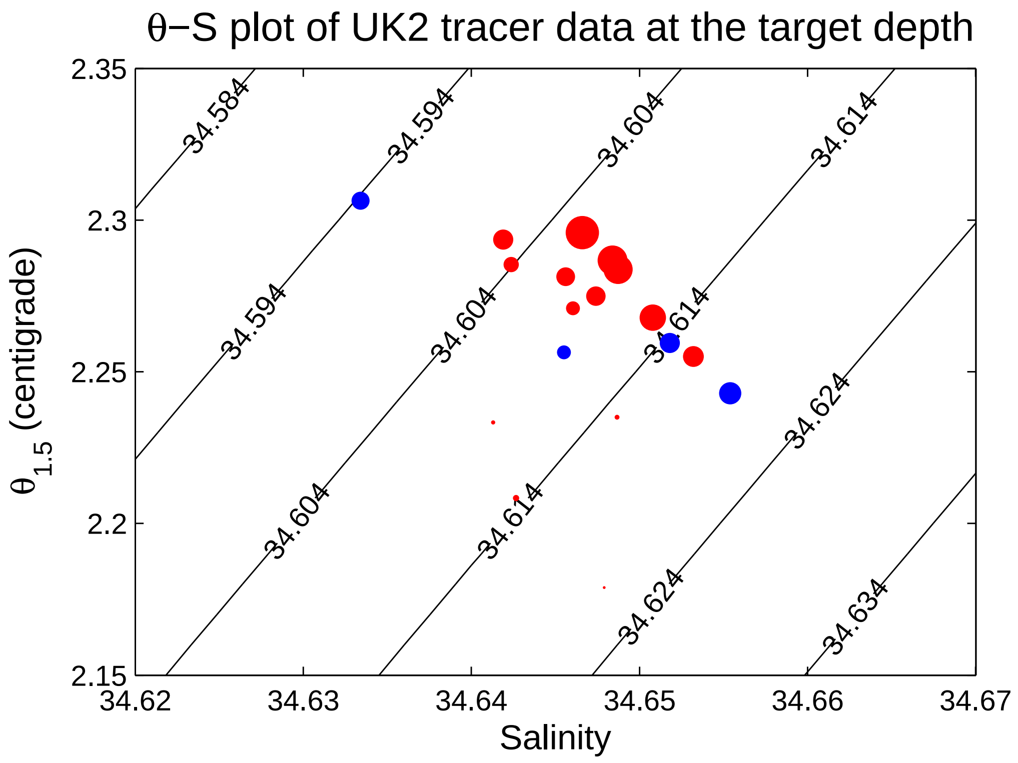

Figure 2.16: $\theta - S$ plot of the tracer data at the depth of the peak tracer concentration for stations on the UK2 Albatross (red) and UK2 SR1 (blue) transects. For each transect, the size of the point is proportional to the peak concentration found. Points from the SR1 transect are scaled twice as large as the Albatross transect so that they are visible. The contours are potential density referenced to 1500 dbar (the target density is $34.614\,\mathrm{kgm}^{-3}$).

of the tracer has become much more Gaussian. Stations 24 and 42 are examples of profiles where an intrusion has occured, resulting in a very wide vertical spread.

2.3.5 Cabelling

During UK2, it was noted that the mixing measured by the microstructure team seemed to be too small to account for the spread of the tracer between the Albatross and SR1 transects. One possible explanation for this discrepancy might be cabelling, since this would cause the diapycnal spread of the tracer without the associated turbulent mixing detectable by microstructure. Figure 2.16 shows the temperature and salinity at the target depth for tracer stations on the SR1 and Albatross transects on UK2. If cabelling were contributing to the diapycnal mixing seen between these two transects, a separation should be visible between the T-S properties of the two transects, implying isopycnal mixing across a front had taken place in between. For example if isopycnal mixing had occurred with water from south of the polar front, the SR1 data would be offset towards the cooler, fresher area of the plot. Since no such offset is evident, it was concluded that cabbeling is not playing a significant role in the observed diapycnal mixing of the tracer.

2.4 Summary

In this chapter some results from measurements of the DIMES tracer on oceanographic cruises approximately 1.9 years, 2.2 years, and 3 years from release have been presented. The key result is that enhanced diapycnal mixing was seen in Drake Passage when compared with the Southeast Pacific. However, since the vertical spread of the tracer gives only a time and spatially averaged measure of the mixing, numerical models are needed to fully interpret the data. Such work will be the focus of the chapters that follow. There have also been questions raised concerning the horizontal distribution of the diapycnal mixing, and of an apparent discrepancy between mixing implied by the tracer and that diagnosed from microstructure measurements. These will be examined in Chapters 4 and 5.

Chapter 3

A 2D advection-diffusion model

3.1 Introduction

The tracer experiment described in chapter 2 provides us with a direct measurement of diapycnal mixing over a long time period and a wide area through the increase in the vertical spread of the tracer with time. However, the raw tracer profiles provide only a time- and spatially-averaged measure of the mixing experienced by the tracer from its release to the point of measurement. In order to extract useful information about the spatial distribution of diapycnal mixing in an inhomogeneous environment, and subsequently attempt to make inferences about the causes of the mixing, a numerical model is required. In this chapter, a simple model is used in conjunction with tracer measurements from the UK2, UK2.5 and UK3 cruises to diagnose diapycnal mixing rates in the Southeast Pacific and Drake Passage. Some of the work presented represents a contribution to Watson *et al.* (2013) (see section 3.4.1).

In the next section of this chapter, the numerical model used will be described. In the third section, details of methods used to compare model output with the tracer measurements and optimise model parameters for the best model-data fit will be given. The fourth section will detail the results of the model to tracer data comparison.

3.2 Model description

3.2.1 Model fundamentals

The model, coded in Matlab, has been adapted from a model written by Jim Ledwell (personal communication, 2011). Its dimensions are along-stream and depth, covering an area from 180°W to 0°W in the horizontal and 300m above and below the tracer target surface in the vertical. The along-stream path for the tracer advection is assumed to be zonal, an approximation that is reasonable for the tracer's progression from the Southeast Pacific into Drake Passage, but that breaks down once it enters the Scotia Sea, where the ACC turns northwards. The resolution is 10m in the vertical and 1 degree in the along-stream/zonal direction. Zonal distances are converted from degrees to metres assuming an average latitude of the tracer patch of 60°S using the relationship $distance\ (m) = 111000 \times cos(60°)$, an approximation also appropriate for the tracer's transit from the Southeast Pacific into Drake Passage. With the model dimensions in metres, a two-dimensional realisation of the advection-diffusion equation is solved for the tracer:

$$\frac{\partial C}{\partial t} = \nabla \cdot (K \nabla C) - u \cdot \nabla C \tag{3.1}$$

where C is the tracer concentration, t is time, K is a diffusivity tensor made up of along stream (K_h) and vertical (K_z) components, and u is the advection velocity.

The model is run from the tracer release for 3 years to produce outputs corresponding to the midpoints of UK2 (1.9 years), UK2.5 (2.2 years) and UK3 (3 years). Cross sections of tracer concentration through the model in the vertical direction may then be obtained at points on the model grid corresponding to the approximate average longitudes of transects on the three cruises. These are at 79°W, 68°W, and 58°W (UK2 Pacific, Albatross, and SR1 transects, respectively, see figure 2.2); 78°W and 57°W (UK2.5 Pacific and SR1 transects, respectively); and 67°W, 57°W and 48°W (UK3 Albatross, SR1 and North Scotia Ridge transects, respectively). The North Scotia Ridge actually runs approximately west to east at the northern boundary of the Scotia Sea (see figure 2.2), and the longitude of this transect has been taken to be the longitude of Shag Rock's passage, a deep passage in the ridge through which the ACC flows (and therefore through which much of the tracer may be expected to pass).

3.2.2 Initial condition

The initial tracer distribution is modelled as a small 2D Gaussian patch according to the following equation:

$$C_0(x,z) = \frac{N}{2\pi LH} exp\left[\frac{-z^2}{2H^2} - \frac{(x-x_0)^2}{2L^2}\right] \tag{3.2}$$

where C_0 is the tracer concentration, x and z are the model along-stream and vertical coordinates, x_0 is the zonal coordinate of the release location, N is the total amount of injected tracer in moles (76kg = 388 moles), and L and H are estimates of the zonal and vertical widths of the tracer patch, respectively. The resulting initial tracer distribution is centred around $z = 0, x = -107°$W, equivalent to the target surface at the release longitude. $C_0(x,z)$ in fact does not represent a concentration, but an integral through the meridional extent of the tracer patch at the given (x,z) coordinates, since the third spatial dimension is absent from the model.

3.2.3 Model parameters

Three key parameters may be varied to produce model output for comparison with the tracer data: the zonal velocity u, the horizontal (effectively isopycnal) diffusivity K_h and the vertical (effectively diapycnal) diffusivity K_z. Here, horizontal/vertical is equivalent to isopycnal/diapycnal since there is no density and no vertical velocity in the model, so the tracer advects at constant model depth $z = 0$, equivalent to along isopycnal advection in the ocean. The parameters u and K_h vary with height within the model according to $q(z) = exp(z/h_q)q$, where q is either u or K_h and h_q is the scale height, with $h_u = 1500$m and $h_{Kh} = 1000$m.

The model domain is divided zonally into sections, designed broadly to represent the different mixing regimes experienced by the tracer. In a 2-zoned realisation, the domain is split into a ‘Pacific’ and a ‘Drake Passage’ zone, with the boundary at 67°W. Each zone has its own value for the u, K_h and K_z parameters, with the value being specified at $z = 0$ in the case of depth-dependent quantities. The boundary is chosen as the approximate longitude that the rough topography of Drake Passage begins (see figure 2.2); however some optimisation of the boundary position using methods described in section 3.3 found that this longitude was also the best position for producing model outputs consistent with the tracer measurements. In this realisation, the two zones are broadly characterised as relatively slow advection and weak diapycnal mixing in the Pacific, and relatively fast advection and strong diapycnal mixing in Drake Passage. An alternative realisation was tested adding a third zone for the Scotia Sea, with the boundary between this and the Drake Passage zones at $57°$W. However, this proved difficult to optimise, and was abandoned in favour of the two-zone model on the grounds that the model assumptions as laid out in section 3.2 are not valid in the Scotia Sea. Comparisons that were carried out between model outputs and the tracer data gathered at the North Scotia Ridge aimed at diagnosing the Scotia Sea mixing are consequently left out of the analysis that follows.

3.3 Model optimisation

3.3.1 Cost function

Having obtained model profiles of tracer concentration with depth at the longitudes and times corresponding to the transects where tracer measurements were taken, a cost function is used to quantify how well the model output fits the data. The cost function, χ^2, compares the vertical widths and peak concentrations of all the individual measured tracer profiles on a transect (obtained using the methods described in section 2.3.1.2) with the vertical width and peak concentration of the model profile corresponding to that transect. The following equation is used:

$$\chi^2 = \sum_T \sum_{i=1}^{n_T} \frac{(w_i - W_T)^2}{{\sigma_{w_T}}^2} + \frac{(c_i - C_T)^2}{{\sigma_{c_T}}^2} \tag{3.3}$$

where w_i and c_i are individual measured profile vertical widths and peak concentrations, ${\sigma_{w_T}}^2$ and ${\sigma_{c_T}}^2$ are the variances of the measured widths and concentrations on a particular transect, and W_T and C_T are the model profile vertical width and peak concentration for that transect. The inner sum is over all the profiles on a transect, n_T, and the outer sum may be over a number of the transects, T, sampled on the UK2, UK2.5 and UK3 cruises. The measurements compared are from the Pacific, Albatross, SR1 and North Scotia Ridge transects on these three cruises as described in section 3.2. Individual transects or groups of transects may be included in the cost function, for example to make a comparison only with data in the Pacific or with data gathered on a particular cruise; equally the contributions of the vertical widths and peak concentrations may be examined separately or together.

The expectation value of the cost function, if the distribution of the measured data on a transect is assumed to be normal, is $N - q$, where N is the number of measurements to be compared (equal either to the number of profiles or twice that number if both widths and concentrations are included in the cost function), and q is the number of model parameters that are varied to minimise the cost function. These parameters may be the whole set, or a subset of u, K_h and K_z for each model zone as described in section 3.2.3. An estimate of the uncertainty on the model parameters may then be made by varying a parameter about its optimum value (that which minimises χ^2), since a departure of 1σ by a parameter from its optimum increases the value of χ^2 by one (see Bevington and Robinson, 1992).

3.3.2 Methods of optimisation

Three methods of optimising the model parameters to minimise the cost function were tested. The first used Matlab's `fminsearch` routine to optimise all parameters simultaneously. This has the advantage that it should theoretically converge on the combination of parameters that give the lowest value of χ^2 to a high degree of precision. However, since `fminsearch` does not allow limits to be placed on the range of input parameters, it often results in unphysical values, for example negative horizontal diffusivities. In addition, for the two-zone model, for example, there are six parameters to optimise (one in each zone for u, K_h and K_z), which means that `fminsearch` takes a long time to find a solution and may never converge.

A second method involved setting all the parameters to an initial guess, and optimising one at a time using `fminsearch`. Once the first value, e.g. u_p (the advection velocity in the Pacific zone), had been optimised with all the other values fixed, the next value, K_{hp} (the horizontal diffusivity in the Pacific zone), would be optimised with u_p set to its newly optimised value, then u_p and K_{hp} would be set while K_{zp} (the vertical diffusivity in the Pacific zone), was optimised, and so on. Once all values have been optimised, the process is repeated with the newly optimised values fixed, and the whole set of values looped round repeatedly until they converge on their individual solutions. The major disadvantage of this method is that it is extremely time-consuming, and still can result in unrealistic values for some parameters, although the tendency for converging on a completely unphysical solution is reduced. There is also some question as to whether the order in which the parameters are optimised matters, since all other values are fixed while a particular parameter is optimised, so there may be a tendency for this method to lead the solution in a particular direction.

In the third method, a range of possible values for each parameter was chosen, and a series of nested loops in Matlab were constructed to find the value of χ^2 for every combination of parameter values within the defined ranges. This was done first with a coarse resolution over a wide range of values for each parameter, and then with finer resolution over a narrower range to home in on the solution. This method allows sensible ranges to be set for all the parameters, and is much less time consuming than method 2, while also avoiding the problem of the solution being led in a particular direction by the order of parameter optimisation. Once an optimum solution for all parameters has been found to a reasonable degree of precision, all values but one are then fixed and `fminsearch` used to further optimise the key parameters individually. These key parameters are K_{zp} and K_{zd}, respectively the vertical diffusivities in the Pacific and Drake Passage. Finally, uncertainties may be found on these key parameters by varying them from their fully optimised values to increase χ^2 by one as described in section 3.3.1. This optimisation method was used to arrive at the results presented in section 3.4.

3.3.3 Optimising for widths and concentrations

The first set of parameter optimisations made use of the contributions of both the vertical widths and the peak concentrations of tracer profiles to the cost function. The vertical widths may be compared directly as described in section 3.3.1, but the peak concentrations of the model profiles must be divided by a factor to account for the spread of the tracer in the meridional direction. A number of options for estimating the meridional width of the tracer patch on each cruise were investigated. Figure 3.1 shows the meridional distribution of column integrals for tracer stations on selected transects from the UK2, UK2.5 and UK3 cruises. An estimate for the total meridional extent of the tracer patch may be made from

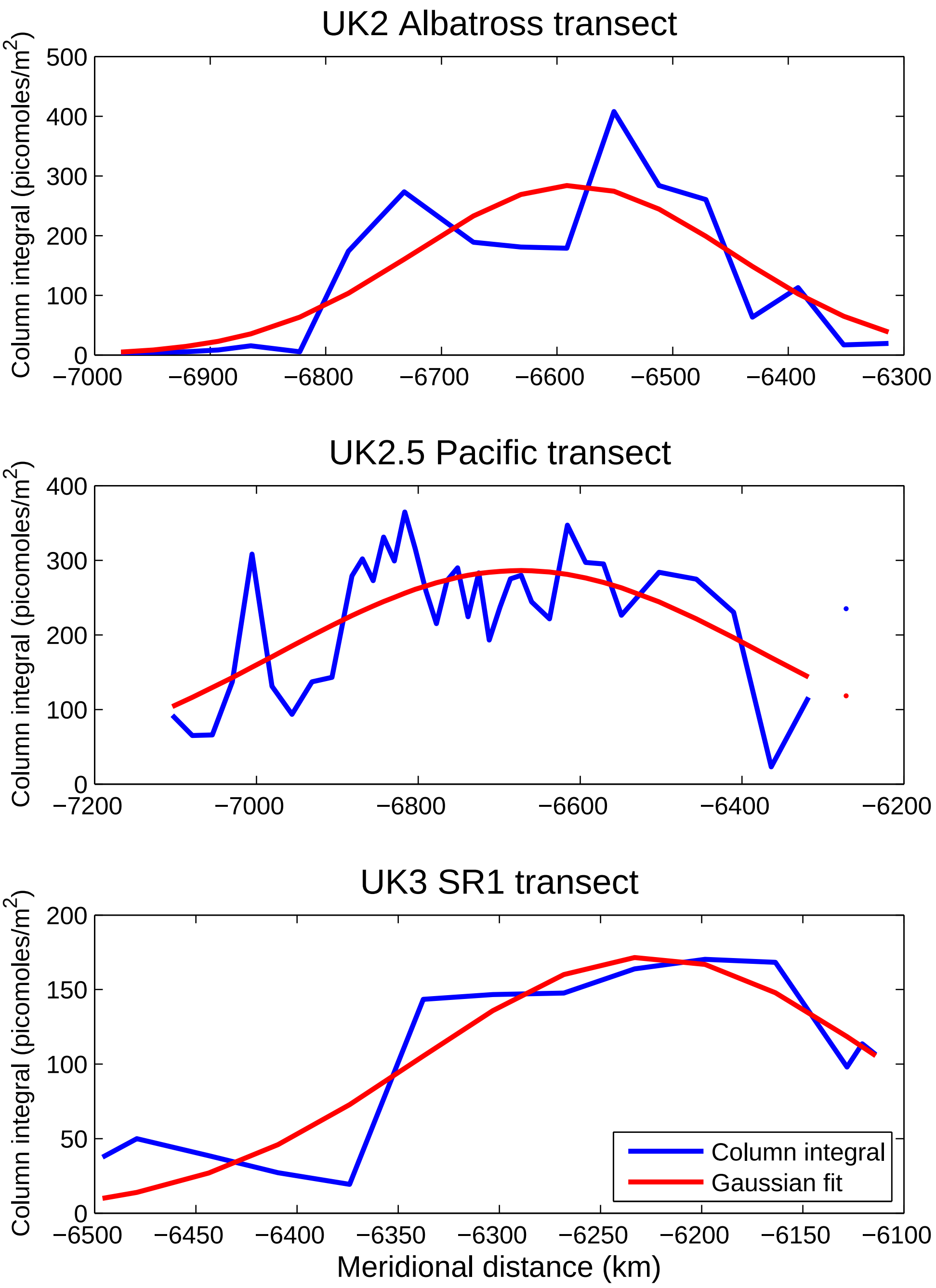

Figure 3.1: Meridional distribution of column integrals for tracer stations measured on the UK2 Albatross (top), UK2.5 Pacific (middle) and UK3 SR1 (bottom) transects. Column integrals in blue; Gaussian fits in red.

four times σ for the Guassian fit (see equation 2.1), since this should encompass 95% of the tracer if its distribution were Gaussian. The transects were chosen to reflect the closest available estimate for the meridional spread of the tracer in Drake Passage on each cruise. However, with the exception of the UK2 Albatross transect, the meridional distributions of the column integrals are not very close to Gaussian, and without zeros in concentration at the northern and southern extremes of each transect it is impossible to know how much of the extent of the tracer patch has been surveyed.

A second approach involved using outputs from the 3D model described in Chapter 4. For a modelled tracer distribution it is possible to calculate the meridional first moment of the tracer patch, $\bar{y}$, using the following equation:

$$\bar{y} = \frac{\sum_i I_i \times y_i}{\sum_i I_i} \tag{3.4}$$

where I_i are the column integrals for every point on the horizontal model grid, and y_i are their meridional coordinates in metres (relative to the equator). The square root of the meridional second moment of the modelled tracer distribution is then used to estimate the meridional width of the real tracer patch, and is calculated as follows:

$$\sigma_y = \left[\frac{\sum_i I_i \times (y_i - \bar{y})^2}{\sum_i I_i}\right]^{\frac{1}{2}} \tag{3.5}$$

The meridional extent of the tracer patch is then taken to be $4\sigma_y$. However, the 3D model was only run from release to UK2.5, so it was necessary to extrapolate the growth of the meridional second moment to derive an estimate for UK3. Several attempts were made to fit an equation to the growth of the second moment with time from release to UK2.5, but none was found that made reasonable predictions for UK3. Therefore it was decided that the meridional width of the tracer patch within Drake Passage, where the measurements were to be compared, would be assumed not to increase beyond the time of UK2.5. This is likely to be a close approximation, since the tracer is prevented from spreading isopycnally in the meridional direction by the ACC fronts and the continents to the north and south of Drake Passage.

3.3.4 Optimising for widths only

The difficulty in estimating the meridional width of the tracer patch means that the reliability of comparing modelled with measured tracer profile peak concentrations is questionable. The values for the meridional width are very uncertain, and due to the difficulty in arriving at these estimates, the same spread factor was applied to model outputs at all transects, which may not be appropriate. Changing the spread factor also has a significant effect on the diapycnal diffusivities diagnosed using this optimisation method. For example, the difference between the Drake Passage diapycnal diffusivity optimised using meridional spreads estimated from Gaussian fits to column integral data as opposed to those estimated from the 3D model second moments (as described in section 3.3.3) is a factor of 1.5. However, if the contribution of the peak concentrations is removed from the cost function, the value of the optimised diapycnal diffusivity is completely insensitive to changes in the spread factor. Consequently the widths-only comparison is considered to be the preferred method of optimisation.

The model profile peak concentrations are affected by the zonal velocity and horizontal diffusivity, since these parameters determine how much of the tracer arrives at a particular transect at a given time. Without the peak concentrations to pin down these quantities in the optimisation, other methods must be used to make reasonable estimates of their values. In the original version of the 2D advection-diffusion model inherited from Jim Ledwell, values of K_h were included which had been estimated from floats released in the LANL 0.1 degree model by Mat Maltrud and Julie McClean. The optimisations using only vertical widths to diagnose diapycnal diffusivities reverted to these values for K_h. Values of u were estimated from SatGEM, an altimetry based product which includes three-dimensional time-varying velocity fields for the Southern Ocean (Meijers and Bindoff, 2011), and which is used with the 3D model in Chapters 4 and 5. Velocities to use in the 2D model for the Pacific and Drake Passage zones were calculated as follows: a latitude range of $55.5°$S to $63.3°$S for the tracer patch was estimated from the meridional second moment of the tracer distribution output from the 3D model at a time corresponding to UK2.5. Longitude ranges of $120°$W-$67°$W and $67°$W-$57°$W were designated as corresponding to the Pacific and Drake Passage zones, respectively. The western boundary of the Pacific zone is chosen to be far enough west of the tracer release location

Cruises	Obs.	ρ	K_{zp} (range) ($\times 10^{-5}\ \mathrm{m^2\,s^{-1}}$)	K_{zd} (range) ($\times 10^{-4}\ \mathrm{m^2\,s^{-1}}$)	χ^2 (expectation)
UK2+UK2.5	W	γ_n	1.75 (1.69-1.80)	3.4 (3.0-3.9)	83.0 (74)
UK2+UK2.5	W	$\sigma_{1.5}$	1.71 (1.66-1.76)	3.4 (2.9-3.9)	76.6 (74)
UK2+UK2.5+UK3	W	γ_n	1.72 (1.67-1.77)	3.0 (2.7-3.3)	108.5 (94)
UK2+UK2.5+UK3	W	$\sigma_{1.5}$	1.69 (1.65-1.74)	3.3 (2.9-3.6)	100.3 (94)
UK2+UK2.5	W+C	$\sigma_{1.5}$	1.71 (1.66-1.76)	2.5 (2.2-2.8)	152.9 (146)
UK2+UK2.5+UK3	W+C	$\sigma_{1.5}$	1.69 (1.65-1.74)	2.8 (2.5-3.1)	201.7 (186)

Table 3.1: Diapycnal diffusivities resulting from various optimisations of the 2-zone 2D advection-diffusion model. Columns 1 and 2 detail the cruise transects and the types of observation (vertical widths, W and peak concentrations, C) contributing to the cost function. The transects included are the Pacific, Albatross and SR1 transects on UK2, the Pacific and SR1 transects on UK2.5 and the Albatross and SR1 transects on UK3. Column 3 gives the density system used for interpolating the tracer measurements before calculating the vertical widths, either neutral density (γ_n) or potential density referenced to 1500m ($\sigma_{1.5}$). Columns 4 and 5 give the optimised Pacific and Drake passage diapycnal diffusivities with their 1σ uncertainty ranges in brackets. Column 6 gives the value of the cost function at the minimum, with the expectation value in brackets.

(107°W) to incorporate any area occupied by the tracer resulting from its horizontal diffusion westwards following release. The eastern boundary of the Drake Passage zone is chosen as an approximate eastern extent of Drake Passage, and is also the longitude of the SR1 transect. Means were then taken over these coordinate ranges in each SatGEM snapshot in time (or ‘time slice’) and a mean over all time slices of these means used as the velocity estimate in each zone. The SatGEM velocities used were all at the depth of the tracer target isopycnal, the velocities having been interpolated onto isopycnal surfaces. Uncertainties on the velocities in each zone were taken as the standard error on the global means of the velocities within the established $55.5°$S-$63.3°$S latitude range. The SatGEM velocity ranges were calculated both from the combination of the zonal and meridional components by Pythagoras, and by taking the zonal velocity only. It was decided that only the zonal component would be used, since the approximation of zonal flow, in particular with respect to the conversion of latitude into along-stream distance in metres, had been applied to other aspects of the 2D model.

3.4 Results

3.4.1 Diapycnal diffusivities

Table 3.1 shows the diapycnal diffusivities in the Pacific and Drake Passage zones diagnosed using various optimisations of the 2D model. The first four rows are the results from optimisations where only the vertical widths were allowed to contribute to the cost function; the last two rows are from optimisations where the peak concentrations were included. The widths-only optimisations were carried out using concentration data interpolated onto both potential density referenced to 1500m ($\sigma_{1.5}$) and neutral density (γ_n). The interpolated concentrations were transformed from density to depth using the mean depth-density relations for UK2.5. Optimisations using both density systems were carried out in order that the effect of an issue with the neutral density calculation in Drake Passage alluded to in section 2.3.1.1 might be quantified. The issue arises from the fact that during the neutral density calculation's iteration process, an artificial barrier was placed in Drake Passage to allow the calculation to be performed (see Jackett and McDougall, 1997, for details). A table giving details of the parameter space searched during the optimisations in table 3.1 can be found in Appendix A.

The key result common to all optimisations is that the diapycnal diffusivity in the Drake Passage zone of the model is 15-20 times larger than in the Pacific zone. This result is significant because it implies strongly enhanced mixing averaged over a wide area - that occupied by the tracer between the Albatross transect at 68°W and SR1 at 57°W. This means that there are likely to be local pockets of much higher rates of mixing in Drake Passage, and also the fact that the spatial average implied is 1.9-2.6 times the value of $1.3 \times 10^{-4}\ \mathrm{m}^2\,\mathrm{s}^{-1}$ required by Munk (1966) to maintain the abyssal stratification (see section 1.2.2) has implications for the global overturning circulation. Based on very similar results from an earlier optimisation of this model using the same methods as employed for the first row in table 3.1, Watson *et al.* (2013) estimated an average diapycnal diffusivity for the whole ACC of $(0.6 - 1) \times 10^{-4}\ \mathrm{m}^2\,\mathrm{s}^{-1}$ by extrapolating based on estimates of lee wave generation. They conclude that 20-30% of the southern ocean component of the overturning circulation at mid depths is sustained by diapycnal mixing, concentrated over regions of rough topography such as Drake Passage, the Scotia Sea, Crozet-Kerguelan and the southeast Indian ridge. The favoured result from table 3.1 is from the optimisation using the UK2, UK2.5 and UK3 cruises, using the potential density grid and where only the vertical widths have been allowed to contribute to the cost function (row 4 of the main body of the table). These diffusivity values of $K_z = 1.69 \pm 0.05 \times 10^{-5}$ m^2 s^{-1} in the Pacific and $K_z = 3.3 \pm 0.4 \times 10^{-4}$ m^2 s^{-1} in Drake Passage are quoted in the abstract of this thesis, and represent the key quantitative result of this chapter. This particular optimisation is chosen because it includes UK3, so makes use of more of the available observations, avoids the problems with neutral density, and avoids the problems of estimating the model peak concentrations detailed in section 3.3.4.

The differences between the $\sigma_{1.5}$ and γ_n optimisations are small, both for the diapycnal diffusivities inferred in the Pacific and in Drake Passage, and in all cases agree within their uncertainties. The larger value of the cost function at the minimum for both the optimisations using γ_n compared with those using $\sigma_{1.5}$, and the fact that the latter χ^2 values are closer to the expectation may indicate that the $\sigma_{1.5}$ widths are more appropriate to use. However it is concluded based on these results that the differences in diagnosed diffusivities are small enough that the density system used is not important. Therefore the analysis that follows in Chapter 4, which was carried out using neutral densities before the problems with the system in Drake Passage came to light, may be considered to be unaffected.

A comparison may also be drawn between the values of diapycnal diffusivity obtained from optimisations where stations on the UK3 Albatross and SR1 transects were allowed to contribute to the cost function with those values obtained where only stations on UK2 and UK2.5 contributed. For the optimisations carried out in neutral density, a very small reduction in K_{zp} and a larger reduction in K_{zd} is seen when UK3 is included, although these reductions are within uncertainties. For the optimisations in potential density where only the widths were included in the cost function, there is also a small reduction in both K_{zp} and K_{zd} when UK3 is included, although the reduction in K_{zd} is smaller than for the neutral density optimisations. However, in the optimisations where peak concentrations were included in the cost function, there is an increase in K_{zd} where UK3 stations are are included compared with where they are not. Therefore it is concluded that the leading edge effect suggested by the measured mean profile widths (see section 2.3.2) cannot be confirmed by the results from this model.

The differences between the optimisations that include the contributions of the peak concentrations to the cost function and those that do not are the most significant. While the estimate for K_{zp} remains the same, the optimised K_{zd} is reduced by 15-26$\%$. This is due to the fact that the Drake Passage advection velocity u_d reduces to between 0.04ms^{-1} and 0.06ms^{-1} when it is fully optimised using the concentrations, whereas it is constrained to be between 0.0605ms^{-1} and 0.0723ms^{-1} for the widths-only optimisations, the velocity ranges having been obtained from SatGEM as described in section 3.3.4. The slower speed of advection through Drake Passage in the bottom two optimisations means that the same increase in tracer profile vertical width implies a smaller diffusivity. Due to the difficulties in estimating the model peak concentrations as described in section 3.3.3, the diffusivities derived assuming advection velocities calculated from SatGEM and including only the contribution of the widths to the cost function are considered to be the most robust. However, the method of averageing SatGEM velocities over a wide area is an over simplification for the tracer advection. A 3D model that allows for both the meridional variation in the velocity field and the inclusion of eddies to be represented would be much more appropriate. The implementation of such a model is the subject of Chapter 4.

Figure 3.2 gives a visual representation of the uncertainties in the diapycnal diffusivities in the Pacific and Drake Passage. The values of χ^2 for combinations of K_{zp} and K_{zd} are calculated by fixing all other parameters at their optimum values and varying the diapycnal diffusivities with nested loops in the same way as described in section 3.3.2. The optimisations shown were those where $\sigma_{1.5}$ interpolated tracer data was used, and only the vertical widths allowed to contribute to the cost function. Each contour corresponds to an increase in χ^2 of one from its value at the minimum, therefore the innermost and second innermost contours represent the 1σ and 2σ uncertainty ranges on the K_z parameters. The 1σ uncertainty on the Pacific diffusivity is small, around +/- 3$\%$ of the optimised value, and is similar whether or not the UK3 stations are included. This reflects the fact that we have a large number of profiles helping to tie down the Pacific zone diffusivity (57 for the Pacific and Albatross transects on UK2 and UK2.5 plus 4 for the Albatross transect on UK3), and that the variation in the vertical widths across transects is relatively small. The 1σ uncertainty in the Drake Passage diffusivity is rather larger at around +/-

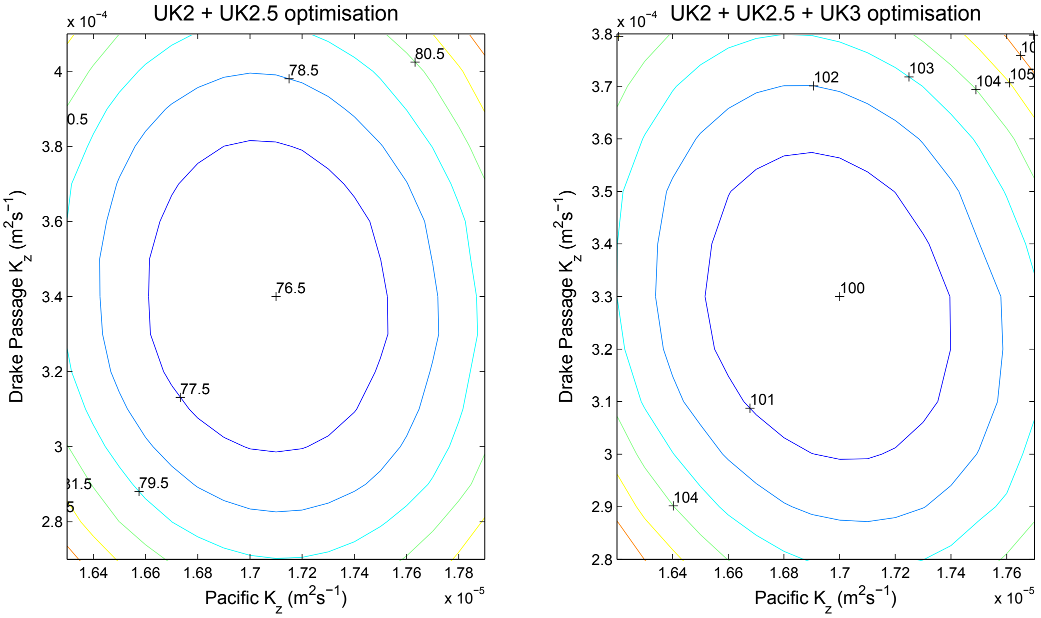

Figure 3.2: Contour plots of the cost function for different combinations of K_{zp} and K_{zd} for the $\sigma_{1.5}$ optimisations where the widths from UK2 and UK2.5 contribute to χ^2 (left panel) and where the widths from UK2, UK2.5 and UK3 contribute (right panel). The contours are where χ^2 is the optimum value +1, +2, etc.

15% of its optimum for the UK2 + UK2.5 comparison, reducing slightly to +/- 12% when UK3 stations are included. This reflects the smaller number of observations at SR1 (18 for UK2 and UK2.5 plus 16 for UK3), the transect which gives us information about the tracer's transit through Drake Passage, and the fact that the variation in individual profile widths is much greater. This greater variation in the observations is due to the relative inhomogeneity of the mixing in Drake Passage when compared with the Southeast Pacific. For the results presented in table 3.1, the optimised u_p was between 0.028 and 0.029ms^{-1}, u_d was between 0.04 and 0.07ms^{-1}, and K_{hp} and K_{hd} were 3000m^{2}s^{-1} and 1000m^{2}s^{-1}, respectively. It is noted that the optimised horizontal diffusivities obtained by including the contribution of the peak concentrations in the cost function are the same as the values from model floats (as introduced in section 3.3.4) which were used in the widths-only optimisation.

3.4.2 Sensitivity of χ^2 to model parameters

Table 3.2 shows the results of a sensitivity analysis for the secondary model parameters (i.e. those other than the vertical diffusivities). These were obtained by taking a full set

Optimisation	u_p range (ms^{-1})	u_d range (ms^{-1})	K_{hp} range (m^{2}s^{-1})	K_{hd} range (m^{2}s^{-1})
Widths only	-0.041-0.059	0.051-0.071	1600-8100	0-9100
Widths and concentrations	0.0275-0.0292	0.033-0.048	2800-3900	0-3500

Table 3.2: Sensitivity of χ^2 to secondary model parameters. Parameters are the advection velocities in the Pacific (u_p) and Drake Passage (u_d) zones, and the horizontal diffusivities in the Pacific (K_{hp}) and Drake Passage (K_{hd}) zones. Ranges are those required to increase the cost function by one from its value when the parameters are optimised. The transects from the UK2 and UK2.5 cruises were allowed to contribute to the cost function.

of optimised values, and varying each parameter individually to increase the value of the cost function by one. The two sets of optimised values used were from the optimisations where UK2 and UK2.5 transects were allowed to contribute to the cost function; the first set of values were where vertical widths only were compared, and the second set of values were where both vertical widths and peak concentrations were compared (the second and fifth optimisations from table 3.1, respectively).

When both vertical widths and peak concentrations are allowed to contribute to the cost function, χ^2 is highly sensitive to u_p, and somewhat sensitive to u_d, K_{hp} and K_{hd}. When only the widths are compared, there is very little sensitivity to u_p, some sensitivity to u_d, and little sensitivity to K_{hp} or K_{hd}. The lack of sensitivity to u_p is unexpected, but an inspection of the output model tracer fields with varying values of u_p reveals that it does not affect the shape of the tracer distribution at the measured transects: although with zero or negative advection velocity the concentrations around the Pacific - Drake Passage zone transition are very small, the vertical distributions of concentrations (and hence the vertical widths) remain the same. By contrast, the horizontal diffusivities do affect the shape of the tracer patch, causing it to elongate in the zonal direction under larger K_h, so there is some sensitivity to these parameters. Equally, variation of u_d causes zonal elongation of the tracer patch as it advects between the Pacific and the Drake Passage zones, which explains the sensitivity of the cost function to u_d where there is little sensitivity to u_p.

3.4.3 Model profiles

Figures 3.3 to 3.6 show the model profiles of tracer concentration with depth compared to their equivalent mean profiles for the measured tracer for various optimisations of the

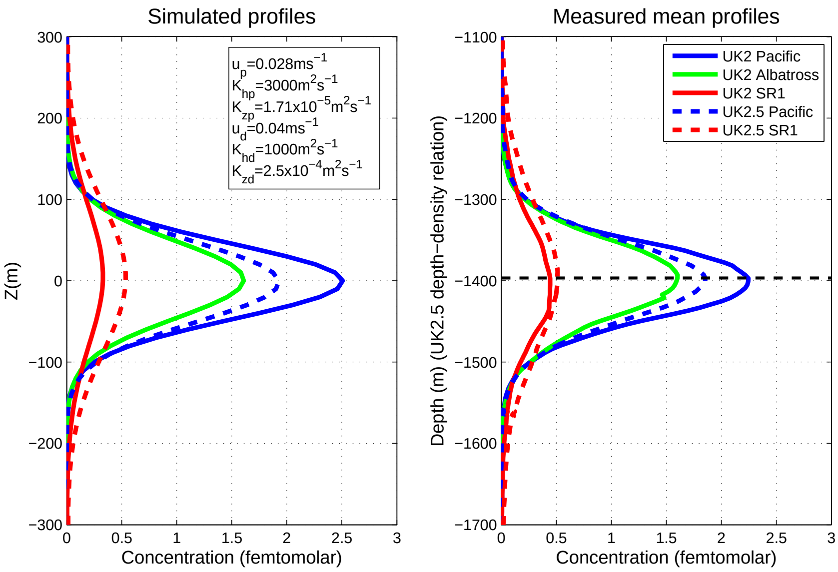

Figure 3.3: Model profiles (left) and measured mean profiles (right) for the 2-zone model optimised for UK2 + UK2.5 vertical widths and peak concentrations. Pacific (blue), Albatross (green) and SR1 (red) transects from the UK2 (solid lines) and UK2.5 (dashed lines) cruises. The optimised values of $u_p, K_{hp}, K_{zp}, u_d, K_{hd}$ and K_{zd} are displayed on the left panel.

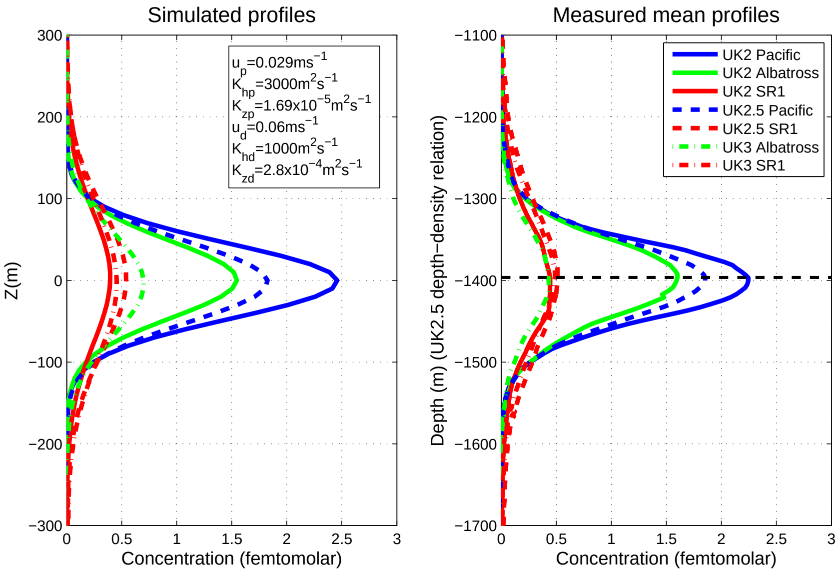

Figure 3.4: As figure 3.3, but optimised for UK2 + UK2.5 + UK3 vertical widths and peak concentrations. Pacific (blue), Albatross (green) and SR1 (red) transects from the UK2 (solid lines) and UK2.5 (dashed lines) and UK3 (dotted-dashed lines) cruises.

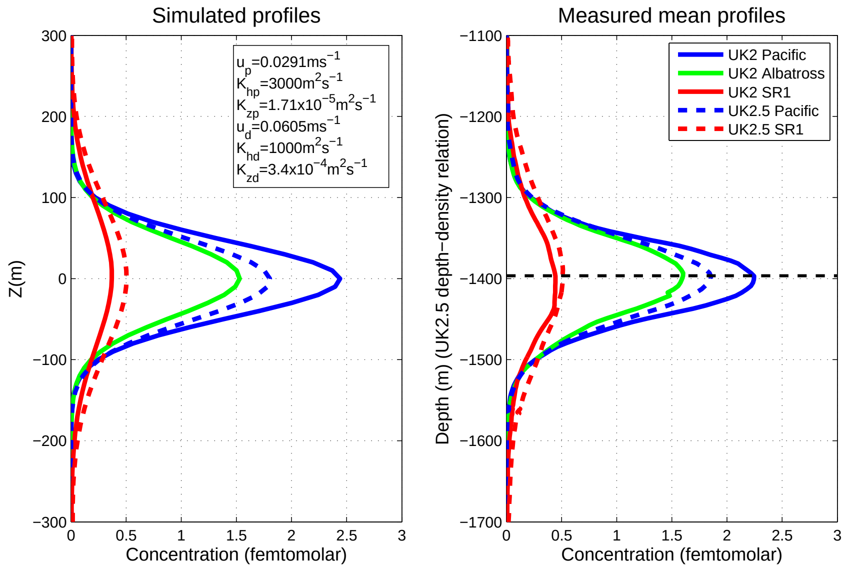

Figure 3.5: As figure 3.3, but optimised for UK2 + UK2.5 vertical widths only. Pacific (blue), Albatross (green) and SR1 (red) transects from the UK2 (solid lines) and UK2.5 (dashed lines) cruises.

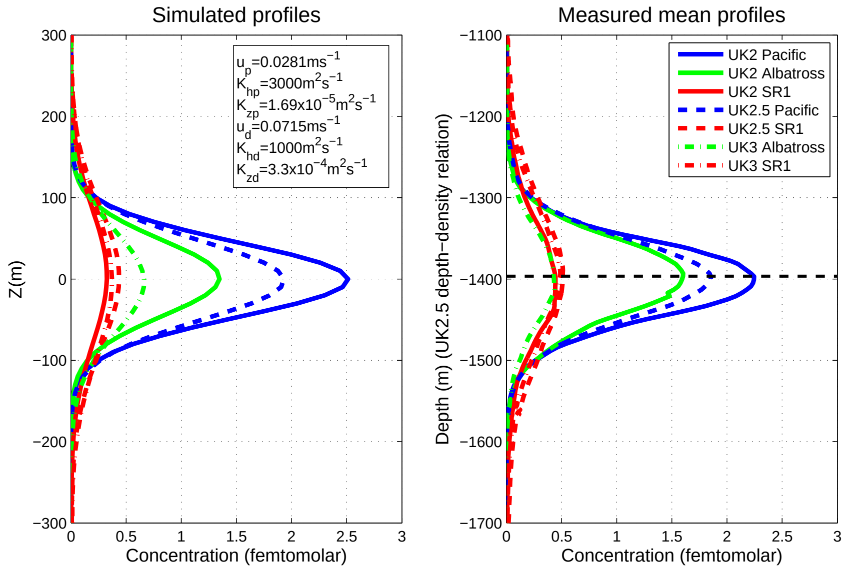

Figure 3.6: As figure 3.3, but optimised for UK2 + UK2.5 + UK3 vertical widths only. Pacific (blue), Albatross (green) and SR1 (red) transects from the UK2 (solid lines) and UK2.5 (dashed lines) and UK3 (dotted-dashed lines) cruises.

model parameters. Figures 3.3 and 3.4 show model outputs resulting from optimisations where both the vertical widths and the peak concentrations contributed to the cost function; figures 3.5 and 3.6 result from optimisations with only the vertical widths. Figures 3.3 and 3.5 result from optimisations where only data from the UK2 and UK2.5 cruises contributed to the cost function; for figures 3.4 and 3.6 the UK3 data was included (hence the profiles from the SR1 and Albatross transects on UK3 appear in the latter). The measured mean profiles differ slightly from those in figure 2.7, as in order to make the comparison with the optimised model output, only the stations contributing to the cost function have been included in the measured transect means (some stations are not included in the cost function because they do not fit a Gaussian). The model does seem to reproduce the tracer transect mean profiles reasonably well, and the differences are small between optimisations. I refrain from drawing any detailed conclusions on the model skill at reproducing the tracer advection, because of the uncertainties in the model peak concentrations as explained in section 3.3.4, and also because of inherent differences between individual versus transect mean tracer profiles. Individual profiles may have peak concentrations at depths other than the centre of their distribution, whereas for transect mean profiles these differences tend to be smoothed out, the mean profile maximum concentration almost always appearing in the centre. Since the cost function compares model profiles, equivalent to transect means, with individual profile peak concentrations, the peak concentrations of the model profiles resulting from the optimisation may therefore be different from those of their equivalent measured transect mean profiles. This may be considered an additional argument for excluding the peak concentrations from the cost function when calculating estimates of diapycnal diffusivity.

3.4.4 Concentration to width relationship

During the UK2 cruise, an inverse relationship was noticed between the vertical width, σ, and the peak concentration of individual tracer profiles. It was hypothesised that this might be because tracer at the leading edge of the tracer patch, hence found in lower concentrations, had experienced stronger vertical mixing due to having travelled faster, resulting in wider profiles. The plots in figure 3.7 explore this relationship with the help of the 2D model. The panel (a) shows the relationship between peak concentration and

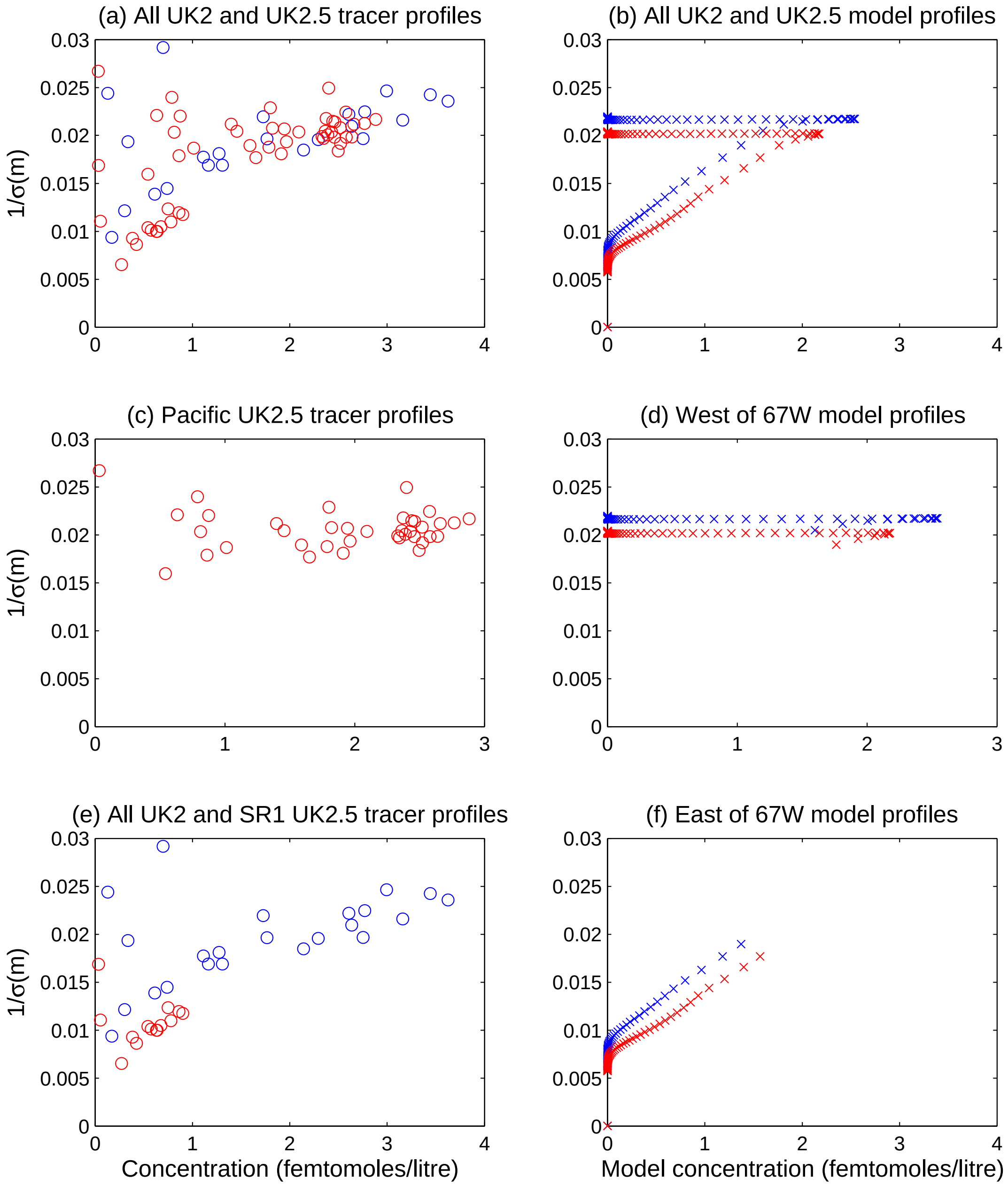

Figure 3.7: Scatter plots of the relationship between vertical width (σ) and peak concentration for UK2 and UK2.5 tracer profiles. UK2 stations are in blue; UK2.5 stations are in red. Tracer observations are on the left (circles); model profiles are on the right (crosses). Top two panels show measured profiles from the Pacific and SR1 transects on UK2 and UK2.5 and from the Albatross transect on UK2 (left), and all model profiles from UK2 and UK2.5 (right). Middle two panels show measured profiles from the Pacific transect on UK2.5 (left) and model profiles from the Pacific zone on UK2 and UK2.5 (right). Bottom two panels show measured profiles from all transects on UK2 and the SR1 transect on UK2.5 (left) and model profiles from the Drake Passage zone on UK2 and UK2.5 (right).

$1/\sigma$ for all the observed tracer profiles on UK2 and UK2.5. On panel (b) is the same relationship for model profiles obtained by taking a vertical slice through the model grid at every point in the along-stream direction (i.e. every 1 degree longitude), for model outputs at UK2 and UK2.5. Panel (c) shows the measured stations only on the Pacific transect of UK2.5, where there does not appear to be a relationship between vertical width and peak concentration. Panel (d) has model profiles only in the low vertical diffusivity Pacific zone, where the values of $1/\sigma$ are indistinguishable from each other within each cruise. Finally panel (e) shows all the stations from UK2, and only the stations from the SR1 transect on UK2.5. A proportional relationship between peak concentration and $1/\sigma$ seems to exist for these stations. On panel (f), the model profiles for the high diffusivity Drake Passage zone, into which the leading edge of the tracer patch is emerging during the UK2 and UK2.5 cruises, very clearly show this proportional relationship. Although the relationship appears similar for both model and experimental tracer results, the explanation for the behaviour is different. In the case of the tracer, the stations sampled on UK2 and on the SR1 transect on UK2.5 represent tracer towards the leading edge of the patch, therefore these stations have profiles with lower peak concentrations which have travelled further and faster, probably in frontal jets, and consequently have mixed more strongly. In the model, there is no third (meridional) dimension to allow the tracer to arrive at a given point downstream via varying paths and at varying speeds. The explanation here is simply that the high mixing region is downstream of the low mixing region, so model tracer at the leading edge of the patch at a given time will have spent more time in the high mixing region, resulting in more diffusion and wider profiles. The plots of tracer concentration over the whole model grid in figure 3.8 further illustrate the effect, with the tracer fanning out as its leading edge enters the Drake Passage zone.

3.4.5 Model tracer evolution

During the optimisation of the 2D model, it was discovered that the alteration of the model velocities from those with which it was originally written had some unexpected consequences on the model tracer field, in particular that a sharp increase in velocity between the two zones seemed to hinder the tracer advection. An investigation was therefore

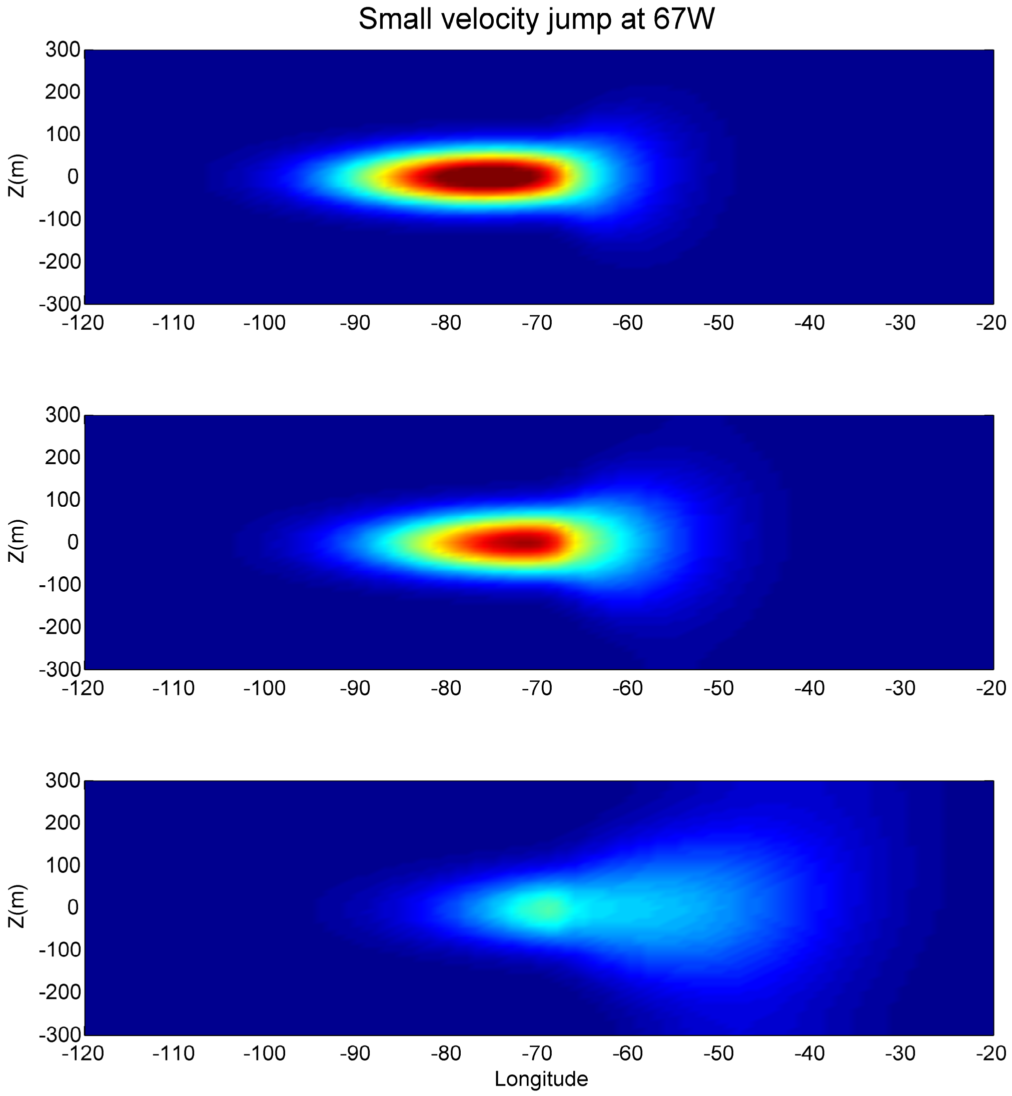

Figure 3.8: Distributions of tracer concentrations in the 2D advection-diffusion model. Outputs correspond to UK2 (top), UK2.5 (middle) and UK3 (bottom). The model is divided into two zones, split at 67°W, with low along-stream velocity, low diapycnal diffusivity in the Pacific zone ($u_p = 0.0291\text{ms}^{-1}, K_{z_p} = 1.7 \times 10^{-5}\ \text{m}^2\,\text{s}^{-1}$), and slightly higher along-stream velocity, high diapycnal diffusivity in the Drake Passage zone ($u_d = 0.035\text{ms}^{-1}, K_{z_d} = 3.3 \times 10^{-4}\ \text{m}^2\,\text{s}^{-1}$). Colour scales are the same for all three panels.

carried out into the behaviour of the model tracer evolution under the influence of different velocity fields. Figures 3.8 to 3.10 illustrate the effects of the change in velocity between the Pacific and Drake Passage zones on the evolution of the tracer in the model. In figure 3.8, the distribution of tracer within the model is shown for outputs corresponding to UK2, UK2.5 and UK3 where there is a small step-change in velocity between the

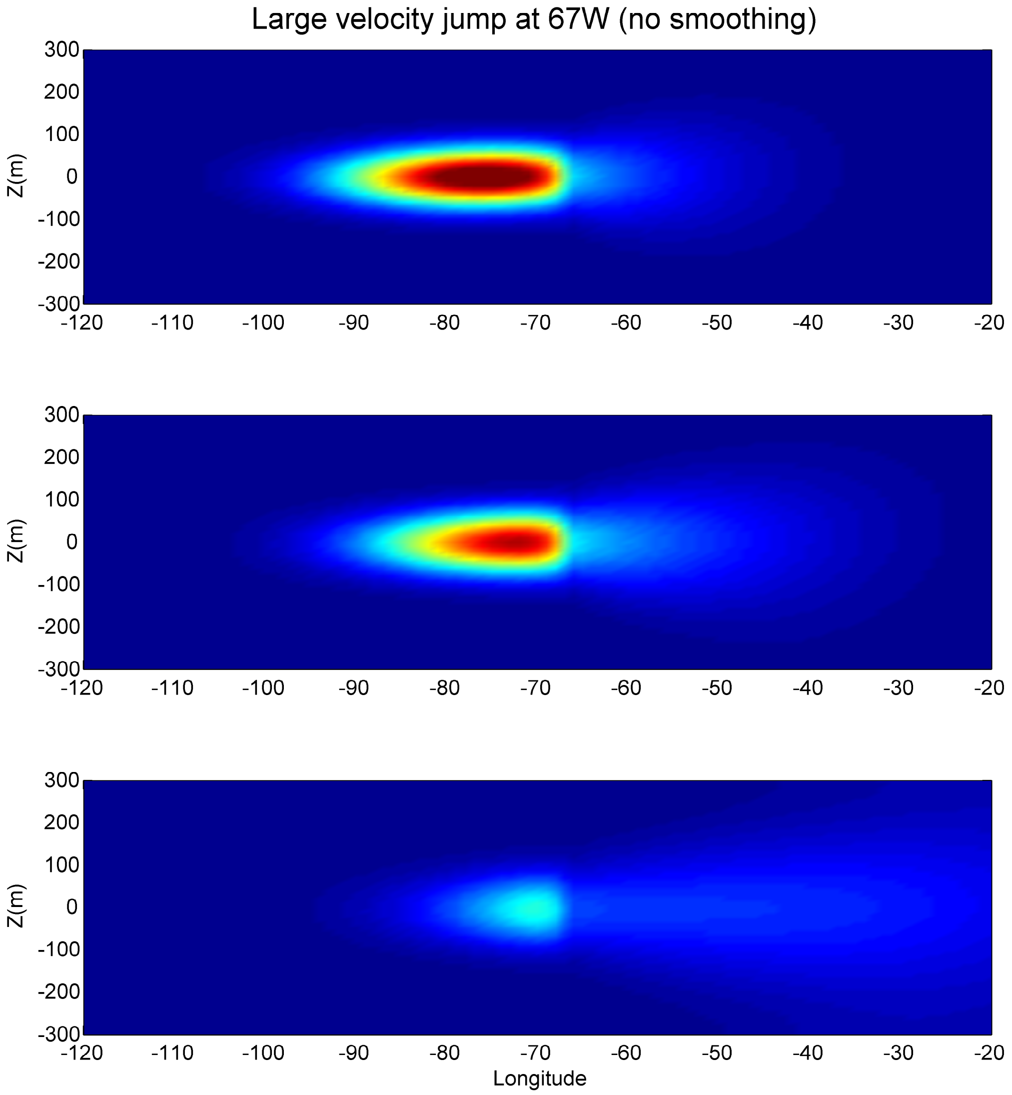

Figure 3.9: As figure 3.8 but with larger jump in velocity between Pacific and Drake Passage zones ($u_p = 0.0291\mathrm{ms}^{-1}, K_{zp} = 1.7 \times 10^{-5}\ \mathrm{m}^2\,\mathrm{s}^{-1}, u_d = 0.06\mathrm{ms}^{-1}, K_{zd} = 3.3 \times 10^{-4}\ \mathrm{m}^2\,\mathrm{s}^{-1}$).

two zones at 67°W from $u_p = 0.029\mathrm{ms}^{-1}$ to $u_d = 0.035\mathrm{ms}^{-1}$. In this model configuration, the tracer seems to transition smoothly from one zone to another, and continues to advect normally into the higher velocity, high diapycnal diffusivity zone. In figure 3.9, the step change in velocity between the two zones is much larger, with $u_d = 0.06\mathrm{ms}^{-1}$. Here there appears to be a blocking effect, where the tracer is held up at the boundary in a bottleneck, apparently delaying its progress into Drake Passage. In order to try to mitigate this effect, the transition between the velocities in the two zones has been smoothed over 6

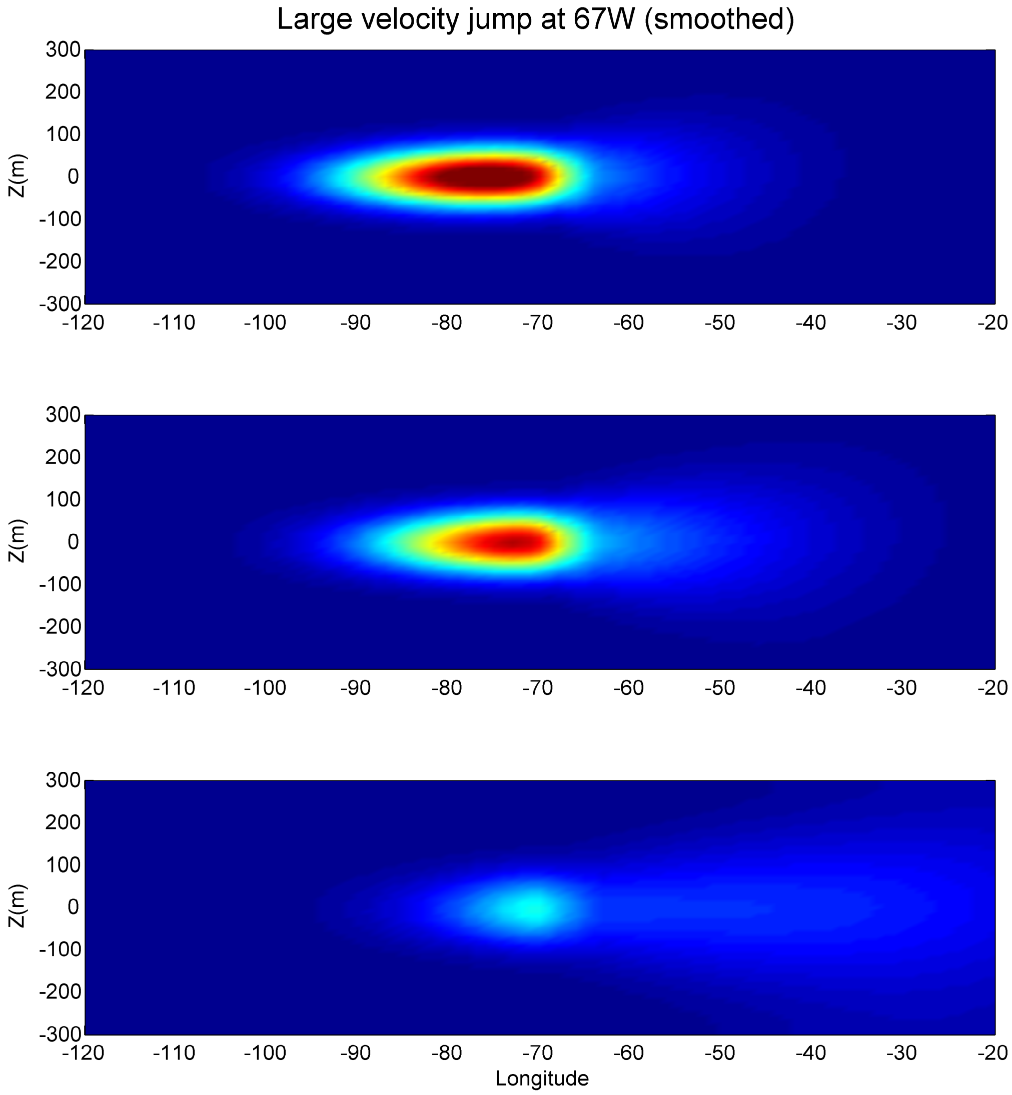

Figure 3.10: As figure 3.9 but velocity transition is smoothed over 6 degrees of longitude.

degrees of longitude in the model configuration shown in figure 3.10. Here the concentrations of tracer in Drake Passage are still substantially reduced due to its advecting further when compared with figure 3.8, but the bottleneck effect of figure 3.9 is not evident. The smoothed transition in velocity is used for the analysis presented in sections 3.4.3 to 3.4.4; however it is possible that this one-dimensional change in velocity has affected the concentrations, and perhaps the vertical widths, of the model profiles beyond Drake Passage in an unrealistic way. This is a further argument for the exclusion of the peak concentrations in the final analysis carried out using the cost function, but also highlights the need for a more realistic, 3D model.

The total amount of tracer in the model domain at a given time is calculated by multiplying the quantity of tracer in each grid square (for example as represented in figure 3.8) by the area of the squares and summing over the model grid:

$$T = \sum_i C_i dx dz \tag{3.6}$$

where T is the total tracer, C_i is the amount of tracer in grid square, $dx = 55500$m is the horizontal size and $dz = 10$m is the vertical size of the grid squares. Over the course of a run from release for three years, the total amount of tracer changes by no more than 1.7% for the runs presented in table 3.1, meaning conservation within the model is good.

3.5 Summary

In this chapter, a simple 2D advection-diffusion model with dimensions of along-stream and depth was used to model the evolution of the DIMES tracer from release to UK3. Outputs were compared with data from the experimental tracer and the model-data fit quantified using a cost function. With the model split into 2 zones representing the South-east Pacific and Drake Passage, model parameters for along-stream advection velocity, horizontal diffusivity and diapycnal diffusivity in each zone were optimised to minimise the cost function and hence find estimates of diapycnal diffusivity in each zone. The best estimates were obtained by comparing the vertical widths calculated from tracer data interpolated in potential density and transformed to depth using the mean depth-density relation for UK2.5 with model outputs from UK2, UK2.5 and UK3 corresponding to the Pacific, Albatross and SR1 transects. The diapycnal diffusivities found were $1.69 \pm 0.05 \times 10^{-5}$ $\mathrm{m^2\,s^{-1}}$ in the Pacific and $3.3 \pm 0.4 \times 10^{-4}$ $\mathrm{m^2\,s^{-1}}$ in Drake Passage, where uncertainties are 1σ. This 20-fold increase between the two regions, the Pacific characterised by smooth topography, and Drake Passage characterised by rough topography and energetic near-bottoom flows, provides evidence for the idea that strongly enhanced diapycnal mixing is associated with the interaction of strong bottom flows with rough topography. Such mixing in the Southern Ocean may be powered by the generation of lee waves as described in section 1.3.3.2, and has the potential to explain a significant portion of that required to close the global overturning circulation.

A ‘leading edge’ effect, whereby tracer moving faster at the front of the tracer patch had experienced stronger diapycnal mixing than tracer further back that had moved more slowly, had been suggested by the evidence from mean tracer profiles seen in Chapter 2. The investigation into this using the model proved inconclusive: diapycnal diffusivities calculated from comparisons with UK2 and UK2.5 data when the tracer was first entering Drake Passage, and those calculated from comparisons including UK3 data when the tracer had been there for some time were not noticeably different. However an observed relationship between tracer profile vertical widths and peak concentrations on UK2 and UK2.5 was reproduced by the model, the model outputs suggesting a strong link between vertical widths and peak concentrations as the leading edge of the tracer patch enters a region of high vertical diffusivity.

While the simplicity of the model meant that it was highly appropriate for the process of optimising input parameters to best fit the data, it being possible to carry out many hundreds of model runs in a relatively short time, its usefulness is limited. Peak concentrations were hard to estimate, requiring knowledge of the meridional spread of the tracer patch which was only partially available, and consequently the problem of estimating advection velocities and horizontal diffusivities, the former of which in particular have an impact on the inferred rates of diapycnal mixing, was difficult to solve. In order to derive more robust estimates of the mixing, and also to investigate more precisely the horizontal distribution of vertical mixing, a 3D model is required. Investigations using such a model will be the subject of Chapters 4 and 5.

Chapter 4

Modelling the tracer in 3D

4.1 Introduction

4.1.1 Chapter motivation and outline

In this chapter a model of the evolution of the DIMES tracer in three dimensions will be introduced. The 3D model has significant advantages over the simple 2D model presented in Chapter 3. First, tracers in the ocean are not advected by the large scale velocity (Gent *et al.*, 1995), as was assumed in the 2D model where an 'along stream' velocity was defined. The Southern Ocean is a region where energetic geostrophic eddies are a dominant feature of the flow, and it is a combination of these eddies and the mean flow provided by the ACC that are responsible for the advection of the DIMES tracer. Adding the meridional direction to the model dimensions allows these eddies to be introduced. Secondly, a 3D domain allows the meridional variation as well as the zonal variation in the diapycnal mixing of the tracer to be modelled, and this means that far more may be inferred about the possible causes of the mixing.

The remainder of this section will introduce some background theory to the modelling approach. In section 2, the details of the methods used will be described, including the 3D model framework, the velocity fields which are used to advect the tracer, the comparison of model outputs with the experimental results, and three categories of diapycnal diffusivity fields prescribed to the model. In section 3, results of model runs using the different types of diapycnal diffusivity fields will be presented, and outputs from some alternative methods will also be shown and compared with the main results. Section 4 will discuss their implications for diapycnal mixing.

4.1.2 Modelling the advection of a tracer in the ocean

In the absence of diapycnal diffusion, a passive tracer such as the one used in the DIMES experiment will be advected along isopycnal surfaces, with its evolution governed by the following equation (from Gent *et al.*, 1995):

$$\frac{\partial C}{\partial t} + \mathbf{u} \cdot \nabla_\rho C = \frac{1}{h_\rho} \nabla_\rho \cdot (K_h h_\rho \nabla_\rho C) \tag{4.1}$$

where C is the tracer concentration, t is time, $\mathbf{u}$ is the along-isopycnal velocity vector, ∇_ρ is the horizontal gradient operator applied at constant density ρ (i.e. along isopycnals), h_ρ is the vertical density gradient ($= -\partial z / \partial \rho$ where z is depth), and K_h is an isopycnal diffusivity. Equation 4.1 assumes small isopycnal slopes. Adding in diapycnal diffusion from equation 1.7, this becomes:

$$\frac{\partial C}{\partial t} + \mathbf{u} \cdot \nabla_\rho C = \frac{\partial}{\partial z}(K_z \frac{\partial C}{\partial z}) + \frac{1}{h_\rho} \nabla_\rho \cdot (K_h h_\rho \nabla_\rho C) \tag{4.2}$$

where K_z is the diapycnal diffusivity.

I have chosen to use MITgcm, a depth-coordinate model, to model the DIMES tracer, since it can be run ‘offline’ (see section 4.2.1) using velocity fields from a previous calculation, and also allows the prescription of a three-dimensionally varying diapycnal diffusivity field. Here, however, the model’s depth levels are treated as isopycnals, and the vertical component of the model velocities, which are defined by $\mathbf{u} = (u, v, w)$, is set to zero everywhere, ensuring no tracer can cross isopycnals other than by diapycnal diffusion. Each model depth level is then associated with a neutral density γ_n. The model solves the following advection-diffusion equation for the tracer:

$$\frac{\partial C}{\partial t} + \nabla \cdot (\mathbf{u} C) = \nabla \cdot (\mathbf{K} \nabla C) \tag{4.3}$$

where here ∇ is the three-dimensional gradient operator and $\mathbf{K}$ is a tensor representing the isopycnal and diapycnal diffusivities, of which the isopycnal component K_h is a constant. The gradient operators ∇_ρ and ∇ are equivalent in my model setup, since depth levels are isopycnals and $w = 0$ everywhere. The second term on the LHS of equation 4.2

and the second term on the LHS of equation 4.3 are equivalent if the horizontal (approximately equivalently along-isopycnal) components of velocity (u, v) are non-divergent, so equation 4.3 becomes:

$$\frac{\partial C}{\partial t} + \mathbf{u} \cdot \nabla C = \nabla \cdot (\mathbf{K} \nabla C) \tag{4.4}$$

To match the RHS of 4.2 and 4.4, I make an approximation of constant h_ρ; equivalently that the stratification is constant throughout the model domain. This last assumption amounts to neglecting two 'pseudo velocities' which result from temporal and spatial variations in h_ρ. The first is contained in the LHS of equation 4.1, where the velocity may be expressed as:

$$\mathbf{u} = \bar{\mathbf{u}} + (\overline{h'_\rho \mathbf{u}'})/\overline{h_\rho} \tag{4.5}$$

where overbars represent time- and spatial averages, and primes denote the local, instantaneous departures from these averages (Gent *et al.*, 1995). The second term on the RHS of equation 4.5 is known as the 'bolus velocity' (McDougall, 1991). The second neglected pseudo velocity comes from the RHS of equation 4.1, which may be split, assuming constant K_h, into:

$$\nabla_\rho \cdot K_h \nabla_\rho C + \frac{K_h \nabla_\rho h_\rho}{h_\rho} \cdot \nabla_\rho C. \tag{4.6}$$

The first term in equation 4.6 is the horizontal part of what is solved by the model on the RHS of 4.3. The second term is the second neglected pseudo velocity, $(K_h \nabla_\rho h_\rho)/h_\rho$, multiplied by $\nabla_\rho C$, and may be subtracted from the second term on the LHS of equation 4.4.

A final effect of the constant h_ρ concerns the diapycnal diffusion. The 'thickness' of an isopycnal layer, h, is defined (from Hallberg, 2000) as:

$$h = -\int \frac{dz}{d\rho} d\rho. \tag{4.7}$$

In the model, h is represented by the vertical distance between model z levels, and is static, varying spatially only in the vertical dimension. However, since in the real ocean h varies spatially and temporally, and diapycnal diffusion is independent of $dz/d\rho$ and therefore h, this means that where the local instantaneous thickness of an isopycnal layer in the real ocean h_{ocean} is greater than the thickness assigned to the model h_{model} (equivalently the real stratification is weaker than the model 'stratification'), diapycnal diffusion will be stronger in the model than in the ocean. Conversely, if $h_{ocean} < h_{model}$, the model diffusion will be weaker than in the real ocean. The effects of the constant h approximation on the results presented will be discussed in section 4.4.3.

4.2 Methods

4.2.1 MIT model

The offline version of the MITgcm accepts inputs from a previous model run, leaving only the advection diffusion equation (equation 4.3) left to solve. The inputs expected are the diapycnal diffusivity K_z, the isopycnal diffusivity K_h, the velocity components u, v, w in the zonal, meridional and vertical directions, respectively, and a convective diffusivity which enhances the background K_z. K_z is represented by a three-dimensional matrix which is static in time, and K_h is a single value across the whole of the model domain. The velocities consist of a 3D matrix for each component, and are time-dependent, the model reading in the instantaneous fields of u, v and w at regular intervals. The time period between instantaneous velocity inputs will be 1 week, determined by the SatGEM product from which the fields are derived (see section 4.2.2). The convective diffusivity is most important in the mixed layer where significantly enhanced mixing is observed due to interactions with the atmosphere. Since the DIMES experiment is concerned principally with mid-depth mixing, the tracer isopycnal being below the mixed layer across most of the extent of the tracer patch, I have set the convective diffusivities to zero everywhere, so in effect the model assumes that the tracer is not affected by the mixed layer, and diapycnal mixing coefficients are defined solely by K_z. This has the advantage of comparative simplicity when it comes to parameterising the vertical mixing and subsequent interpretation of the results.

The model domain has 67 depth levels, each assigned to a neutral density between $27.8\,\mathrm{kgm}^{-3}$ and $28\,\mathrm{kgm}^{-3}$, with $0.003\,\mathrm{kgm}^{-3}$ spacings between the levels. The density range was chosen to match that of the widest profiles measured on the tracer surveys to be compared with the model outputs. In the model, the density grid is a conceptual one, the offline MITgcm having no knowledge of the densities, and is used when mapping model output tracer distributions in density space. In terms of the model configuration, the levels are separated by distances in metres (see section 4.2.6). The horizontal domain extends from 120°W to 30°W zonally and from 70°S to 40°S meridionally, with horizontal grid spacing of $\frac{1}{8}^{\circ}$. This is a larger area than occupied by the tracer between its release and the UK2.5 cruise 27 months later, which is the period over which outputs from these model runs are to be compared with the experimental results. The extent of the domain ensures that tracer does not spill over the boundaries of the model during this period.

The "Prather" advection scheme is used, which has a superior accuracy and reduced numerical diffusion compared to other available schemes (Prather, 1986). Tests carried out using some alternative advection schemes available with MITgcm confirmed the Prather scheme to be the most numerically stable.

4.2.2 SatGEM

Rather than using an output from a previous online MITgcm run for the u, v, w inputs to the offline model, I have chosen to use a product called 'SatGEM' (see Meijers and Bindoff, 2011, for full details of their methods). It contains time-evolving three-dimensional fields of $u, v,$ temperature (T), and salinity (S) for the Southern Ocean calculated using a combination of climatological data and satellite altimetry. The horizontal resolution of the fields is $\frac{1}{3}^{\circ}$, and they have 36 pressure levels between the surface and 5400 dbar. SatGEM contains snapshots, or 'time slices' every 7 days, and the data used in my model covers the period from February 2009, when the tracer was released, to April 2011 when the UK2.5 cruise took place.

The SatGEM T-S fields were generated using hydrographic bottle and CTD data and Argo float data to produce vertical profiles indexed by longitude and dynamic height. These profiles were then combined with satellite altimetry to produce the time-dependent three-dimensional fields. The method used to construct the T-S profiles is known as the 'Gravest Empirical Mode' (GEM) method (Meinen and Watts, 2000).

With the density field reconstructed from the T-S fields, geostrophic velocities may then be calculated using the geopotential surfaces inferred from the density structure. The geostrophic velocities are defined by:

$$u = -\frac{1}{f}\frac{\partial \phi}{\partial y}, \qquad v = \frac{1}{f}\frac{\partial \phi}{\partial x} \tag{4.8}$$

where u and v are the zonal and meridional components velocity, f is the Coriolis parameter, x and y are coordinates in the zonal and meridional directions in metres, and ϕ is the geopotential. The surface velocities can be obtained directly from satellite observations of the sea surface height anomaly. In the interior, the vertical current shear, also known as the thermal wind, is calculated from:

$$\frac{\partial v}{\partial p} = -\frac{1}{f}\frac{\partial \alpha}{\partial x}, \qquad \frac{\partial u}{\partial p} = \frac{1}{f}\frac{\partial \alpha}{\partial y} \tag{4.9}$$

where

$$\alpha = \frac{\partial \phi}{\partial p} = -\frac{1}{\rho}, \tag{4.10}$$

p is the pressure and ρ is the density. The shear is then combined with the surface velocities to produce the 3D, time-evolving SatGEM velocity fields.

The key advantage of the SatGEM fields is that they are derived directly from observations, so should result in a reasonably accurate reproduction of the tracer advection, which is important for diagnosing the diapycnal diffusivities. Meijers and Bindoff (2011) report that the SatGEM fields have been compared with available observations, and show good agreement. However it does have limitations. Firstly the velocities do not include the ageostrophic component, and are only resolved to $\frac{1}{3}^{\circ}$, so smaller scale features of the flow, in particular the submesoscale horizontal processes, are not captured. The horizontal mixing therefore must be parameterised by K_h. Secondly the fields are not constrained to be non-divergent, which is in conflict with the MITgcm's expected inputs, and means that the advection terms in equations 4.2 and 4.3 are not equivalent. The SatGEM velocities are therefore adjusted to render them non-divergent before feeding them into the model (see section 4.2.3). Finally the fields have only been calculated in places where the water depth is at least 2000m, which leaves gaps, most importantly to the north and south of Drake Passage through which the tracer is advected.

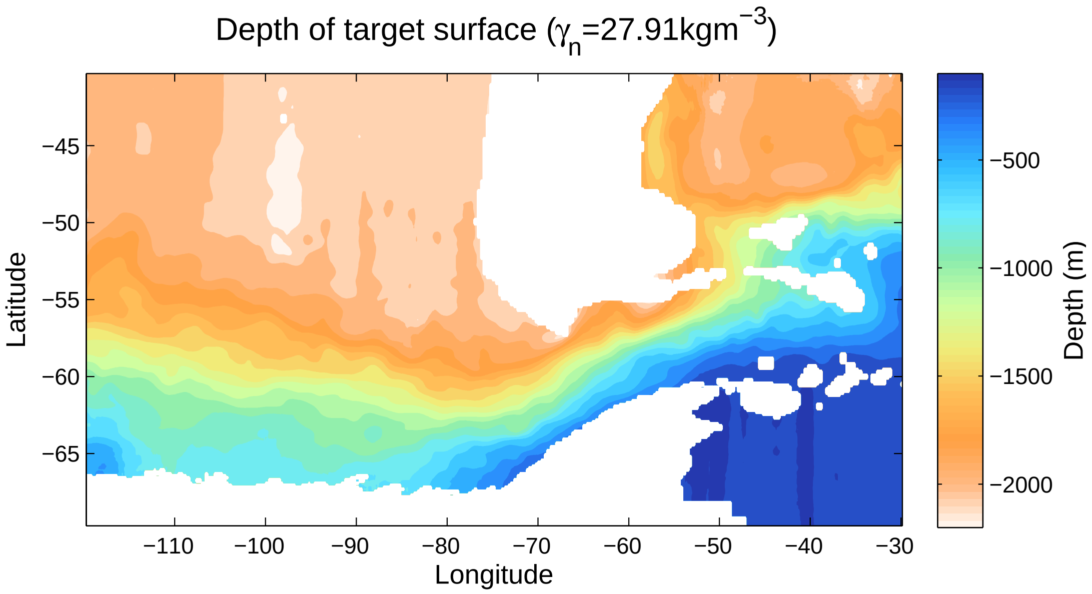

Figure 4.1: The depth of the target surface from SatGEM for the model domain. The depths are a time-mean over SatGEM time slices from 27th January 2010 to 13th April 2011. The white areas are outside the geographical limits of the SatGEM T-S data.

4.2.3 Using SatGEM in MITgcm

In order to use the SatGEM velocities in the MITgcm model framework, they must be interpolated onto the model grid. First, γ_n is calculated for each time slice using the SatGEM T and S data referenced by latitude, longitude and depth. Then the SatGEM velocities are interpolated first horizontally onto the model latitude/longitude grid, and then vertically onto isopycnals, using the γ_n values to map onto the model density grid. The horizontal interpolation is done such that the zonal velocities, u, are mapped onto the western faces of the model grid cells, and the meridional velocities, v, are mapped onto the southern faces to conform to the expected configuration for MITgcm.

The depths associated with the isopycnal surfaces at each point on the model grid are also recorded for each time slice. The depth of the tracer target density for a time mean over the period from 27th January 2010 to 13th April 2011 is shown on figure 4.1. This time period, from the US2 to the UK2.5 tracer survey, is that of the main model runs. The gentle slope of the isopycnal can be seen, from near the surface around the Antarctic Peninsular, to around 2000m depth to the North of Drake Passage where it intersects with the South American continental slope.

Having been interpolated onto the model grid, the velocity fields must then be rendered horizontally non-divergent. This is achieved using some code developed specifically for use with MITgcm, documented in Marshall *et al.* (2006). The method defines the final velocity $\mathbf{u}$ as consisting of a geostrophic component $\mathbf{u}_g$ (in this case the interpolated SatGEM velocity) and an adjustment $\nabla\chi$:

$$\mathbf{u} = \mathbf{u}_g + \nabla\chi. \tag{4.11}$$

The divergent adjustment is then calculated from

$$\nabla^2\chi = -\nabla \cdot \mathbf{u}_g \tag{4.12}$$

with a boundary condition of

$$\nabla\chi \cdot \mathbf{n} = -\mathbf{u}_g \cdot \mathbf{n} \tag{4.13}$$

where $\mathbf{n}$ is the unit vector perpendicular to the boundary. The non-divergence code was developed for a two-dimensional velocity field, and the fields being used here are three-dimensional. Each SatGEM time slice is therefore split into the 67 individual model levels before being fed into the non-divergence code, and the corrected fields are recombined at the end.

The fact that the SatGEM fields are limited to regions where the water depth is at least 2000 m presents an additional challenge for the non-divergence process. If a boundary is placed at the edge of the SatGEM fields, the boundary condition will force the velocities to be directed parallel to the boundary, significantly modifying the flow at these points. In reality, the flow should continue over the edge of the SatGEM fields, but we have no information about what the velocities should be there. The compromise that has been implemented is to set the velocities to zero where we do not know them, and using bathymetry data from Sandwell *et al.* (2002), define a land boundary everywhere that the depth is zero. This introduces a ‘buffer’ zone where the effect of the divergent velocity correction is distributed between the region containing the known geostrophic velocities, and the region where velocities are set to zero. The model bathymetry is shown on figure 4.2. Depths are everywhere simply the sum of the distances between the model depth levels (see section 4.2.6 for an explanation of these distances), except in places that land

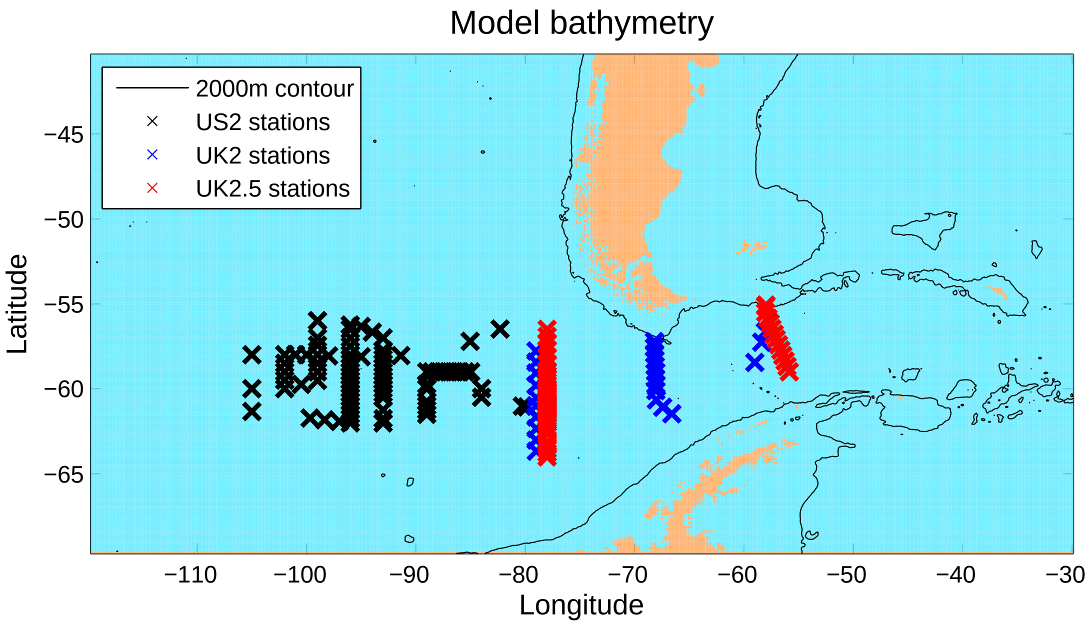

Figure 4.2: The bathymetry defined for use in the model. Depths are the full vertical extent of the model everywhere (light blue areas) except where land has been identified from Sandwell *et al.* (2002), where model depth is set to zero (brown areas). The 2000 m contour representing the limits of the SatGEM fields is marked in black. The stations where profiles of tracer were collected on the US2 (black crosses), UK2 (blue crosses) and UK2.5 (red crosses) cruises are also marked.

has been identified, where the depth is zero. This simple approach of having no intermediate model depths is most sensible because of the time dependent nature of the depths of isopycnal surfaces, which means that the real depths associated with the model levels are changing with time, and any intersection with the bottom topography that might occur would also be time dependent. In addition to the land, a line along the southern edge of the model domain where the depth is zero can also been seen on figure 4.2. This has been added because the non-divergence code fails to render the fields non-divergent without it. The divergence of the model velocity fields at the target depth before and after running the non divergence code is shown on figure 4.3 (a) and (b). The divergence is:

$$\nabla \cdot \mathbf{u} = \frac{\partial u}{\partial x} + \frac{\partial v}{\partial y} + \frac{\partial w}{\partial z}. \tag{4.14}$$

Since w is zero everywhere, the third term is zero. The zonal (x) and meridional (y) coordinates at each model grid latitude (lat) and longitude (lon) are calculated as follows:

$$x(lat, lon) = lon \times 111177.5 \times cos\left(\frac{\pi\, lat}{180}\right), \qquad y(lon) = 111177.5 \times lat \tag{4.15}$$

(a) Divergences on a density surface before running non-divergence code

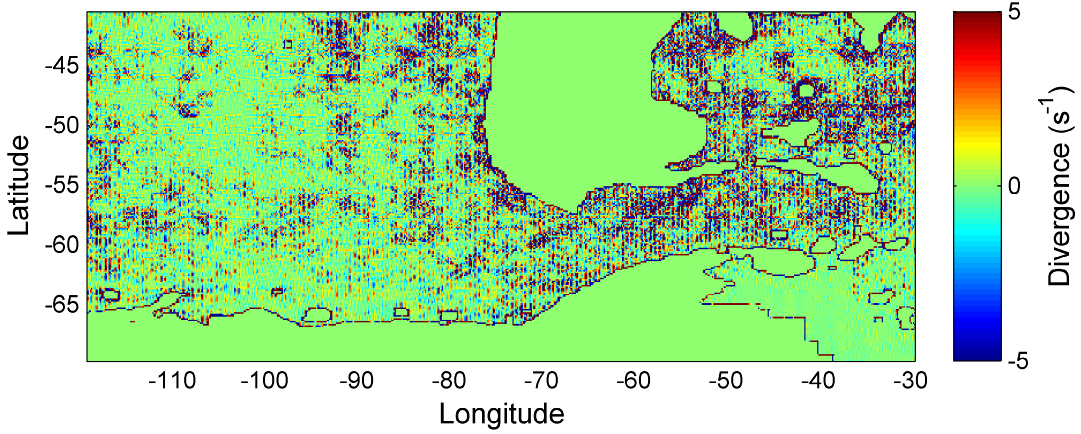

(b) Divergences on a density surface after running non-divergence code

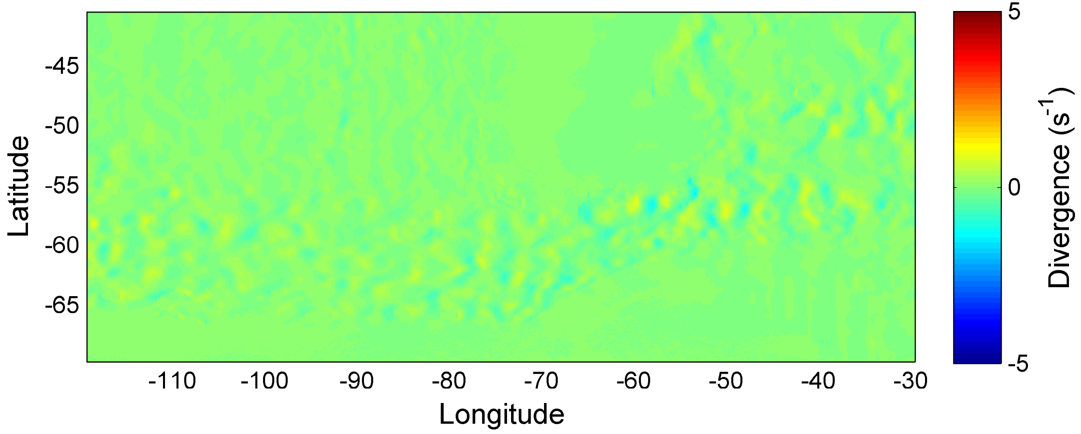

(c) Divergences on a pressure surface

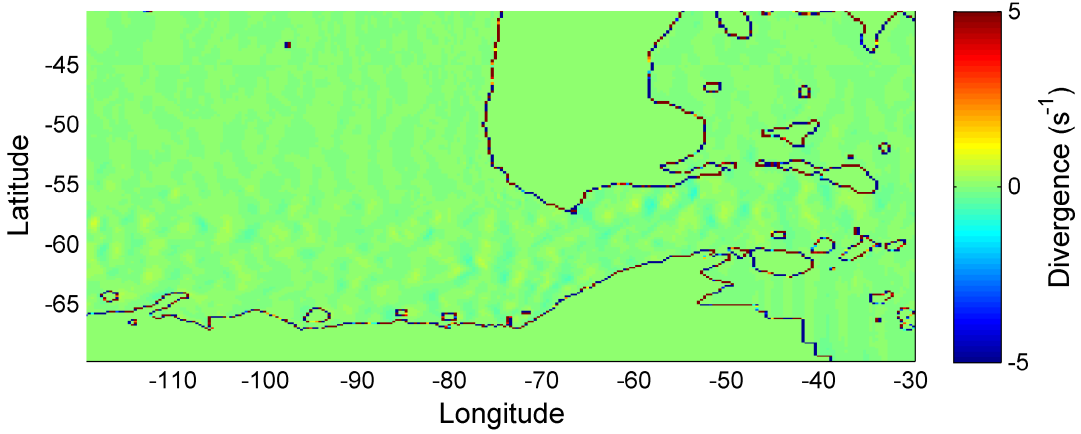

Figure 4.3: Divergences of the SatGEM velocity fields (a) interpolated onto the target density surface before running the non-divergence code (b) on the target density surface after running the non-divergence code and (c) uninterpolated, on a pressure surface at 1300m depth.

where lat and lon are in degrees. The means of the absolute divergences before and after running the non-divergence code are $\sim\, 2 \times 10^{-7}\, s^{-1}$ and $\sim\, 1 \times 10^{-8}\, s^{-1}$. The means of the actual divergences before and after running the code are $\sim\, -1 \times 10^{-9}\, s^{-1}$ and $\sim\, 1 \times 10^{-12}\, s^{-1}$. Also on figure 4.3 (c) is the divergence of the SatGEM velocities on a pressure surface, before they have been interpolated onto density surfaces and onto the regular model grid. While the divergence is still high at the boundaries of SatGEM, the values are much lower over the rest of the grid, indicating that the interpolation is responsible for the majority of the divergence shown in (b). The SatGEM velocity vectors at the target depth before and after running the non-divergence code are shown on figure 4.4. The time slice shown is from 27th January 2010, which coincides with the midpoint of the US2 cruise. In most places the changes in the velocities are small, but in the regions where no SatGEM velocities are available (white areas in panel (a)), new non-zero velocities that permit the non-divergent closure of the fields can be seen in panel (b).

4.2.4 Comparing model outputs with experimental observations

4.2.4.1 Obtaining model tracer profiles

The model is run for a period from the tracer release in February 2009 up to the UK2.5 cruise in April 2011. Model outputs of the tracer field are extracted at times corresponding to the US2 (January - February 2010), UK2 (December 2010 - January 2011) and UK2.5 (April 2011) cruises. Making the assumption that the length of the cruises is short compared with the length of the experiment, one snapshot in time of the model output is chosen to represent the tracer patch for each cruise. The output coinciding with 27th January is taken as corresponding to the US2 cruise; the output from 29th December 2010 is taken as corresponding to UK2; and the output from 13th April 2011 is taken as corresponding to UK2.5.

For each output, model vertical profiles of tracer concentration are obtained at coordinates corresponding to the locations of stations surveyed on the corresponding cruise. These locations are shown on figure 4.2 for US2 (black crosses), UK2 (blue crosses) and UK2.5 (red crosses). The 2000m contour is also marked as this represents the limits of the SatGEM fields. The position of a station on the model grid is identified as the grid cell

(a) Velocities before running non-divergence code

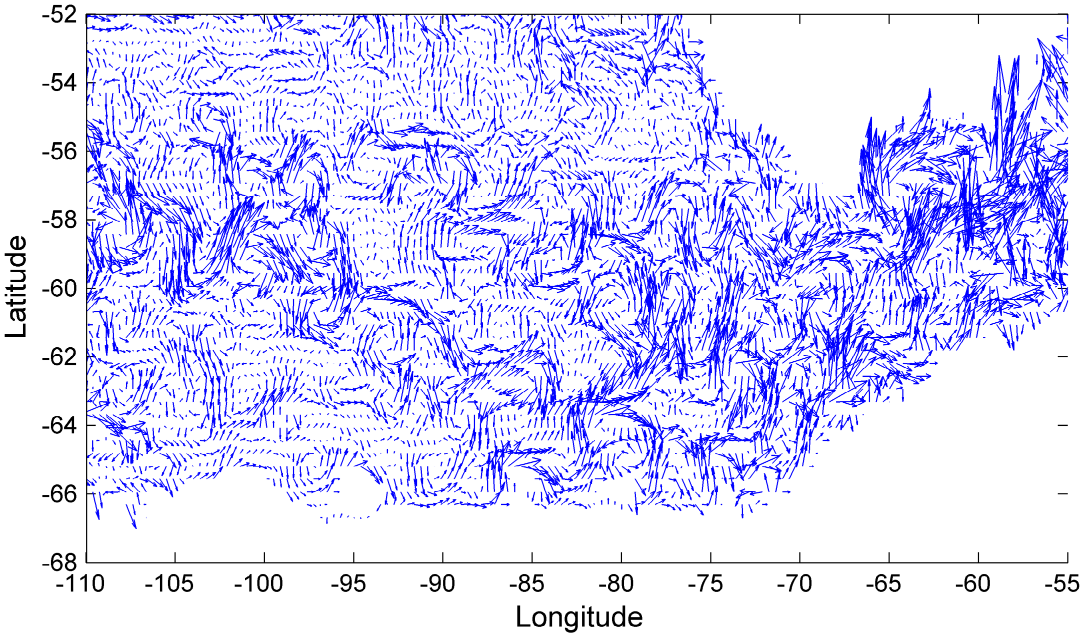

(b) Velocities after running non-divergence code

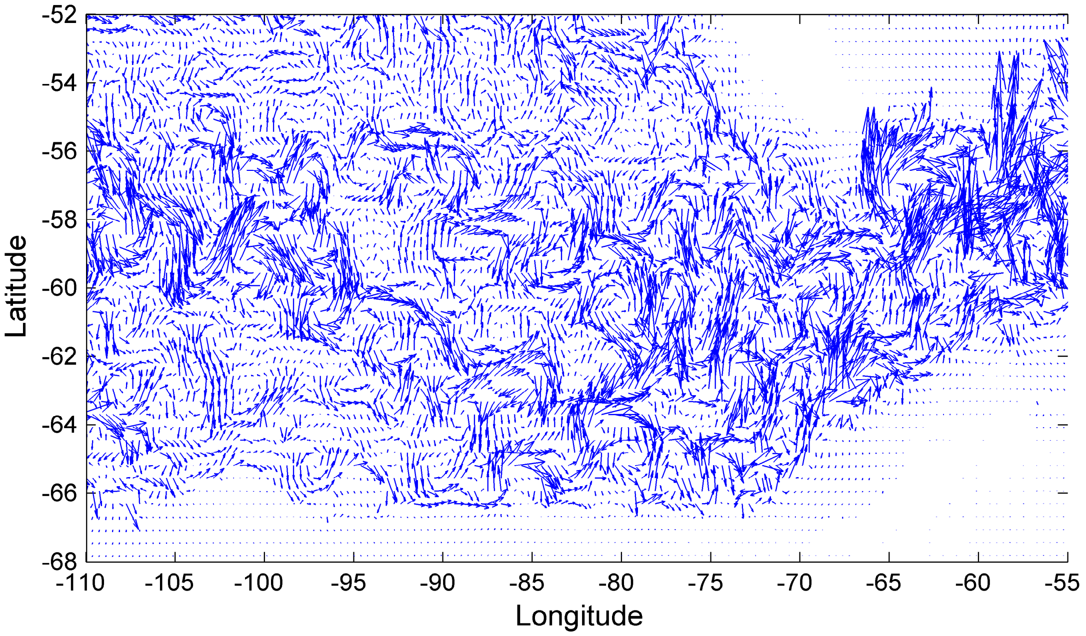

Figure 4.4: The model velocities for the 27th January 2010 SatGEM time slice at the target density (a) before and (b) after running the non-divergence code. The arrows point in the direction of the velocity vectors $\mathbf{u} = (u, v)$, and their length is proportional to the magnitude of the velocity.

for which the latitude and longitude at its centre is closest to the latitude and longitude recorded for the cruise station. Each model tracer profile represents a profile of tracer concentration in density space, since the model levels have been assigned to neutral densities. In order to compare them with the experimental profiles, the UK2.5 depth-density profile (as introduced in section 2.3.1.1) is interpolated onto the model density grid, and is then used to transform model tracer profiles from density to depth. Experimental profiles of tracer concentration with density are also mapped from density to depth using the UK2.5 depth-density profile. Vertical widths and peak concentrations for each of the model and experimental tracer profiles are then obtained, the peak concentration taken as the highest concentration value in the profile, and the vertical width calculated by fitting a Gaussian in the same manner as was described in section 2.3.1.2.

Model profiles are very Gaussian, but the real experimental profiles are more variable, so some consideration must be given as to which profiles to include in the model to experimental data comparison. Some profile inclusions and exclusions are illustrated on figure 4.5. Station 17 on UK2 is a typical profile, and is very Gaussian, so is included. Station 8 is a very low concentration profile, and is clearly not able to fit a Gaussian, so is excluded. Stations 4 and 26 are more marginal as it is possible to fit a Guassian to them, but they are not perfectly Guassian in shape. Station 26 is included because the non-Gaussian nature of the profile has not significantly affected the vertical width, whereas station 4 is excluded because the non-Gaussian shape, caused by an intrusion of non-local water masses mixed in isopycnally, has significantly increased the vertical width implied by the Gaussian fit.

4.2.4.2 Cost function

To quantify the model-experimental data fit, a cost function of a similar form to that introduced in Chapter 3 is used. However, whereas with the 2D model individual experimental tracer profiles were compared with a single model profile per transect on each tracer survey, here the profiles are compared one-to-one. The equation for the new cost function is as follows:

$$\chi^2 = \sum_{T} \sum_{i=1}^{n_T} \frac{(w_i - W_i)^2}{{\sigma_{w_T}}^2} + \frac{(c_i - C_i)^2}{{\sigma_{c_T}}^2} \tag{4.16}$$

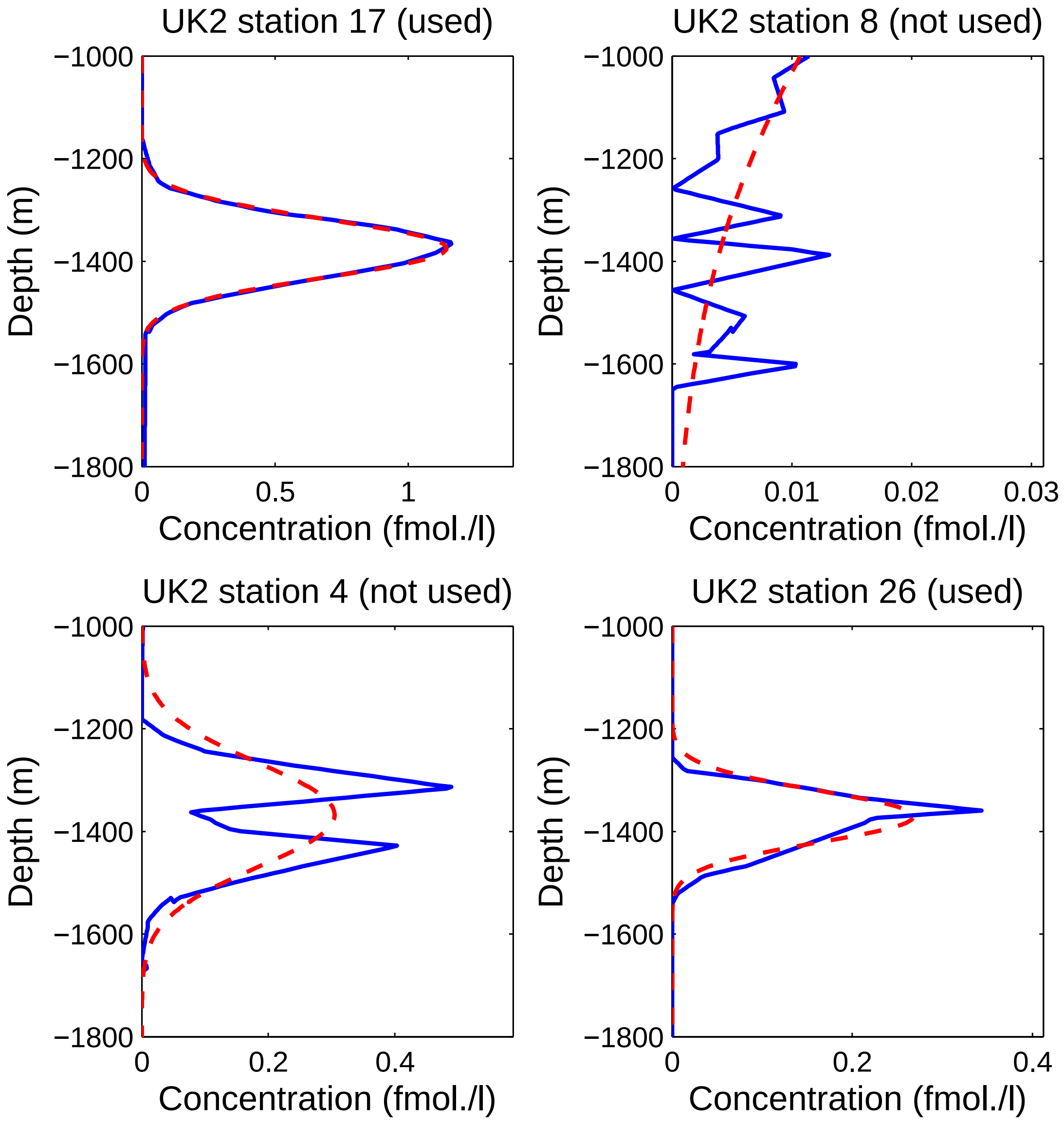

Figure 4.5: Some example experimental tracer profiles to illustrate inclusions in and exclusions from the model-data comparison. Solid blue lines are the tracer profiles; red dashed lines are the Gaussian fits. All tracer profiles have been plotted against the UK2.5 depth-density profile.

where w_i and W_i are the experimental and modelled individual profile widths, c_i and C_i are the experimental and modelled individual profile peak concentrations, and ${\sigma_{w_T}}^2$ and ${\sigma_{c_T}}^2$ are the variances of the measured widths and peak concentrations on a given transect T. The inner sum is over all the profiles on a transect, and the outer sum is over a number of transects. When comparing between the model output and the US2 stations, the whole survey, which is a continuous track, is treated as one transect. When comparing output with UK2 and UK2.5, the transects are (west to east), the Pacific, Albatross and SR1 transects as shown on figure 4.2. The cost function is weighted in inverse proportion to the variability of the experimental observations on each transect as represented by σ^2. So a transect that has a large variation in, for example, the vertical widths will be given a lower weighting than a transect where the variation is smaller. This helps to compensate for the relatively coarse horizontal resolution of the model, which limits its ability to capture the smaller scale variability of the observations. As in Chapter 3, the contributions of the vertical widths and peak concentrations from individual transects to the overall cost function may be assessed individually. Also as previously, the expectation value of the cost function is the number of degrees of freedom of the system, approximately equal to the number of profiles compared.

4.2.5 Model initialisation

The initial tracer distribution to model the tracer release is a 3D Gaussian, defined by:

$$C(x,y,z) = \frac{N}{(2\,\pi)^{\frac{3}{2}}\sigma_x\sigma_y\sigma_z} exp\left[-\frac{x-x_0}{2{\sigma_x}^2} - \frac{y-y_0}{2{\sigma_y}^2} - \frac{z-z_0}{2{\sigma_z}^2}\right] \tag{4.17}$$

where C is the tracer concentration, x, y, z are the model zonal, meridional, and vertical coordinates in metres, N is the total tracer released in femtomoles, σ_x, σ_y, and σ_z are the zonal, meridional, and vertical widths of the initial tracer patch, and x_0, y_0 and z_0 are the zonal, meridional and vertical coordinates of the release in metres. The total tracer quantity is 76 kg, which from the molar mass of $\mathrm{CF_3SF_5}$, which is 196 g, is equivalent to 388 moles. The widths are taken from the account by Ledwell *et al.* (2011) of the tracer release, with $\sigma_x = \sigma_y = 20\,\mathrm{km}$ and $\sigma_z = 5\,\mathrm{m}$. The release horizontal coordinates, also from Ledwell *et al.* (2011), are $x_0 = 107°\mathrm{W},\ y_0 = 58°\mathrm{S}$. These and the model coordinates x, y are converted to metres using the same relationship as was given in equation 4.15. The vertical coordinate z_0 is the model depth at the centre of the 36th level, the model level corresponding to the target density. The total tracer quantity in the initial tracer distribution is checked by integrating the concentrations over the model domain, and should be equal to the injected amount:

$$N = \int\int\int C(x,y,z)\; dx\, dy\, dz \tag{4.18}$$

However it is found that due to the small size of the Gaussian shaped patch compared with the size of the discrete grid cells, the result of this integral is slightly too large. The input quantity N is therefore adjusted by a factor of 1/1.04742, ensuring that the total quantity of injected tracer is correct. The initial tracer field having been defined, the model is run for 1 year up to US2, and the model parameters K_z and K_h are optimised using the cost function to give the best fit to the US2 experimental data. For this stage, K_z is set to a constant value throughout the model domain. The output from the optimised run is then used as the initial field for further runs, beginning at the time of US2 and running on for 15 months to UK2.5.

4.2.6 Model vertical grid

Since the model depth levels are treated as corresponding to isopycnals, the depths assigned to them determine the physical thickness h of an isopycnal layer, where for a given model level i, $h_i = z(i + \frac{1}{2}) - z(i - \frac{1}{2})$, if i increases with increasing depth z. The layer thicknesses are determined from the SatGEM depth-density relation, as illustrated on figure 4.6. In order to minimise the error introduced by the approximation that h is constant in time and horizontal space, in particular to attempt to avoid any systematic error associated with large scale changes in stratification, the distance between model levels was calculated using a time- and spatial- mean of h, where the local instantaneous values of h were calculated from the SatGEM derived density fields. The spatial variation in h for a $0.003\,\mathrm{kgm}^{-3}$ thick isopycnal layer at the target density, calculated from a time mean of the SatGEM density fields over the period 27th January 2010 - 13th April 2011, is shown on figure 4.7. To obtain the spacings between model depth levels for the release - US2 runs, the time mean of h for the whole three-dimensional model domain was taken over the period 4th February 2009 to 27th January 2010, and then a spatial mean taken horizontally over the area indicated by the red box on figure 4.7 (note that the h field shown is for the US2 - UK2.5 time mean, but the pattern is very similar). The model depth level spacings for the US2 - UK2.5 runs are obtained in the same way, but using the 27th January 2010 - 13th April 2011 time mean, and the spatial mean over the area indicated by the blue box on figure 4.7. The areas are chosen to correspond to the area occupied by the model tracer for the course of each run. The resultant h for the model density grid for the

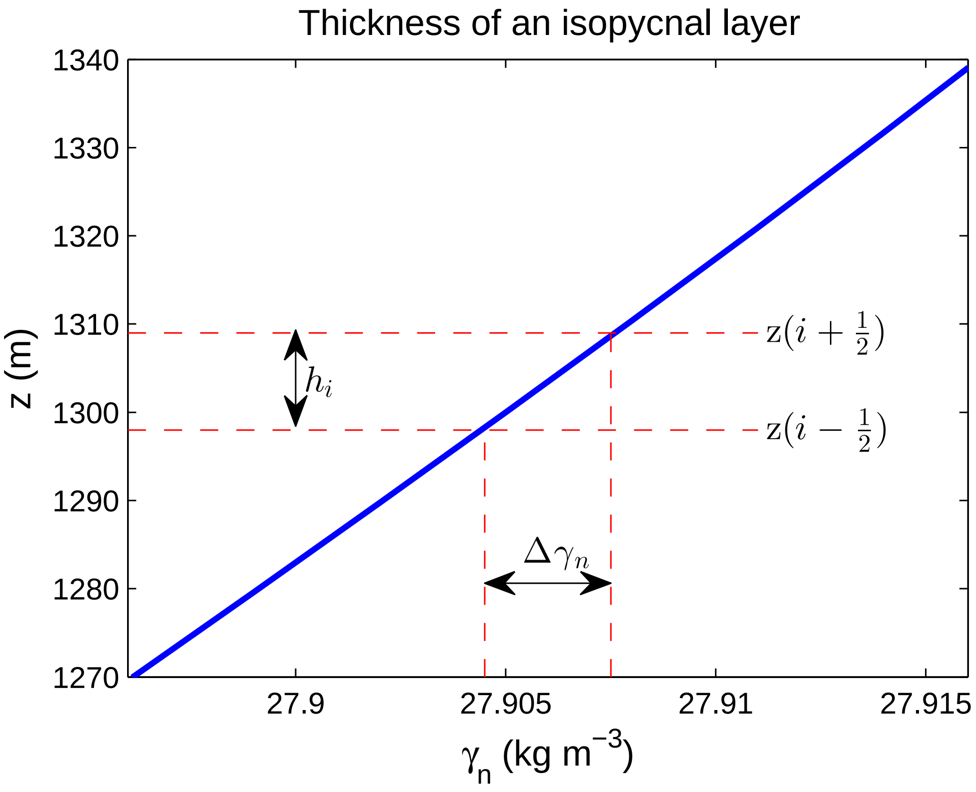

Figure 4.6: An illustration of the method used to calculate the thickness of the model isopycnal layers. The SatGEM depth-density relation (blue line) is used to determine the change in depth, h_i, that corresponds to a change in neutral density, $\Delta\gamma_n$, of $0.003\,\mathrm{kgm}^{-3}$ on a given density level, i. The dashed red lines illustrate the upper and lower limits of an isopycnal layer centred on the tracer target density.

release - US2 and US2 - UK2.5 runs is shown on figure 4.8.

The change in the model profile of h between the release to US2 runs and the US2 to UK2.5 runs means that, in order to preserve the total quantity of tracer in the model, concentration values need to be adjusted. This is done such that the total quantity of tracer in a model isopycnal layer, T_k, remains constant:

$$T_k = \int_{k-\frac{1}{2}}^{k+\frac{1}{2}} \int\int C(x,y,z)\,dx\,dy\,dz = h_k \int\int C(x,y,z)\,dx\,dy \tag{4.19}$$

where the two inner integrals are over the full horizontal extent of the model domain. The concentrations in each layer are then corrected by:

$$C_{(i,j,k)} = C_{(i,j,k)} \frac{h_{k-old}}{h_{k-new}} \tag{4.20}$$

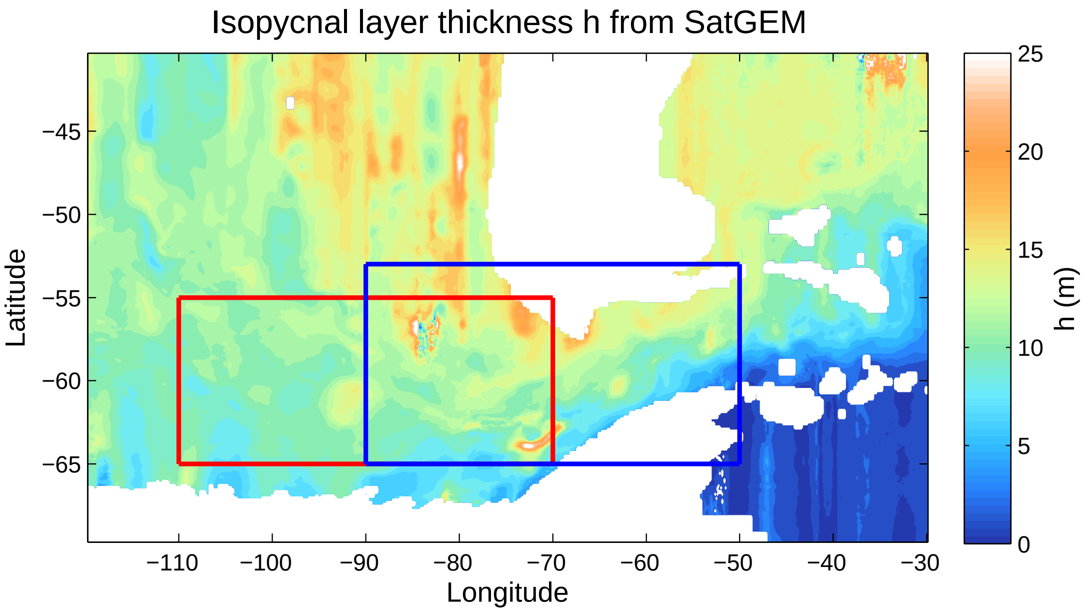

Figure 4.7: A map of the isopycnal layer thickness calculated from the SatGEM fields at the target density. The values shown are time means for the period 27th January 2010 - 13th April 2011 (US2 to UK2.5). The red box represents the horizontal area over which the values are averaged to obtain the depth level spacings for the release to US2 model runs. The blue box represents the area over which the values are averaged for the US2 to UK2.5 runs. The values of h are for an isopycnal layer of thickness $0.003\,\mathrm{kgm}^{-3}$.

where (i, j, k) are the indexes of the model grid (x, y, z) coordinates and h_{k-old} and h_{k-new} are the thicknesses of density layer k in the release - US2 and US2 - UK2.5 model grids, respectively.

4.2.7 Diapycnal diffusivity fields

Three categories of diapycnal diffusivity field are used for the model runs presented in this chapter. For the release - US2 runs, a single value of K_z is assigned to the whole model grid. This is justified by the fact that mixing in the Southeast Pacific region that the tracer occupied between its release and the US2 cruise is expected to be fairly homogeneous, as the bottom topography is smooth here. In addition, the focus of the study is on Drake Passage, so the distribution of the mixing further to the west is of secondary importance. As will be seen in section 4.3.1, a single value of diffusivity for the release - US2 runs does a reasonable job of reproducing the mixing experienced by the experimental tracer. The second category is a ‘2 zone’ approach, where K_z is set to one value in the Southeast Pacific, and a different value in Drake Passage where rough topography and fast bottom flows are known to produced enhanced rates of mixing. The boundary between the Pacific

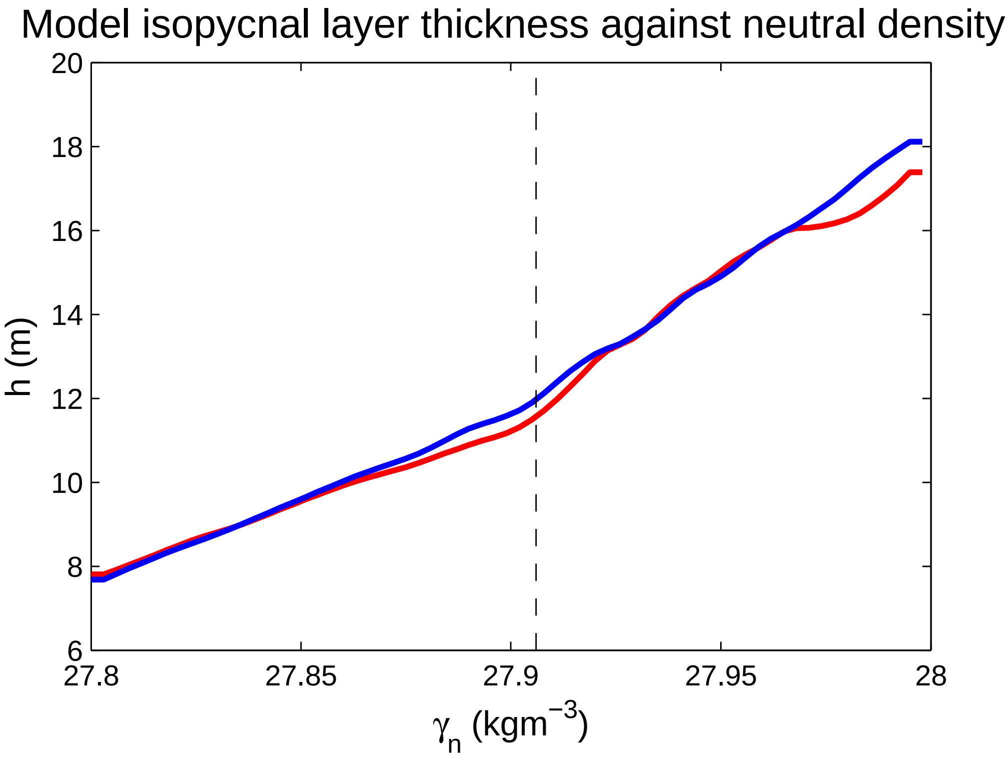

Figure 4.8: The relationship between the density and the thickness h of a $0.003\,\mathrm{kgm}^{-3}$ isopycnal layer for the model grid. The release - US2 time- and spatial average is shown by the red line; the US2 - UK2.5 average is shown by the blue line. The black dashed line indicates the tracer target density.

and Drake Passage zones was chosen to be $67°W$, as this is a reasonable estimate for longitude where the rough topography of Drake Passage begins (see figure 2.2), and was found in Chapter 3 to give a good fit to the tracer data when applied to the 2D model. The values of K_z in the Pacific and Drake Passage zones are then optimised for the best model-data fit using the cost function.

The third category is based on the idea that enhanced mixing is associated with the bottom topography. A background value representative of the Southeast Pacific mixing is set, and a single enhanced value of diffusivity K_{z-top} is defined at locations where the tracer target isopycnal surface comes within a given distance, d, of the bottom. In the first instance, K_z is enhanced everywhere that $hab_{target} <= d$, where hab_{target} is the height above the bottom of the target surface. To locate the depth of the target isopycnal at each point on the model grid, the time mean of the SatGEM fields over the US2 - UK2.5 time period is used (see figure 4.1). This is combined with water depths from Sandwell *et al.* (2002) to identify the horizontal coordinates of locations where $hab_{target} <= d$.

The value of K_z is then set to be enhanced at all depths throughout the model's vertical extent at these locations. It may be that some of the energy generated at topography is carried away by internal waves, which then break, causing enhanced mixing in places some distance from the generation site. The method is therefore extended by identifying additional regions of enhanced mixing within a given radius R of points around each location that $hab_{target} <= d$. Due to the eddying nature of the velocity fields, it is assumed that the direction of propagation of energy is symmetrical about the generation site, therefore a circular area of additional enhanced mixing is appropriate. Figure 4.9 shows the regions of the model grid for which enhanced mixing is defined for various values of d and R. This third category of diffusivity field will hereafter be referred to as the 'enhanced K_z' model.

4.3 Results

4.3.1 Release to US2 model runs

4.3.1.1 Runs using nondivergent velocities

The tracer distributions resulting from a number of model runs from release to US2 with varying values of K_h are shown on figure 4.10. As K_h increases, horizontal tracer gradients decrease so the filamented, or 'streaky' nature of the tracer disappears; however the large-scale shape and size of the tracer patch is unaffected. On figure 4.11 are shown the peak concentrations of model tracer profiles from a selection of these runs compared with the tracer. The cruise track (see black crosses on figure 4.2) began in the north east, moved quickly westward and then zig-zagged its way back eastward from the most westerly point. The model has captured one or two of the features of the experimental tracer profiles' peak concentration distribution, such as the low concentrations around station 40, but misses much of the variability. The effect of increasing K_h is to homogenise the model peak concentrations.

The cost function for the optimisations of K_h and K_z for the release to US2 runs is shown on figure 4.12. The contribution from the vertical widths at the optimal value of K_z is very close to the expectation value, indicating that the model gives a good fit to the observations. The contribution from the peak concentrations at the optimal value of

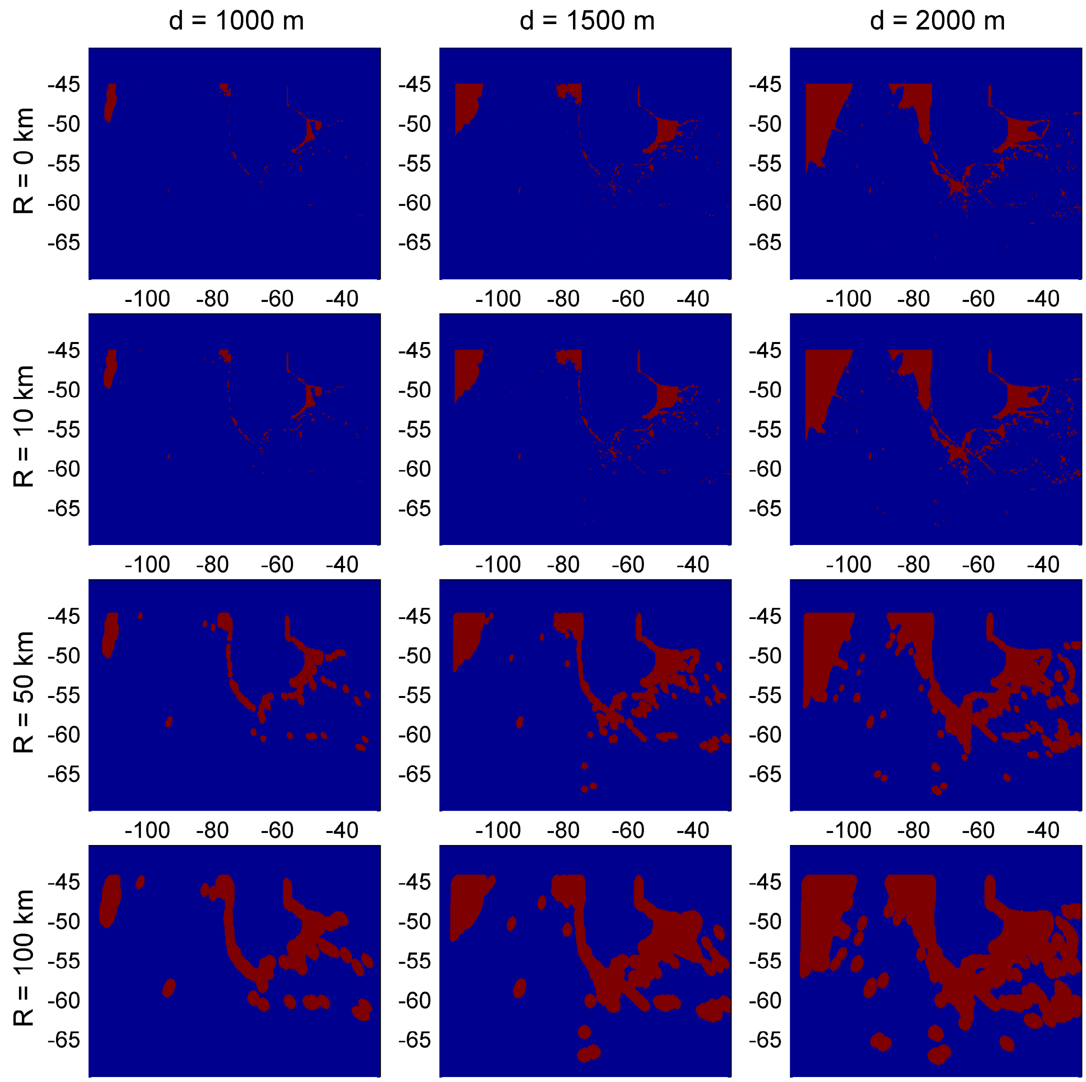

Figure 4.9: Regions where diapycnal diffusivity is enhanced above the backround level for various values of d and R, where d is the maximum height above topography of the target surface for the locations of enhanced mixing, and R is the maximum radius for further enhanced mixing around these locations. The horizontal and vertical axes are degrees longitude and latitude. Regions of enhanced mixing are shown in red.

K_h is some way above the expectation value, as the fixed velocity fields, rather than the value of K_h, are the main factor influencing the model-data fit. The value for K_h may be an overestimate, as in places where high model concentrations have coincided with low experimental tracer concentrations (and conversely where low model concentrations coincide with high experimental ones), the contribution of these stations to the cost function is large, and these effects are reduced when the model peak concentrations are smoothed out by larger K_h. The output of a run with the optimised parameters of $K_h = 100\,\mathrm{m}^2\,\mathrm{s}^{-1}$ and $K_z = 1.0 \times 10^{-5}\,\mathrm{m}^2\,\mathrm{s}^{-1}$ is used as the initial condition for the US2 - UK2.5 runs.

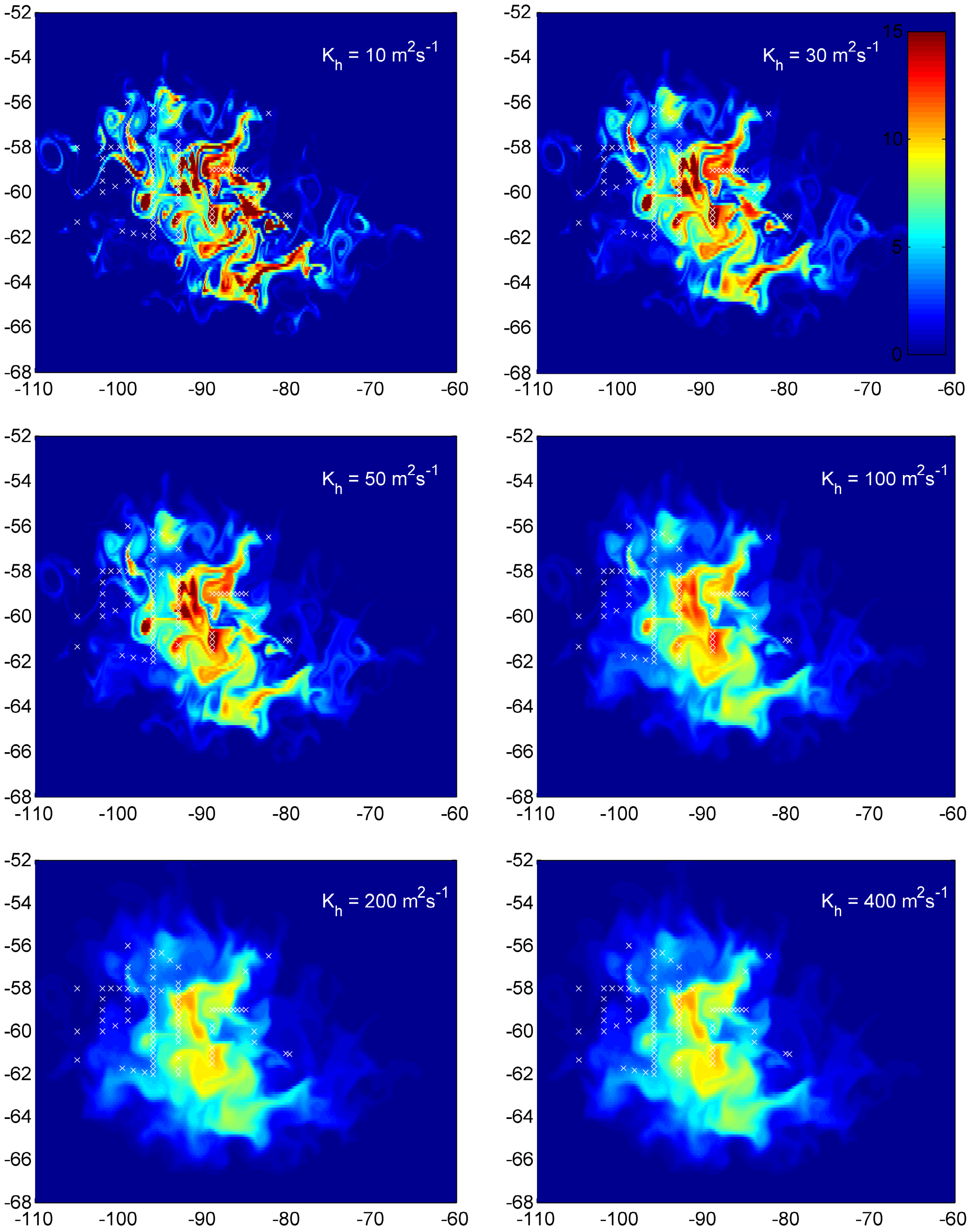

Figure 4.10: Maps of tracer concentration for release - US2 model runs with a range of values of isopycnal diffusivity K_h. The x and y axes are longitude and latitude, and the colour scale is in femtomoles/litre. The locations of the US2 stations included in the cost function for the model-data comparison are marked with white crosses.

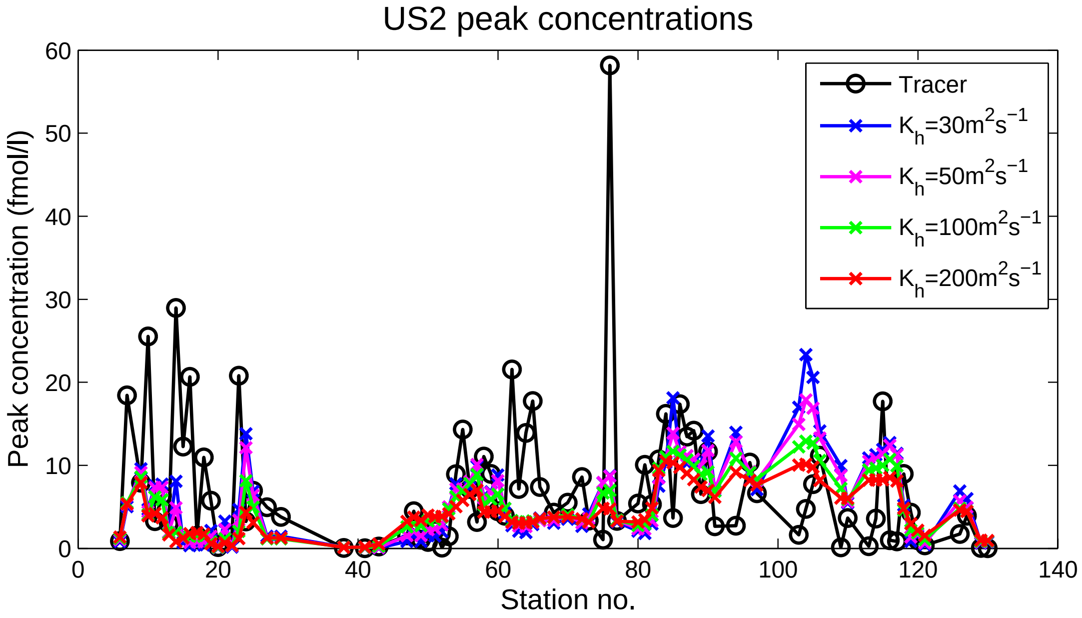

Figure 4.11: Peak concentrations of model tracer profiles for release - US2 model runs compared with the experimental tracer for $K_z = 1.0 \times 10^{-5}$ m^2 s^{-1}, variable K_h. Model profiles of tracer concentration with depth were obtained at the locations corresponding to the US2 stations (as shown by the black crosses on figure 4.2). On the x-axis, the station numbers correspond to the chronological order of the cruise stations. Experimental tracer results are in black; model profiles from runs with varying K_h are in colour.

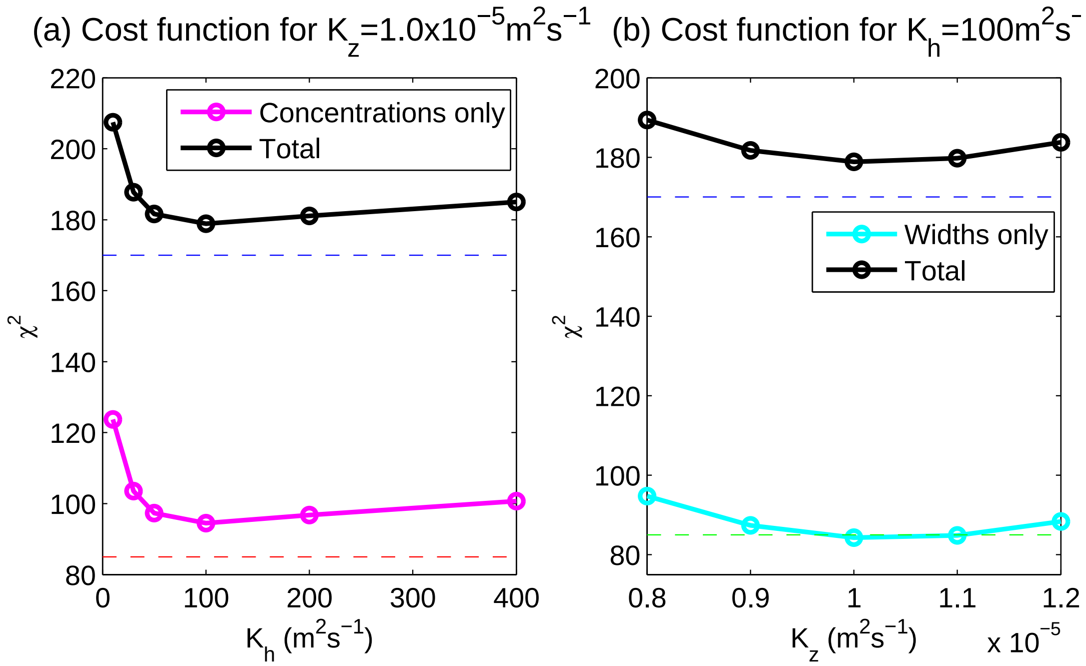

Figure 4.12: Cost function values for release-US2 runs. On panel (a) the optimisation for K_h with fixed K_z is shown. On panel (b) is the optimisation for K_z with fixed K_h. The light blue line shows the contribution to the cost function from the vertical widths, the pink line the contribution from the peak concentrations, and the black line the cost function total. The dashed lines give the respective expectation values of the cost function components.

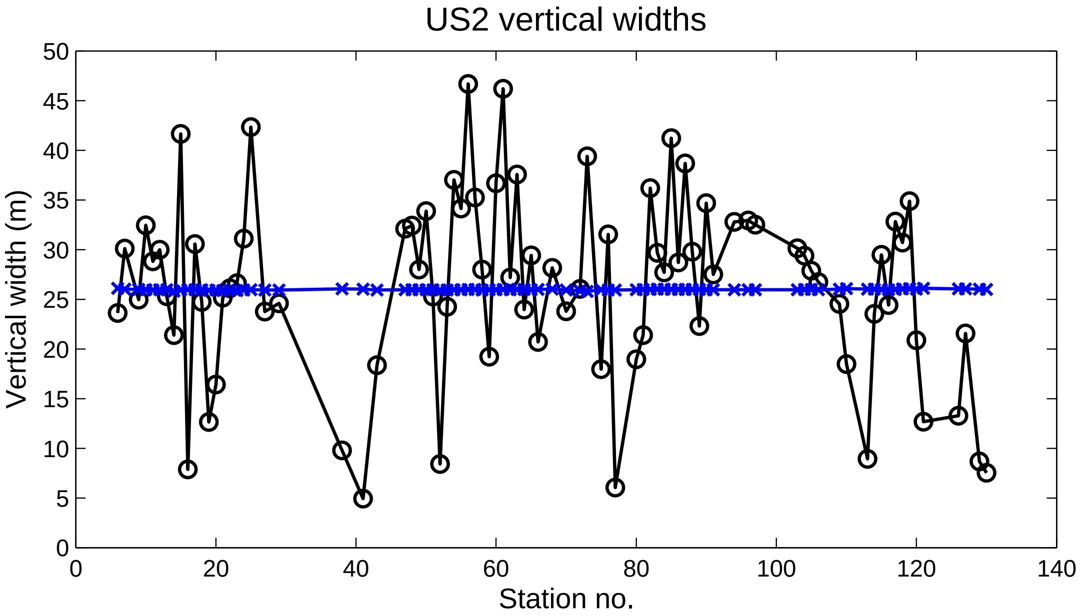

Figure 4.13: Vertical widths of model tracer profiles for a release - US2 model run compared with the experimental tracer for $K_h = 100 \text{ m}^2 \text{ s}^{-1}$, $K_z = 1.0 \times 10^{-5} \text{ m}^2 \text{ s}^{-1}$. Experimental tracer results are in black; model output is in blue.

The vertical widths for a release - US2 run with optimised K_h and K_z compared with the tracer are shown on figure 4.13. There is quite a bit of variability in the vertical widths of the observations, which is not captured by the model since K_z is not spatially variable for these runs. The optimised K_z is therefore treated as a best estimate of the average mixing for this stage of the experiment.

Tests were carried out on the effect on the cost function of moving the release location x_0, y_0 by $0.2°$ in one direction or another. The value $0.2°$ was chosen as an estimate of the uncertainty of the release site, which was reported to be 'near 58°S, 107°W' by Ledwell *et al.* (2011). Moving the release $0.2°$ south of 58°S increases the cost function value by 0.2, and moving it $0.2°$ north decreases it by 3.4. Moving the release $0.2°$ west of 107°W increases the cost function by 3.1, and moving it $0.2°$ east decreases it by 2.3. Nearly all of the variation comes from the contribution of the peak concentrations to the cost function, with the contribution of the vertical widths changing by no more than 0.01 between these runs. The uncertainty on the peak concentrations due to the release location means that the optimum value for K_h could be as low as $50 \text{ m}^2 \text{ s}^{-1}$ or as high as $200 \text{ m}^2 \text{ s}^{-1}$, but the estimate in the optimum value for K_z is unaffected.

4.3.1.2 Comparison using uncorrected velocity fields

The distribution of model tracer at the target depth at US2 resulting from a run which used the SatGEM velocities before they had been corrected to render them non-divergent is shown in figure 4.14 (a), compared with an equivalent run using the non-divergent velocities in figure 4.14 (b). Small differences can be seen in the progress of the tracer at this stage, the output from the non-divergent run showing higher concentrations in the southeast corner of the tracer patch. The peak concentrations for model runs using the uncorrected SatGEM velocity fields for a range of values of K_h compared with the experimental tracer are shown in figure 4.15. There are visible differences between these runs and those using the non-divergent field (figure 4.11), particularly for lower K_h, for example around station 100. The contribution to the cost function of the peak concentrations for $K_h = 100\ \mathrm{m}^2\ \mathrm{s}^{-1}$ is 85.9 for a run using the uncorrected velocities (the expectation value is 85), which compares with 94.5 for the non-divergent velocities and the same K_h. The optimum value of K_h when using the uncorrected velocities is $50\ \mathrm{m}^2\ \mathrm{s}^{-1}$, which is likely to be due to the uncorrected fields having reproduced the tracer advection slightly more closely, so the additional smoothing effect of higher K_h is not required to reduce the cost function. The optimum value for K_z of $1.0 \times 10^{-5}\ \mathrm{m}^2\ \mathrm{s}^{-1}$ is unchanged for the runs using the uncorrected velocities.

4.3.2 2 zone diffusivity fields

4.3.2.1 Runs using nondivergent velocities

The tracer concentrations at the target density for a US2 to UK2.5 model run, output at the times corresponding to the UK2 and UK2.5 cruises, are shown on figure 4.16. Figure 4.17 shows the model peak concentrations for the two cruises compared with the tracer for a number of runs with varying K_h. On figure 4.16 the run shown had $K_h = 200\ \mathrm{m}^2\ \mathrm{s}^{-1}$. At the time of UK2, the model appears to have captured the east-west distribution of the tracer well, with similar transect-averaged concentrations in the model at each transect as were observed. The meridional variation at UK2 has been captured less well. The tracer concentrations on the northern end of the Pacific transect have been underestimated, which may indicate that the centre of mass of the tracer is too far south at this point. This inference is supported by the fact that at the southern edge of the Albatross transect, where

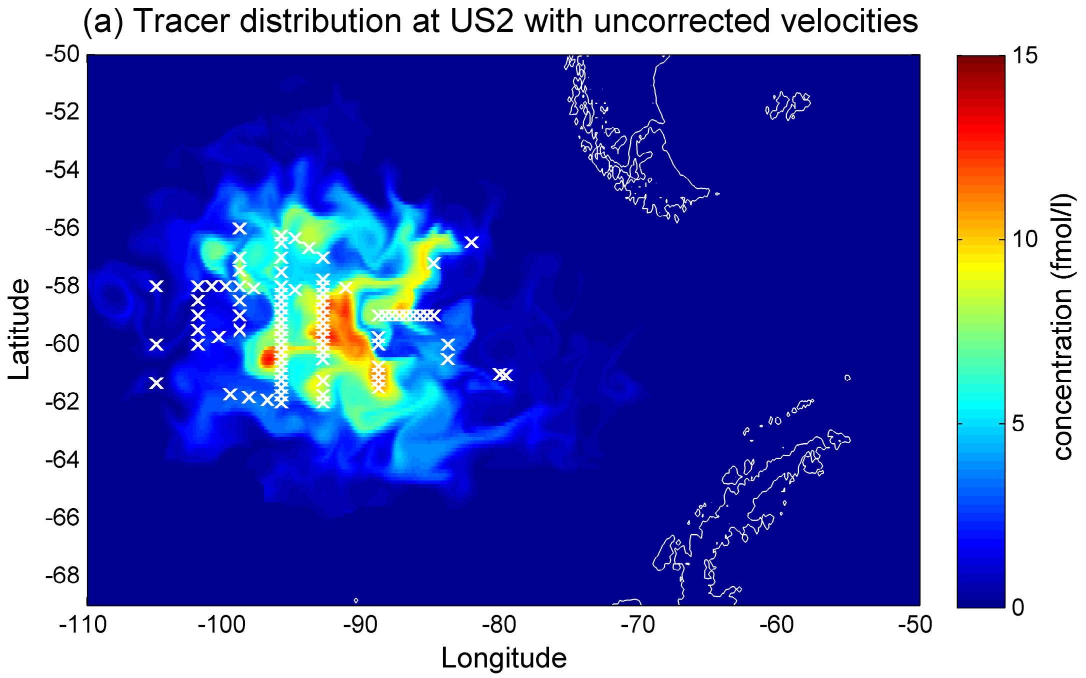
(a) Tracer distribution at US2 with uncorrected velocities

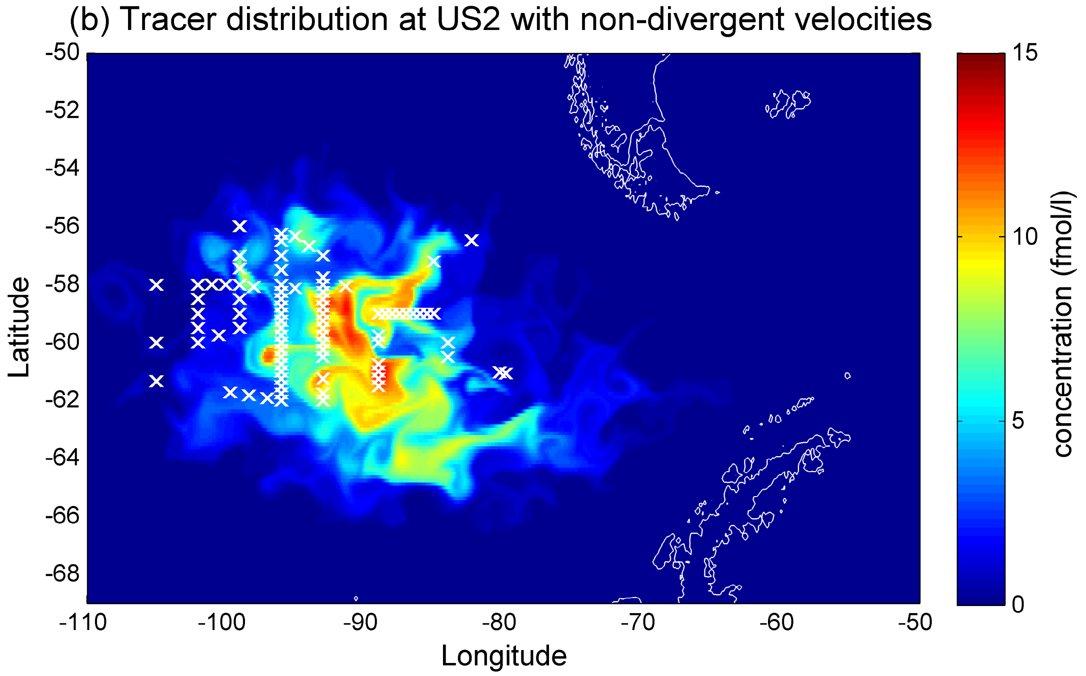
(b) Tracer distribution at US2 with non-divergent velocities

Figure 4.14: Maps of tracer concentration at the target density for model runs from release to US2. On panel (a) is the output from a run using the uncorrected SatGEM velocity fields, and on panel (b) the velocities used had been rendered non-divergent. The stations where experimental tracer sampled on US2 is compared with the model outputs (white crosses) and the South American and Antarctic continents (white contour lines) are overlayed.

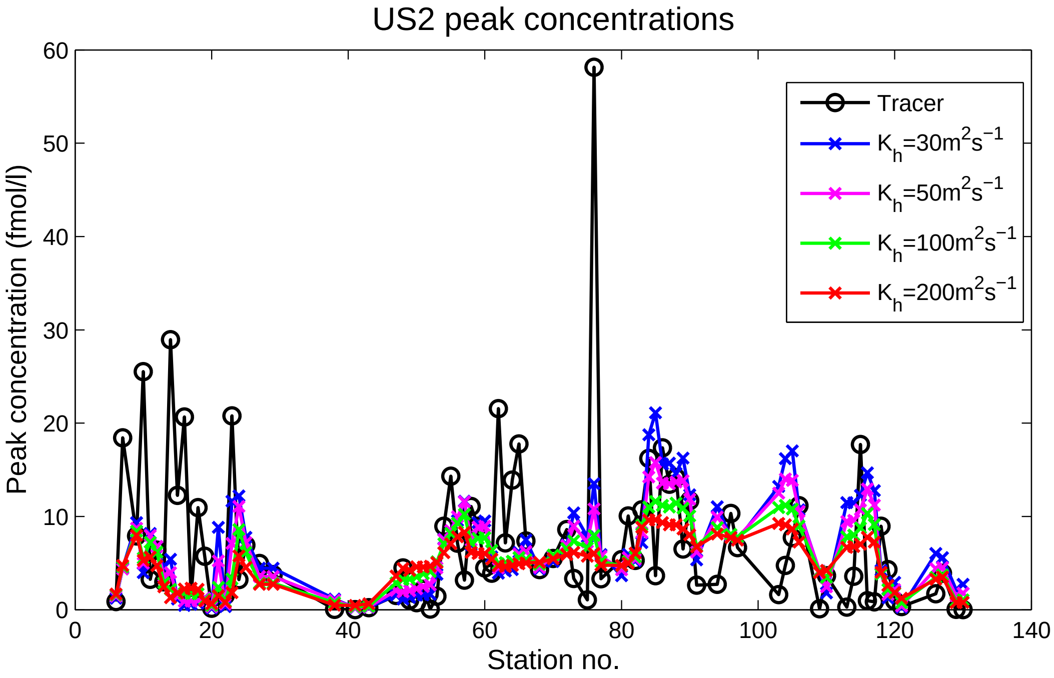

Figure 4.15: Peak concentrations for release - US2 runs using the SatGEM velocities not corrected to render them non-divergent. Experimental tracer is in black; model runs with varying values of K_h are in colour.

no tracer was measured, there are significant amounts of model tracer. On SR1 the model tracer concentrations are about right on average, but are overestimated at the southern end for lower values of K_h, these effects being smoothed out as K_h increases. At UK2.5, the concentrations are in general too low on the Pacific transect, and the smaller scale meridional variability captured by the high-resolution section in the tracer survey is not reproduced by the model.

The vertical widths for model outputs at UK2 and UK2.5 compared with the tracer for the same series of runs with varying K_h are shown on figure 4.18. The only transect on which K_h can be seen to homogenise meridional variations in the vertical widths is SR1. However, the effect is not nearly as marked as it is for the peak concentrations, with the distribution of vertical widths only changing slightly for a 16-fold increase in K_h.

The contributions of different components to the cost function for the three phases of the optimisation of the 2 zone model are shown on figure 4.19 to 4.21. In general, the contributions to the cost function of the vertical widths on each transect are close to the expectation values, indicating that these diffusivities give a reasonably good fit to the data.

(a) Tracer distribution at UK2

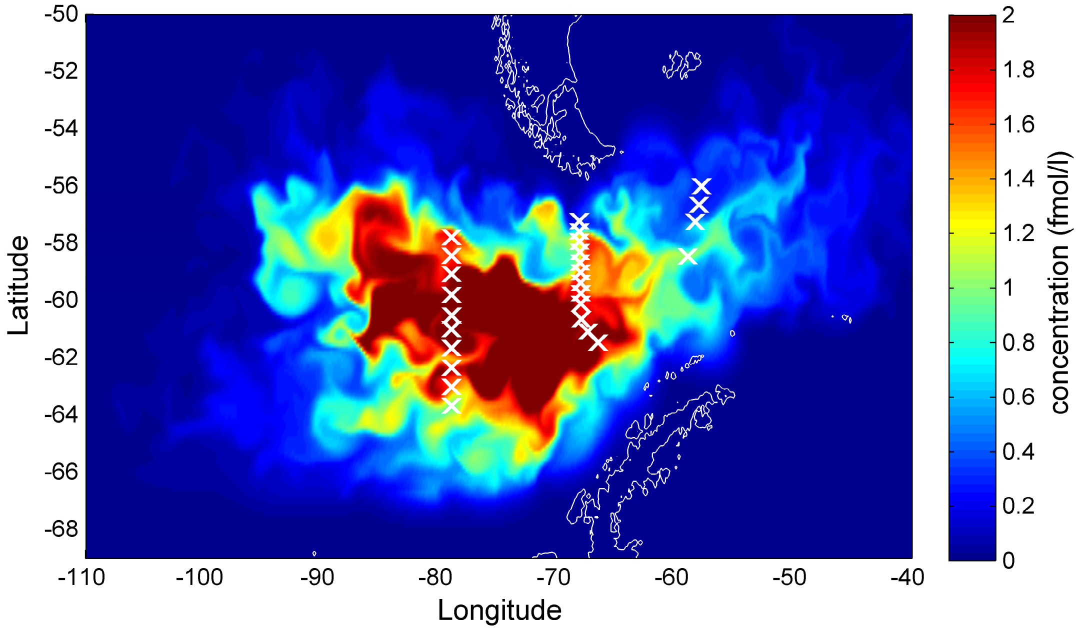

(b) Tracer distribution at UK2.5

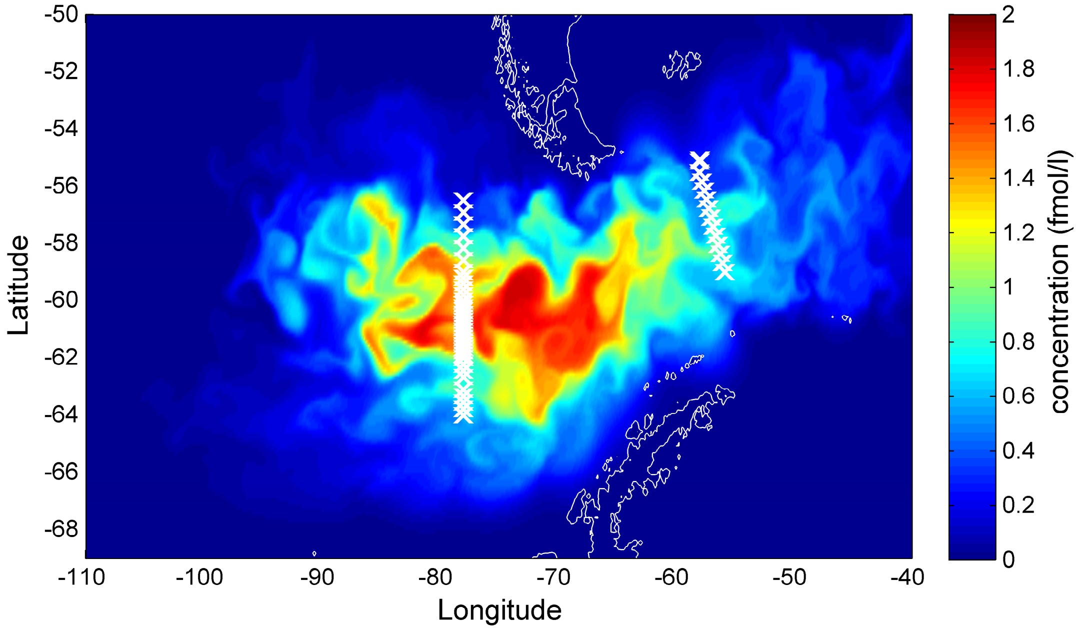

Figure 4.16: Maps of tracer concentration at the target density for a model run from US2 to UK2.5. Panel (a) is the model output corresponding to UK2, and panel (b) the output corresponding to UK2.5. The stations where experimental tracer sampled on each cruise is compared with the model outputs are overlayed (white crosses).

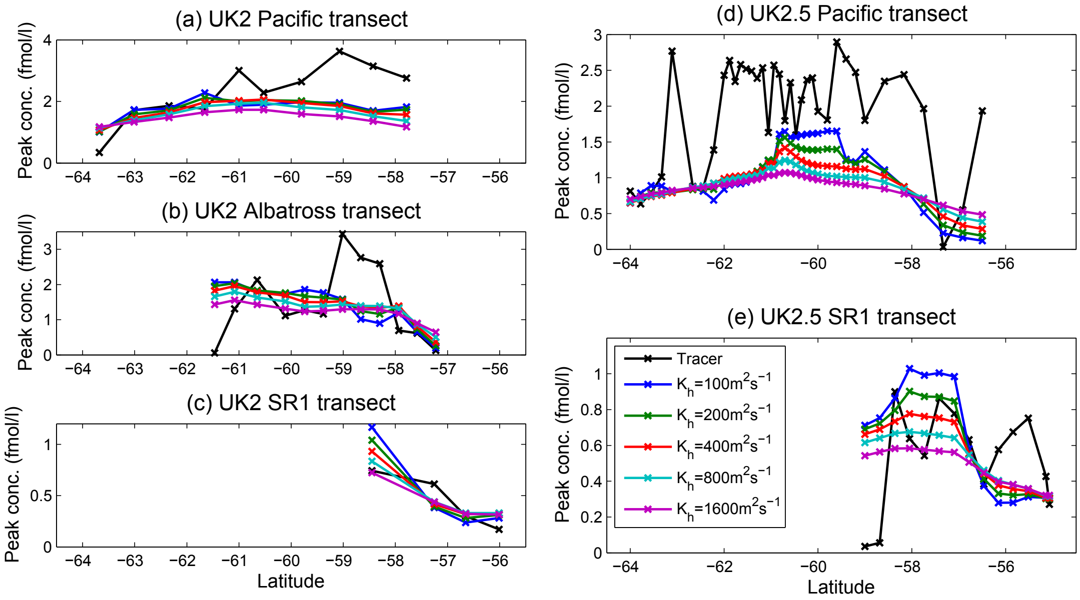

Figure 4.17: Peak concentrations from model output from US2 - UK2.5 runs with varying values of the isopycnal diffusivity K_h. Experimental tracer stations are shown by the black line and model outputs with varying K_h are in colour. The stations shown are from the Pacific (a), Albatross (b) and SR1 (c) transects on UK2, corresponding to the westernmost, central, and easternmost transects on figure 4.16 (a); and the Pacific (d) and SR1 (e) transects on UK2.5 corresponding to the westernmost and easternmost transects on figure 4.16 (b).

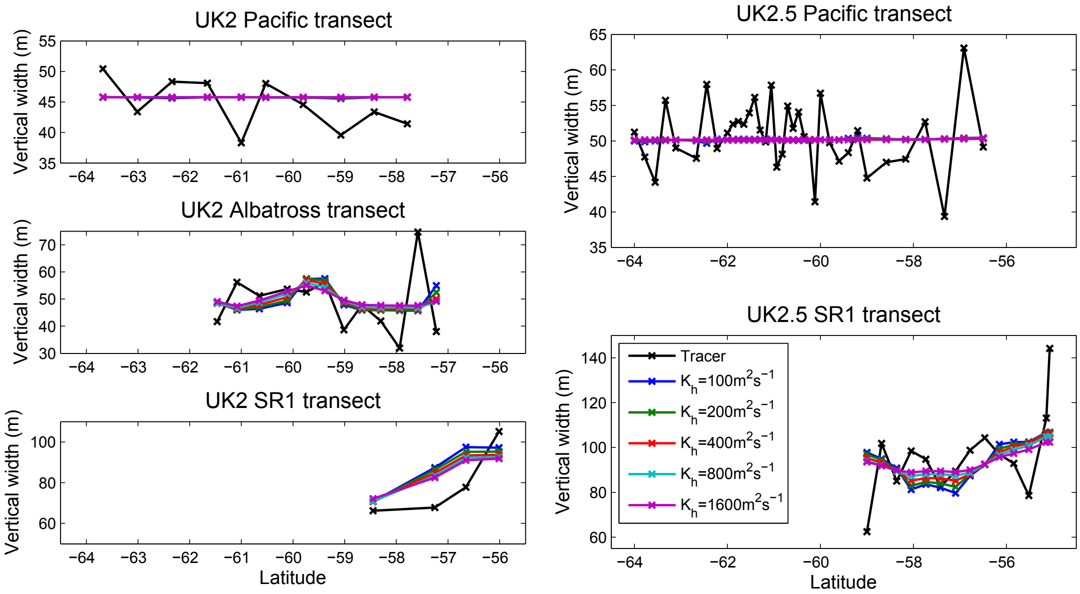

Figure 4.18: As figure 4.17 but for vertical widths.

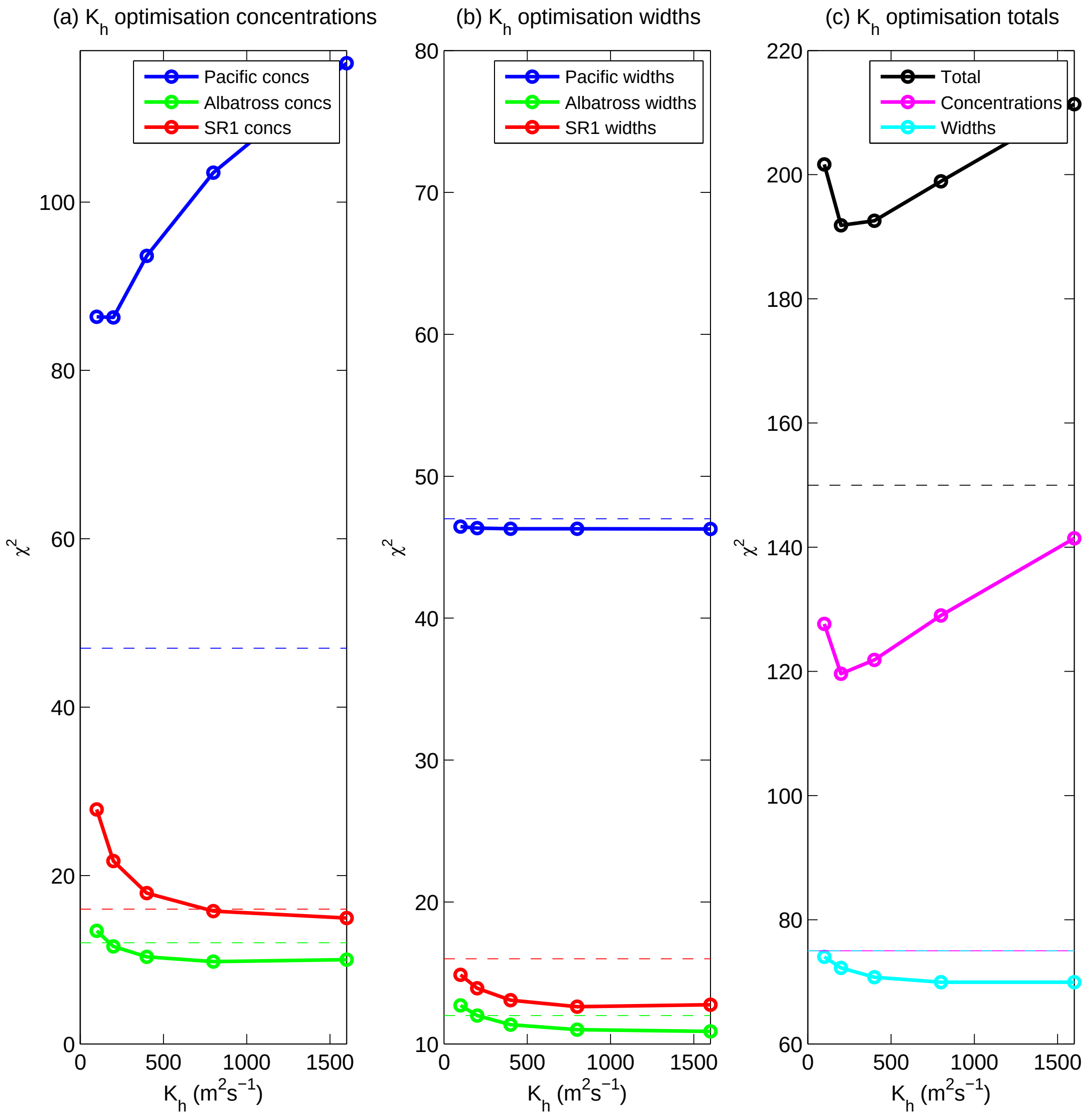

Figure 4.19: Contribution to the cost function for the runs with optimised K_z, variable K_h. On panel (a) are shown the contributions to the cost function from the peak concentrations on the Albatross transect (green), SR1 transect (red) and Pacific transect (blue). On panel (b) are the contributions from the vertical widths. On panel (c) are the contributions of the vertical widths (light blue), the peak concentrations (pink) and the total cost function (black). The dashed lines are the expectation value for each part of the cost function.

The contribution from the peak concentrations is in general above the expectation value because the main influence on the quality of the model-data fit is the SatGEM velocity fields, which are fixed. However, the contribution of the peak concentrations to the cost function is influenced to some degree by the diapycnal and isopycnal diffusivities. In the optimisation of K_h, changes in the overall cost function are dominated by the contribution from the peak concentrations on the Pacific transect (Fig 4.19 (a)), which rapidly increases for $K_h > 200$ m^2 s^{-1}. Referring back to figure 4.17, this increase results largely from

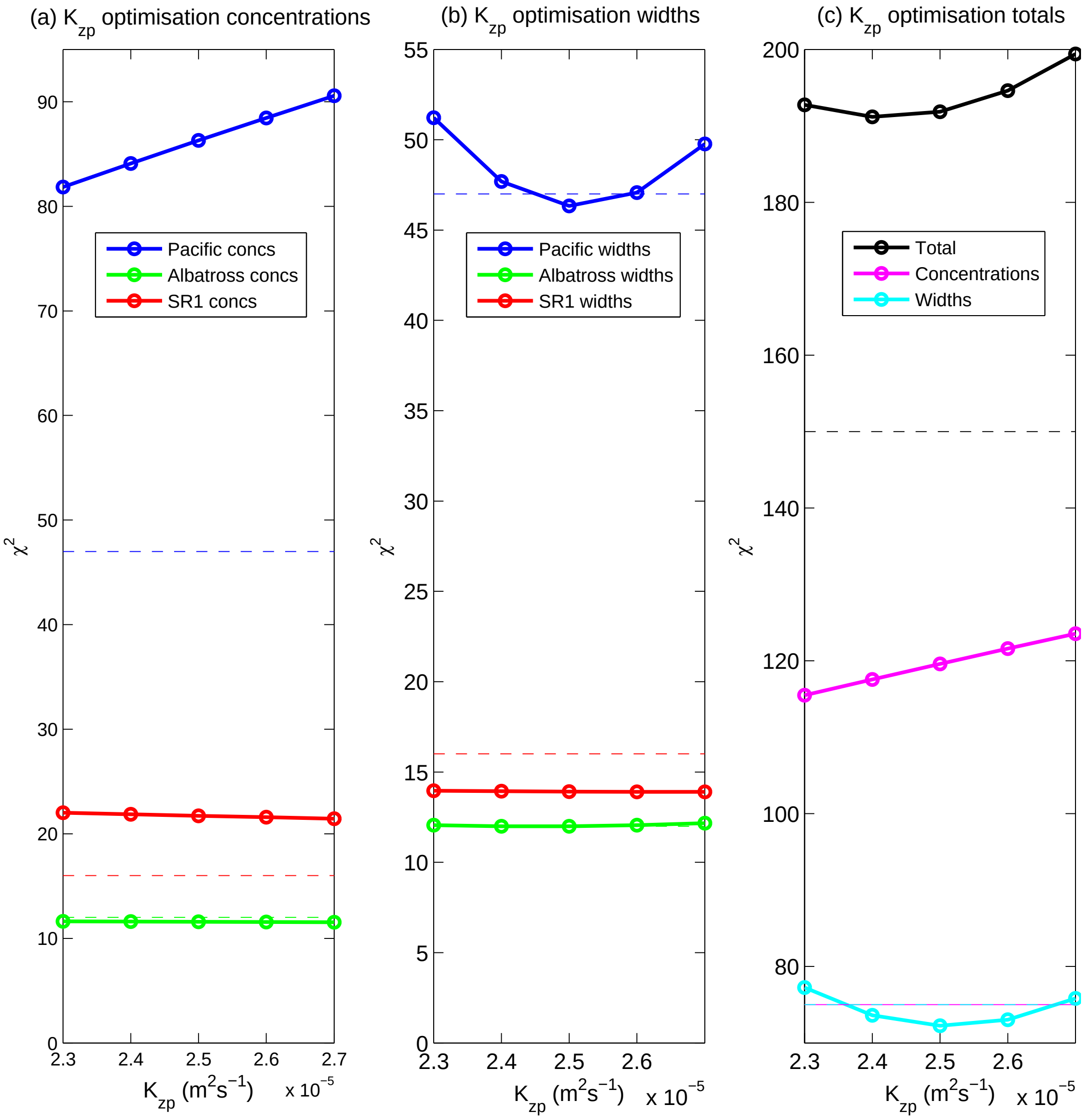

Figure 4.20: As figure 4.19 but for optimised K_h and K_{z_d}, variable K_{z_p}.

the comparison with UK2.5, where the already underestimated concentrations are reduced across the centre of the transect for increasing K_h. The contributions from the Albatross and SR1 sections improve slightly up to $K_h = 800 \text{ m}^2 \text{ s}^{-1}$. The optimum value of $K_h = 200 \text{ m}^2 \text{ s}^{-1}$ is used for subsequent model runs, but this value is only considered to be a guideline, with the true value probably lying between $200 \text{ m}^2 \text{ s}^{-1}$ and $800 \text{ m}^2 \text{ s}^{-1}$. For the optimisation of K_{z_p} (figure 4.20), the contribution of the vertical widths to the change in the cost function is dominated by the Pacific transect. The optimised value of $2.5 \times 10^{-5} \text{ m}^2 \text{ s}^{-1}$ gives a slightly better fit to the UK2.5 Pacific transect than the UK2 Pacific transect (see figure 4.23) due to the larger number of stations sampled on

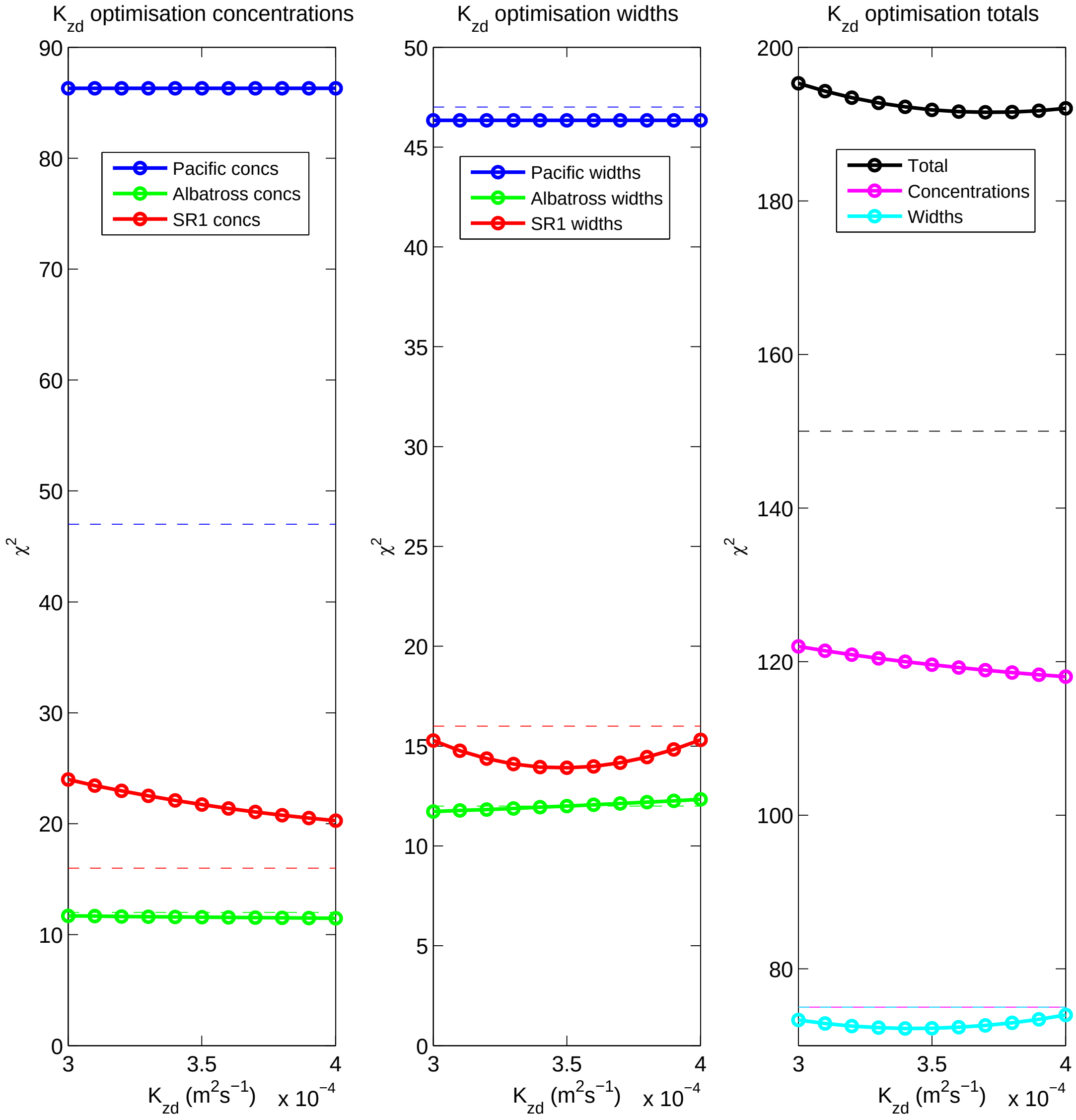

Figure 4.21: As figure 4.19 but for optimised K_h and K_{z_p}, variable K_{z_d}.

UK2.5 which means the UK2.5 transect contributes more to the cost function. The contribution from the peak concentrations on the Pacific transect increases with increasing K_{z_p} because the peak concentrations decrease as the profiles widen, exacerbating the underestimate of the concentrations here. The contribution of the Pacific widths to the cost function is taken to be the best indicator of the appropriate diffusivity, so the value of $K_{z_p} = 2.5 \times 10^{-5}$ m^2 s^{-1} is used for the Pacific zone for runs with fixed K_{z_p}. Assuming that an increase by 1 of the contribution to the cost function by the Pacific widths is associated with a 1σ departure of the value of K_{z_p} from its optimum, the uncertainty bounds indicated by this optimisation are $2.4 - 2.6 \times 10^{-5}$ m^2 s^{-1}. The fact that the value of K_{z_p} at the minimum is very close to the expectation value (the blue dashed line on figure

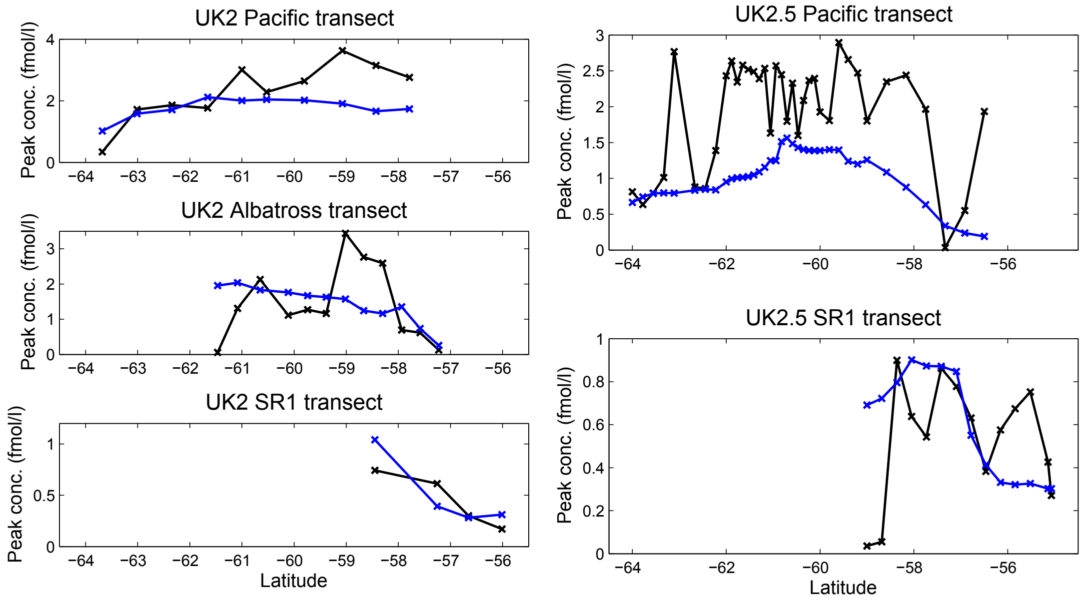

Figure 4.22: Peak concentrations for the fully optimised 2 zone model. The Pacific zone diapycnal diffusivity K_{z_p} is $2.5 \times 10^{-5}\ \mathrm{m}^2\ \mathrm{s}^{-1}$, the Drake Passage zone diapycnal diffusivity K_{z_d} is $3.5 \times 10^{-4}\ \mathrm{m}^2\ \mathrm{s}^{-1}$ and the isopycnal diffusivity K_h is $200\ \mathrm{m}^2\ \mathrm{s}^{-1}$. Experimental tracer results are in black, model output is in blue.

4.20 (b)) indicates that the use of the cost function here is appropriate.

The Drake Passage diffusivity indicated by the contribution to the cost function of the SR1 vertical widths is $3.5 \times 10^{-4}\ \mathrm{m}^2\ \mathrm{s}^{-1}$, with 1σ uncertainty bounds of $3.0 - 3.9 \times 10^{-4}\ \mathrm{m}^2\ \mathrm{s}^{-1}$. If the peak concentrations are taken into account, from which the contribution to the cost function decreases with increasing K_{z_d} over the optimal range indicated by the vertical widths, the optimised Drake Passage diffusivity increases slightly to $3.7 \times 10^{-4}\ \mathrm{m}^2\ \mathrm{s}^{-1}$. Both of these values agree within error with the values derived from the 2D model in Chapter 3. This optimisation for K_{z_d} was carried out with K_h set to the optimised value of $200\ \mathrm{m}^2\ \mathrm{s}^{-1}$. If a value of $400\ \mathrm{m}^2\ \mathrm{s}^{-1}$ is used, the optimised Drake Passage diapycnal diffusivity is still $3.5 \times 10^{-4}\ \mathrm{m}^2\ \mathrm{s}^{-1}$. The peak concentrations and vertical widths for the 2 zone model output with the optimised parameters of $K_{z_p} = 2.5 \times 10^{-5}\ \mathrm{m}^2\ \mathrm{s}^{-1}, K_{z_d} = 3.5 \times 10^{-4}\ \mathrm{m}^2\ \mathrm{s}^{-1}$ and $K_h = 200\ \mathrm{m}^2\ \mathrm{s}^{-1}$ compared with the tracer are shown on figure 4.22 and 4.23. The model has reproduced the average vertical widths fairly well on all transects, but fails to capture the large-scale meridional variation on all but the Albatross transect.

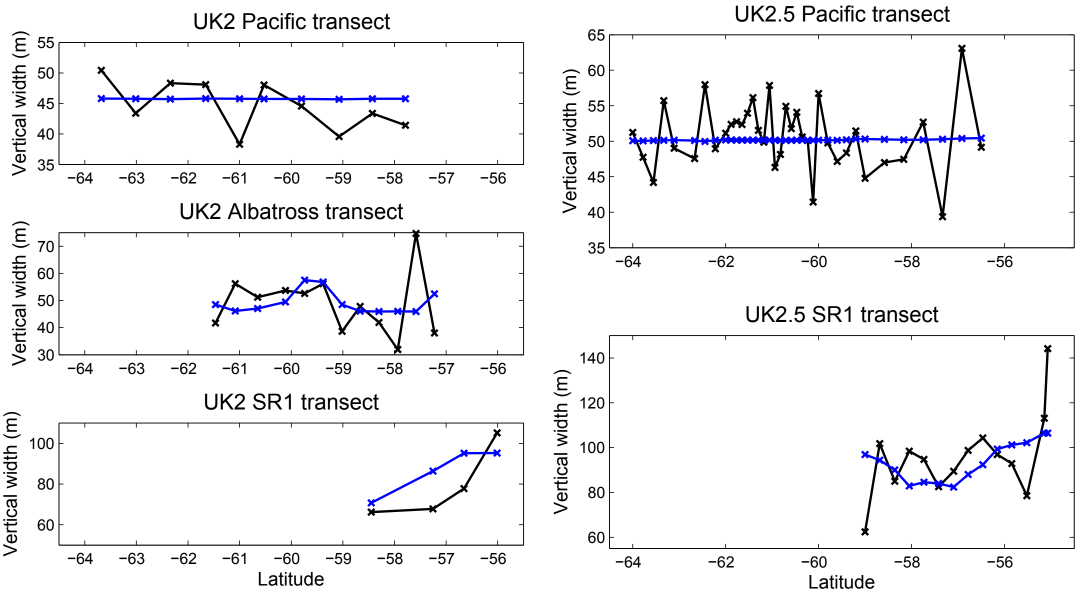

Figure 4.23: As figure 4.22 but for vertical widths

4.3.2.2 Effects of modifying the SatGEM velocity fields

The tracer distributions at the target density from a model run using the SatGEM velocities without having corrected them to render them divergence free are shown in figure 4.24. Compared with the distributions shown in figure 4.16 there are clear differences. The centre of mass of the tracer patch is slightly further south and east in the non-divergent run compared with the run using the uncorrected fields. It is difficult to say which is the more realistic version of the advection, since there are errors introduced in the velocity fields due to the non-divergence process, particularly around the limits of SatGEM to the north and south of Drake Passage, but equally there may be unwanted numerical effects in the model for the uncorrected velocities due to the divergence of the fields. However, examining the information we have about the tracer advection from the profile peak concentrations at the sampled stations, it can be seen from figure 4.25 that the uncorrected velocities do a slightly better job of the tracer advection. In particular the increase northward in the concentrations on the UK2 Pacific transect and the decrease in concentrations at the southern edge of the tracer patch observed on the Albatross transect are reproduced with the uncorrected velocities. The contribution to the cost function of the peak concentrations for the run using the uncorrected velocities was 88.6, which compares to 119.6 for the run using the non-divergent velocities. The non-divergence correction has therefore

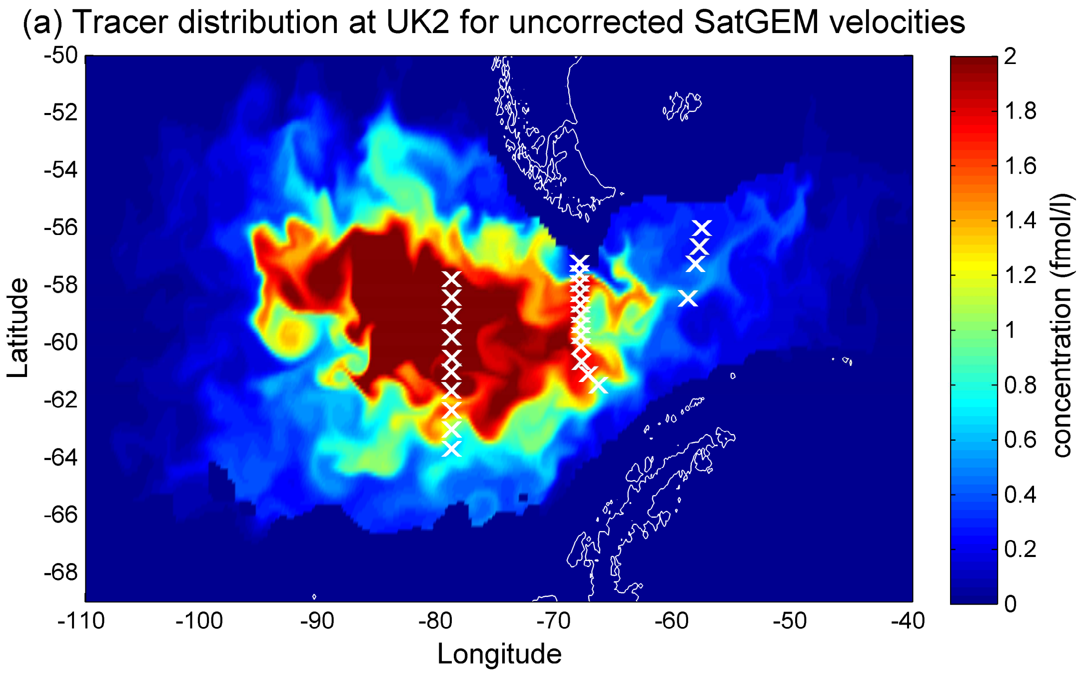

(a) Tracer distribution at UK2 for uncorrected SatGEM velocities

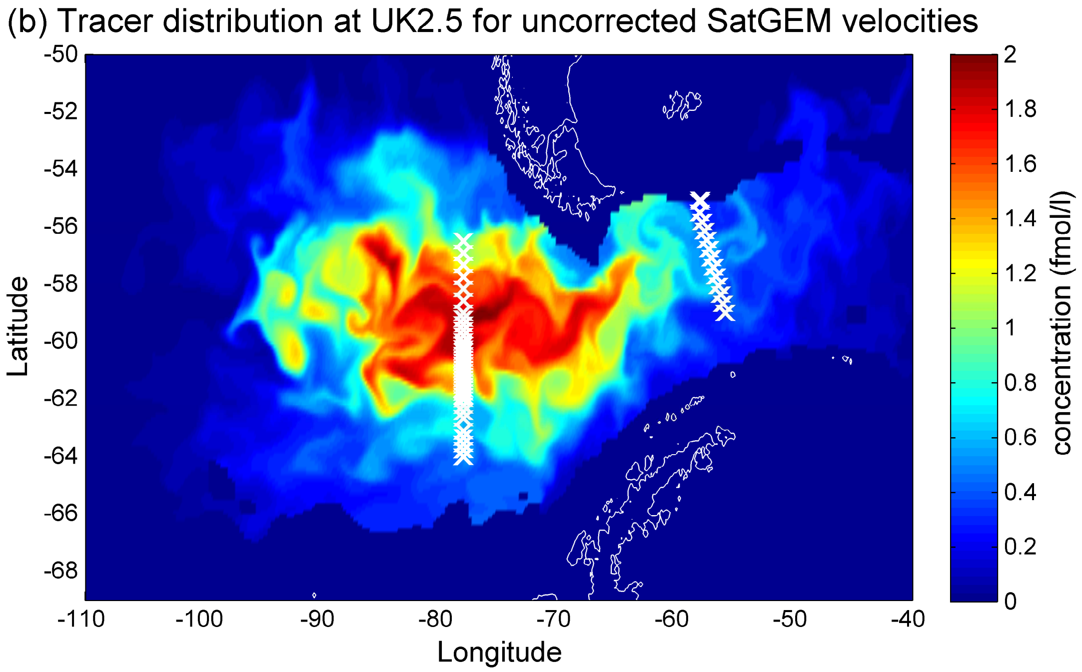

(b) Tracer distribution at UK2.5 for uncorrected SatGEM velocities

Figure 4.24: Distribution of tracer at the target depth at (a) UK2 and (b) UK2.5 for a model run using the SatGEM velocities not corrected for divergence. The tracer stations for each survey are overlayed (white crosses).

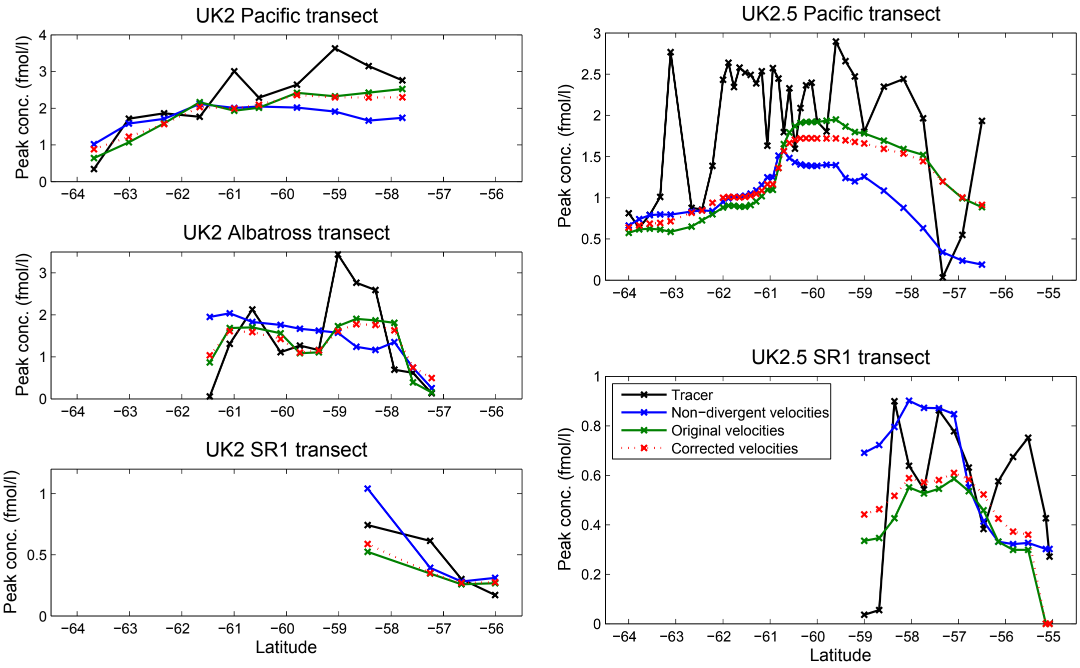

Figure 4.25: Peak concentrations at UK2 and UK2.5 for model runs using the SatGEM velocities before (green solid line) and after (blue solid line) they have been rendered non-divergent, and for a run where the velocities have been adjusted for thickness by subtracting the pseudo velocity in the second term in equation 4.6 (red dotted line). Experimental tracer peak concentrations are marked in black. The model parameters for the uncorrected and non-divergent runs were $K_{z_p} = 2.5 \times 10^{-5}$ m^2 s^{-1}, $K_{z_d} = 3.5 \times 10^{-4}$ m^2 s^{-1}, $K_h = 200$ m^2 s^{-1}, and for the thickness corrected run were $K_{z_p} = 2.5 \times 10^{-5}$ m^2 s^{-1}, $K_{z_d} = 3.5 \times 10^{-4}$ m^2 s^{-1}, $K_h = 400$ m^2 s^{-1}.

had a noticeable effect on the advection. Also on figure 4.25 are the results of a run which used the divergent SatGEM velocities, but with a correction factor applied to each u and v to account for the neglected pseudo velocity in equation 4.6. This has a smaller impact on the advection than the non-divergence correction, and results in a reduced contribution to the cost function from the peak concentrations of 85.0. Figure 4.26 compares the vertical widths from the same three runs. The difference between the divergent and non-divergent runs is considerably less obvious than it is for the peak concentrations, with only a slight increase in widths on the SR1 transect for the non-divergent velocities. This implies that the K_{z_d} optimised using the non-divergent velocities may be an underestimate, as a slight increase in diffusivity for the uncorrected run would bring the SR1 vertical widths closer to those of the tracer. Comparing with model outputs from the K_{z_d} optimisation, it is estimated this discrepancy amounts to no more than 0.5×10^{-4} m^2 s^{-1}, and is probably nearer 0.2×10^{-4} m^2 s^{-1}. Although optimisations have been carried out using the original and thickness-corrected velocities, it is not possible to make a direct comparison

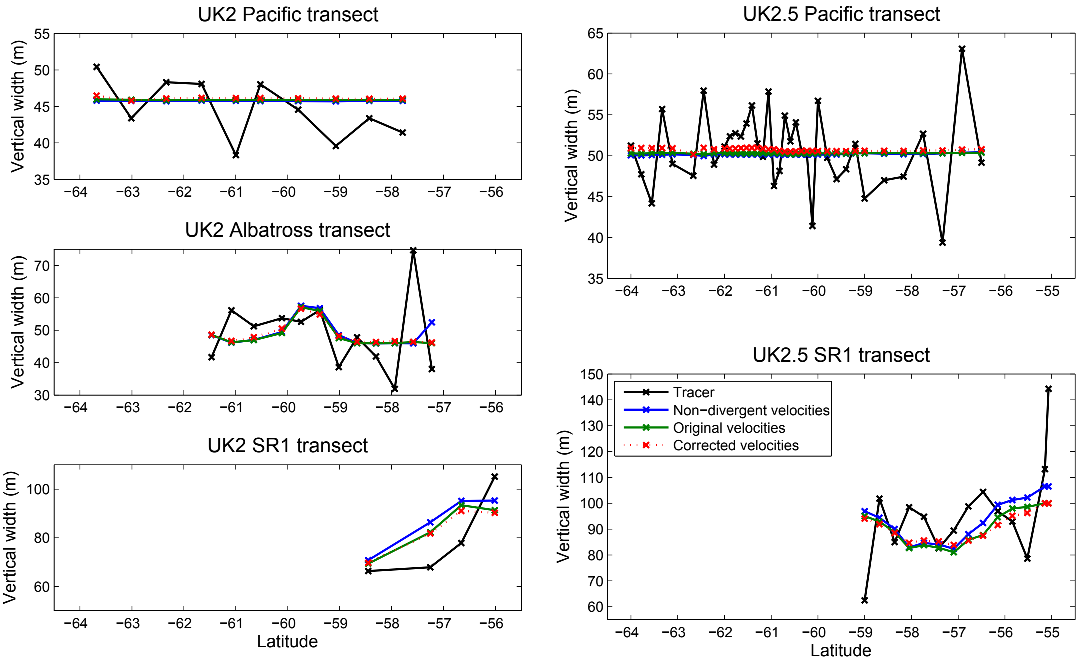

Figure 4.26: As figure 4.25 but for vertical widths.

between these and the non-divergent runs because the former do not include the two most northerly stations on SR1 in the cost function, these stations being beyond the limits of the original SatGEM fields. The optimised Drake Passage diffusivities both for runs using the original SatGEM fields and those with the thickness correction is $3.5 \times 10^{-4}\ \mathrm{m}^2\ \mathrm{s}^{-1}$. However this value would increase if it were possible to include the missing profiles since they are both very wide, the tracer sampled here most likely to have been affected by boundary mixing due to the proximity of the stations to the continental slope.

The difference in the tracer advection that results from the inclusion of the effects of thickness on the RHS of equation 4.1 is small, so its neglect seems reasonable. The difference introduced by the non-divergence correction is larger; however, the advantages it confers in terms of the internal consistency of the model, and the avoidance of the likelihood of any numerical issues, mean that the use of the corrected velocities seems justified. It is comforting to observe that their use had only a small impact on the key result from the 2 zone model, the inferred diapycnal diffusivity in Drake Passage. The improvement in the conservation of tracer that results from the use of the non-divergent velocity fields compared with the uncorrected ones can be seen in figure 4.27.

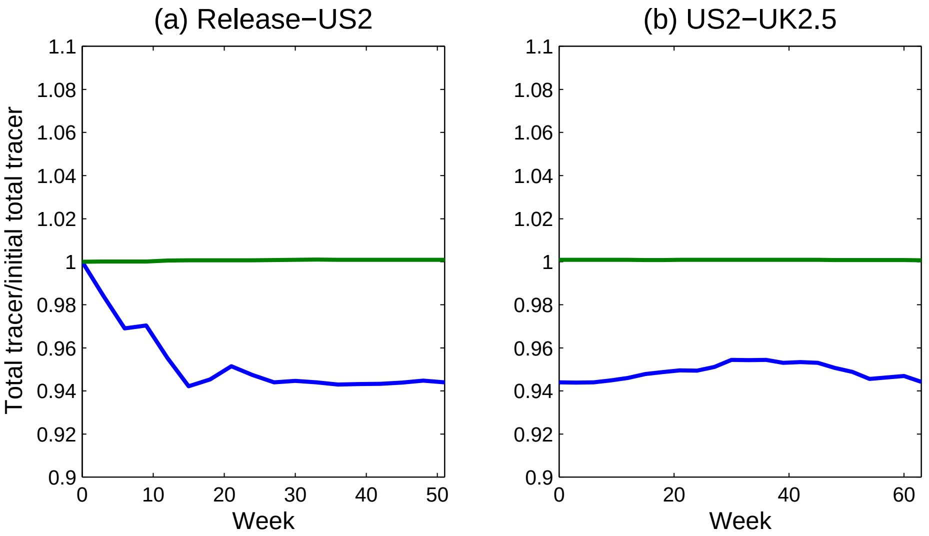

Figure 4.27: Conservation of tracer in the model for a run using the uncorrected SatGEM velocity fields (blue line) and one using fields that have been rendered non-divergent (green line). On panel (a) is a run from the tracer release-US2, and on panel (b) a subsequent run from US2 to UK2.5 using the output of the first run as the initial condition.

4.3.3 Enhanced K_z diffusivity fields

The peak concentrations and vertical widths for a number of model runs where K_z is enhanced near topography according to certain criteria are shown in figure 4.28 and 4.29. A number of combinations of the model parameters d, R and K_{z-top} as explained in section 4.2.7 have been experimented with, and a consistent pattern emerges (the $d-R$ parameter space has also been explored using a larger K_{z-top} of 1×10^{-3} m^2 s^{-1}, but these are not shown). For small d and small R, the profile widths at the Pacific transects are close to those seen in the experimental tracer, as for these runs the model tracer does not encounter any regions of enhanced diffusivity in the Pacific where the ocean is deep. However, the model profiles at SR1 are much narrower than the experimental ones, because the very small areas of enhanced diffusivity are not enough to account for the mixing experienced by the tracer in Drake Passage (see figure 4.9 for maps of enhanced K_z). As d and R are increased, mixing is enhanced over a wider area in Drake Passage, but the effect of this is only evident in the vertical widths of profiles on the northern half of SR1 on UK2.5, the profiles on the southern half of the transect remaining largely unaffected. Simultaneously, profiles are widening on the Albatross Pacific transects, first at the northern end, and, for the largest values of d and R, along their whole length. At the same time as there being a significant northern bias in the widening of the profiles on SR1 due to enhanced

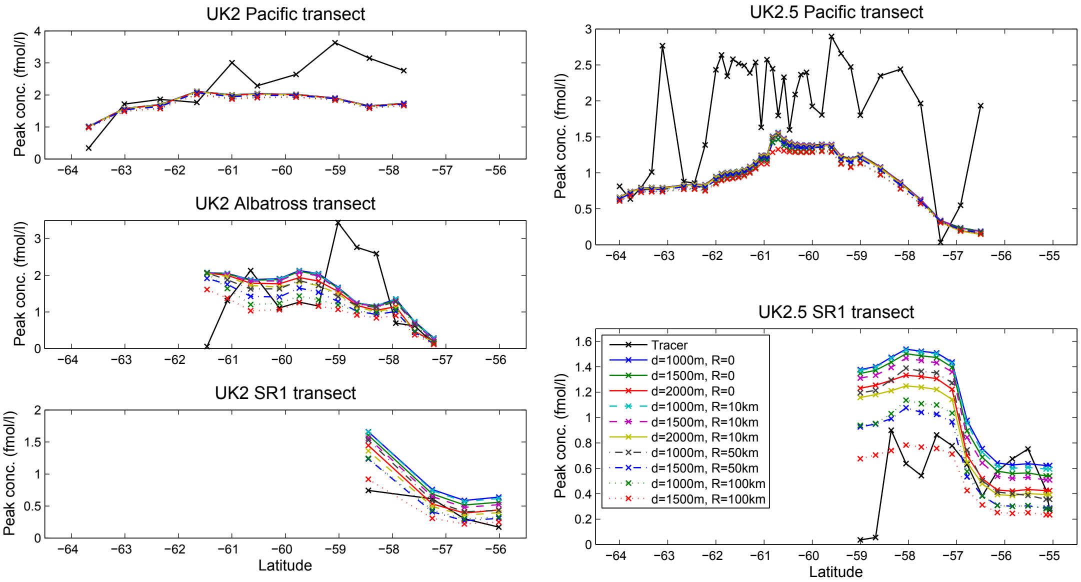

Figure 4.28: Peak concentrations for a selection of runs where K_z has been enhanced above background levels according to certain criteria. The background diffusivity is $2.5 \times 10^{-5}\ \mathrm{m}^2\ \mathrm{s}^{-1}$, and the enhanced diffusivity is $5 \times 10^{-4}\ \mathrm{m}^2\ \mathrm{s}^{-1}$. The areas of enhanced diffusivity are determined by a maximum distance above topography d, and a radius R as described in section 4.2.7 and illustrated in figure 4.9. The tracer peak concentrations are in black; model outputs from various runs are in colour.

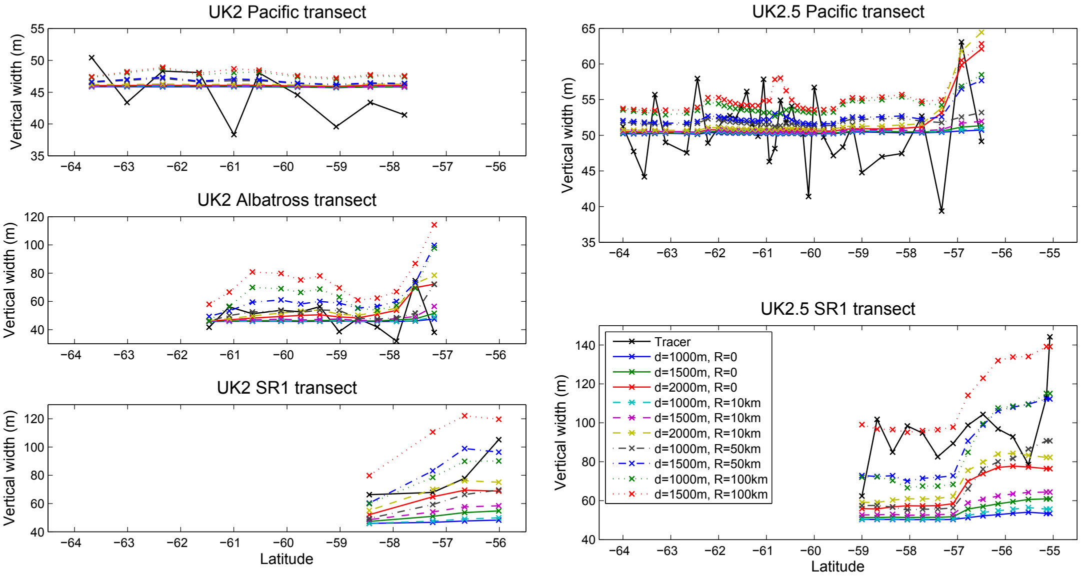

Figure 4.29: As figure 4.28 but for vertical widths.

K_z, the peak concentrations are much too high in the southern half of the transect where the vertical mixing has been underestimated. What seems to be suggested by the pattern of the experimental tracer profile widths on UK2.5 SR1 is that there is enhanced mixing throughout the meridional extent of the tracer patch in Drake Passage, with extremely high mixing on the continental slope as indicated by the two most northerly profiles. None of the combinations of d, R and the coefficient of vertical mixing in the enhanced regions K_{z-top} investigated have reproduced this pattern.

Figure 4.30 shows the cost functions for the model runs presented in figure 4.28 and 4.29. Where $d = 1000$ m, the cost function decreases for increasing R, as the increase in the areas of enhanced K_z causes the contribution from the SR1 transect to fall rapidly while the Pacific and Albatross contributions slowly increase. With $d = 2000$m, the cost functions increase rapidly for $R > 10$ km as an overestimate in the Pacific mixing results in a large contribution from the Pacific transect. The best overall fit is found where $K_{z-top} = 5 \times 10^{-4}$ m^2 $\mathrm{s}^{-1}, d = 1500$m, and $R = 50$km, however for this run the contribution from the widths on the Albatross transect is still some way above the expectation value. To try to reduce this effect, the background diffusivity was reduced to 2×10^{-5} m^2 s^{-1} for the runs presented in figure 4.31 and 4.32. Here a range of horizontal diffusion coefficients have been used to try to homogenise the effects of the bias towards higher mixing in the northern half of Drake Passage. A high value of K_h does have some effect in redistributing the vertical mixing from north to south, but the bias still remains, suggesting that to produce the pattern of wide profiles all the way along SR1, there need to be additional sources of enhanced mixing further south. The effect of varying K_h for these runs on the cost function is shown in figure 4.33. Increasing K_h improves the fit for all the vertical widths to the point where the Pacific and SR1 contributions are very near their expectations values, however the Albatross transect widths still make a large contribution due to the overestimate in the mixing to the west of the transect. The contribution of the peak concentrations increases with increasing K_h due to the comparison with the UK2.5 Pacific transect, giving an overall optimal value for K_h of 800 m^2 s^{-1}.

With some optimisation of the model parameters, it has been possible to reproduce some of the features of the mixing observed in the experimental tracer. However, by enhancing mixing by a uniform amount everywhere near topography, the wide profiles on the SR1

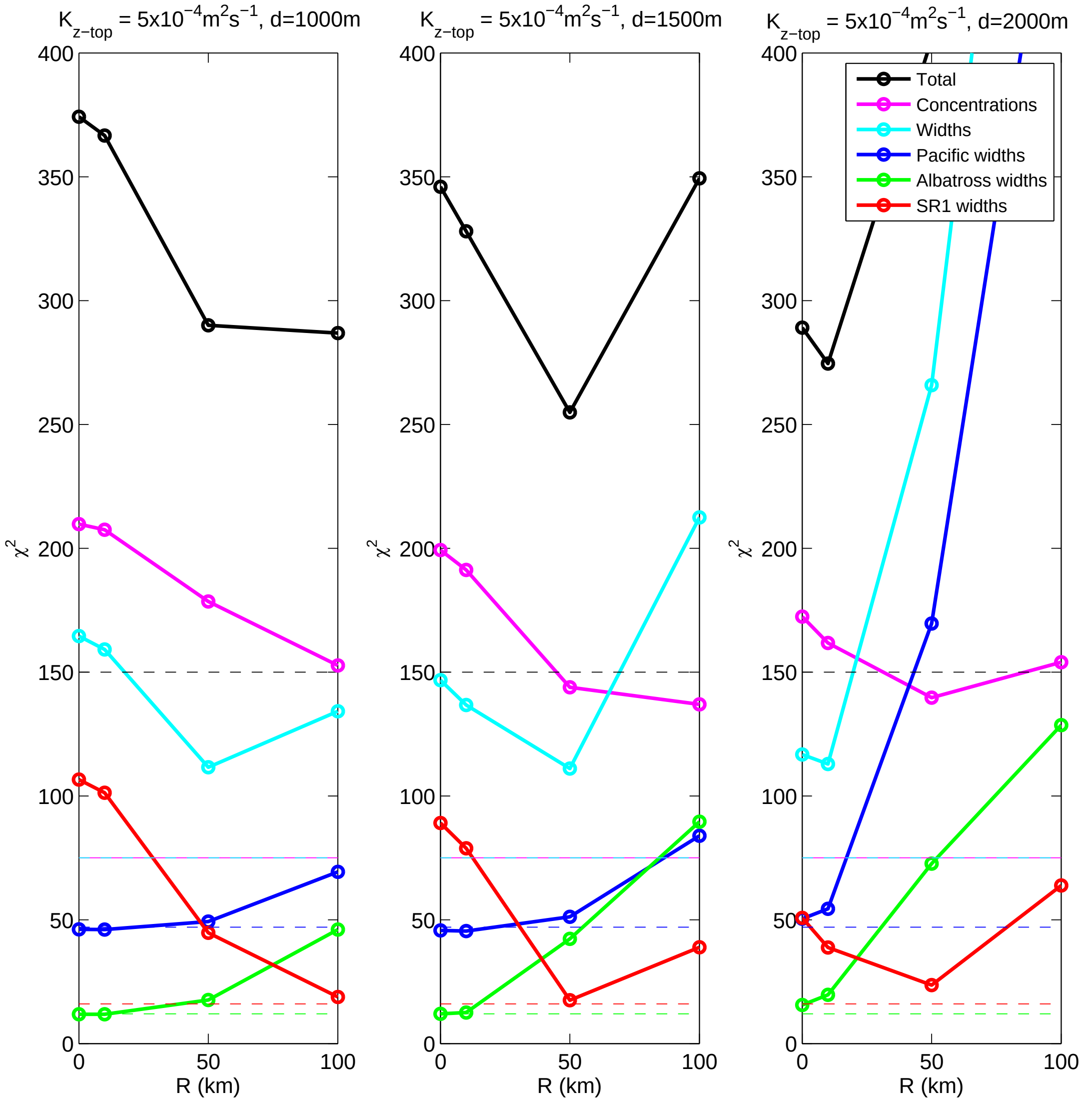

Figure 4.30: Contributions of different components to the cost function for model runs with K_z enhanced near topography at locations defined by d and R as described in section 4.2.7. The contributions from the Pacific transect widths (blue), Albatross transect widths (green), SR1 widths (red) all widths (light blue) all concentrations (pink) and the total cost function (black) are shown on all three panels. The background diffusivity is 2.5×10^{-5} m^2 s^{-1} and the enhanced diffusivity $K_{z-top} = 5 \times 10^{-4}$ m^2 s^{-1}.

transects have only been reproduced while overestimating the widths of the profiles on the Albatross transect. Observations have shown that the structure of bottom topography is important to mixing, rather than simply proximity to it (e.g. Polzin *et al.*, 1997), so it may be that smoother topography to the west of the Albatross line can explain the discrepancy. It has also been possible to reproduce the average mixing implied by the profile widths on SR1, but with a strong bias towards wider profiles in the northern half of the transect which is not observed in the experimental tracer. In addition, the only model runs which

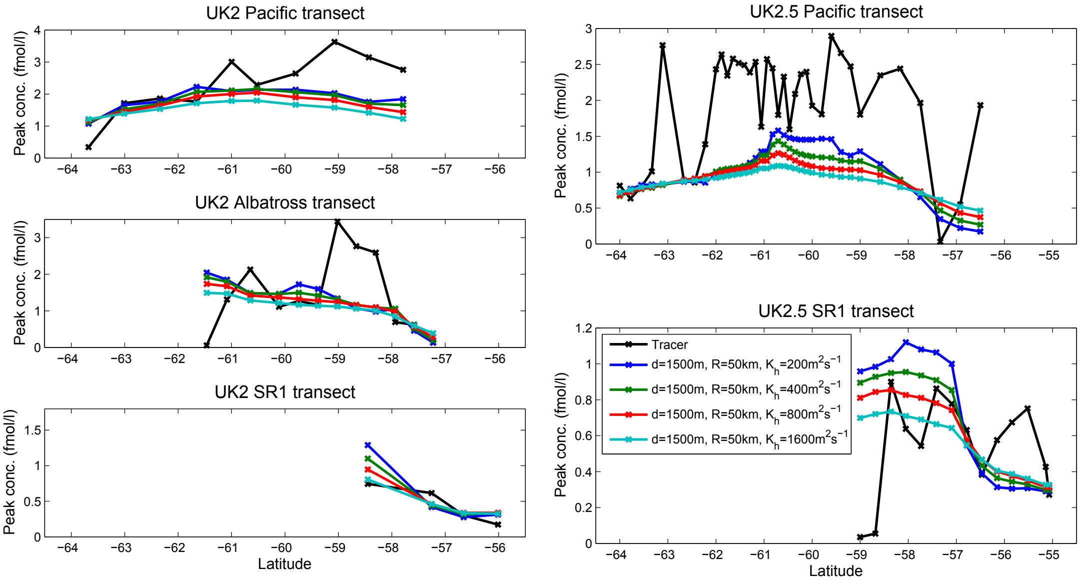

Figure 4.31: Peak concentrations for model outputs where K_z was enhanced near topography for $d = 1500\text{m}$, $R = 50\text{km}$ with varying K_h. The background diffusivity is $2 \times 10^{-5}\ \text{m}^2\ \text{s}^{-1}$, and the enhanced diffusivity $K_{z-top} = 5 \times 10^{-4}\ \text{m}^2\ \text{s}^{-1}$.

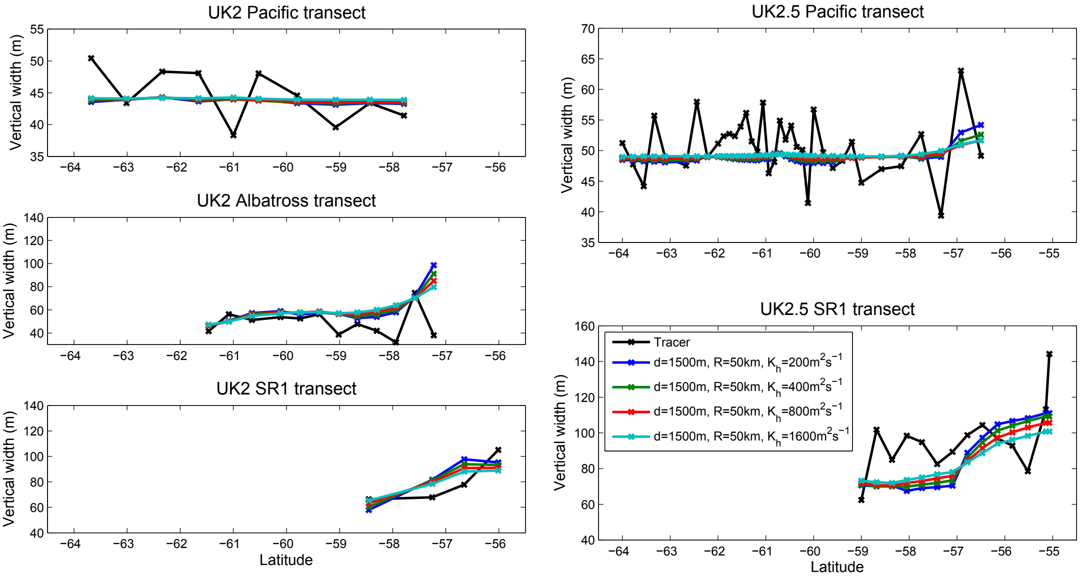

Figure 4.32: As figure 4.31 but for vertical widths.

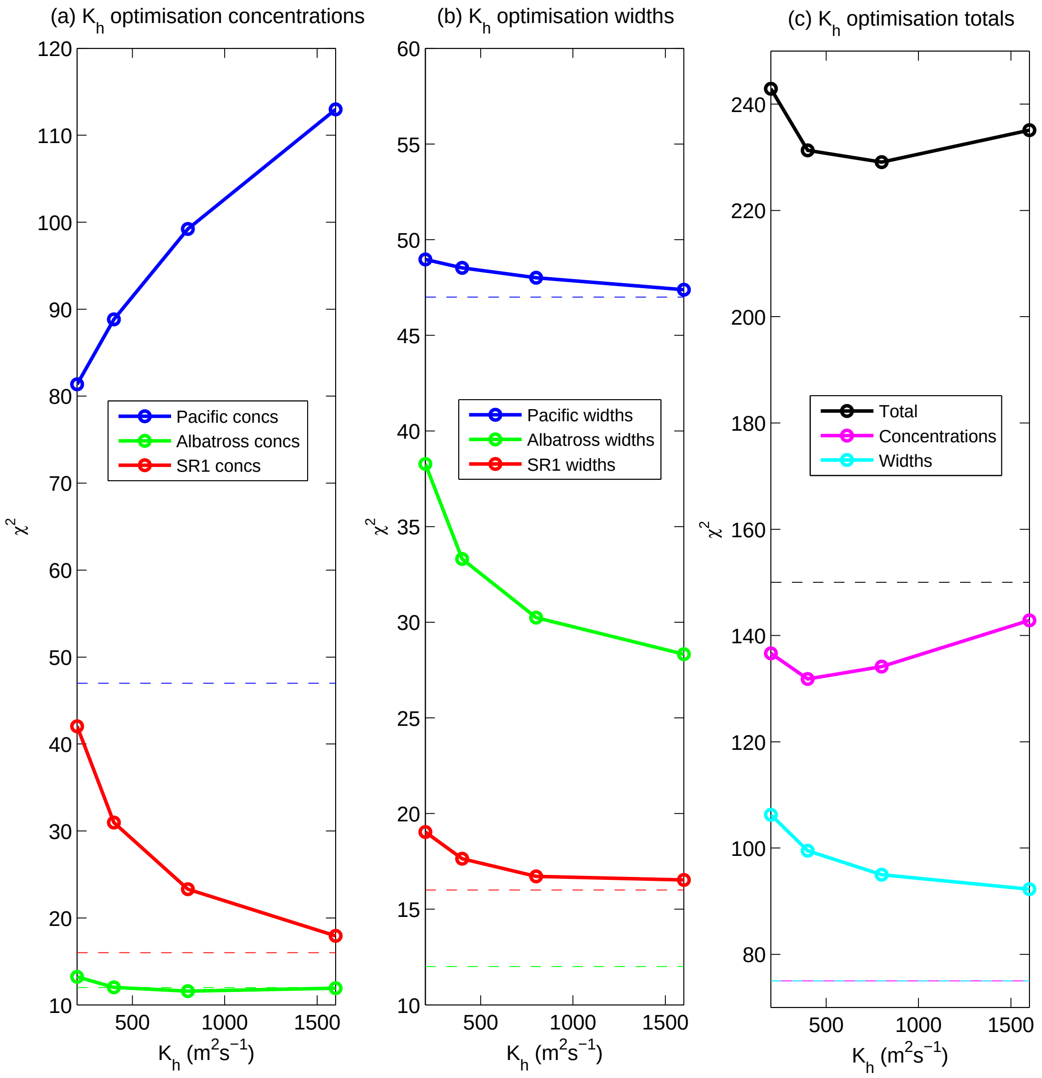

Figure 4.33: Contributions of different components to the cost function for model runs with K_z enhanced over topography for varying K_h. Diffusivity field parameters are $d = 1500$m, $R = 50$km, $K_{z-top} = 5 \times 10^{-4}$ m^2 s^{-1}, with a background K_z of 2×10^{-5} m^2 s^{-1}. On panel (a) are the contributions to the cost function from the peak concentrations on the Pacific (blue), Albatross (green) and SR1 (red) transects. On panel (b) are the contributions from the vertical widths on the same three transects. On panel (c) are the total contributions from the vertical widths (light blue), the peak concentrations (pink), and the total cost function (black).

had strong enough mixing in the south of Drake Passage to reproduce the wide profiles on the southern half of SR1 were those with $R = 50$ or 100 km. It may be that internal waves are able to translate energy from its source at rough topography to a remote site, however in the case of lee waves, which are believed to be the main source of enhanced mixing in this region of the Southern Ocean, they are expected to be locked to the topography from which they were generated. This raises a question as to what might be the source of energy for the mixing observed.

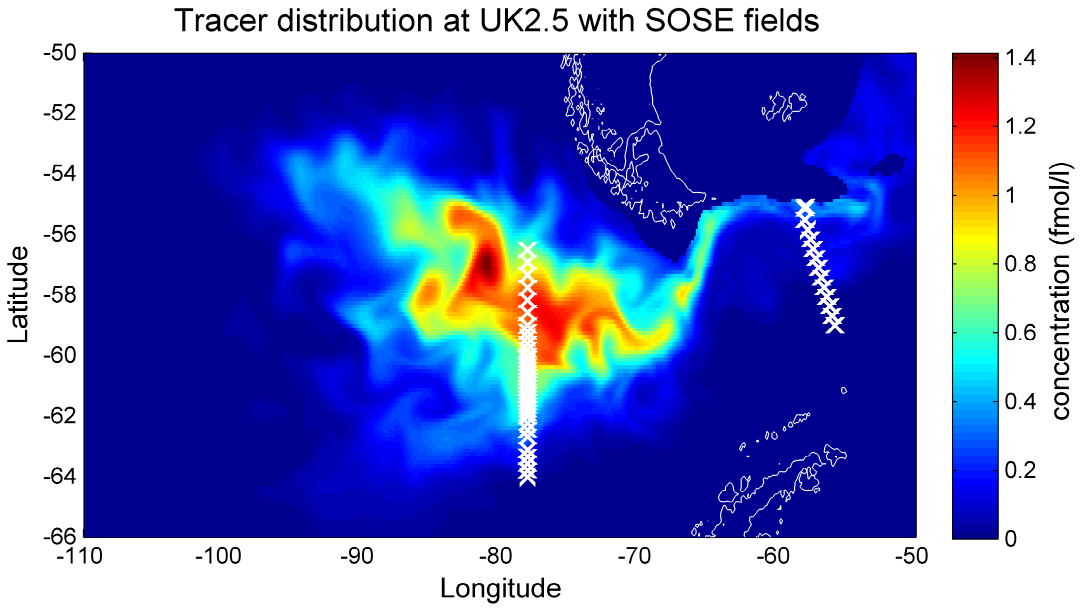

Figure 4.34: A map of tracer concentration at a depth of 1440m for model output at UK2.5 using the SOSE velocity fields. The UK2.5 tracer stations are overlayed (white crosses).

4.3.4 The Southern Ocean State Estimate

The Southern Ocean State Estimate (SOSE) is a three-dimensional time-evolving velocity field based on outputs from the MITgcm adjusted using data assimilation (see Mazloff *et al.*, 2010, for details). For comparison with the model outputs using SatGEM, the model was run using SOSE fields corresponding to the time period from January 2008 to April 2009, as the 2010-11 fields were not available. Since SOSE contains all three components of the 3D velocity u, v, w these were interpolated onto a vertical grid in depth coordinates with 20m between depth levels, and horizontally onto the same grid as was used for the SatGEM runs. Model depth levels therefore correspond to depth levels in the ocean, rather than isopycnals as for the SatGEM setup. The tracer concentrations from the output of a model run using the SOSE velocity fields are shown on figure 4.34. Compared with the SatGEM runs, the centre of mass of the tracer patch is further north and somewhat further west, and the leading edge has moved much more quickly through Drake Passage and is confined to a narrow jet. The isopycnal diffusion coefficient K_h for this run was 200 $\mathrm{m}^2\ \mathrm{s}^{-1}$. The model peak concentrations and vertical widths for the SOSE run compared with the tracer are shown on figure 4.35 and 4.36. The peak concentrations are a somewhat poorer fit to the data than is obtained from the SatGEM runs, with the model concentrations understimated nearly everywhere. The discrepancy is

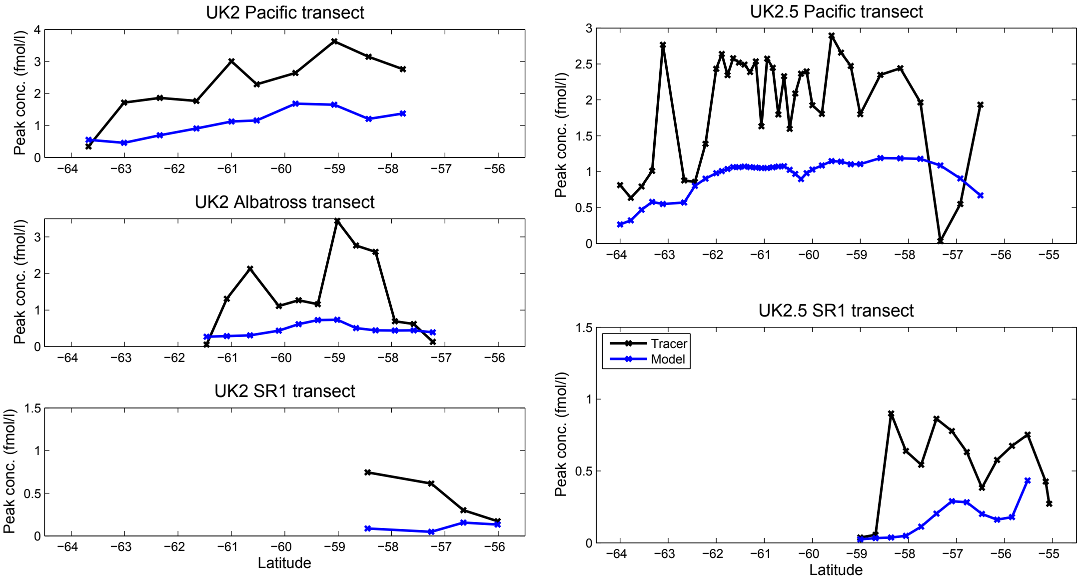

Figure 4.35: Peak concentrations for a model run using the SOSE velocity fields (blue) compared with the tracer (black).

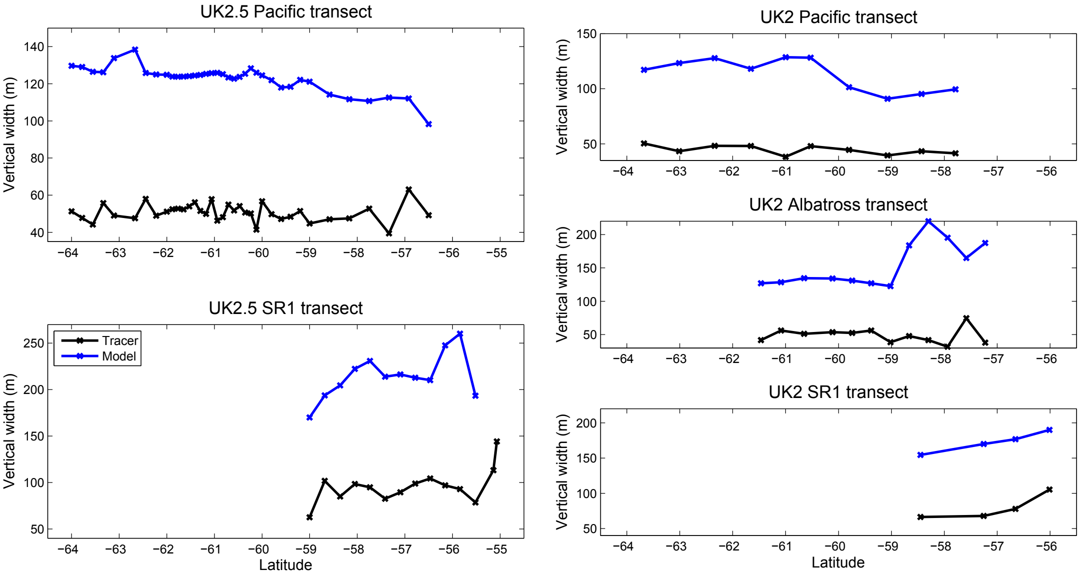

Figure 4.36: Vertical widths for a model run using the SOSE velocity fields (blue) compared with the tracer (black).

much worse when comparing the vertical widths, which are all far too wide. The diapycnal diffusion coefficient K_z was set to zero everywhere for this run, so the vertical spread in the tracer is due entirely to the action of the velocity fields. My interpretation is that the vertical resolution of the SOSE velocity fields is too low to allow for accurate enough representations of w to avoid spurious effects on the vertical tracer distribution. The approach using SatGEM and an isopycnal framework is therefore much better suited for the purposes of this work. It should be noted that the version of SOSE that was available when this test was carried out was not a final version for the time period corresponding to the fields, so a later iteration may give better results.

4.4 Discussion

4.4.1 Horizontal distribution of vertical mixing

Of the two types of three dimensional diapycnal diffusivity fields that were tested for how well they were able to reproduce the vertical distribution of the DIMES tracer as it was measured on the UK2 and UK2.5 cruises, the closest fit to the measured tracer distribution was found using the simple ‘2 zone’ model. Models of diffusivity based on the proximity of the tracer target surface to the bottom topography produced a poorer fit to the data in two main areas. Firstly, mixing was overpredicted in the region just to the west of the Albatross transect, leading to wider profiles in the model than were measured here. Secondly, all of the enhanced mixing regions identified in Drake Passage were in the northern half, leading to a strong bias towards wider profiles on the northen half of the SR1 transect in the model. This contrasts with the experimental tracer measured on UK2.5 where the profiles were wide along the full extent of the transect.

Table 4.1 and figure 4.37 compare the runs from each type of diffusivity field that give the best fit to the tracer. Neither model of diffusivity has been able to capture the meridional variability in the tracer profile widths on each transect. Although the 2 zone model vertical widths on the Albatross transect follow the general pattern of the tracer widths, this is simply an artifact of the location of the Albatross transect just to the west of the border between the low and high diffusivity zones. The 2 zone model does give a better fit than the Enhanced K_z model, however, on both the Albatross transect, where the latter

Table 4.1: Comparison of the model outputs from each type of diffusivity field that give the closest fit to the experimental tracer. In the 'Cost' column is the contribution to the cost function from the vertical widths, with the expectation value in brackets at the top. Columns 3-7 give the mean vertical widths of model outputs by transect (all quantities are in metres), with experimental tracer transect means in brackets at the top. Transects from left to right: UK2 SR1, UK2 Albatross, UK2 Pacific, UK2.5 Pacific, UK2.5 SR1.

Run	Cost	UK2 SR1	UK2 Alb	UK2 Pac	UK2.5 Pac	UK2.5 SR1
	(77)	(79.3)	(48.7)	(44.5)	(50.7)	(95.9)
2 zone	72.3	86.9	49.2	45.8	50.2	93.7
Enhanced K_z	95.0	81.2	59.5	43.8	49.1	85.5

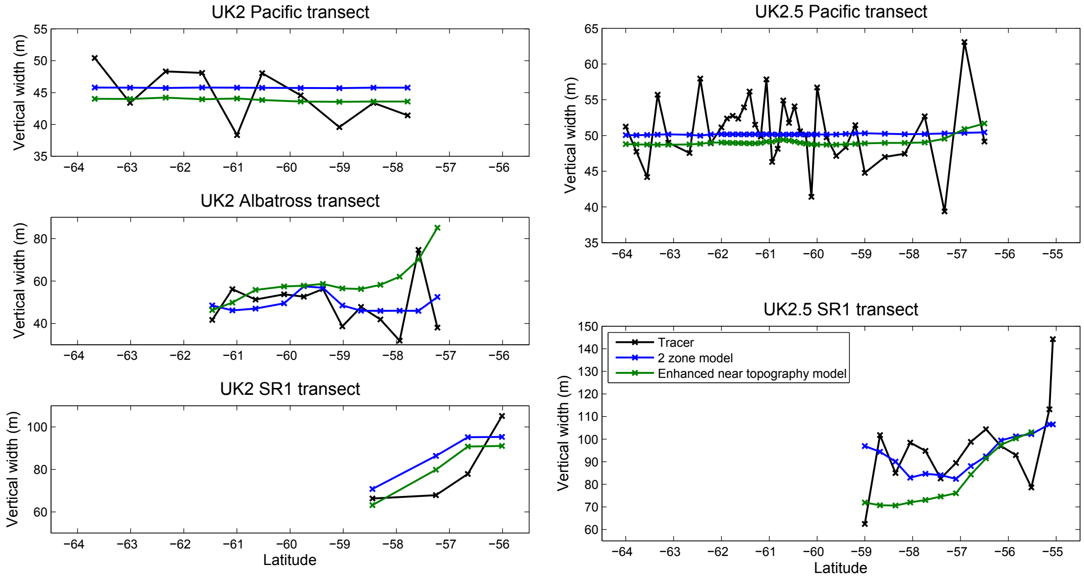

Figure 4.37: Vertical widths for runs that give the best fit to the tracer data. 2 zone run with $K_{z_p} = 2.5 \times 10^{-5}$ m^2 s^{-1}, $K_{z_d} = 3.5 \times 10^{-4}$ m^2 s^{-1}, $K_h = 200$ m^2 s^{-1} in blue; enhanced run with background $K_z = 2 \times 10^{-5}$ m^2 s^{-1}, $K_{z-top} = 5 \times 10^{-4}$ m^2 s^{-1}, $d = 1500$m, $R = 50$km, $K_h = 800$ m^2 s^{-1} in green; tracer in black.

has overestimated the mixing on the northern half, and on the UK2.5 SR1 transect, where only the 2 zone model has reproduced the wide profiles seen on all but the most southerly station in the experimental tracer.

The cost function has been used as a means of assessing the model-data fit, but the results must be interpreted in the context of the qualitative comparison. The 2 zone model gives a reasonable fit to the vertical widths on the UK2.5 SR1 transect, not because it has reproduced exactly the pattern of the meridional variation observed, but because the model has little inherent variation, so we do not see large discrepancies, for example, as might occur if a tracer profile which is above the transect average were to be compared with a model profile which is below it. However, the use of the cost function to arrive at an estimate for the area-averaged mixing in Drake Passage inferred from the tracer using the 2 zone model does seem appropriate, since varying the value of K_{z_d} only has the effect of shifting all the widths on the SR1 transect up or down, and does not affect the meridional distribution.

4.4.2 Magnitude of mixing

In the Pacific, the optimisations carried out using the 2 zone model yielded estimates for diapycnal diffusivity of $1.0 \pm 0.1 \times 10^{-5}\ \mathrm{m}^2\ \mathrm{s}^{-1}$ for the period from release to US2, and of $2.5 \pm 0.1 \times 10^{-5}\ \mathrm{m}^2\ \mathrm{s}^{-1}$ for US2 to UK2.5. The first value agrees within error with the value of $1.3 \pm 0.2 \times 10^{-5}\ \mathrm{m}^2\ \mathrm{s}^{-1}$ obtained by Ledwell *et al.* (2011) for the same period using a 1D model. The second value is slightly larger than the value obtained in Chapter 3. This can be explained by the fact that whereas the 3D model was run from release to US2 and one value of the Pacific diffusivity optimised to fit the US2 data, then a separate run and a separate diffusivity obtained for the runs from US2 to UK2.5, the 2D model was run from release to UK2.5 with no intermediate optimisation at US2. The Pacific result from the 2D model therefore represents an average for the mixing between release and UK2.5, whereas the 3D model is optimised for the US2-UK2.5 time period. The increase in K_z in the Pacific region between year 1 and year 2 of the tracer experiment may be due to the tracer having moved eastwards into a slightly more energetic region, or it may be that year 2 was a more energetic period of time in terms of mixing. Since the internal wave energy in the Pacific has been found to be predominantly downward propagating (Sheen *et al.*, 2013), temporal variation in mixing in the region on these timescales due to atmosphere-ocean interactions seems plausible.

The optimised diapycnal diffusivity in Drake Passage was $3.5 \pm 0.5 \times 10^{-4}\ \mathrm{m}^2\ \mathrm{s}^{-1}$, a 14-fold increase on the value in the Pacific. This represents an estimate for the time- and spatially-averaged mixing over an area between 67°W and 57°W in the zonal direction, and approximately 56°S to 62°S meridionally. This result, which is three times larger than the global average predicted by Munk to be needed to close the global overturning circulation, confirms the belief that mixing in Drake Passage plays an important role in the MOC. As outlined in Chapter 1, the main driver for this mixing is likely to be lee waves generated by the deep reaching currents of the ACC flowing over rough bottom topography. However, numerical modelling work such as that by Nikurashin and Ferrari (2010b) suggests that lee waves are responsible for enhanced mixing mainly in the bottom 1km above the bottom topography. The attempt in this chapter to model mixing as being enhanced only in regions where the target isopycnal comes within a certain distance above the bottom found that $d = 1000\mathrm{m}$ did not identify enhanced mixing over nearly a wide enough area to account for the average mixing implied by the tracer measurements, even if the diffusivity in these regions was as large as $1 \times 10^{-3}\ \mathrm{m}^2\ \mathrm{s}^{-1}$. With d allowed to increase to 1500m, it was still necessary to assume a large horizontal radius of influence for the internal waves generated at topography in order for the model to come close to an estimate for the mixing in Drake Passage that was consistent with the tracer measurements.

4.4.3 Neglected effects of thickness

In section 4.3.2.2, an estimate of the likely impact on the tracer advection of the neglected pseudo velocity on the RHS of equation 4.1 was made, and found to be small. The other missing pseudo velocity, the second term on the RHS of equation 4.5, is not possible to calculate directly from the available information. However, an estimate of its effect may be made from what is already known about the large-scale circulation. As was explained in section 1.2.5, the meridional transport in the Southern Ocean occurs due to the action of eddies. Since eddies are circulatory by their nature, the only way that they can effect a net transport is through changes in the thicknesses of isopycnal layers. Therefore by assuming that the meridional overturning is achieved through the ‘thickness flux’, which we have neglected, it is possible approximately to quantify its effect as follows: the circumpolar MOC, estimated at $62°$S to be 12.5 Sv (Lumpkin and Speer, 2007), distributed over a 2000 m thick layer around the whole of the ACC gives a velocity of $0.0003\mathrm{ms}^{-1}$. Over the 2.2 years from the tracer release to UK2.5, this amounts to 21km, or $0.2°$ of meridional displacement. What is important to the estimate of diapycnal diffusivity is that the transit time distribution of the tracer - the time it takes for the tracer to arrive at a particular time and place where we sample it and compare it with the model - is approximately correct. Since the tracer measurements are along transects designed to intersect the ACC, the transit time of the tracer in between these transects is governed by the ACC transport,

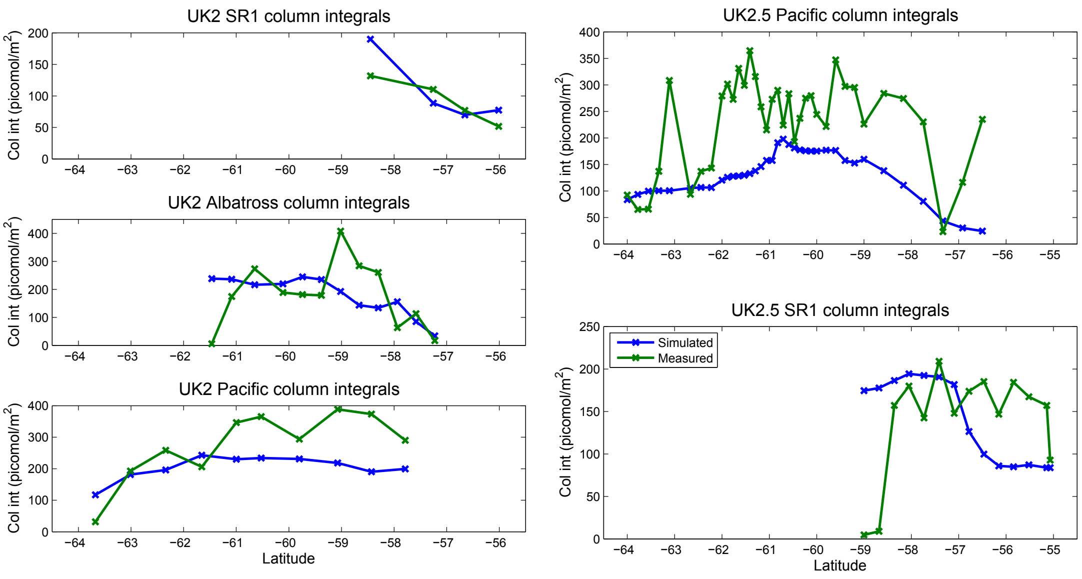

Figure 4.38: Column integrals for the model (blue) compared with the experimental tracer (green).

which at 137 Sv is an order of magnitude larger than the strength of the MOC here. The zonal displacement of the centre of mass of the model tracer patch from release to UK2.5 is 40°. Therefore if the thickness flux in the zonal direction is assumed comparable to the meridional component, then its contribution to the tracer transport is negligible in comparison to the ACC contribution. In addition, comparing the column integrals of model and observed tracer at the UK2 and UK2.5 stations gives further evidence for the fact that the zonal tracer distribution has been reproduced reasonably well as was suggested by the comparisons with the peak concentrations (see figure 4.38).

4.5 Summary

In this chapter, the evolution of the DIMES tracer was simulated using a 3D model which combines 3D time-evolving geostrophic velocities from the SatGEM product and prescribed isopycnal and diapycnal diffusivities to solve the advection diffusion equation for the tracer. The parameters in a simple 2-zone model of diapycnal diffusivity with one value west of 67°W and a different value east of that longitude were optimised using a cost function to give the best fit to the tracer data, yielding values of $K_{z_p} = 2.5 \times 10^{-5}\ \mathrm{m}^2\ \mathrm{s}^{-1}$ and $K_{z_d} = 3.5 \times 10^{-4}\ \mathrm{m}^2\ \mathrm{s}^{-1}$ for the Pacific and Drake Passage zones, respectively. The Drake Passage value is in agreement with the value previously calculated in Chapter 3 using a 2D model, and the Pacific value is slightly higher. A more complex model for the diapycnal diffusivity which defined areas of enhanced mixing based on the proximity of the tracer target isopycnal to the bottom topography was able to predict the enhancement of mixing in Drake Passage compared with the Southeast Pacific, but only while overpredicting the widths of profiles on the Albatross transect, and failing to predict the wide profiles along almost the full meridional extent of the SR1 transect measured on UK2.5. The latter pattern was reproduced by the 2 zone model, meaning that it gave the best overall fit to the tracer as measured by the cost function. The model for enhanced mixing over topography was also only able to predict the quantity of mixing observed in Drake Passage by extending the range of influence of topography beyond what would be predicted by current theories of lee wave generation.

The models presented use fairly crude criteria for identifying regions of enhanced mixing. In particular, neither implementation has any depth dependence for diapycnal mixing rates, therefore they do not properly take account of the sources of energy for the mixing, since dissipation rates will tend to decay with distance away from sites of internal wave generation. Secondly, the enhanced K_z model does not take account of the fact that the structure of bottom topography, or bottom 'roughness' is important to predicting enhanced mixing, nor the role of the speed of the currents whose interactions with the bottom topography produce the internal waves that drive the mixing. A more empirical approach, which makes use first of dissipation data gathered using microstructure profilers on several of the DIMES cruises, and then of predictions for rates of lee wave generation in the Southern Ocean, is the subject of Chapter 5.

Chapter 5

Semiempirical models of diffusivity

5.1 Introduction

5.1.1 Chapter motivation and outline

In Chapter 4 a 3D model was introduced with the capability for defining a three dimensionally varying diapycnal diffusivity field. Some simple models of the diffusivity for the Southeast Pacific and Drake Passage regions of the Southern Ocean were tested for their ability to reproduce the magnitude and spatial variabilty of the diapycnal mixing undergone by the DIMES tracer during the first 2 years of the experiment. However these models are simplistic, since they do not take into account the depth dependence of mixing, and only a crude attempt has been made to reproduce the horizontal variability, with factors such as bottom roughness and bottom current speed not taken into account. In this chapter the 3D model framework is used to test some diapycnal diffusivity fields that have been based on empirical data from microstructure collected as part of the DIMES project. Historically when microstructure measurements have been employed alongside a tracer in ocean mixing experiments, the two methods have agreed within a factor of two in regions of homogeneous mixing (e.g. Ledwell *et al.*, 1998, 2011), but less well in heterogeneous regions (e.g. Ledwell *et al.*, 2000). The first objective of this chapter is to ascertain whether the instantaneous, localised measurements of dissipation made from microstructure in the DIMES experiment are consistent with the temporally and spatially integrated mixing observed by the tracer in Drake Passage, where we expect to see vigorous and inhomogeneous mixing. The microstructure data are subsequently combined with a model of rates of lee wave generation for the Southern Ocean to produce and test a diapycnal diffusivity field based on the factors that are expected to determine mixing rates, principally bottom roughness, bottom current speed, and proximity to topography. The remainder of this section will provide some background theory to the models of diffusivity used in this chapter. Section 2 will give an overview of the DIMES microstructure data to be used in the models presented, followed by descriptions of the methods used to construct the microstructure based and lee wave based diffusivity fields. In section 3 the results of model simulations using the two types of diffusivity field will be presented and compared, and section 4 will discuss the implications of the study for our understanding of diapycnal mixing in the Southern Ocean. The chapter contains sections of work that are under review for publication in the Journal of Physical Oceanography, and contributions from co-authors are credited as appropriate.

5.1.2 Mixing from microstructure

The microstructure data used in this chapter were gathered using a Vertical Microstructure Profiler (VMP) and a High Resolution Profiler (HRP), and full details of the methods used may be found in Sheen *et al.* (2013) and St. Laurent *et al.* (2012). The profilers are free-falling devices which measure vertical velocity shear variance on centimetre scales, and from which the dissipation rate of turbulent energy ϵ may be obtained using the following equation (Oakey, 1982, introduced in Chapter 1):

$$\epsilon = \frac{15}{2}\nu\overline{\left(\frac{\partial u}{\partial z}\right)^2}. \tag{5.1}$$

The expression $\overline{\left(\frac{\partial u}{\partial z}\right)^2}$ is the shear variance, and ν is the molecular viscosity. The evidence from microstructure surveys (previously detailed in section 1.4.4) is that dissipation is enhanced near the bottom over rough topography, in particular where bottom flows are strong (e.g. Polzin *et al.*, 1997; Waterman *et al.*, 2013; St. Laurent *et al.*, 2012; Sheen *et al.*, 2013). Height above the bottom is chosen as the vertical coordinate with which to index the DIMES microstructure data for use in the models of diffusivity constructed in this chapter (see section 5.2.1.1).

Finestructure data from a CTD and LADCP were gathered concurrently with the microstructure measurements, and these data are used to determine the ratio of counter-clockwise polarised shear variance (CCW) to clockwise polarised shear variance (CW), giving the polarisation ratio $R_{pol} = CCW/CW$. This polarisation ratio may then be used to determine whether the direction of propagation of the internal wave energy is predominantly upward or downward, since in the Southern Hemisphere a predominance of downward propagating energy is associated with a dominance of counter-clockwise shear variance, i.e. $R_{pol} > 1$ (Gonella, 1972). This information allows the source of energy driving the mixing to be inferred, by assuming that upward propagating energy must have been generated on the ocean floor, e.g. as lee waves or internal tides due to the interactions of bottom currents with topography, and that downward propagating energy must have been generated at the surface, e.g. as inertial waves due to interactions with the atmosphere.

5.1.3 A model of lee wave generation

Nikurashin and Ferrari (2010a,b) developed a model for the rate of generation of lee waves by geostrophic flows over bottom topography, which they then apply to the whole ocean (Nikurashin and Ferrari, 2011) to produce estimates of the lee wave fluxes (their model is hereafter referred by the abbreviation 'NF'). Using a model for the spectrum of the bottom topography from Goff and Jordan (1988), they fit observations from ship soundings, which resolve the structure of the bottom topography on scales of a few km, to the topographic spectrum:

$$P_{1\mathrm{D}}(k) = \overline{h^2}{\kappa_0}^{\mu-2}(\mu-2)B\left[\frac{1}{2}, \frac{(\mu-1)}{2}\right] \times ({\kappa_0}^2 + k^2)^{-(\mu-1)/2}, \tag{5.2}$$

where k is a wavenumber representing the periodicity of topography, h is a topographic height, κ_0 is a characteristic horizontal wavenumber for the topography, assuming horizontal isotropy, μ is the slope of the spectrum at higher wavenumbers, and B is the beta function. The parameters h, κ_0, and μ are optimised so that the spectrum $P_{1\mathrm{D}}(k)$ gives the best fit to the available topographic data. Based on Bell (1975), they then define the rate of lee wave energy generation as:

$$E = \frac{1}{\pi}\rho_0 P_0 N |U_0|^2 \frac{|U_0|^{1/2}}{|f|^{1/2}} \left[\frac{9}{5} - \frac{7}{3}\sqrt{\frac{|f|}{N}} + O\left(\frac{f^2}{N^2}\right) \right], \tag{5.3}$$

where ρ_0 is a reference density, N is the bottom stratification, U_0 is the bottom velocity, f is the Coriolis frequency (assummed $<< N$), and P_0 represents the topographic spectrum. P_0 is given by:

$$P_0 = \overline{h^2} {\kappa_0}^{\mu-2} (\mu - 2) B\left(\frac{1}{2}, \frac{\mu}{2}\right), \tag{5.4}$$

which is a simplified version of the 1D topographic spectrum given in equation 5.2, and E and P_0 have been integrated over all wavenumbers k. The lee waves fluxes are thus the result of the sum of interactions by bottom currents with periodic topography which has a range of scales. The value of P_0 is calculated by Nikurashin and Ferrari (2011) for the whole ocean, averaged on a 3° × 3° grid. Values of U_0 and N are obtained from, respectively, a $1/8°$ isopycnal ocean model (Adcroft *et al.*, 2010) and a WOCE climatology (Gouretski and Koltermann, 2004). The results of the calculations of the lee wave fluxes in the Southern Ocean from Nikurashin and Ferrari (2011) are used in the construction of diapycnal diffusivity fields described in section 5.2.2.1.

From equation 5.3, Nikurashin and Ferrari (2010a) estimate the lee wave flux in the Pacific and Drake Passage regions. In the Southeast Pacific they estimate the bottom energy radation is $0.5 - 3.9\text{mW}\,\text{m}^{-2}$, and in Drake Passage they find $14 - 42\text{mW}\,\text{m}^{-2}$. They carried out numerical simulations using MITgcm to compare with the predictions of linear theory. They found the characteristics and magnitude of the radiated waves were dependent upon the 'steepness parameter', S, which characterises the interaction of the bottom flow with topography. For $S < 0.3$ over smooth topography, characteristic of the Southeast Pacific region, linear theory applies and only 10% of the energy was dissipated locally. For $S > 0.3$, characteristic of Drake Passage, more lee wave energy is generated and waves become time-dependent, with vigorous inertial oscillations and wave breaking, resulting in around 50% of the energy dissipating in the bottom 1km.

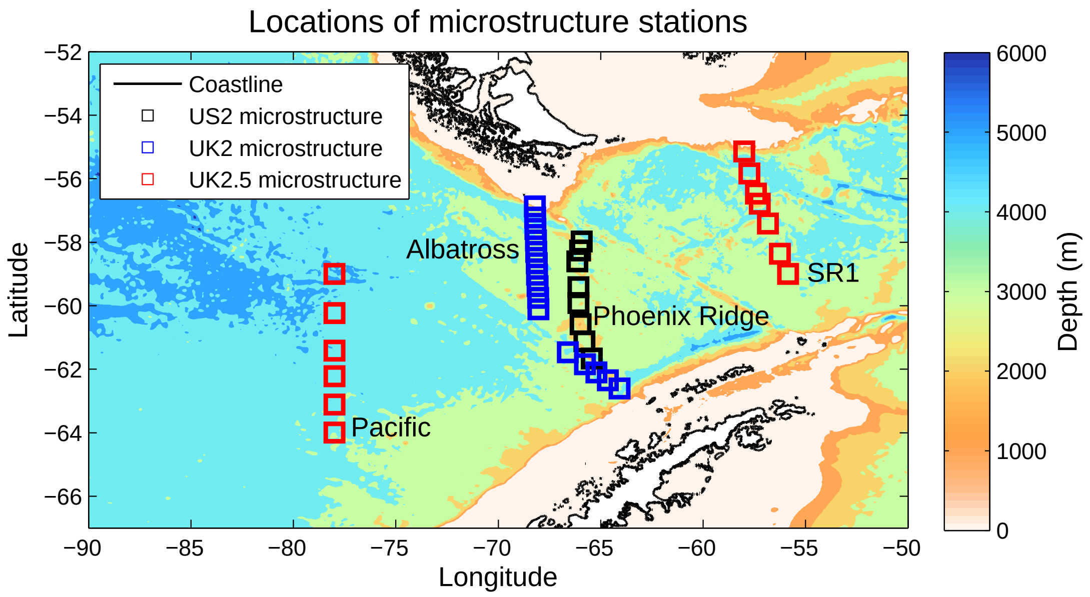

Figure 5.1: Map of stations where vertical profiles of turbulent energy dissipation that were obtained using microstructure profilers on the US2 (black squares), UK2 (blue squares) and UK2.5 (red squares) cruises are used to construct model diapycnal diffusivity fields. The background colours are water depths from Smith and Sandwell (1997), and the coastline of the South American and Anatarctic continents is overlayed (black contour).

5.2 Methods

The model framework is the same as that described in Chapter 4 sections 4.2.1 to 4.2.6, using the same model domain, velocity fields, and the same methods for comparing the model output with experiment. All of the model runs presented in this chapter are for the period from US2 to UK2.5, and use the same initial condition as was used for these runs in Chapter 4. The diapycnal diffusivity fields as described in the following sections are the new element for this chapter.

5.2.1 Microstructure based diffusivity fields

5.2.1.1 Constructing microstructure model diffusivities

The locations of stations where vertical profiles of ϵ were obtained on 3 of the DIMES cruises are shown on figure 5.1. At each station, the overall water depth, and the depth associated with each ϵ measurement is recorded. The dissipation profiles for each station are then referenced according to their height above the bottom (hab).

The hab referenced profiles of ϵ from the microstructure measurements are then grouped

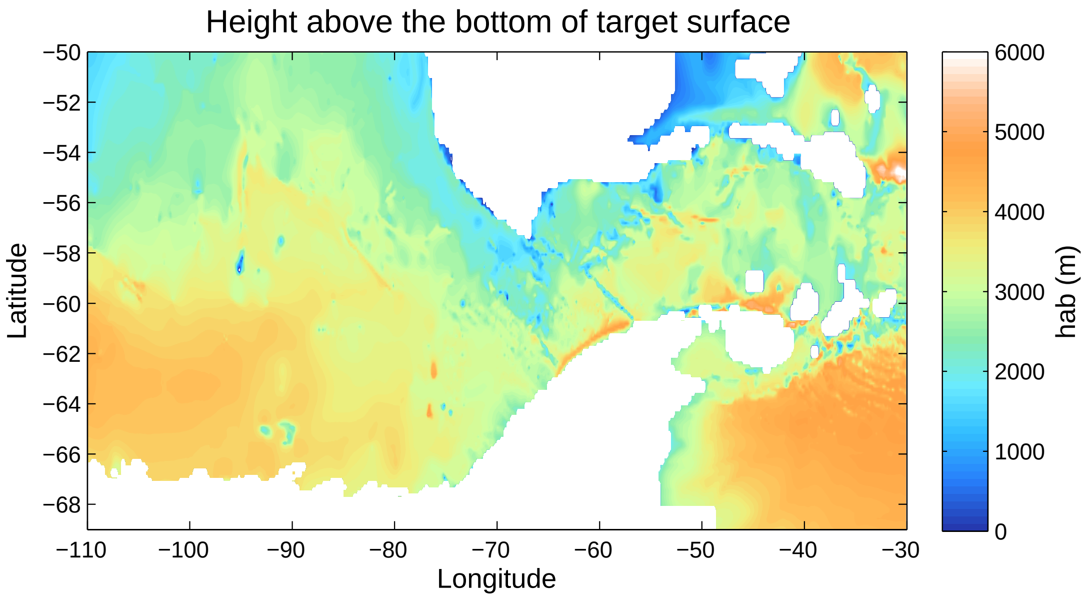

Figure 5.2: Height above the bottom (hab) of the model level corresponding to the tracer target isopycnal surface.

in order to obtain one mean profile of ϵ against hab representative of the Southeast Pacific, and another representative of Drake Passage. The Pacific profile is a mean of the hab referenced profiles from stations on the Pacific transect (see figure 5.1); the Drake Passage may be a mean over the Albatross, Phoenix Ridge and SR1 transects, or for a slightly higher estimate the Albatross stations are excluded, since generally lower values of dissipation were found here (see Sheen *et al.*, 2013). The hab referenced ϵ profiles averaged in this way were provided by Katy Sheen (personal communication). The mean profiles for the Pacific (a) and Drake Passage (b) regions are shown on figure 5.3 (solid blue lines).

An estimate on the upper bound for the region-averaged $hab - \epsilon$ profiles is made by bootstrapping of the station profiles that make up the mean, taking the 95th percentile. These upper bounds are shown for the Pacific (solid red line on figure 5.3 (a)), Drake Passage (solid red line on figure 5.3 (b)) and Drake Passage excluding the Albatross transect (dashed pink line on figure 5.3 (b)). An alternative upper estimate for Drake Passage is made based the fact that there is evidence of enhanced mixing in the deep reaching frontal jets of the ACC (e.g. Naveira Garabato *et al.*, 2004; St. Laurent *et al.*, 2012). Stations in jets are defined as those where the current speed is higher than the transect mean, and a mean of these stations is taken to produce the region-averaged $hab - \epsilon$ profile (dashed

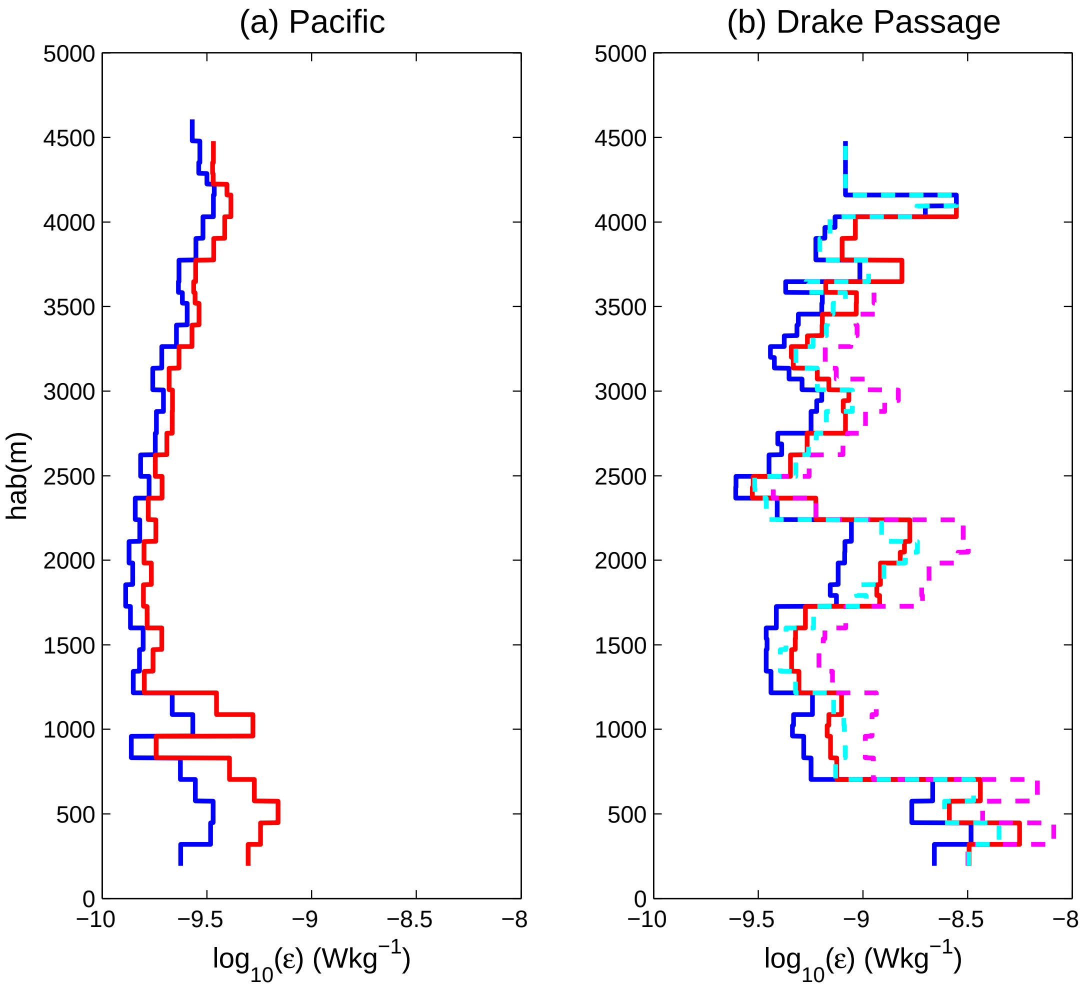

Figure 5.3: Region-averaged profiles of dissipation against height above the bottom for (a) the Pacific and (b) Drake Passage. Profiles shown are the mean (solid blue line), maximum from bootstrapping (solid red line), maximum excluding the Albatross transect (dashed pink line) and mean in jets (dashed light blue line).

light blue line on figure 5.3 (b)).

A value of hab for each point on the three-dimensional model grid is then required to construct the diffusivity fields. Since the depths of isopycnal surfaces are fluctuating with time, a time average over the period from US2 to UK2.5 of the depths recorded with the SatGEM velocity fields is used (see section 4.2.3). The depths of each model isopycnal level are subtracted from the water depth from Sandwell *et al.* (2002) to obtain hab. The height above the bottom of the model level assigned to the tracer target density is shown on figure 5.2.

The hab referenced ϵ profiles for each region are then combined with the model hab values to assign a value of ϵ for each point on the model grid. The boundary between the two regions is adjusted to reflect the data used to construct each profile, with a value of 74°W used when the Drake Passage average includes the Albatross transect, this being approximately the longitude of the midpoint between the Albatross and Pacific transects, and a value of 67°W used when the Albatross transect was excluded from the average, this being between Albatross and the Phoenix Ridge.

Having constructed the field of ϵ for the model domain, diffusivities are then calculated from the Osborn relation (previously introduced in Chapter 1):

$$K_z = 0.2\frac{\epsilon}{N^2} \tag{5.5}$$

The buoyancy frequencies (N^2) are based on the fixed model depth-density relation (as described in section 4.2.6), and are calculated as follows for each model level k:

$$N^2{}_k = -\frac{g}{\rho_k}\frac{\delta\rho}{\delta z}, \tag{5.6}$$

where g is the acceleration due to gravity ($= -9.81\text{ms}^{-2}$), ρ_k is the density assigned to the model level k, $\delta\rho$ is $0.003\,\text{kgm}^{-3}$, the model level spacing, and δz is the physical thickness of the model level in metres (see section 4.2.6 for an explanation of the model level thicknesses). Having calculated K_z from the model fields of ϵ and N, gaps remain in the diffusivity values due to the limits of SatGEM (see section 4.2.2), and these locations are filled in with a background value of 2×10^{-5} m^2 s^{-1}. The area to which the background value is applied is small enough that the results are not sensitive to its magnitude.

5.2.1.2 Lookup tables

A refinement to the model based on the idea that mixing rates are enhanced in jets is implemented using lookup tables for ϵ referenced according to height above the bottom and bottom speed, $\mathbf{u}_{bot}$. Microstructure dissipation values are binned according their associated hab and $\mathbf{u}_{bot}$, the latter calculated as a mean over the bottom 500m for each station, the velocities having been measured by LADCP. Lookup tables are then constructed for each region from the mean ϵ in each bin over the appropriate stations. Figure 5.4 shows the lookup tables for (a) the Pacific and (b) Drake Passage. In the Pacific there is little

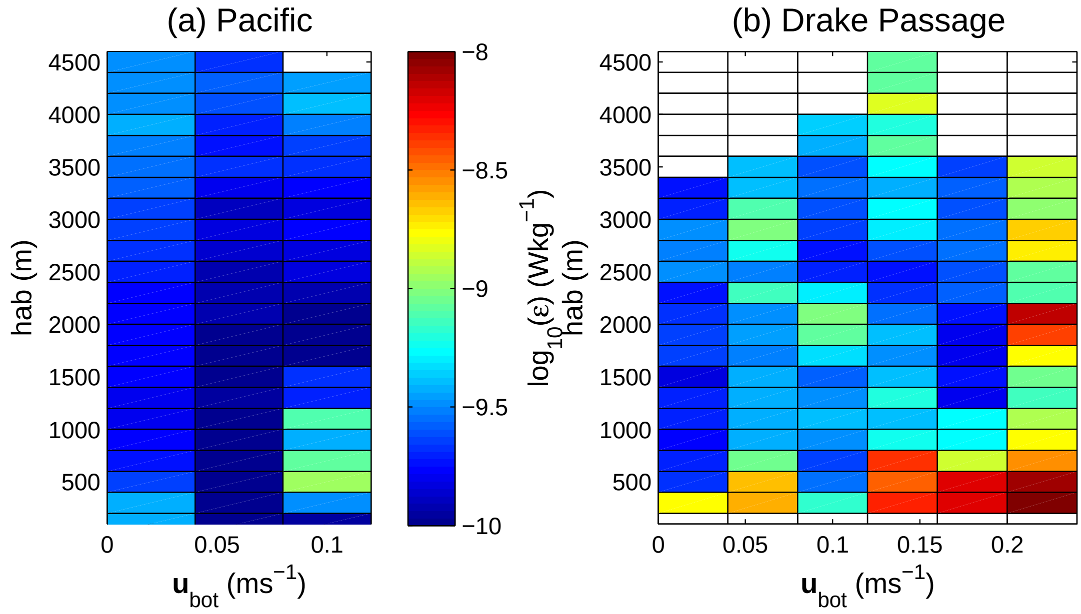

Figure 5.4: Lookup tables of $log_{10}(\epsilon)$ based on bottom speed, averaged over the bottom 500m, and height above the bottom. Dissipation values in each $hab/\mathbf{u}_{bot}$ bin are a mean over (a) stations on the Pacific transect and (b) stations on the Albatross, Phoenix Ridge and SR1 transects.

enhancement, and bottom speeds are comparitively low here. In Drake Passage, clear enhancement in dissipation can be seen near the bottom for all values of $\mathbf{u}_{bot}$, and throughout the water column for $\mathbf{u}_{bot} > 0.2\text{ms}^{-1}$. The lookup tables were provided by Katy Sheen (personal communication). A lookup table which included a third dimension of bottom roughness was also investigated, but the microstructure data proved to be too sparse for this to be viable, since less than a fifth of the bins in the table were populated.

To apply the lookup table to calculate model diffusivities, a value of bottom speed must be calculated for the model grid. First, the u and v components of the full-depth SatGEM velocity fields are interpolated horizontally onto the model grid for the time slices corresponding to the US2 - UK2.5 model run. Then speeds $\mathbf{u}$ are calculated from $\mathbf{u} = \sqrt{u^2 + v^2}$. A time mean is then taken over the period of the run, yielding time-averaged speeds at all depths. The bottom speeds $\mathbf{u}_{bot}$ are then calculated from the mean over the bottom 500m. The speeds are calculated first because the time-dependent eddying nature of the fields means that positive and negative velocities will cancel each other out in the time average. This is important because it is the instantaneous bottom speed that is associated with enhanced mixing; the time average is used to give a good representation of the bottom speeds over the course of the run, since the model K_z is time invariant. The

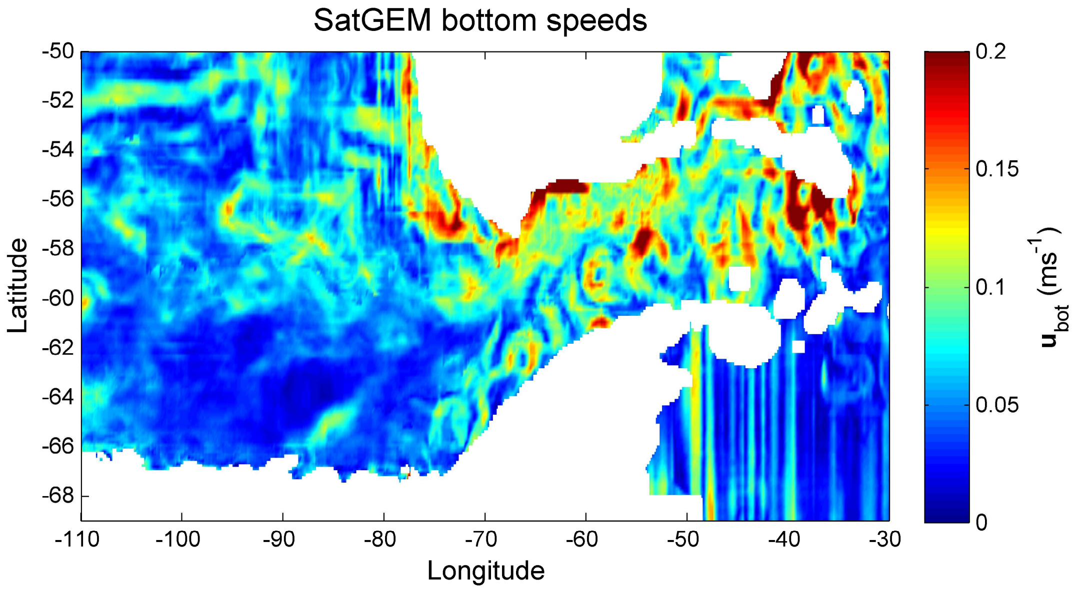

Figure 5.5: Mean bottom speeds from SatGEM, averaged over the time slices corresponding to US2 to UK2.5, and over the bottom 500m.

SatGEM bottom speeds are shown on figure 5.5.

5.2.2 Lee wave flux based diffusivity fields

5.2.2.1 Constructing lee wave model diffusivities

The lee wave fluxes from the NF model described in section 5.1.3 are shown in figure 5.6, interpolated onto my model horizontal grid. The substantial increase in predicted rates of lee wave generation in Drake Passage compared with the Southeast Pacific can be clearly seen. Sheen *et al.* (2013) have identified a predominance of downward propagating internal wave energy flux over upward propagating flux in the DIMES microstructure stations on the Pacific transect, and a predominance of upward propagating flux in the Drake Passage stations. This is explained by the idea that energy in the topographically smooth region of the Southeast Pacific is largely provided by the interaction of the wind with the sea surface; whereas in Drake Passage the energy is dominated by lee waves from abyssal flows interacting with rough topography. In order to take account of the downward propagating flux, a background profile of ϵ is constructed from the Pacific microstructure stations where $R_{pol} > 1$, calculating an upper bound from boostrapping as for the microstructure model. The resulting profile is plotted on figure 5.7 down to a depth of 3000m, which is the depth of the deepest part of the model grid as calculated from the

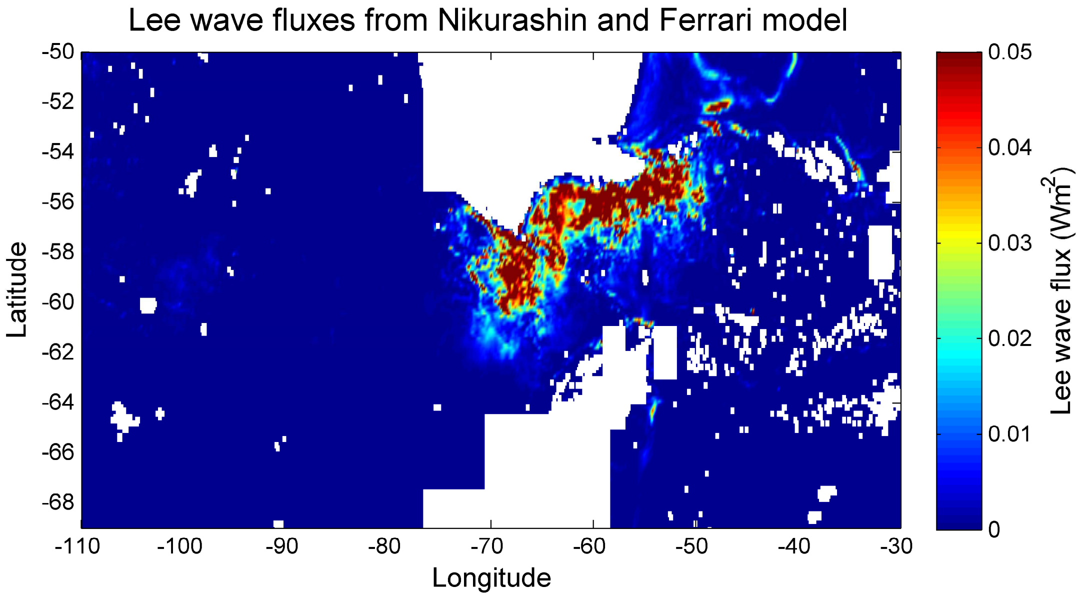

Figure 5.6: Lee wave fluxes from Nikurashin and Ferrari (2011), interpolated horizontally onto the model grid.

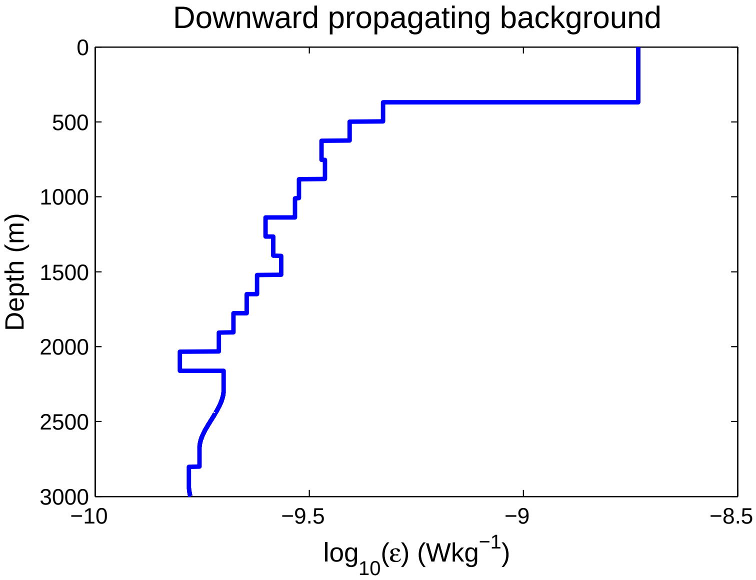

Figure 5.7: Dissipation due to the downward propagating background as a function of depth, calculated from the upper bound from bootstrapping of microstructure stations in the Pacific where $R_{pol} > 1$.

US2 - UK2.5 time average.

A profile must also be constructed of how the NF lee wave fluxes are dissipated throughout the water column. Using the mean microstructure profiles of dissipation from section 5.2.1.1, the dissipation is integrated upwards from the bottom, producing profiles of total dissipated power against hab. The power dissipated in each 1m hab bin is then divided by the total power dissipated in the water column to give a ratio, $\alpha(hab)$. The α profiles

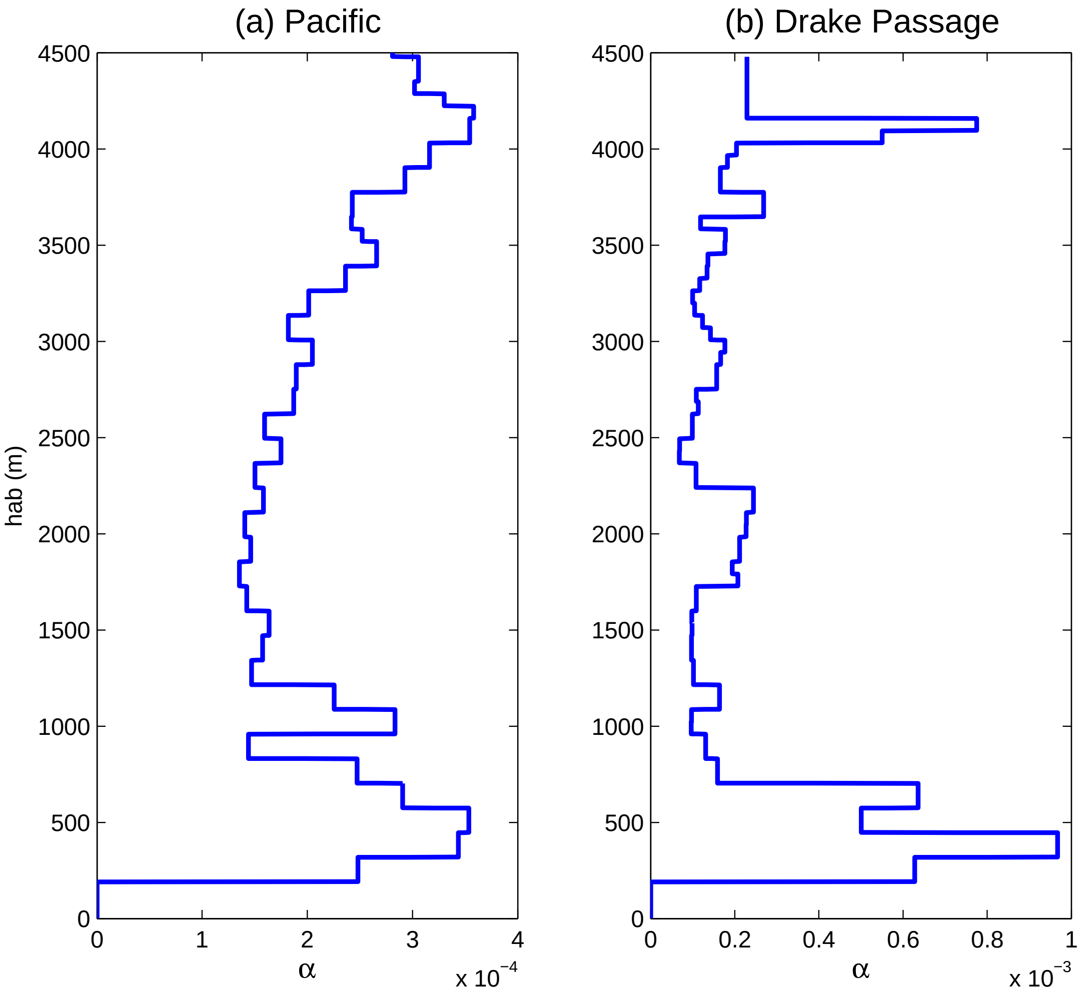

Figure 5.8: Power dissipated at each height above the bottom as a fraction of the total dissipated power in the water column, derived from mean microstructure profiles of dissipation in (a) the Pacific and (b) Drake Passage. The sum of the values on each profile is 1.

are shown on figure 5.8.

Finally, the values of dissipation for the model grid, ϵ_{model} are calculated by combining the downward propagating background, $\epsilon_{background}$ with the NF lee wave fluxes E_{NF} (E from equation 5.3) according to the following formula:

$$\epsilon_{model}(x, y, z) = \epsilon_{background}(z) + \frac{\beta\alpha(hab)}{\rho(z)} E_{NF}(x, y), \tag{5.7}$$

where β is an adjustable scale factor and ρ is the density, the latter converting flux in Wm^{-3} to dissipation in Wkg^{-1}. The range above the bottom over which the lee wave flux is assumed to be dissipated is set to one value for the Pacific region, R_{Pac} and another value for Drake Passage, R_{DP} to account for the fact that enhanced dissipation due to lee waves is observed to extend to a greater or lesser height above the bottom in different areas (St. Laurent *et al.*, 2012; Sheen *et al.*, 2013). The values of β, R_{Pac}, R_{DP} and the longitude at which the two regions are split may then be adjusted to give a good fit to either the tracer data, or to the microstructure data (see section 5.2.2.2). Once the dissipation values for the model grid have been determined from equation 5.7, the diffusivities are then calculated with the Osborn relation as for the microstructure based fields. It is necessary to set an upper limit for K_z of 5×10^{-3} m^2 s^{-1} for numerical stability, which is imposed after the fields had been calculated. The parameterisation in equation 5.7 is somewhat analagous to that of St. Laurent (2002) for mixing due to internal tides, with their $F(z)$ replaced here by the microstructure-derived $\alpha(hab)$, and their efficiency factor q replaced by β. However, here β does not represent a proportion of locally dissipated flux as it does in St. Laurent (2002), since in that case the fraction $1 - q$ that is radiated away is due to low mode internal tides, whereas lee waves are locked to the mean flow and the topography from which they were generated. Instead the adjustment of β is necessary to compensate for limitations of the NF lee wave model (see section 5.4).

5.2.2.2 Optimising the lee wave model to fit microstructure

In order to fit the lee wave model dissipation values to the microstructure observations, a cost function similar to that used to assess model-data fits in other chapters is applied to comparing the model and observed dissipations at the target depth:

$$\chi^2 = \sum_T \sum_{i=1}^{n_T} \frac{\left(\epsilon_{model_i} - \epsilon_{micro_i}\right)^2}{{\sigma_T}^2}, \tag{5.8}$$

where the inner sum is over all the microstructure stations, i, on a transect; the outer sum is over all four transects, T (Pacific, Albatross, Phoenix Ridge and SR1 on figure 5.1); ϵ_{model_i} and ϵ_{micro_i} are the model and observed dissipations at the target depth; and ${\sigma_T}^2$ are the variances of the observed dissipations on each transect. The ϵ_{model_i} values are taken from the target density at the coordinates on the model grid corresponding to the microstructure station locations. The values of ϵ_{micro_i} are taken from the upper bound $hab - \epsilon$ profiles at the hab corresponding to the target density, according to the model hab grid, at the same horizontal coordinates. The dissipations at each station with the model parameters optimised are shown on figure 5.9. The optimised parameters are $\beta =$

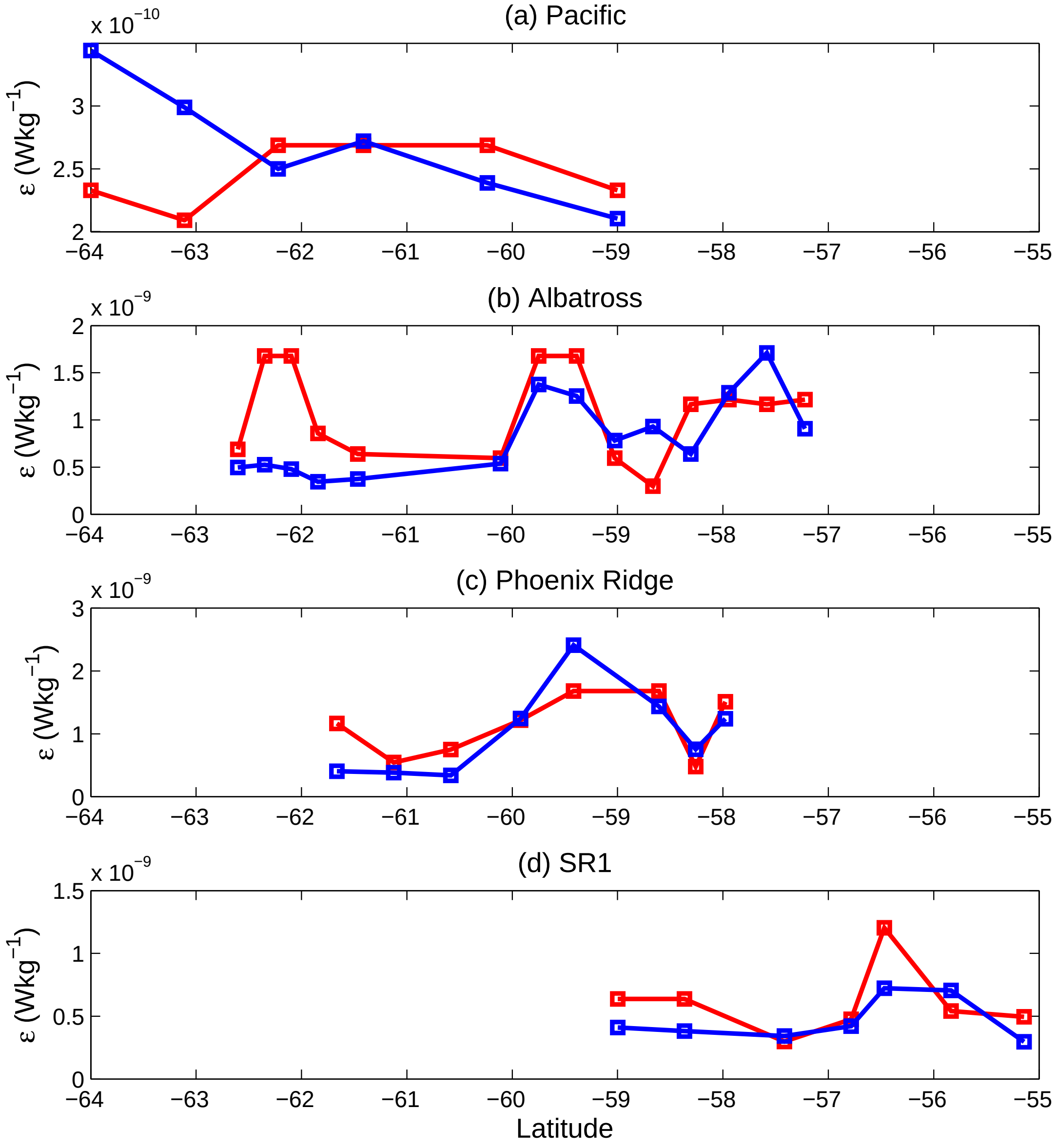

Figure 5.9: Microstructure (red) and lee wave model (blue) derived dissipations at the target density where lee wave model parameters have been optimised to give the best fit to the microstructure data. Transects compared are (a) UK2.5 Pacific, (b) UK2 Albatross, (c) US2 Phoenix Ridge and (d) UK2.5 SR1.

0.08, $R_{Pac} = 2$km, and $R_{DP} = 4.5$km, with a longitude of 74°W for the split between the Pacific and Drake Passage regions; however the values of R_{Pac} and R_{DP} are poorly constrained by the optimisation.

A summary of the diapycnal diffusivity fields used in this chapter, with the terms that are used to refer to each run in section 5.3, is given in table 5.1.

Table 5.1: A summary of the model runs presented and the details of their 3D diapycnal diffusivity fields.

Category	Run name	Description	Southeast Pacific field	Drake Passage field	Split	Depends on
Simple	2 zone	2 values of K_z, one at all depths and all latitudes in each region	Optimised to fit tracer	Optimised to fit tracer	67°W	Longitude
Simple	Enhanced K_z	2 values of K_z, one background value and one enhanced near topography	Enhanced regions according to d and R (see section 4.2.7)	Enhanced regions according to d and R (see section 4.2.7)	N/A	Height above the bottom of the target surface
Microstructure	Micro mean	K_z constructed from the mean of microstructure measured dissipation	Mean of microstructure stations on Pacific transect (figure 5.3 (a) solid blue line)	Mean of microstructure stations on Albatross, Phoenix Ridge and SR1 transects (figure 5.3 (b) solid blue line)	74°W	Height above the bottom, Longitude
Microstructure	Micro max	K_z constructed from the upper bound of microstructure measured dissipation (95th percentile from bootstrapping)	Upper bound of microstructure stations on Pacific transect (figure 5.3 (a) solid red line)	Upper bound of microstructure stations on Albatross, Phoenix Ridge and SR1 transects (figure 5.3 (b) solid red line)	74°W	Height above the bottom, Longitude
Microstructure	Micro Pho/Sr1 max	K_z constructed from the upper bound of microstructure measured dissipation (95th percentile from bootstrapping)	Upper bound of microstructure stations on Pacific transect (figure 5.3 (a) solid red)	Upper bound of microstructure stations on Phoenix Ridge and SR1 transects (figure 5.3 (b) dashed pink line)	67°W	Height above the bottom, Longitude
Microstructure	Micro jets	K_z constructed from the mean of microstructure measured dissipation for stations in jets	Upper bound of microstructure stations on Pacific transect (figure 5.3 (a) solid red line)	Mean of microstructure stations in jets on Albatross, Phoenix Ridge and SR1 transects (figure 5.3 (b) dashed light blue line)	74°W	Height above the bottom, Longitude
Microstructure	Micro lookup	K_z constructed using a lookup table of dissipation averaged over microstructure stations and binned by height above the bottom and bottom speed, combined with SatGEM velocities	Mean of microstructure stations on Pacific transect	Mean of microstructure stations on Albatross, Phoenix Ridge and SR1 transects	74°W	Height above the bottom, bottom speed, Longitude
Lee wave	Lee wave micro	K_z constructed from microstructure background added to lee wave fluxes from Nikurashin and Ferrari. Fluxes distributed in depth using microstructure profiles, and dissipations calculated using equation 5.7. β, R_{Pac}, R_{DP} and split longitude optimised for best fit to microstructure	$R_{Pac} = 2000\,\mathrm{m}, \beta = 0.08; \alpha$ profile from mean of microstructure stations on Pacific transect	$R_{DP} = 4500\,\mathrm{m}, \beta = 0.08; \alpha$ profile from mean of microstructure stations on Albatross, Phoenix Ridge and SR1 transects	74°W	Height above the bottom, bottom speed, bottom roughness, bottom stratification, Longitude
Lee wave	Lee wave tracer	K_z constructed from microstructure background added to lee wave fluxes from Nikurashin and Ferrari. Fluxes distributed in depth using microstructure profiles, and dissipations calculated using equation 5.7. β, R_{Pac}, R_{DP} and split longitude optimised for best fit to tracer	$R_{Pac} = 4500\,\mathrm{m}, \beta = 0.5; \alpha$ profile from mean of microstructure stations on Pacific transect	$R_{DP} = 3500\,\mathrm{m}, \beta = 0.5; \alpha$ profile from mean of microstructure stations on Albatross, Phoenix Ridge and SR1 transects	67°W	Height above the bottom, bottom speed, bottom roughness, bottom stratification, Longitude

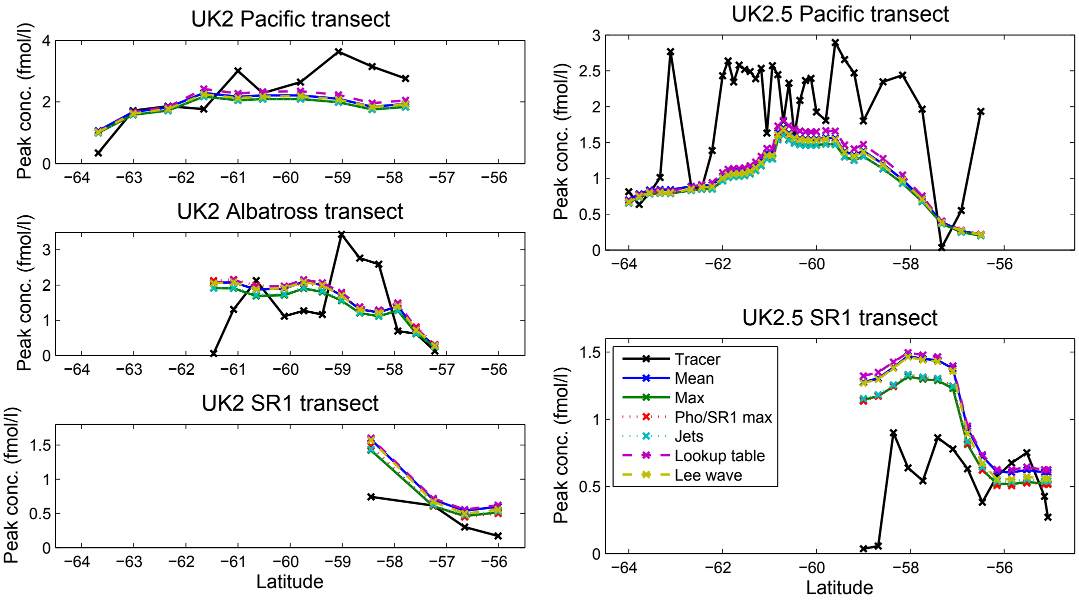

Figure 5.10: Peak concentrations from model runs using microstructure based K_z fields. The outputs shown are from the 'Micro mean' (solid blue line), 'Micro max' (solid green line), 'Micro Pho/SR1 max' (dotted red line), 'Micro jets' (dotted light blue line), 'Micro lookup' (dashed pink line) and 'Lee wave micro' (dashed yellow line) runs as summarised in table 5.1.

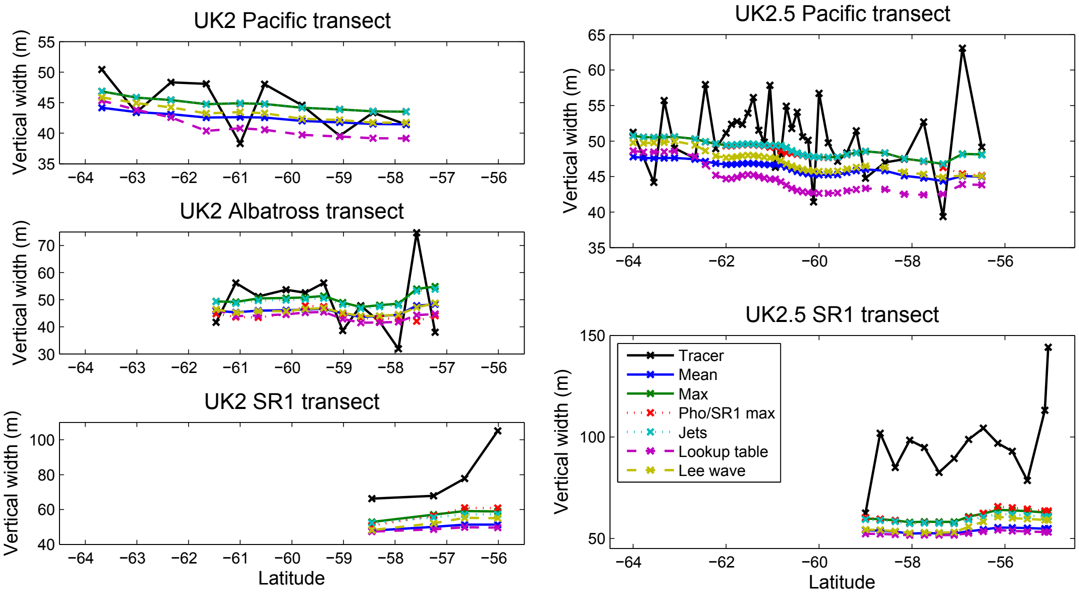

Figure 5.11: As figure 5.10 but for vertical widths

5.3 Results

5.3.1 Microstructure model

The peak concentrations and vertical widths from a number of model runs where diapycnal diffusivity fields were based on microstructure measurements are shown in figures

5.10 and 5.11. In the Pacific, the mixing of the tracer has been reproduced well, including some of the larger scale meridonal variation as evidenced by the vertical widths on the Pacific and Albatross transects. The contribution to the cost function of the Pacific widths for the ‘Micro mean’ run (see table 5.1) is 77.6 (compared with an expectation value of 47), as the vertical widths are slightly underestimated. This reduces to 48.6 where the estimate of the maximum dissipations from bootstrapping is used. The diffusivities calculated from the upper bound are used in the Pacific region for the ‘Micro max’, ‘Micro jets’ and ‘Micro Pho/SR1 max’ runs. In Drake Passage, however, the mixing has been significantly underestimated in all cases, leading to profile widths that are much narrower than the tracer on the SR1 transects, particularly on UK2.5. The Micro Pho/SR1 max run gives the best fit to the widths on SR1, with a contribution to the cost function of 69.4 (expectation 18). The Micro jets run gives mixing close to the upper bound estimates, but still nowhere near that required to reproduce the mixing implied by the tracer. The peak concentrations are a reasonable fit to the observations, except on the UK2.5 SR1 transect, where they are much too high in the southern half, but fairly close in the north. Referring back to Chapter 4 figure 4.38, this can be explained by the fact that the column integrals are a reasonable fit on the southern half of the transect, so an underestimate in the vertical widths leads to an overestimate in the peak concentrations; and the column integrals are too low on the northern half, which is therefore compensated for by the underestimate in the vertical widths. The model diffusivities at the target depth and profiles of model diffusivity with depth for the Micro max run are shown on Fig 5.12 and 5.13. It is clear that the mixing will not have been strong enough to reproduce the average mixing implied by the tracer in Drake Passage, since from the 2 zone model in Chapter 4 this was found to be 3.5×10^{-4} m^2 s^{-1}, and there are only a few regions in the microstructure based K_z field where diffusivity at the tracer level is above 1×10^{-4} m^2 s^{-1}. The patterns of mixing predicted by the microstructure model can be explained by referring back to figure 5.2 and 5.3. For virtually the entire Southeast Pacific sector occupied by the tracer west of 70°W, the tracer target isopycnal is more than 3000 m above the bottom and therefore occupies a region of the water column with no significant enhancement in diffusivity. In Drake Passage, dissipation is enhanced throughout the water column when compared with

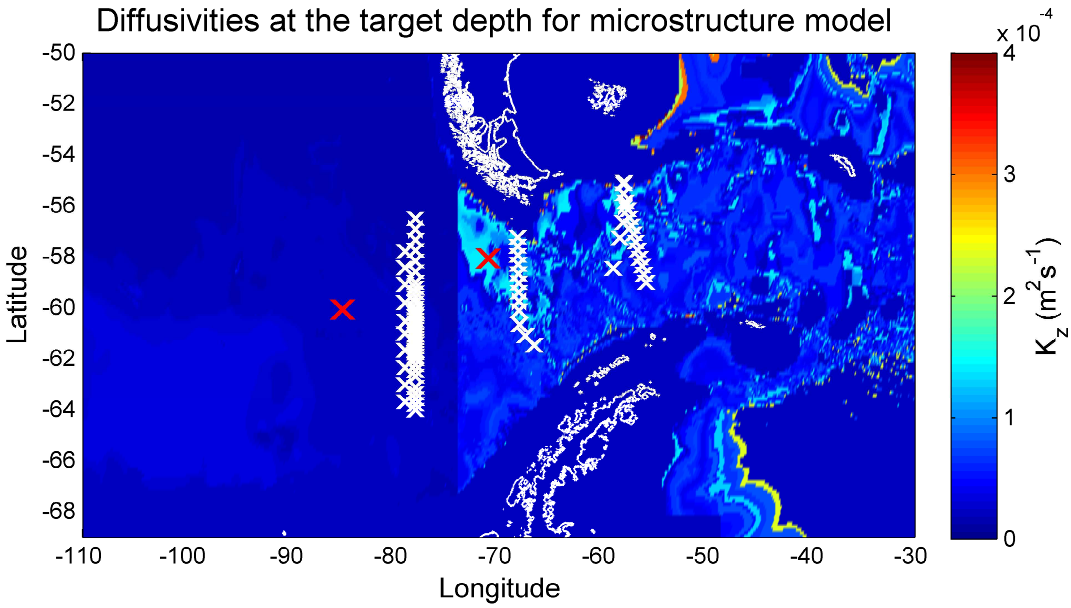

Figure 5.12: Map of K_z at the target depth estimated from microstructure. The upper bound from bootstrapping for the $\epsilon - hab$ profile was used in both the Pacific and Drake Passage regions. Locations of tracer stations on the UK2 and UK2.5 cruises (white crosses) are overlayed. The full profiles of K_z through the model's vertical extent in the two regions at the locations indicated by the red crosses are plotted on figure 5.13

the Pacific stations, with further enhancement up to 700 m above the bottom in all profiles, and between 1700 m and 2200 m above the bottom in the maximum, mean in jets, and profiles excluding the Albatross transect. However, the areas where the tracer isopycnal comes within 700 m of the bottom are limited to a narrow slither around the edge of the South American continental slope: insufficient to have any discernable impact on the mixing of the model tracer. Extending the range to 2200 m above the bottom includes a large area to the west of the Albatross transect following the South American continental slope, but still includes less than half of the region occupied by the model tracer between 68°W and 58°W, the approximate longitudes of the Albatross and SR1 transects. These observations would seem to account for the fact that, in the Drake Passage region, the microstructure dissipations are not enhanced sufficiently over a wide enough area to reproduce the mixing to which the tracer was subjected.

The run which used lookup tables to predict the mixing based on bottom speed and height above the bottom gives lower predictions for the mixing both in the Pacific and Drake Passage than the other runs. Since the SatGEM velocities are extrapolated downwards from absolute velocities at the surface (as was described in section 4.2.2), the bottom speeds,

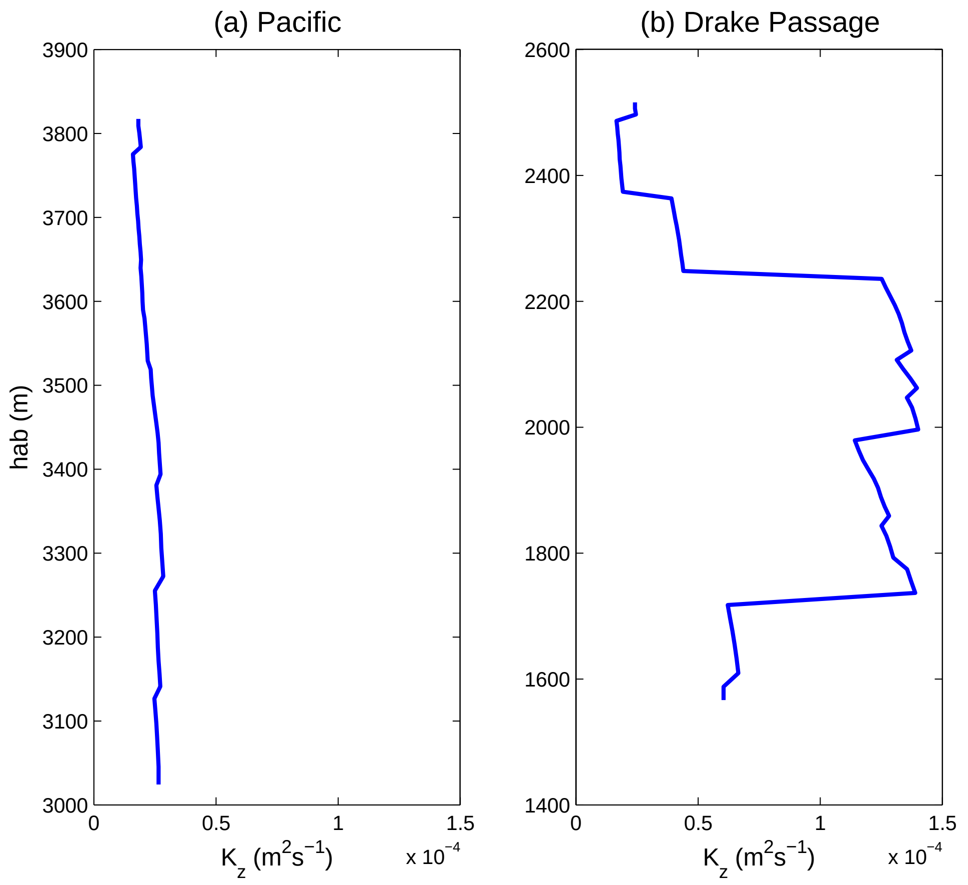

Figure 5.13: Vertical profiles of K_z from the microstructure model at locations in (a) the Pacific and (b) Drake Passage indicated by the red crosses on figure 5.12.

which were fed into the lookup tables, may not be reliable. To investigate the possibility that the SatGEM bottom speeds were underestimated, leading to an underestimate in the mixing, bottom speeds calculated from the SatGEM velocities were compared with those calculated from velocities recorded by the DIMES mooring array. The mooring is situated in Drake Passage at 57.8°W, 56.0°S (the northern end of SR1), and has 12 current meters at depths ranging from around 400 m to around 3600 m. Speeds calculated from the second deepest current meter were compared with SatGEM-derived speeds at the location of the mooring and at the same depth, over the time period corresponding to the model run. The second deepest meter was chosen because the deepest is within the bottom boundary layer. The comparison, shown on figure 5.14, reveals that SatGEM misses some of the temporal variability of the mooring data on the timescale of the SatGEM fields. However while the frequency distributions of the speeds do display some differences, if anything the SatGEM speeds are slightly larger than those at the mooring. This therefore suggests that an underestimate in mixing using the lookup tables may not be attributed to an underestimate in the bottom speeds. It should be noted, however, that the velocities at the location of the mooring array may not be representitive of the rest of the Drake Passage. The mooring data were provided by Alex Brearley (personal communication). An additional drawback with using the lookup tables to estimate the diffusivities is that the tables are sparsely populated, with some $hab/\mathbf{u}_{bot}$ bins constructed from only 1 VMP profile, and a number with no data at all.

Averaged over Drake Passage at the target density between $67°$W and $58°$W, the diffusivity from the microstructure based run that gave the best fit to the tracer was $6.7 \times 10^{-5}\ \mathrm{m}^2\ \mathrm{s}^{-1}$, only 20% of that required to match the measured tracer results as inferred from the 2 zone model. This leads to the conclusion that the instantaneous estimates of K_z obtained from microstructure measurements used in this study were not a good predictor of long term time-averaged mixing at mid-depths in this region.

The run using the lee wave model for diffusivities, optimised to give the best fit to the microstructure data upper limit estimate as described in section 5.2.2.2, results in vertical widths somewhere in between the various microstructure runs. The purpose of the microstructure-fitted lee wave model was to test the theory that the underprediction by microstructure was due to undersampling of the regions of most intense mixing, by using the lee wave fluxes to extrapolate spatially from locations where dissipation was measured. If the distribution of mixing in the lee wave model is correct, and the fit between the model and the microstructure data is good on all transects, as it appears to be from figure 5.9, then the model might be expected to produce a good spatial extrapolation of the mixing as measured by microstructure. However, the method used for optimisation, using average $\epsilon - hab$ profiles to calculate values of ϵ_{micro} for comparison with the model, does not allow for spatial variations between the microstructure observations to be properly reproduced. Therefore it is difficult to draw any firm conclusions from the results of this run.

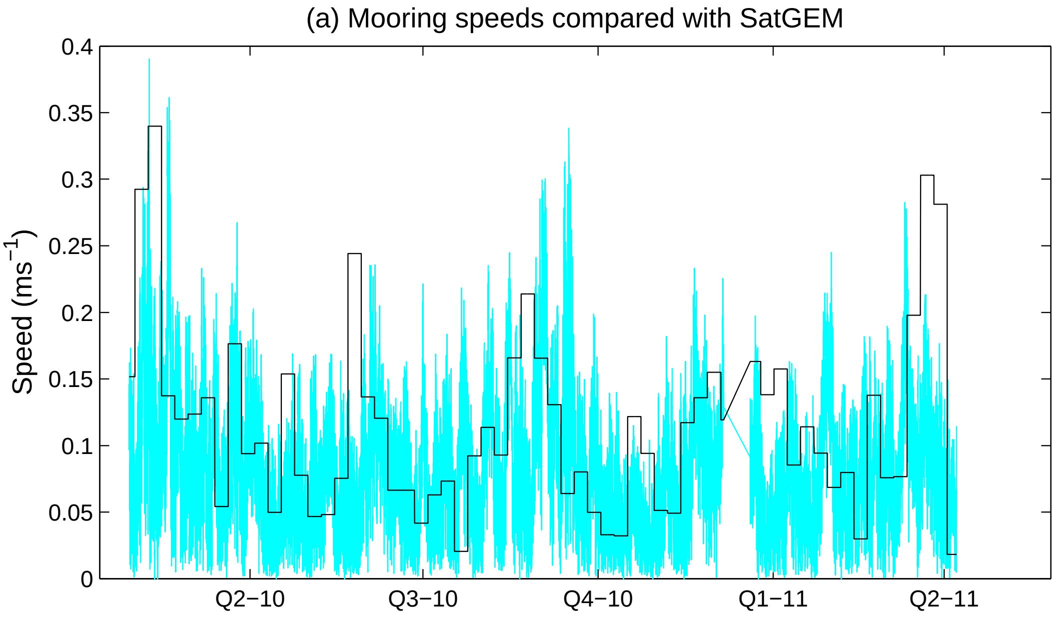
(a) Mooring speeds compared with SatGEM

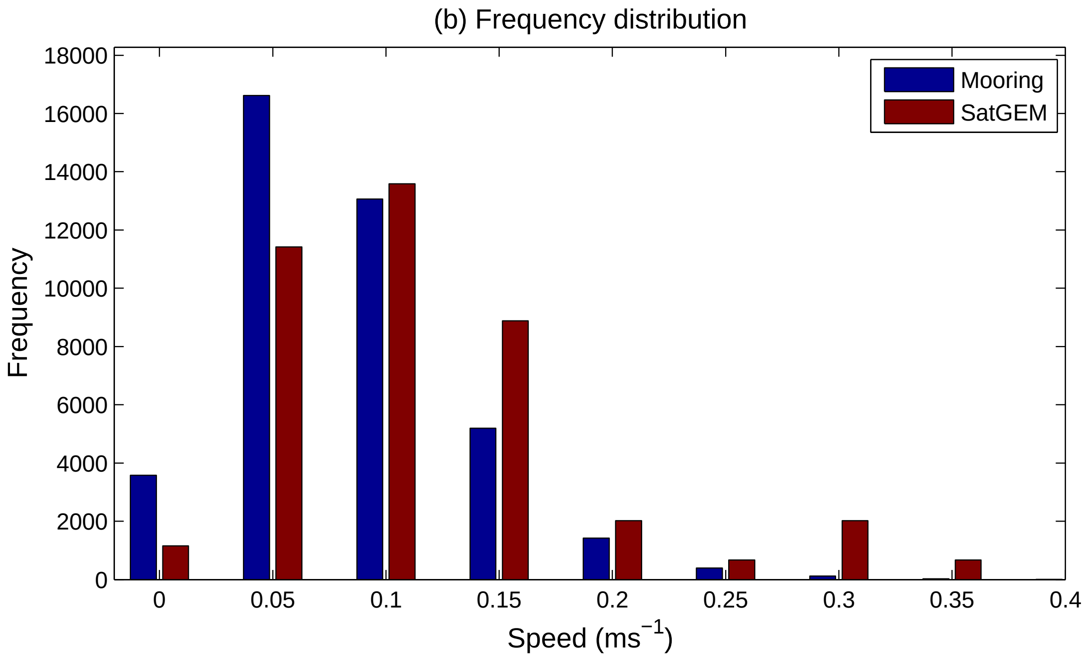
(b) Frequency distribution

Figure 5.14: Comparison of SatGEM bottom speeds with data from the DIMES mooring for January 2010 - April 2011, the period corresponding to the model runs. In (a) a time series of bottom speeds from the mooring (light blue line) and SatGEM (black line) are compared. In (b) is a histogram of the frequency distribution of the speeds.

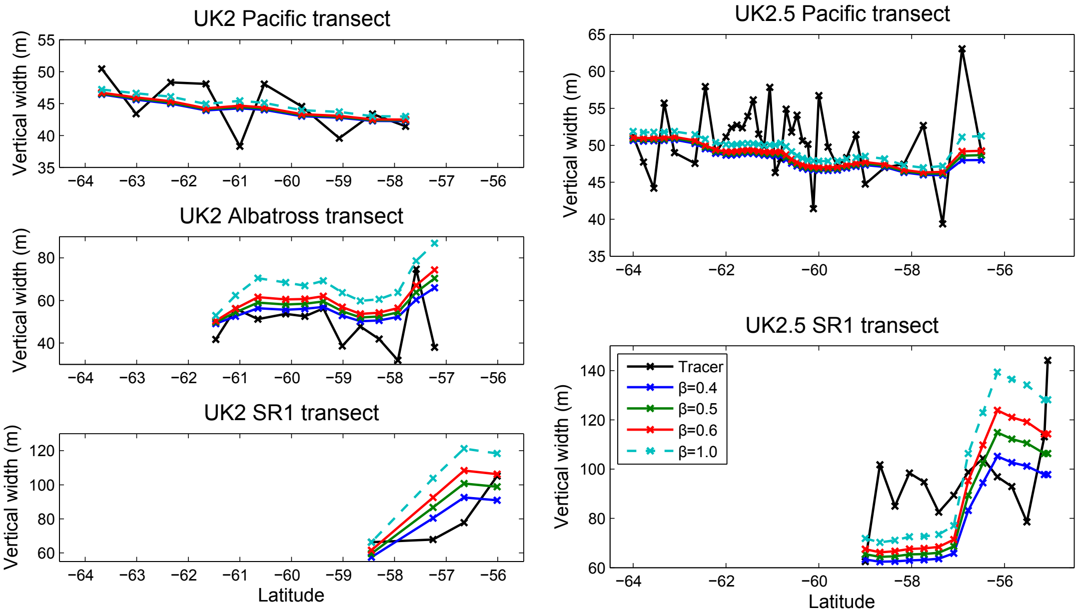

Figure 5.15: Vertical widths for runs using the lee wave model with varying values of β. Tracer is in black and model runs are in colour. For the runs with β =0.4, 0.5 and 0.6, indicated by the solid lines, the other model parameters were R_{Pac} =4 km and R_{DP} =3.5 km. For the run with $\beta = 1$, indicated by a dashed line, the parameters were $R_{Pac} = R_{DP} = 4.5$ km.

5.3.2 Lee wave model

The vertical widths for runs using the lee wave model for diffusivity for varying values of β are shown on figure 5.15. The solid coloured lines show the runs for β near the optimum with the best R_{Pac} and R_{DP}, the optimal value of β being 0.5. The Pacific mixing is captured well, showing similar patterns in the vertical widths on the Pacific transect as resulted from the microstructure runs. However, profiles are too wide along the length of the Albatross transect, increasingly so at the northern end. Referring back to figure 5.6, the highest lee wave fluxes in the NF model extend as far west as 70°W, with significantly enhanced fluxes all the way to around 72°W when compared with the Pacific. The fact that this pattern has resulted in an overestimate of the profile widths at the Albatross transect may due to the $3^\circ \times 3^\circ$ grid used by Nikurashin and Ferrari (2011) to average observations used to calculate the topographic spectrum. If the bottom roughness just to the west of the Albatross transect is overestimated due to the grid resolution, this would lead to an overestimate in the lee wave fluxes. On SR1, the profiles are too wide in the northern half of the transect, where the model tracer has been through the region of the highest lee wave fluxes, and too narrow in the southern half, where there is little to no enhancement over

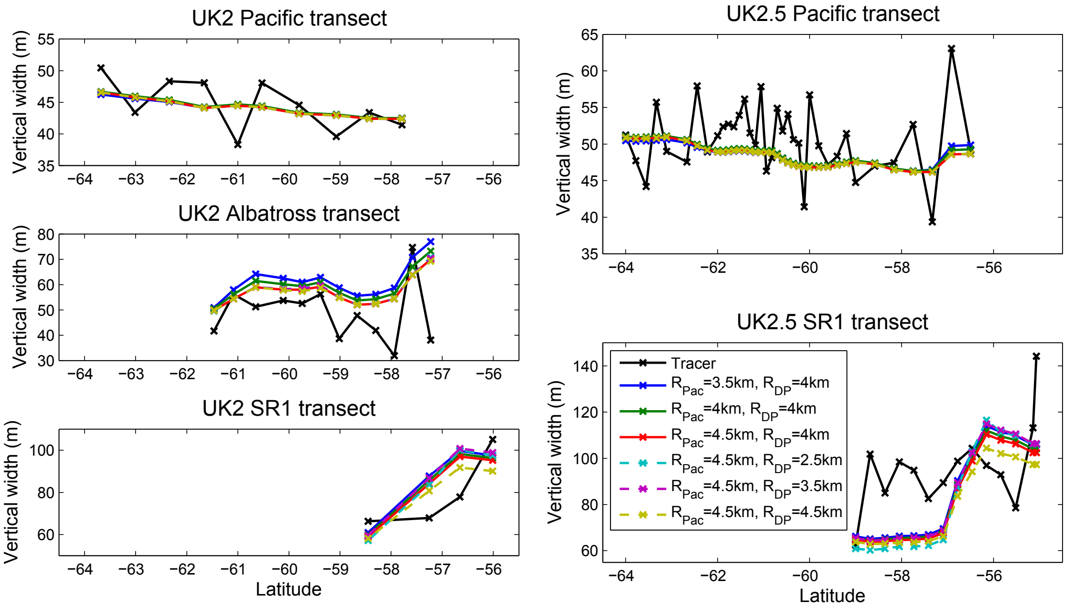

Figure 5.16: Vertical widths for runs using the lee wave model with varying values of R. Tracer is in black and model runs are in colour. The value of β was 0.5 for all the runs shown.

background levels in the model. These results look very similar to the pattern produced by the enhanced K_z model of Chapter 4. If a value of $\beta = 1$ is used, as shown by the dashed line, thereby applying the NF fluxes as they were originally calculated, the overprediction of mixing in the northern half of Drake Passage is quite significant, and the overprediction west of the Albatross transect has also worsened. The vertical widths in the southern half of the SR1 transect on UK2.5 are still underpredicted for $\beta = 1$.

The vertical widths for lee wave runs with various values of R_{Pac} and R_{DP} are shown on figure 5.16. The variation of the range of propagation of lee waves in a given region has two simultaneous effects: increasing, say, R_{DP} will increase the area in Drake Passage over which the lee wave fluxes reach the tracer depth, at the same time as reducing the amount of flux dissipated at each depth. Since the Albatross transect is situated largely in a region where the height above the bottom of the target is less than 2000m, most values of R_{Pac} will result in a large area of enhanced diffusivity influencing the widths of these profiles. Therefore a larger value of R_{Pac} helps to compensate for the apparent overestimate of lee wave fluxes here. In Drake Passage, a value of R_{DP} that results in large diffusivities at the target depth while still allowing the lee wave fluxes to reach the target depth over as wide an area as possible gives the best fit to the data at SR1. The optimised values are $R_{Pac} = 4$ km, $R_{DP} = 3.5$ km.

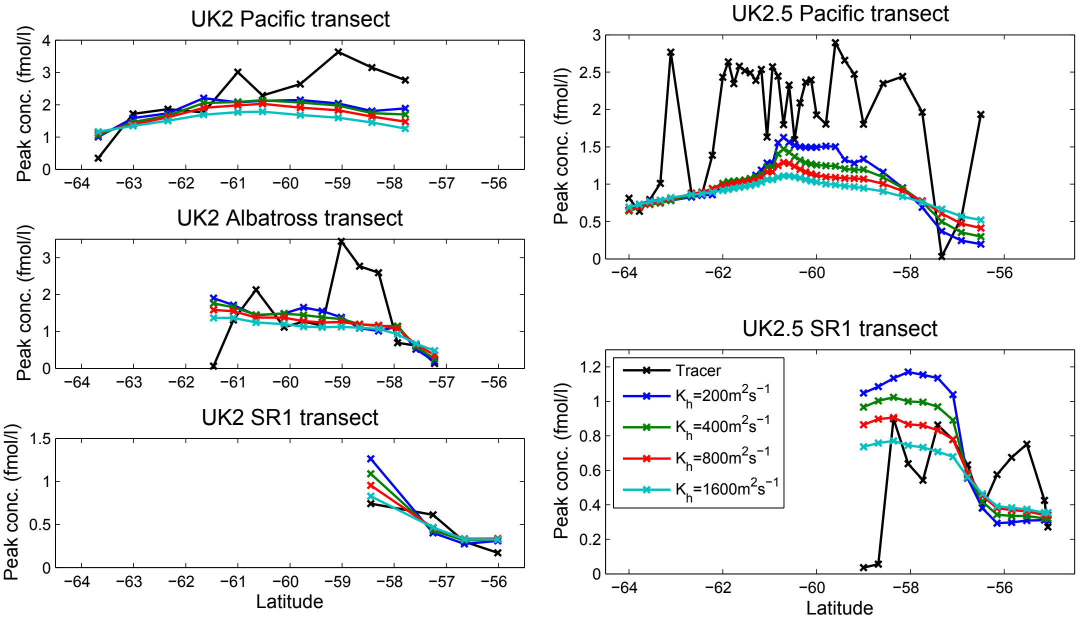

Figure 5.17: Peak concentrations for runs using the lee wave model with varying values of K_h. Tracer is in black and model runs are in colour.

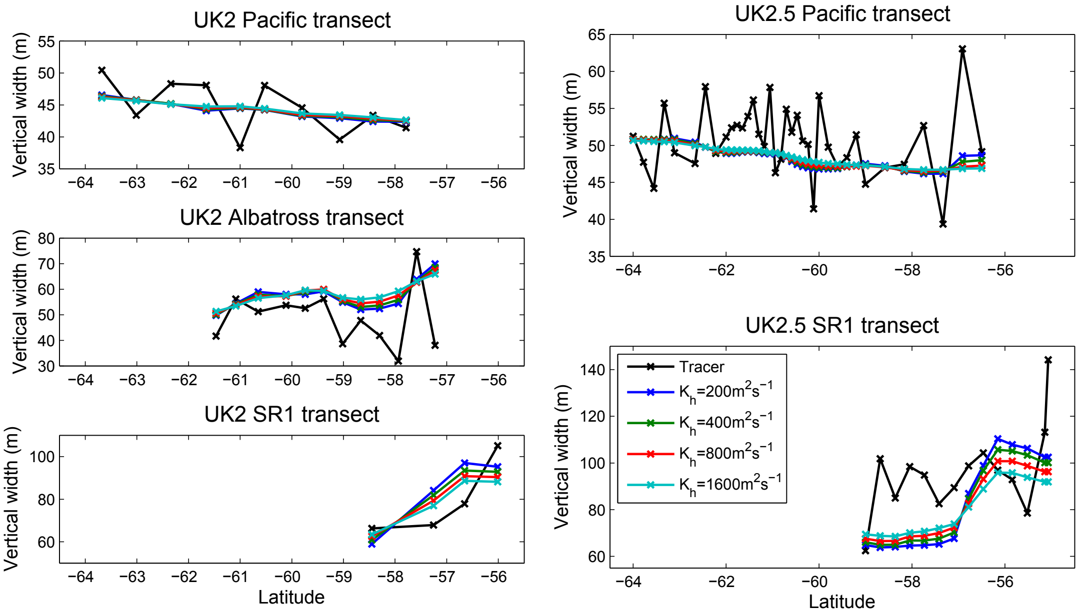

Figure 5.18: As figure 5.17 but for vertical widths.

The peak concentrations and vertical widths for runs using the lee wave model for diffusivity for varying values of K_h are shown on figure 5.17 and 5.18. For $K_h = 200\,\mathrm{m}^2\ \mathrm{s}^{-1}$, which is the value used when optimising the other parameters, peak concentrations on the southern half of SR1 are much higher than the tracer observations. This results from the combination of the underprediction of the vertical widths and the tracer advection, as

Table 5.2: Contributions to the cost function from each transect for lee wave model runs with various parameters. Columns 5 to 7 give the contribution to the cost function from the vertical widths on the Pacific, Albatross and SR1 transects; column 8 the contribution from the peak concentrations on all transects, column 9 the total cost function. Expectation values are in brackets at the top of each column. The split between the Pacific and Drake Passage regimes was 67°W for all runs.

β	R_{Pac} (km)	R_{DP} (km)	K_h ($\mathrm{m^2\ s^{-1}}$)	Pac widths (47)	Alb widths (12)	SR1 widths (18)	Concs (77)	Total (154)
1.0	4.5	4.5	200	42.2	43.5	40.1	135.8	261.6
0.4	4.5	3.5	200	52.5	13.9	26.9	144.0	237.1
0.5	4.5	3.5	200	50.0	17.4	25.3	140.5	233.2
0.6	4.5	3.5	200	47.9	21.8	27.7	138.1	235.4
0.5	3.5	4.0	200	48.4	25.9	24.3	139.2	237.8
0.5	4.0	4.0	200	47.9	20.8	24.6	140.9	234.1
0.5	4.5	4.0	200	50.0	17.1	25.1	141.6	233.8
0.5	4.5	2.5	200	50.0	17.6	28.9	149.7	246.2
0.5	4.5	4.5	200	50.0	16.7	26.4	143.5	236.5
0.5	4.5	4.0	400	50.5	17.5	23.1	133.7	224.8
0.5	4.5	4.0	800	50.6	18.3	22.0	133.6	224.6
0.5	4.5	4.0	1600	50.0	19.1	22.0	140.7	231.8
0.5	4.5	3.5	800	50.6	18.6	20.7	133.3	223.1

was seen with the microstructure model in section 5.3.1. As K_h is increased, the peak concentrations on the UK2.5 SR1 transect are smoothed out, but the fit to the data on the Pacific transect is worsened. As was found with the Enhanced K_z model in Chapter 4, the vertical widths are redistributed to a degree by high isopycnal diffusivity, but north-south trend remains. The optimal value for K_h is $800\,\mathrm{m^2\ s^{-1}}$.

Table 5.2 gives the contributions of various components to the cost function from a number of the runs involved in the optimisation of the lee wave model parameters to fit the tracer data. The optimisations of β, R_{Pac} and R_{DP} are complex because both β and R can affect the magnitude of the mixing in a given region. For example with $\beta = 0.6, R_{Pac} = 4.5\,\mathrm{km}, R_{DP} = 3.5\,\mathrm{km}$ (row 4) the total cost function is higher than it is with the same R values and $\beta = 0.5$ (row 3), but lower than if $\beta = 0.5, R_{Pac} = 3.5\,\mathrm{km}, R_{DP} = 4.0\,\mathrm{km}$ (row 5). The the row 4 and 5 combinations give a better fit to the Pacific transect by increasing the mixing here, but to the detriment of the fit on the Albatross transect. Out of these three runs the best fit to the SR1 widths is row 5, but this also has the worst fit to the Albatross transect, because the effects of higher mixing in the Drake Passage region are evident here. The increase of K_h (rows 10-12) improves the fit for the vertical widths

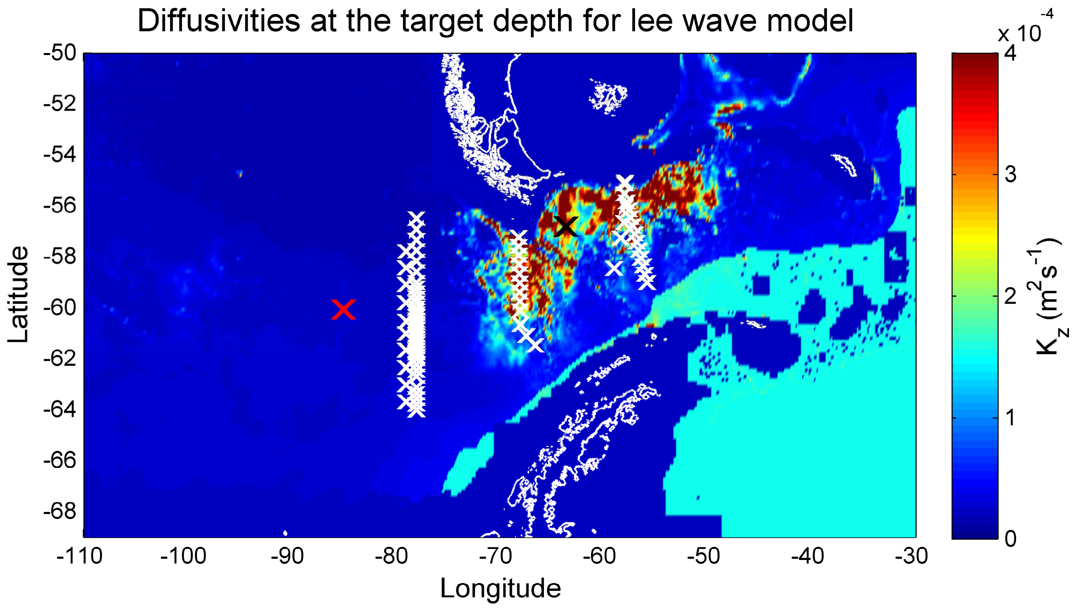

Figure 5.19: Map of diffusivity at the target depth for the lee wave model, with optimised parameters $\beta = 0.5, R_{Pac} = 4\,\text{km}, R_{DP} = 3.5\,\text{km}$, and a split longitude of 67°W between the Pacific and Drake Passage regimes. The positions of the UK2 and UK2.5 tracer stations are overlayed (white crosses). Also marked are locations in the Pacific (red cross) and Drake Passage (black cross) where the vertical profiles of model diffusivity are plotted on figure 5.20.

on SR1, while worsening it on the Albatross transect. Therefore while the fully optimised set of parameters (row 13) undoubtedly gives a better fit to the tracer data than any arbitrary combination within the range studied, none of the parameters may be individually regarded to be very well constrained. The diffusivity field that results from the optimisation of the lee wave model parameters is shown in figure 5.19 and 5.20. The location of the vertical profile in Drake Passage is chosen to represent a region of high mixing, and has a value of $5 \times 10^{-4}\ \text{m}^2\ \text{s}^{-1}$ at the target depth.

5.3.3 Comparison of models of diffusivity

The vertical widths and peak concentrations for the optimised run from each category of diapycnal diffusivity field presented in Chapters 4 and 5 are shown on figure 5.21 and 5.22. In general, the observation-based fields (microstructure and lee wave) have reproduced slightly more closely some of the meridional variation in the vertical widths on the Pacific transects when compared with the simple models (2 zone and enhanced K_z). On the Albatross transect, the 2 zone and microstructure runs give the closest fit, where the lee wave and enhanced K_z runs have overestimated the widths across most of the transect,

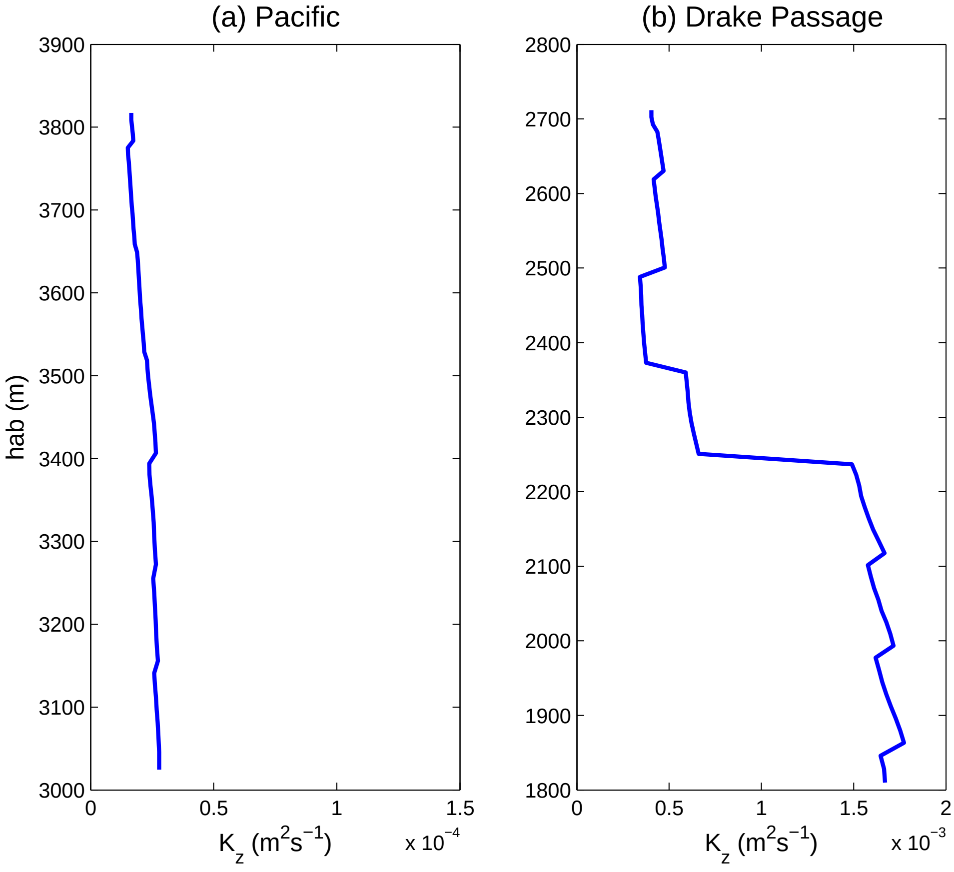

Figure 5.20: Vertical profiles of diffusivity from the lee wave model in (a) the Pacific and (b) Drake Passage. The profiles are at locations marked on figure 5.19 by (a) a red cross and (b) a black cross.

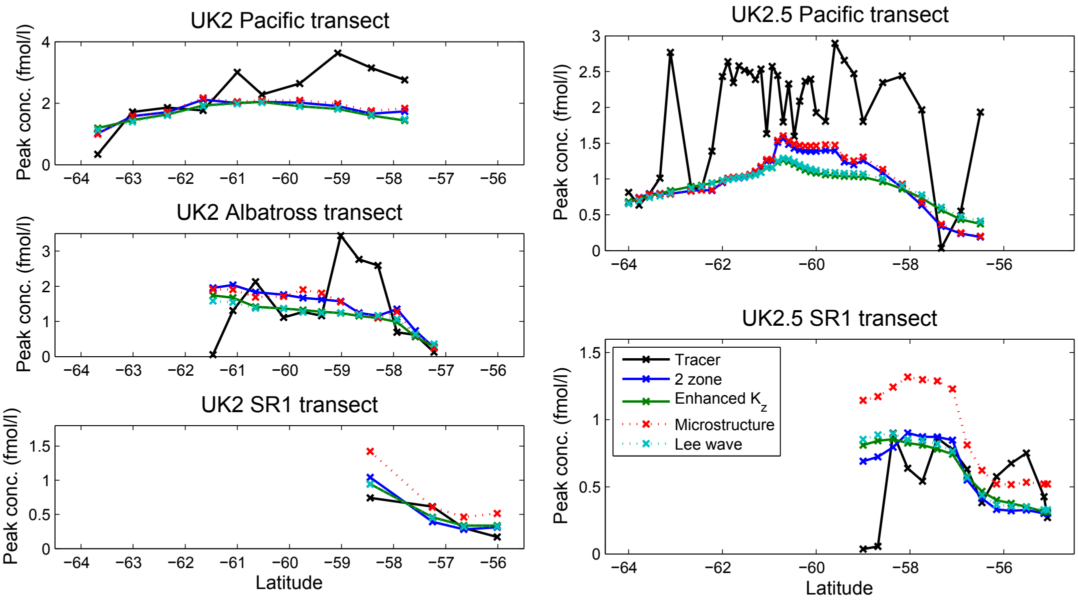

Figure 5.21: Peak concentrations for the optimised runs from each category of diffusivity field presented compared with the tracer.

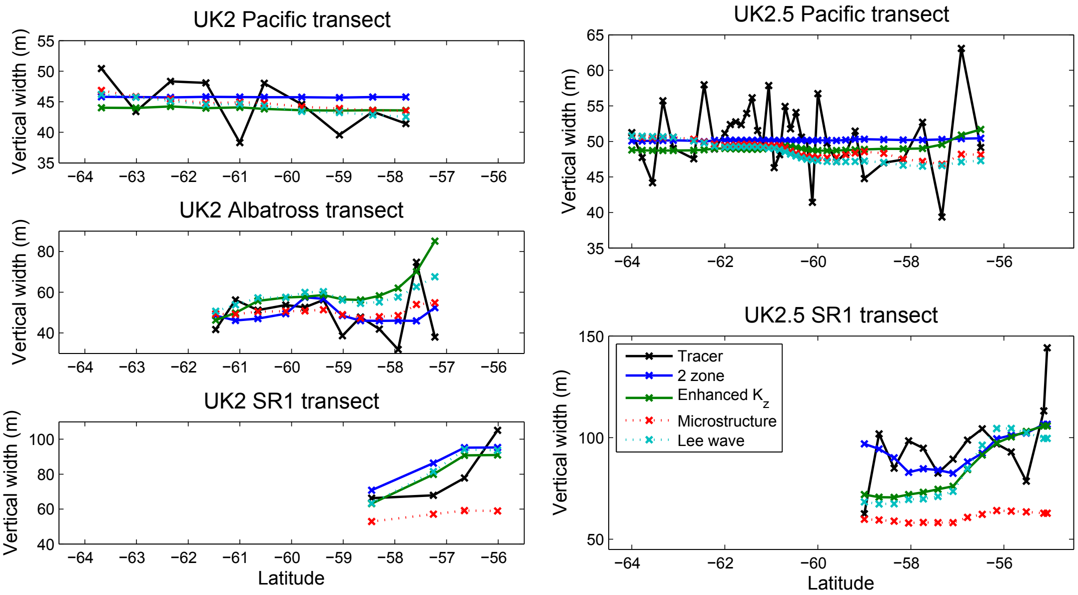

Figure 5.22: As figure 5.21 but for vertical widths.

and particularly in the northern half. On SR1 the differences between the runs is most stark. The microstructure gives the poorest fit, having substantially underpredicted the mixing leading to narrow profiles across SR1. The lee wave and enhanced K_z runs give very similar results, both yielding wider profiles on the north of the SR1 transect than the south, in contrast to the tracer, where profiles are wide all the way along. The 2 zone run, where mixing is enhanced everywhere east of 67°W, is the only model to reproduce this pattern on SR1. The contributions to the cost function from the vertical widths on each transect are shown on figure 5.23, and the transect mean vertical widths are summarised in table 5.3.

Table 5.3: Comparison of the model outputs from each type of diffusivity field that give the closest fit to the experimental tracer. Columns 2-6 give the mean vertical widths of model outputs by transect (all quantities are in metres), with experimental tracer transect means in brackets at the top. Transects from left to right: UK2 SR1, UK2 Albatross, UK2 Pacific, UK2.5 Pacific, UK2.5 SR1.

Run	UK2 SR1	UK2 Alb	UK2 Pac	UK2.5 Pac	UK2.5 SR1
	(79.3)	(48.7)	(44.5)	(50.7)	(95.9)
2 zone	86.9	49.2	45.8	50.2	93.7
Enhanced K_z	81.2	59.5	43.8	49.1	85.5
Microstructure	57.0	50.3	44.8	48.9	60.7
Lee wave	83.1	57.7	44.3	48.5	84.2

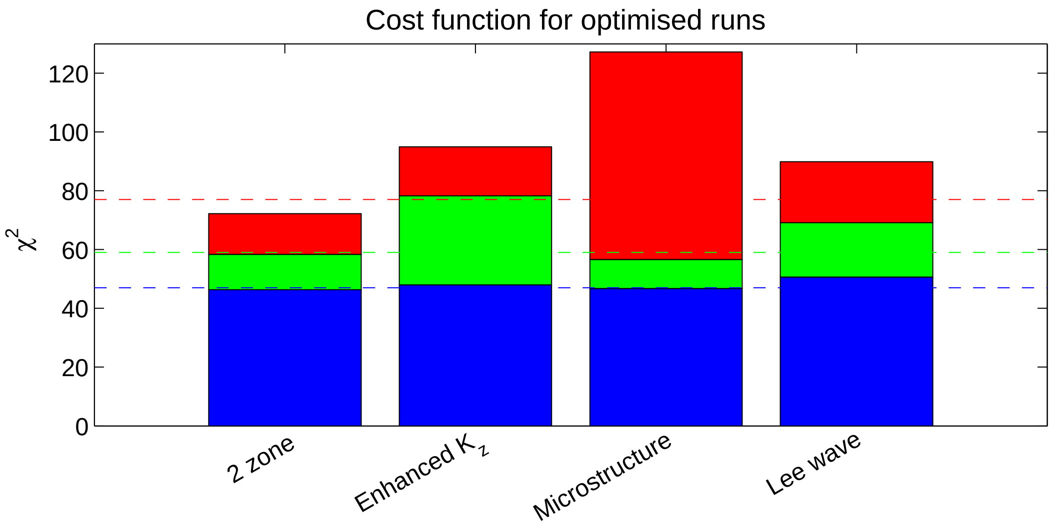

Figure 5.23: Contributions to the cost function from the vertical widths on the Pacific (blue), Albatross (green), and SR1 (red) transects for optimised model runs in each category of diffusivity field. Expectation values are shown by the dashed lines.

5.4 Discussion

Three possible explanations are suggested for the underprediction of the tracer mixing by microstructure, the first two of which involve the ability of limited microstructure sampling to capture the spatial and temporal variation in mixing. To address the issue of temporal variation, a time series of finestructure-based diffusivity estimates from an ADCP on the DIMES mooring array referred to in section 5.3.1 was used. Daily estimates of K_z at 2800-3300 m were inferred from buoyancy-normalized shear spectra using the method described in Gregg et al. (2003) for the period 12 December 2009 to 6 March 2012, and the distribution of this time series was investigated. K_z shows a strong positive skew, and in fact has a distribution that is (very approximately) log-normal in shape, indicating that average mixing may be dominated by a few, strong events. The shape of the distribution inevitably favours an underestimate of the mean value by sparsely sampled measurements, as the median is significantly smaller than the mean. A simple Monte Carlo simulation suggests that if this time series were sampled on 10 days (approximately equivalent to the microstructure sampling), the probability of an underestimate of the true mean value would be 60%. However, despite this tendency, the difference between the median and mean (25%) is very likely to be too small on its own to explain the 80% K_z discrepancy in Drake Passage. It should be noted that the location of the mooring array at the north end of SR1 and generally north of the Sub-Antarctic Front may not be representitive of the rest of Drake Passage; and also that K_z here is based on a finescale parameterisation, with the uncertainties that entails (see e.g. Polzin *et al.*, 2013, and references therein). The investigation into the temporal variation of diffusivities from the mooring observations was carried out by Alex Brearley.

Regarding the spatial sampling, the result that the microstructure based K_z fields were able to reproduce the mixing experienced by the tracer in the Southeast Pacific but not in Drake Passage is consistent with prevous evidence cited in section 5.1.1 that microstructure measurements have tended to underestimate mixing compared with tracers in inhomogeneous regions. The mixing in Drake Passage is likely to be both temporally and spatially highly inhomogeneous due to meandering jets interacting with complex topography. For example, we would expect intense mixing on the South American continental slope where the tracer isopycnal comes close to the bottom topography (indeed such mixing is suggested by the very wide tracer profiles at the northern end of UK2.5 SR1 - see figure 5.22), and also south of Burdwood Bank (around 60°W, 55°S) where RAFOS float tracks released at the tracer depth indicate a large standing meander (Brearley *et al.*, 2014); two areas sampled only once each by microstructure. However, for the lack of sampling in these relatively small areas to account for the microstructure model/tracer discrepancy further south on SR1, vertical mixing would have had to have been a) extremely high in these locations and b) redistributed further south by isopycnal mixing (the latter possibility is discussed further later in this section). The pattern of the tracer vertical widths on UK2.5 SR1 when compared with the microstructure model suggests that intense mixing was missed by microstructure both in the above identified key areas, and over a wider area covering the entire northern half of Drake Passage.

The third explanation involves the mechanisms of cabbeling and thermobaricity, which cause the vertical advection of tracer particles through isopycnal mixing due to nonlinearities in the equation of state of seawater, and hence may contribute to the widening of vertical tracer profiles. These processes are not associated with the dissipated turbulent motions measured by microstructure profilers, and are likely to become more important in the Drake Passage region where along isopycnal temperature and salinity gradients and isopycnal diffusivities are enhanced (Klocker and McDougall, 2010b). However, it should be noted that nonlinearities are likely to be at most a small contribution to the discrepancy, since their effects would tend to cause the vertical tracer distribution to be skewed towards higher densities, and the tracer profiles do not obviously show this (see Appendix B).

To summarise, some proportion of the large discrepancy between the rates of diapycnal mixing implied by microstructure and tracer measurements in this region may be explained by a combination of a lack of microstructure sampling, both spatial and temporal, with perhaps a smaller contribution from nonlinear effects. However the question of whether these explanations can account for the whole of the mismatch highlighted by this study remains open.

A model fitting lee wave fluxes to the tracer came closer to capturing the zonal variation in vertical mixing, but predicted too much meridional inhomogeneity for the mixing in Drake Passage. It appears that the tracer has undergone strong vertical mixing across its entire meridional extent, a fact that does not seem consistent with theoretical predictions about where we should expect intense lee wave driven mixing. None of the model runs reproduce strong mixing in the south, because in this region the tracer target isopycnal is far from the bottom as it shoals towards Antarctica, and in addition the predicted rates of bottom lee wave generation are low due to weaker stratification (Nikurashin and Ferrari, 2010a). One possibility is that isopycnal processes have acted to homogenise the vertical mixing of the tracer, although this is not indicated by the investigation into the model horizontal diffusion coefficient K_h. It may be that eddies associated with higher baroclinic modes not captured by the SatGEM fields are causing the observed homogenisation in a manner not reproduced by K_h. Brearley *et al.* (2014) have proposed that such eddies, which have scales of 10-30 km, are responsible for the disintegration just upstream of the northern end of SR1 of a boundary current which flows southward along the coast of Chile and into Drake Passage at a depth slightly below the DIMES tracer isopycnal. Naveira Garabato *et al.* (2007) found the high helium signature from this boundary current to be highly homogenised downstream of Drake Passage, a fact consistent with isopycnal mixing by these eddies. If tracer were strongly diapycnally mixed due to lee waves in the northern half of Drake Passage, then recirculated by eddies before continueing to SR1, it is conceivable that this might produce the pattern of mixing observed. In particular, the fact that between $56.5°$S and $58.5°$S on SR1 at the time of UK2.5 (see figure 5.22), tracer profile widths are around 90m on average, whereas in the same latitude range 3 months earlier at the time of UK2, the average width at 70m is significantly less, seems consistent with this theory.

An alternative explanation to the horizontal homogenisation of lee wave-induced vertical mixing is that there is a tidal contribution in the south of Drake Passage. Nikurashin and Ferrari (2013) found that M2 conversion to internal tides is large in Drake Passage when compared with the rest of the Southern Ocean, and although at the DIMES mooring site the energy is small compared with the lee wave contribution (Brearley 2013, personal communication), this may not be the case in other areas. Finally, the fact that the model seems to overpredict the mixing in the northern half of Drake Passage, as highlighted in particular by the $\beta = 1$ run illustrated on figure 5.15, may be explained by simplifications adopted in the NF model. For example, if the steering of some proportion of the bottom flow around bottom topography is taken into account this reduces lee wave estimates (Nikurashin *et al.*, 2014). Empirical evidence for this overprediction by lee wave theory, particularly in regions of rough topography, is also shown by Waterman *et al.* (2013), Sheen *et al.* (2013) and Brearley *et al.* (2013).

There are also conclusions to be drawn from the 2-zone model and its comparison with the other, more empirically based realisations. First, the combined use of the model with the tracer release experiment have proven that significantly enhanced diapycnal mixing is occurring at mid-depths in Drake Passage, an energetic region with rough topography, compared with that found in the quieter Southeast Pacific. This contributes to the base of evidence that mixing in this and similar regions is important to the global overturning circulation. A likely reason that the 2-zone model was best at reproducing the observed tracer mixing is that sources of enhanced mixing are so localised that the model tracer advection is not precise enough to reproduce the interaction with these sources in a realistic way. Since in the 2-zone model mixing is enhanced everywhere, the path of the tracer through Drake Passage becomes less important to reproducing the measured amount of integrated mixing. In addition, the likely time dependence of mixing in the real ocean would be missed by the microstructure and lee wave models which use a time-invariant diffusivity field, but would be compensated for in the 2-zone model in the same way as it compensates for the spatial variation.

A useful extension of this work would be to expand the methods used to predict diapycnal diffusivities to a wider area, for example the whole of the Southern Ocean. With an adjustment for the overestimate of lee wave flux by the NF model, the magnitude of the average mixing in both the Southeast Pacific and Drake Passage has been reproduced, but a method is needed for setting the appropriate ranges for the upward propagation of lee waves. Sheen *et al.* (2013) explain the variation in the upward penetration of lee waves observed in the microstructure data on the four transects (Pacific, Albatross, Phoenix Ridge and SR1) as described in section 5.1.2 in terms of the steepness parameter S introduced in section 5.1.3. They attribute the Pacific transect as corresponding to the $S < 0.3$ regime; the Phoenix Ridge as corresponding to the $S > 0.3$ regime; and the Albatross and SR1 transects as a mixture of the two. From the microstructure profiles they find 26% of the energy is dissipated in the bottom km on the Pacific transect; 63% on the Albatross transect, 76% on the Phoenix Ridge and 40% on SR1. The optimised values of the range over which energy is dissipated for the lee wave model are explained as follows: in the Pacific, the $S < 0.3$ regime applies and fluxes may penetrate all the way up through the water column, so the maximum range of $R_{Pac} = 4.5\,\mathrm{km}$ is appropriate. In Drake Passage, the Phoenix Ridge represents a small area where the $S > 0.3$ regime applies, but this is a small contribution to the overall mixing in the region. The majority of Drake Passage is more likely to be characterised by the mixed regime, meaning an intermediate value for R_{DP} of 3.5 km is appropriate. We therefore suggest that setting R according to the steepness parameter might allow for an extrapolation of the predicted diapycnal mixing rates to the rest of the Southern Ocean. It should be noted, however, as was detailed in section 5.3.2, the caveat to this analysis that the values of R_{Pac} and R_{DP} have not been well constrained by the optimisations of the lee wave model.

5.5 Summary

In this chapter, two new types of diapycnal diffusivity field were tested for their ability to reproduce the mixing implied by the DIMES tracer measurements, and the results compared with the models tested in Chapter 4. Diffusivities constructed from microstructure data reproduced the pattern of mixing well in the Southeast Pacific, but entirely failed to capture the strongly enhanced mixing in Drake Passage. An investigation into the temporal variability of turbulent dissipation from mooring data found that it could not account for the 5-fold discrepancy between the mixing implied by microstructure and that inferred from the tracer. It is concluded that a lack of spatial sampling must be the primary cause of the apparent disagreement. A model which used predicted rates of lee wave generation to construct a diffusivity field produced results which were a closer fit to the observations in Drake Passage than the microstructure models, but that still failed to reproduce the wide profiles seen along the length of the SR1 transect on UK2.5. The 2 zone model of Chapter 4 remains the only implementation that resulted in a good approximation to the meridional distribution of the vertical widths measured on this transect, suggesting that either there are homogenising processes at work in the real ocean not captured by the model, or that other sources of energy not predicted by the lee wave theory are responsible for enhanced mixing in the south of Drake Passage.

Chapter 6

Conclusion

6.1 The diapycnal mixing problem

Over the past few decades, considerable effort has gone into measuring rates of diapycnal mixing in the ocean, and into understanding the processes that drive it. An ongoing question has been how to reconcile the diapycnal mixing required to maintain the abyssal stratification and close the overturning circulation as calculated by Munk (1966) with observations of the open ocean. One of the key results of recent research is that diapycnal mixing rates are enhanced in the vicinity of rough topography, which has been attributed to the generation of internal waves which propagate away and then break, causing mixing. In the Southern Ocean, a large input of energy by the strong westerly winds can be transferred to the circulation in part by the conversion through baroclinic instability to geostrophic eddies. These eddy flows generate lee waves when they impinge upon bottom topography, resulting in enhanced rates of diapycnal mixing. The work of this thesis has been to use experimental data from a tracer release experiment and from microstructure and finestructure observations collected as part of the DIMES project combined with numerical models to study the diapycnal mixing in Drake Passage, an important region of the Southern Ocean.

6.2 Summary of key results

In Chapter 2, some results from the DIMES tracer experiment were presented, and mean vertical profiles of tracer concentration were used to ascertain estimates of time- and spatially-averaged mixing. In Chapter 3, a simple 2D model was used to refine these estimates, comparing model vertical tracer profiles with observations and quantifying the model-data fit using a cost function. By setting up the model with two values of diapycnal diffusivity, one west of $67°$W to represent the relatively quiet Southeast Pacific region, and one east of that longitude representing the more energetic Drake Passage, estimates of $K_{z_p} = 1.69 \pm 0.05 \times 10^{-5}\ \mathrm{m}^2\ \mathrm{s}^{-1}$ in the Pacific and $K_{z_d} = 3.3 \pm 0.4 \times 10^{-4}\ \mathrm{m}^2\ \mathrm{s}^{-1}$ in Drake Passage were obtained.

In Chapter 4, a 3D model was applied to the problem of the DIMES tracer evolution, combining offline MITgcm with observation-based velocities derived from SatGEM, a product which uses satellite altimetry with a gravest empirical mode projection of temperature and salinity to produce 3D time-evolving velocity fields for the Southern Ocean. The 3D model revealed estimates for the average diapycnal mixing in the two regions of $K_{z_p} = 2.5 \pm 0.1 \times 10^{-5}\ \mathrm{m}^2\ \mathrm{s}^{-1}$ and $K_{z_d} = 3.5 \pm 0.5 \times 10^{-4}\ \mathrm{m}^2\ \mathrm{s}^{-1}$; the latter value being in agreement with the 2D model, and the former an estimate for the average mixing in year 2 of the experiment, indicating that more mixing occurred in year 2 than year 1 in the Southeast Pacific region. Prescribing diapycnal diffusivity fields to the model where mixing was enhanced according to the proximity of the tracer target isopycnal to the bottom topography reproduced the observed enhancement of mixing in Drake Passage, but the model-data fit was not as good as for the simple 2 zone model. In particular, mixing was overestimated just to the west of Drake Passage, and the mixing in Drake Passage was preferentially enhanced to the north but not to the south, at odds with the tracer observations.

In Chapter 5, the 3D model was used to test diffusivity fields based on DIMES microstructure and finestructure data, and on a model of lee wave generation. Microstructure predicted the mixing implied by the tracer measurements well in the Southeast Pacific, but in Drake Passage the average mixing was five times lower than that diagnosed using the 2 zone model. Lee wave based diffusivity fields produced similar results to the Enhanced K_z model of Chapter 4, finding mixing was overpredicted in the north and underpredicted in the south of Drake Passage. Attempts to homogenise the horizontal distribution of vertical mixing by increasing the parameterised horizontal diffusivity K_h did not have the desired effect, with a bias towards wide tracer profiles in the north of SR1 not present in the observations persisting for large horizontal diffusivities.

6.3 Discussion of methods

6.3.1 Cost function

For all the numerical modelling efforts reported in Chapters 3 to 5, a cost function was used to quantify the fit between model outputs and the tracer observations. Optimisations were carried out to minimise the cost function, and to determine uncertainties on model derived estimates of diapycnal diffusivity. The validity of these uncertainty estimates depends on the assumption inherent in the cost function calculation that the observations are normally distributed. An assesment is therefore made of the frequency distributions on each transect of the two types of observations which were used in the model-data comparison, the tracer concentration profile vertical widths and peak concentrations (see Appendix C for plots of the distributions). Applying the Shapiro-Wilk test to the vertical widths, all transects satisfy normality at the 90% confidence level except for the SR1 transect on UK2, which has too few data points to apply the test. The peak concentrations are in general not normally distributed, which may in part account for the fact that the contributions from the comparison between model and observed peak concentrations to the cost function were above the expectation values (although the model skill in accurately reproducing the tracer advection is likely to be the bigger factor). However, since the peak concentrations' contribution to the cost function were not included in the optimisation of the 2 zone models for diapycnal diffusivities, these uncertainty estimates are unaffected. Since due to various factors it is not possible to compare model and observed tracer profiles at every station, some consideration of which stations to include in the cost function has been made, and the effect of the station selections on the cost function must also be considered. For example the inclusion of the two most northerly stations on the UK2.5 SR1 transect has two simultaneous effects on the optimisation of the 2 zone model: it causes a slight increase in the mixing in Drake Passage required to minimise the cost function since these profiles are very wide, but also lowers the contribution of each profile on this transect by increasing the variance ${\sigma_{w_T}}^2$, hence downweighting the transect. While these limitations mean that there may be some additional uncertainty in the estimates of diapycnal diffusivity obtained using the cost function, the overall conclusions drawn from the optimisations, and from the use of the cost function to compare the skill of different models of diffusivity at reproducing the mixing implied by the tracer observations, are still valid. In particular the qualitative comparison of the model outputs with observations made using plots of the model and observed vertical widths and peak concentrations lends additional credibility to the conclusions.

6.3.2 Constant stratification approximation

The most significant limitation of the 3D model is the assumption of constant stratification, which is required for internal consistency within the framework of MITgcm, since it has been applied to the evolution of the tracer along/across isopycnals. Some investigation into the effect of this approximation on the tracer advection was made in Chapter 4. What is more difficult to quantify is the effect of approximating a constant thickness of isopycnal surfaces on the diagnosed diapycnal diffusion. The model level thicknesses were chosen using a mean (see section 4.2.6), so in theory the places in the model where the stratification is underestimated compared with the real ocean and the places it is overestimated should cancel out. However, if regions of higher diffusivity along the path of the the tracer are correlated with regions of stronger (or weaker) than average stratification in the ocean then the effect of mixing on the tracer profile widths in density space will have been underestimated (or overestimated) leading to an overestimate (or underestimate) of the diffusivity from optimisation. This could lead to a systematic bias on the values of K_z obtained from the optimisation of the 2 zone model, although the size of this bias would be difficult to quantify since the path of the tracer through the model is complex. However, while such a bias might mean that the precise values of K_z are not as robust as they might be, its effect is unlikely to be large enough to change the general conclusion that mixing in Drake Passage is enhanced by at least an order of magnitude compared with the Southeast Pacific. The values of K_z derived from dissipation in Chapter 5 should be immune to this effect, because the diapycnal mixing is related to the dissipation through the Osborn relation, so the diapycnal spreading of the tracer will be appropriate for the model stratification.

6.3.3 SatGEM fields

The velocity fields used to advect the tracer have two significant limitations: the fact that they do not exist where the water depth is less than 2000 m, and their relatively coarse horizontal resolution. The impact of the first issue is that the advection of the tracer in Drake Passage may not have been accurately reproduced following the processing of the velocity fields to render them non-divergent. However, it is not necessarily the case that an alternative product would do a better job; in fact the limited investigation carried out using SOSE in Chapter 4 found its reproduction of the large-scale tracer advection to be inferior to that of SatGEM. Where an alternative velocity field might have a more clear advantage is in superior horizontal resolution, as the limited resolution of SatGEM may have implications for the horizontal mixing of the tracer (see section 6.4.2).

6.4 Discussion of main conclusions

6.4.1 Microstructure-tracer comparison

The result that diapycnal diffusivity fields constructed from microstructure measurements of dissipation were five times too low to account for the mixing implied by the tracer observations must be explicable in the main by a lack of sampling, if we assume that our fundamental understanding of the physics involved is not at fault. The ‘mixing efficiency’ of 0.2 in the Osborn relation has been used when estimating mixing from dissipation, although this value does not necessarily always apply. However, investigations into its variability (e.g. Arneborg, 2002) have found that it may be lower, but not higher. This is unsurprising, since the value of 0.2 in Osborn (1980) was defined as an upper limit. Ledwell *et al.* (2011) explained a two-fold underestimate in the mixing measured by microstructure compared with that implied by the tracer in the first year of the DIMES experiment as resulting from elevated shear variance in the winter relative to the summer when dissipation was measured. They attributed this to downward propagating near-inertial waves caused by high-frequency wind variability at the surface. While this effect may well have had an impact on the tracer evolution in Drake Passage, its contribution will be much smaller as a proportion of the overall mixing, which is an order of magnitude greater due to upward propagating lee waves. Therefore the likelihood is that the underestimate of mixing by microstructure may be attributed in the main to a lack of sampling in the most energetic region encountered by the tracer in Drake Passage, which must be between the Phoenix Ridge and SR1 transects.

6.4.2 Lee wave model-tracer comparison

There were three areas in which the lee wave model of diffusivity was unable to reproduce the pattern of mixing implied by the tracer observations. The first, that mixing was overpredicted west of the Albatross transect, I have suggested may be attributable to the coarse resolution of the grid of topographic roughness. St. Laurent *et al.* (2012) measured lower levels of dissipation on the Albatross transect compared with the Phoenix Ridge, which they attribute to the smaller amplitude abyssal hills which characterise the bottom topography. The second area of discrepancy was that mixing was significantly overpredicted in the north of Drake Passage if the lee wave fluxes were applied with a β factor of 1. This can be explained by topographic steering effects as discussed in section 5.4.

The final issue, that mixing by the lee wave model was underpredicted in the southern half of the tracer patch in Drake Passage leading to narrow profiles on the southern stations of SR1, is the most difficult to explain. Tidal mixing is offered as a candidate contributor to the tracer mixing, but St. Laurent *et al.* (2012) point out that the long timescale of variation of the ACC in the study region is not favourable to the production of tidal induced internal waves. In addition, enhanced tidal driven mixing has been found to decay to background levels away from the topography from which it was generated (e.g. Polzin *et al.*, 1997; Rudnick *et al.*, 2003), so tidal mixing may not be any more likely than lee waves to be responsible for enhanced mixing over a large geographical area.

Waterman *et al.* (2013) report enhanced mixing in the upper 1500 m from a survey in the Southern Ocean north of the Kerguelen Plateaux (around 69°E), but the reported mixing rates are still less than 10^{-4} m^2 s^{-1}, 3-4 times smaller than the average diffusivity diagnosed from the tracer for Drake Passage. Referring back to figure 4.1, the depth of the tracer isopycnal is within 1000m of the surface over the Southern half of Drake Passage, so enhanced mixing due to downward propagating internal waves could be a contributing factor here. If such enhancement does exist, it has been missed by the microstructure observations that were used to construct the downward propagating background for the lee wave model.

Probably the most tenable explanation for the pattern of mixing of the tracer in Drake Passage is that, having been mixed in a few key areas by lee waves, the effect of the diapycnal mixing on the tracer is homogenised by isopycnal processes. Musgrave (1985) found that increasing the value of a parameterised horizontal diffusivity in a model actually decreased the homogenisation of tracers within a gyre. Therefore the fact that increasing K_h in my model was not effective at homogenising the vertical widths of the model tracer profiles does not necessarily indicate that isopycnal mixing can be ruled out of having played this role. It could be that an eddy resolving model would be capable of reproducing the submesocale isopycnal mixing in a way that the model presented here was not.

6.5 Implications for the overturning circulation

This work has demonstrated that significantly enhanced diapycnal mixing driven by bottom generated lee waves over rough topography can penetrate to mid-depths in Drake Passage. This means that diapycnal mixing due to similar processes over the rest of the Southern Ocean where the ACC interacts with such topography may be capable of providing a significant proportion of the upwelling originally predicted by Munk (1966) as required to close the global overturning circulation. The picture of the overturning advocated by Marshall and Speer (2012) (shown on figure 1.1) was of an upper and a lower cell of the circulation separated approximately by the $\gamma_n = 27.6$ isopycnal. At $\gamma_n = 27.906$, the DIMES tracer target surface is situated in the lower cell, but close to the boundary with the upper cell. The high rates of mixing at these depths in Drake Passage, and by extrapolation over other regions of the Southern Ocean, suggest that diapycnal mixing could be responsible for much of the return flow of Antarctic Bottom Water to mid depths in the Southern Ocean, and could also play a key role in linking the upper and lower cells of the MOC. Marshall and Speer's picture of adiabatic upwelling along the sloping isopycnals of the Southern Ocean is undoubtedly part of the solution, but the role of strong diabatic (diapycnal) processes must not be discounted.

The 14-fold increase in area-averaged mixing rates between the Southeast Pacific and Drake Passage regions also highlights the need for a more sophisticated treatment of diapycnal mixing in ocean models. Furthermore, the fact that it was not possible to meaningfully extrapolate from point microstructure measurements taken over 3 separate oceanographic cruises to the wider region in Drake Passage provides evidence for the transient and localised nature of these mixing events. Both the spatial and temporal variability in diapycnal mixing are likely to be crucial to our understanding of the global circulation.

6.6 Recommendations for further work

An extension of the work using the 2D model can be implemented by splitting up the domain into more zones, for example adding a third zone east of Drake Passage to represent the Scotia Sea. More DIMES tracer data collected on cruises from UK3 onwards may then be added to the model-data comparison. A different approach needs to be taken to estimate along-stream distance, however, than the simple assumption of zonal flow that was made in Chapter 3. Such efforts are currently being made by Mills (2014) (in preparation).

The 3D model also has the capability of being run for an extra year to simulate the tracer advection into the Scotia Sea, since the SatGEM velocity fields for this time period are available. The model could then be compared with the UK3 tracer data on the Albatross transect, SR1 and the North Scotia Ridge. The North Scotia Ridge would present challenges, however, for the isopycnal model configuration, since it comes up to the depth of the tracer isopycnal in various places, so some consideration would need to be given to the model bathymetry. With the additional tracer profile data, the mixing estimates using a 2 or 3 zone diffusivity field could be well constrained.

Further work using microstructure data obtained on the UK4 and UK5 DIMES cruises to construct diffusivity fields for the 3D model would also be beneficial. In particular, microstructure has now been sampled in some of the region between the Phoenix Ridge and SR1 which was identified as a likely site of enhanced mixing, which could contribute to reconciling the discrepancy between microstructure and tracer observations identified in this thesis.

Refinements of the NF model of lee wave generation specific to Drake Passage have recently been made Nikurashin *et al.* (2014). If a better fit to the tracer data were achieved by applying the new NF fluxes fluxes to the lee wave model presented here, then this might form the basis for a new parameterisation of diapycnal mixing due to breaking internal lee waves in the Southern Ocean.

Appendix A

2D model optimisations

Table A.1 details the exploration of the parameter space carried out during the optimisations of the 2D model in Chapter 3, the results of which are shown on table 3.1. In most cases there is a pair of optimisations for each of the rows in table 3.1 - the first with a wider range for each variable and coarser resolution (greater step), and the second with a narrower range and smaller step. In the case of the UK2/UK2.5/UK3 widths only optimisation in potential density (row 7 of the main body of table A.1), the full optimisation has been carried out in one. It should be noted that for the optimisations involving only the vertical widths' contribution to the cost function, the range on the velocities is guided by the uncertainties on the SatGEM means as described in section 3.3.4. It should also be noted that the choice of the outer ranges for all parameters was informed by significant numbers of previous optimisations by the other methods outlined in section 3.3.2. The choice of range and step is a compromise between the need to explore the parameter space as thoroughly as possible and the limitations of computation speed. The behaviour of the cost function within the parameter space is also used to guide the optimisations, for example if a minimum is not found using a given range for a particular variable then the range for that variable may be extended at one end. The exception to this is the SatGEM derived velocity ranges for the widths only optimisations. The fully optimised values for K_z shown on table 3.1 are obtained following an additional stage of optimisation using Matlab's `fminsearch` as detailed in section 3.3.2.

Table A.1: Parameter space explored during optimisations of the 2D model. Columnns 1 and 2 detail the cruises and the types of observation (vertical widths, W and peak concentrations, C) which contributed to the cost function. Column 3 gives the density system used for interpolating the tracer measurements before calculating the vertical widths, either neutral density (γ_n) or potential density referenced to 1500m ($\sigma_{1.5}$). The remaining columns give the model velocity (u), horizontal diffusivity (K_h), and vertical diffusivity (K_z) for the Pacific (p) and Drake Passage (d) zones, showing the parameter space explored in the format $[min\ value : step : max\ value]$.

Cruises	Obs.	ρ	u_p $(\mathrm{cm\,s^{-1}})$	K_{hp} $(\times 10^3\ \mathrm{m^2\,s^{-1}})$	K_{zp} $(\times 10^{-5}\ \mathrm{m^2\,s^{-1}})$	u_d $(\mathrm{m\,s^{-1}})$	K_{hd} $(\mathrm{m^2\,s^{-1}})$	K_{zd} $(\times 10^{-4}\ \mathrm{m^2\,s^{-1}})$
UK2+UK2.5	W	γ_n	2.51:0.2:2.91		1.5:0.1:1.9	6.05:0.4:7.65		3.0:0.2:5.0
UK2+UK2.5	W	γ_n	2.51:0.2:2.91		1.6:0.1:1.9	6.05:0.2:7.05		3.0:0.1:4.2
UK2+UK2.5	W	$\sigma_{1.5}$	2.51:0.1:2.91		1.7:0:1.7	6.05:0.1:7.15		2.0:0.2:5.0
UK2+UK2.5	W	$\sigma_{1.5}$	2.51:0.1:2.91		1.6:0.1:1.8	6.05:0.1:7.15		3.0:0.1:4.4
UK2+UK2.5+UK3	W	γ_n	2.51:0.2:2.91		1.6:0.1:1.8	6.05:0.2:7.05		2.0:0.2:4.0
UK2+UK2.5+UK3	W	γ_n	2.51:0.2:2.91		1.65:0.05:1.75	6.05:0.2:7.05		2.3:0.1:3.5
UK2+UK2.5+UK3	W	$\sigma_{1.5}$	2.51:0.1:2.91		1.6:0.1:1.8	6.05:0.1:7.15		2.0:0.1:4.0
UK2+UK2.5	W+C	$\sigma_{1.5}$	2.0:0.3:3.8	1:2:7	1.6:0.1:1.9	4.0:0.5:8.0	1:3:10	2.0:0.4:4.8
UK2+UK2.5	W+C	$\sigma_{1.5}$	2.6:0.2:3.20	2:1:4	1.65:0.05:1.75	3.0:0.5:7.0	1:3:10	2.2:0.1:4.2
UK2+UK2.5+UK3	W+C	$\sigma_{1.5}$	2.0:0.4:4.0	1:2:5	1.6:0.1:1.8	3.0:1.0:8.0	1:3:10	2.0:0.4:4.8
UK2+UK2.5+UK3	W+C	$\sigma_{1.5}$	2.6:0.1:3.0	2:1:4	1.65:0.05:1.75	5.5:0.5:7.5	1:2:7	2.2:0.1:3.4

Appendix B

Symmetry of tracer mean profiles

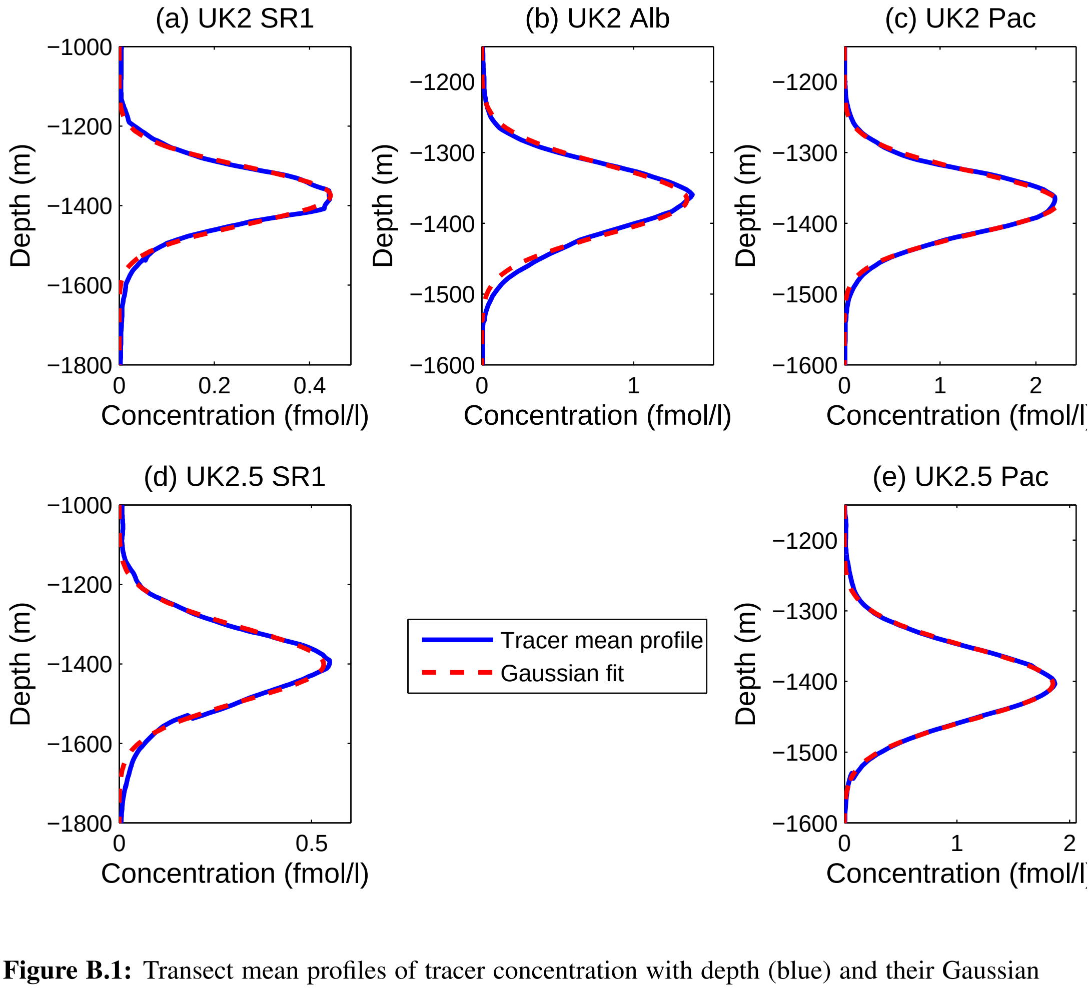

Figure B.1: Transect mean profiles of tracer concentration with depth (blue) and their Gaussian fits (red). Transects are (a) SR1 on UK2, (b) Albatross on UK2, (c) Pacific on UK2, (d) SR1 on UK2.5 and (e) Pacific on UK2.5. Profiles are plotted against the mean depth-density relation for UK2.5. The profiles are in general very close to Gaussian, with a slightly high deep tail on the SR1 and Albatross transects, which is likely to be due to an increase in diffusivity towards the bottom. There is no evidence of a skew towards higher densities in the tracer peaks, which would be expected if mechanisms involving nonlinearities in the equation of state of seawater were contributing significantly to the mixing.

Appendix C

Profile widths and concentrations

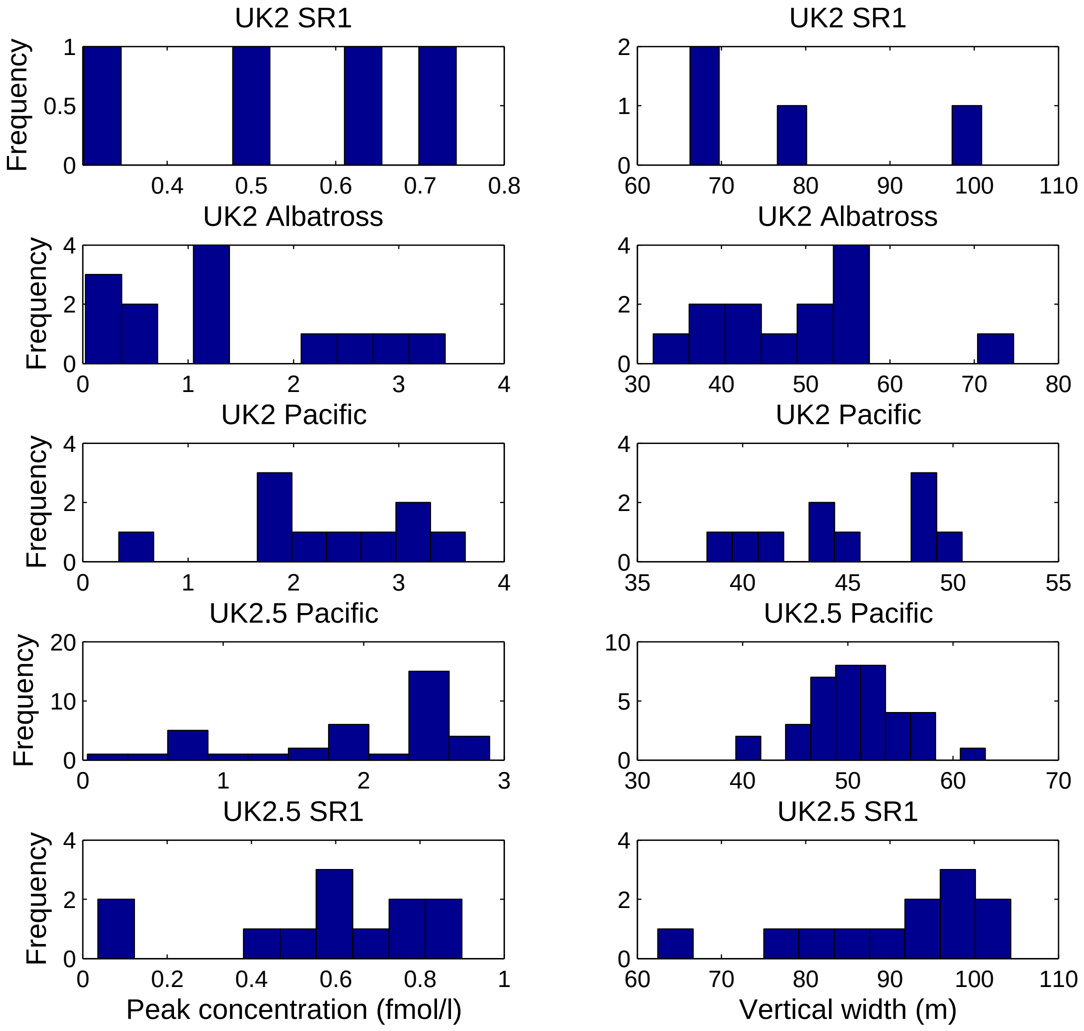

Figure C.1: Histograms of the tracer peak concentrations (left) and vertical widths (right) by transect from the UK2 and UK2.5 cruises.

References

Adcroft, A., R. Hallberg, J. P. Dunne, B. L. Samuels, J. a. Galt, C. H. Barker, and D. Payton (2010), Simulations of underwater plumes of dissolved oil in the Gulf of Mexico, *Geophysical Research Letters*, *37*(18).

Arneborg, L. (2002), Mixing Efficiencies in Patchy Turbulence, *Journal of Physical Oceanography*, *32*(5), 1496–1506.

Bell, T. H. (1975), Topographically generated internal waves in the open ocean, *Journal of Geophysical Research*, *80*(3), 320–327.

Bevington, P., and D. Robinson (1992), *Data reduction and error analysis in the physical sciences*, McGraw-Hill Inc, New York.

Brearley, J. A., K. L. Sheen, A. C. Naveira Garabato, D. A. Smeed, K. G. Speer, A. M. Thurnherr, M. P. Meredith, and S. Waterman (2014), Deep boundary current disintegration in Drake Passage, *Geophysical Research Letters*, *41*(1), 121–127.

Brearley, J. A., K. L. Sheen, A. C. Naveira Garabato, D. A. Smeed, and S. Waterman (2013), Eddy-Induced Modulation of Turbulent Dissipation over Rough Topography in the Southern Ocean, *Journal of Physical Oceanography*, *43*(11), 2288–2308.

Brown, E., A. Colling, D. Park, J. Phillips, D. Rothery, and J. Wright (2007), *Ocean Circulation*, The Open University.

Cairns, J. L., and G. O. Williams (1976), Internal wave observations from a midwater float, 2, *Journal of Geophysical Research*, *81*(12), 1943–1950.

Cox, C., P. Hacker, B. Johnson, and T. Osborn (1970), *Fine Scale of Temperature Gradient*, Tech. rep., Scripps Institution of Oceanography.

Cunningham, S. A., S. G. Alderson, and B. A. King (2003), Transport and variability of the Antarctic Circumpolar Current in Drake Passage, *Journal of Geophysical Research*, *108*(C5), 8084.

Egbert, G. D., and R. D. Ray (2000), Significant dissipation of tidal energy in the deep ocean inferred from satellite altimeter data, *Nature*, *405*, 775–78.

Ewart, T. E., and W. P. Bendiner (1981), An observation of the horizontal and vertical diffusion of a passive tracer in the deep ocean, *Journal of Geophysical Research*, *86*(C11), 10,974.

Ferrari, R., and M. Nikurashin (2010), Suppression of Eddy Diffusivity across Jets in the Southern Ocean, *Journal of Physical Oceanography*, *40*(7), 1501–1519.

Ferrari, R., and C. Wunsch (2009), Ocean Circulation Kinetic Energy: Reservoirs, Sources, and Sinks, *Annual Review of Fluid Mechanics*, *41*(1), 253–282.

Gargett, A. E. (1984), Vertical eddy diffusivity in the ocean interior, *Journal of Marine Research*, *42*(2), 359–93.

Garrett, C., and E. Kunze (2007), Internal Tide Generation in the Deep Ocean, *Annual Review of Fluid Mechanics*, *39*(1), 57–87.

Garrett, C., and W. Munk (1972a), Oceanic mixing by breaking internal waves, *Deep Sea Research and Oceanographic Abstracts*, *19*(12), 823–832.

Garrett, C., and W. Munk (1972b), Space-Time scales of internal waves, *Geophysical Fluid Dynamics*, *3*(1), 225–264.

Garrett, C., and W. Munk (1975), Space-time scales of internal waves: A progress report, *Journal of Geophysical Research*, *80*(3), 291–297.

Garrett, C., and W. Munk (1979), Internal Waves in the Ocean, *Annual Review of Fluid Mechanics*, *11*(1), 339–69.

Gent, P. R., J. Willebrand, T. J. McDougall, and J. C. McWilliams (1995), Parameterizing Eddy-Induced Tracer Transports in Ocean Circulation Models, *Journal of Physical Oceanography*, *25*(4), 463–474.

Gill, A., J. Green, and A. Simmons (1974), Energy partition in the large-scale ocean circulation and the production of mid-ocean eddies, *Deep Sea Research and Oceanographic Abstracts*, *21*(7), 499–528.

Gill, A. E. (1982), *Atmosphere-Ocean Dynamics*, Academic Press.

Goff, J. A., and T. H. Jordan (1988), Stochastic Modeling of Seafloor Morphology: Inversion of Sea Beam Data for Second-Order Statistics, *Journal of Geophysical Research*, *93*(B11), 13,589.

Gonella, J. (1972), A rotary-component method for analysing meteorological and oceanographic vector time series, *Deep Sea Research and Oceanographic Abstracts*, *19*(12), 833–846.

Gouretski, V. V., and K. Koltermann (2004), *WOCE Global hydrographic climatology*, Tech. rep., Alfred Wegener Institute, Bremerhaven.

Gregg, M. C. (1987), Diapycnal mixing in the thermocline: A review, *Journal of Geophysical Research*, *92*(C5), 5249.

Gregg, M. C., T. B. Sanford, and D. P. Winkel (2003), Reduced mixing from the breaking of internal waves in equatorial waters., *Nature*, *422*(6931), 513–5.

Hallberg, R. (2000), Time Integration of Diapycnal Diffusion and Richardson NumberDependent Mixing in Isopycnal Coordinate Ocean Models., *Monthly Weather Review*, (1993), 1402–1419.

Heywood, K. J., A. C. Naveira Garabato, and D. P. Stevens (2002), High mixing rates in the abyssal Southern Ocean., *Nature*, *415*(6875), 1011–4.

Ho, D. T., J. R. Ledwell, and W. M. Smethie (2008), Use of SF5CF3 for ocean tracer release experiments, *Geophysical Research Letters*, *35*(4), 1–5.

Hogg, N. G., P. Biscaye, W. Gardner, and W. J. Schmitz (1982), On the transport and modification of Antarctic Bottom Water in the Vema Channel., *Journal of Marine Research*, *40S*, 231–63.

Hughes, G., and R. Griffiths (2006), A simple convective model of the global overturning circulation, including effects of entrainment into sinking regions, *Ocean Modelling*, *12*(1-2), 46–79.

Jackett, D. R., and T. J. McDougall (1997), A Neutral Density Variable for the Worlds Oceans, *Journal of Physical Oceanography*, *27*(2), 237–263.

Karsten, R., H. Jones, and J. Marshall (2002), The Role of Eddy Transfer in Setting the Stratification and Transport of a Circumpolar Current, *Journal of Physical Oceanography*, *32*(1), 39–54.

Klocker, A., and T. J. McDougall (2010a), Influence of the Nonlinear Equation of State on Global Estimates of Dianeutral Advection and Diffusion, *Journal of Physical Oceanography*, *40*(8), 1690–1709.

Klocker, A., and T. J. McDougall (2010b), Influence of the Nonlinear Equation of State on Global Estimates of Dianeutral Advection and Diffusion, *Journal of Physical Oceanography*, *40*(8), 1690–1709.

Law, C., A. Watson, and M. Liddicoat (1994), Automated vacuum analysis of sulphur hexafluoride in seawater: derivation of the atmospheric trend (19701993) and potential as a transient tracer, *Marine Chemistry*, *48*(1), 57–69.

Ledwell, J., E. Montgomery, K. Polzin, St. Laurent LC, R. Schmitt, and J. Toole (2000), Evidence for enhanced mixing over rough topography in the abyssal ocean, *Nature*, *403*(6766), 179–82.

Ledwell, J. R., and A. Bratkovich (1995), A tracer study of mixing in the Santa Cruz Basin, *Journal of Geophysial Research*, *100*(C10), 20,681–704.

Ledwell, J. R., L. C. St. Laurent, J. B. Girton, and J. M. Toole (2011), Diapycnal Mixing in the Antarctic Circumpolar Current, *Journal of Physical Oceanography*, *41*(1), 241–246.

Ledwell, J. R., and A. J. Watson (1991), The Santa Monica Basin Tracer Experiment: A Study of Diapycnal and Isopycnal Mixing, *Journal of Geophysical Research*, *96*(C5), 8695–718.

Ledwell, J. R., A. J. Watson, and S. Law (1998), Mixing of a tracer in the pycnocline, *Journal of Geophysical Research*, *103*(C10), 21,499–529.

Lumpkin, R., and K. Speer (2007), Global Ocean Meridional Overturning, *Journal of Physical Oceanography*, *37*(10), 2550–2562.

Marshall, D. P., and A. C. Naveira Garabato (2008), A Conjecture on the Role of Bottom-Enhanced Diapycnal Mixing in the Parameterization of Geostrophic Eddies, *Journal of Physical Oceanography*, *38*(7), 1607–1613.

Marshall, J., and R. A. Plumb (2008), *Atmosphere, Ocean and Climate Dynamics*, Elsevier.

Marshall, J., and F. Schott (1999), Open-ocean convection: Observations, theory, and models, *Reviews of Geophysics*, *37*(1), 1.

Marshall, J., E. Shuckburgh, H. Jones, and C. Hill (2006), Estimates and Implications of Surface Eddy Diffusivity in the Southern Ocean Derived from Tracer Transport, *Journal of Physical Oceanography*, *36*(9), 1806–1821.

Marshall, J., and K. Speer (2012), Closure of the meridional overturning circulation through Southern Ocean upwelling, *Nature Geoscience*, *5*(3), 171–180.

Mazloff, M. R., P. Heimbach, and C. Wunsch (2010), An Eddy-Permitting Southern Ocean State Estimate, *Journal of Physical Oceanography*, *40*(5), 880–899.

McDougall, T. J. (1987), Thermobaricity, cabbeling, and water-mass conversion, *Journal of Geophysical Research*, *92*(C5), 5448.

McDougall, T. J. (1991), Parameterizing Mixing in Inverse Models, in: *Dynamics of Oceanic Internal Gravity Waves* (Muller, P., and D. Henderson, eds.), pp. 355–386, Honolulu, HI.

Meijers, A., and N. Bindoff (2011), Estimating the Four-Dimensional Structure of the Southern Ocean Using Satellite Altimetry, *Journal of Atmospheric and Oceanic Technology*, *28*(2004), 548–568.

Meinen, C. S., and D. R. Watts (2000), Vertical structure and transport on a transect across the North Atlantic Current near 42N: Time series and mean, *Journal of Geophysical Research*, *105*(C9), 21,869.

Messias, M.-J., A. Brousseau, N. Mackay, A. Watson, and S. Woodward (2011), *Tracer report RRS James Cook JC054*, Tech. rep.

Mills, B. (2014), Vertical mixing in the Scotia Sea from a tracer release experiment.

Muller, P., and M. Briscoe (2000), Diapycnal Mixing and Internal Waves, *Oceanography*, pp. 98–103.

Müller, P., D. J. Olbers, and J. Willebrand (1978), The Iwex spectrum, *Journal of Geophysical Research*, *83*(C1), 479.

Munk, W. (1966), Abyssal recipes, *Deep Sea Research*, *13*(4), 707–30.

Munk, W., and C. Wunsch (1998), Abyssal recipes II: energetics of tidal and wind mixing, *Deep Sea Research Part I: Oceanographic Research Papers*, *45*(12), 1977–2010.

Musgrave, D. L. (1985), A numerical study of the roles of subgyre-scale mixing and the western boundary current on homogenization of a passive tracer, *Journal of Geophysical Research*, *90*(C4), 7037.

Naveira Garabato, A. C., K. L. Polzin, B. A. King, K. J. Heywood, and M. Visbeck (2004), Widespread intense turbulent mixing in the Southern Ocean., *Science*, *303*(5655), 210–3.

Naveira Garabato, A. C., D. P. Stevens, and K. J. Heywood (2003), Water Mass Conversion, Fluxes, and Mixing in the Scotia Sea Diagnosed by an Inverse Model, *Journal of Physical Oceanography*, *33*(12), 2565–2587.

Naveira Garabato, A. C., D. P. Stevens, A. J. Watson, and W. Roether (2007), Short-circuiting of the overturning circulation in the Antarctic Circumpolar Current., *Nature*, *447*(7141), 194–7.

Nikurashin, M., and R. Ferrari (2010a), Radiation and Dissipation of Internal Waves Generated by Geostrophic Motions Impinging on Small-Scale Topography: Application to the Southern Ocean, *Journal of Physical Oceanography*, *40*(9), 2025–2042.

Nikurashin, M., and R. Ferrari (2010b), Radiation and Dissipation of Internal Waves Generated by Geostrophic Motions Impinging on Small-Scale Topography: Theory, *Journal of Physical Oceanography*, *40*(5), 1055–1074.

Nikurashin, M., and R. Ferrari (2011), Global energy conversion rate from geostrophic flows into internal lee waves in the deep ocean, *Geophysical Research Letters*, *38*(8).

Nikurashin, M., and R. Ferrari (2013), Overturning circulation driven by breaking internal waves in the deep ocean, *Geophysical Research Letters*, *40*(12), 3133–3137.

Nikurashin, M., R. Ferrari, N. Grisouard, and K. Polzin (2014), The impact of finite amplitude bottom topography on internal wave generation in the Southern Ocean, *Journal of Physical Oceanography*.

Oakey, N. S. (1982), Determination of the Rate of Dissipation of Turbulent Energy from Simultaneous Temperature and Velocity Shear Microstructure Measurements, *Journal of Physical Oceanography*, *12*(3), 256–271.

Olbers, D., D. Borowski, C. Völker, and J.-O. Wölff (2004), The dynamical balance, transport and circulation of the Antarctic Circumpolar Current, *Antarctic Science*, *16*(4), 439–470.

Olbers, D., and M. Visbeck (2005), A Model of the Zonally Averaged Stratification and Overturning in the Southern Ocean, *Journal of Physical Oceanography*, *35*(7), 1190–1205.

Osborn, T. R. (1980), Estimates of the Local Rate of Vertical Diffusion from Dissipation Measurements, *Journal of Physical Oceanography*, *10*(1), 83–9.

Osborn, T. R., and C. S. Cox (1972), Oceanic fine structure, *Geophysical Fluid Dynamics*, *3*(1), 321–345.

Polzin, K. L. (1999), *A Rough Recipe for the Energy Balance of Quasi-Steady Internal Lee Waves*, Tech. rep., Woods Hole Oceanographic Institution.

Polzin, K. L. (2004), Idealized Solutions for the Energy Balance of the Finescale Internal Wave Field, *Journal of Physical Oceanography*, *34*(1), 231–246.

Polzin, K. L., A. C. Naveira Garabato, T. N. Huussen, B. M. Sloyan, N. Stephanie, W. Hole, N. O. Centre, and S. Diego (2013), Finescale Parameterizations of Turbulent Dissipation, *Reviews of Geophysics*, (1), 1–30.

Polzin, K. L., J. M. Toole, J. R. Ledwell, and R. W. Schmitt (1997), Spatial Variability of Turbulent Mixing in the Abyssal Ocean, *Science*, *276*(5309), 93–96.

Polzin, K. L., J. M. Toole, and R. W. Schmitt (1995), Finescale Parameterizations of Turbulent Dissipation, *Journal of Physical Oceanography*, *25*(3), 306–328.

Prather, M. J. (1986), Numerical advection by conservation of second-order moments, *Journal of Geophysical Research*, *91*(D6), 6671.

Rahmstorf, S. (2002), Ocean circulation and climate during the past 120,000 years., *Nature*, *419*(6903), 207–14.

Rintoul, S. (2006), The Global Influence of the Southern Ocean Circulation, in: *Proceedings of 8 ICSHMO, Foz do Iguaçu, Brazil, April 2428, 2006, INPE*, pp. 1349–1354, Brazil.

Rintoul, S. R. (2009), Antarctic Circumpolar Current, in: *Encyclopedia of Ocean Sciences* (Steele, J. H., K. K. Turekian, and S. A. Thorpe, eds.), 2nd edn., pp. 178–190, Elsevier.

Ruddick, B., D. Walsh, and N. Oakey (1997), Variations in Apparent Mixing Efficiency in the North Atlantic Central Water, *Journal of Physical Oceanography*, *27*(12), 2589–2605.

Rudnick, D. L., T. J. Boyd, R. E. Brainard, G. S. Carter, G. D. Egbert, M. C. Gregg, P. E. Holloway, J. M. Klymak, E. Kunze, C. M. Lee, M. D. Levine, D. S. Luther, J. P. Martin, M. A. Merrifield, J. N. Moum, J. D. Nash, R. Pinkel, L. Rainville, and T. B. Sanford (2003), From tides to mixing along the Hawaiian ridge, *Science*, *301*(5631), 355–7.

Sandstrom, J. (1908), Dynamische Versuche mit Meerwasser, *Ann. Hydrog. Mar. Meteorol*, *36*, 6–23.

Sandwell, D., S. Gille, and W. Smith (2002), *Bathymetry from Space: Oceanography, Geophysics, and Climate*, Tech. rep., Geoscience Professional Services, Bethesda.

Schmitt, R. W. (1994), Double Diffusion in Oceanography, *Annual Review of Fluid Mechanics*, *26*(1), 255–285.

Schuert, E. A. (1970), Turbulent diffusion in the intermediate waters of the North Pacific Ocean, *Journal of Geophysical Research*, *75*(3), 673–682.

Scott, R. B., J. A. Goff, A. C. Naveira Garabato, and A. J. G. Nurser (2011), Global rate and spectral characteristics of internal gravity wave generation by geostrophic flow over topography, *Journal of Geophysical Research*, *116*(C9), C09,029.

Sheen, K. L., J. A. Brearley, A. C. Naveira Garabato, D. A. Smeed, S. Waterman, J. R. Ledwell, M. P. Meredith, L. St. Laurent, A. M. Thurnherr, J. M. Toole, and A. J. Watson (2013), Rates and mechanisms of turbulent dissipation and mixing in the Southern Ocean: Results from the Diapycnal and Isopycnal Mixing Experiment in the Southern Ocean (DIMES), *Journal of Geophysical Research: Oceans*, *118*(6), 2774–2792.

Sloyan, B. M. (2005), Spatial variability of mixing in the Southern Ocean, *Geophysical Research Letters*, *32*(18), L18,603.

Smethie, W. M., P. Schlosser, G. Bönisch, and T. S. Hopkins (2000), Renewal and circulation of intermediate waters in the Canadian Basin observed on the SCICEX 96 cruise, *Journal of Geophysical Research*, *105*(C1), 1105.

Smith, W. H., and D. Sandwell (1997), Global Sea Floor Topography from Satellite Altimetry and Ship Depth Soundings, *Science*, *277*(5334), 1956–1962.

Speer, K., S. R. Rintoul, and B. Sloyan (2000), The Diabatic Deacon Cell, *Journal of Physical Oceanography*, *30*(12), 3212–3222.

St. Laurent, L. C. (2002), Estimating tidally driven mixing in the deep ocean, *Geophysical Research Letters*, *29*(23), 2106.

St. Laurent, L. C., A. C. Naveira Garabato, J. R. Ledwell, A. M. Thurnherr, J. M. Toole, and A. J. Watson (2012), Turbulence and Diapycnal Mixing in Drake Passage, *Journal of Physical Oceanography*, *42*(12), 2143–2152.

St. Laurent, L. C., and R. W. Schmitt (1999), The Contribution of Salt Fingers to Vertical Mixing in the North Atlantic Tracer Release Experiment, *Journal of Physical Oceanography*, *29*(7), 1404–1424.

St. Laurent, L. C., J. M. Toole, and R. W. Schmitt (2001), Buoyancy Forcing by Turbulence above Rough Topography in the Abyssal Brazil Basin, *Journal of Physical Oceanography*, *31*(12), 3476–3495.

Stommel, H., and A. Arons (1960), On the abyssal circulation of the world ocean II. An idealized model of the circulation pattern and amplitude in oceanic basins, *Deep Sea Research (1953)*, *6*(August), 217–233.

Thorpe, S. A. (1975), The excitation, dissipation, and interaction of internal waves in the deep ocean, *Journal of Geophysical Research*, *80*(3), 328–338.

Toggweiler, J., and B. Samuels (1995), Effect of drake passage on the global thermohaline circulation, *Deep Sea Research Part I: Oceanographic Research Papers*, *42*(4), 477–500.

Trenberth, K. E., and J. M. Caron (2001), Estimates of Meridional Atmosphere and Ocean Heat Transports, *Journal of Climate*, *14*(16), 3433–3443.

Waterman, S., A. C. Naveira Garabato, and K. L. Polzin (2013), Internal Waves and Turbulence in the Antarctic Circumpolar Current, *Journal of Physical Oceanography*, *43*(2), 259–282.

Watson, A. J., J. R. Ledwell, M.-J. Messias, B. A. King, N. Mackay, M. P. Meredith, B. Mills, and A. C. Naveira Garabato (2013), Rapid cross-density ocean mixing at mid-depths in the Drake Passage measured by tracer release, *Nature*, *501*(7467), 408–411.

Watson, A. J., M. Messias, E. Fogelqvist, K. A. V. Scoy, T. Johannessen, K. I. C. Oliver, D. P. Stevens, F. Rey, T. Tanhua, K. A. Olsson, F. Carse, K. Simonsen, J. R. Ledwell, E. Jansen, D. J. Cooper, J. A. Kruepke, and E. Guilyardi (1999), Mixing and convection in the Greenland Sea from a tracer-release experiment, *Nature*, *401*, 902–4.

Wu, L., Z. Jing, S. Riser, and M. Visbeck (2011), Seasonal and spatial variations of Southern Ocean diapycnal mixing from Argo profiling floats, *Nature Geoscience*, *4*(6), 363–366.

Wunsch, C. (1998), The Work Done by the Wind on the Oceanic General Circulation, *Journal of Physical Oceanography*, *28*(11), 2332–340.

Wunsch, C., and R. Ferrari (2004), Vertical Mixing, Energy, and the General Circulation of the Oceans, *Annual Review of Fluid Mechanics*, *36*(1), 281–314.

Zika, J. D., B. M. Sloyan, and T. J. McDougall (2009), Diagnosing the Southern Ocean Overturning from Tracer Fields, *Journal of Physical Oceanography*, *39*(11), 2926–2940.